

Industrial Gas Separations

Industrial Gas Separations

Thaddeus E. Whyte, Jr., EDITOR
Catalytica Associates, Inc.

Carmen M. Yon, EDITOR
Union Carbide Corporation

Earl H. Wagener, EDITOR
Dow Chemical Company

Based on a symposium sponsored
by the ACS Division of Industrial
and Engineering Chemistry,
Washington, D.C.,
June 14–15, 1982

A C S S Y M P O S I U M S E R I E S **223**

AMERICAN CHEMICAL SOCIETY
WASHINGTON, D. C. 1983



Library of Congress Cataloging in Publication Data

Industrial gas separations.

(ACS symposium series, ISSN 0097-6156; 223)

"Based on a symposium sponsored by the ACS Division of Industrial and Engineering Chemistry, Washington, D.C., June 14-15, 1982."

Includes bibliographies and index.

1. Gases—Separation—Congresses. I. Whyte, Thaddeus E., 1937— . II. Yon, Carmen M., 1939— . III. Wagener, Earl H. IV. American Chemical Society. Division of Industrial and Engineering Chemistry. V. Series.

TP242.I65 1983 660.2842 83.6440
ISBN 0-8412-0780-1 1983

Copyright © 1983

American Chemical Society

All Rights Reserved. The appearance of the code at the bottom of the first page of each article in this volume indicates the copyright owner's consent that reprographic copies of the article may be made for personal or internal use or for the personal or internal use of specific clients. This consent is given on the condition, however, that the copier pay the stated per copy fee through the Copyright Clearance Center, Inc. for copying beyond that permitted by Sections 107 or 108 of the U.S. Copyright Law. This consent does not extend to copying or transmission by any means—graphic or electronic—for any other purpose, such as for general distribution, for advertising or promotional purposes, for creating new collective work, for resale, or for information storage and retrieval systems. The copying fee for each chapter is indicated in the code at the bottom of the first page of the chapter.

The citation of trade names and/or names of manufacturers in this publication is not to be construed as an endorsement or as approval by ACS of the commercial products or services referenced herein; nor should the mere reference herein to any drawing, specification, chemical process, or other data be regarded as a license or as a conveyance of any right or permission, to the holder, reader, or any other person or corporation, to manufacture, reproduce, use, or sell any patented invention or copyrighted work that may in any way be related thereto.

PRINTED IN THE UNITED STATES OF AMERICA

**American Chemical
Society Library**

1155 16th St. N. W.

In Industrial Gas Separations, Whyte, Thaddeus E., ed.; ACS Symposium Series; American Chemical Society: Washington, DC, 1983.

ACS Symposium Series

M. Joan Comstock, *Series Editor*

Advisory Board

David L. Allara

Robert Baker

Donald D. Dollberg

Brian M. Harney

W. Jeffrey Howe

Herbert D. Kaesz

Marvin Margoshes

Donald E. Moreland

Robert Ory

Geoffrey D. Parfitt

Theodore Provder

Charles N. Satterfield

Dennis Schuetzle

Davis L. Temple, Jr.

Charles S. Tuesday

C. Grant Willson

FOREWORD

The ACS SYMPOSIUM SERIES was founded in 1974 to provide a medium for publishing symposia quickly in book form. The format of the Series parallels that of the continuing ADVANCES IN CHEMISTRY SERIES except that in order to save time the papers are not typeset but are reproduced as they are submitted by the authors in camera-ready form. Papers are reviewed under the supervision of the Editors with the assistance of the Series Advisory Board and are selected to maintain the integrity of the symposia; however, verbatim reproductions of previously published papers are not accepted. Both reviews and reports of research are acceptable since symposia may embrace both types of presentation.

PREFACE

NEW SEPARATION TECHNIQUES, particularly for improving gas technologies, have increased dramatically in recent years. These advances have stemmed not only from the obvious needs to reduce process costs and environmental pollution, but also from the synthesis and identification of novel materials. Such materials include unique membranes and zeolites.

The use of membranes to separate gases commercially is a relatively new application. Both Du Pont and Union Carbide had ventures in the early 1970s for recovering H₂ and He from industrial processes, but these projects were never fully commercialized. Recently, however, a combination of improved economics and better technology has resulted in membrane products that signal a new era in the commercial use of membranes for large-scale gas separation.

Diffusion processes in polymers have been studied since the 1860s, and gas diffusion in polymers was studied intensively in the 1950s and 1960s by such notables as Weller, Steiner, Kammermeyer, Stannett, Michaels, Rogers, and Stern. Although these studies generated a large amount of permeability data for gas diffusion through polymers, industrial applications were not implemented until nearly 15 years later. Clearly, the use of membranes to separate gases commercially is not a simple task. Companies currently trying to commercialize such processes are well aware of the need to combine basic understanding with sophisticated fabrication technology.

Both the understanding of gas transport and the number of engineering ventures that are using membranes have been growing rapidly. This symposium explores gas-transport mechanisms and models and presents several industrial applications of gas membranes. Although agreement on the transfer mechanism has not yet been reached for either mixed- or single-gas permeation, the understanding is sufficient to develop both energy- and cost-effective purification and bulk separation processes for industrial use.

Adsorption separation—an important unit operation in the separation of industrial gases—is achieved by adsorbing one or more component(s) onto the active sites of a solid adsorbent. For cyclic processes, the solid is regenerated by shifting the equilibrium toward the gas phase by increasing the adsorbent temperature or by decreasing the partial pressure of the adsorbate in the gas. Some of the more important commercial combinations

of adsorbents and regeneration techniques are discussed in a paper in this symposium. As the understanding of cyclic adsorption processes has developed, more and more of the assumptions used in designing systems have been reexamined and discarded for more rigorous treatments. Many more sophisticated models of the adsorption phenomenon are being postulated, such as that offered for pressure swing separation of light gases. In other separations, the molecular size dimensions of the microporous solids are used to control kinetic selectivity as well as or in place of adsorptive selectivity. For example, the natural zeolite clinoptilolite is used for the separation of methane and nitrogen. In some adsorptive processes, the bonding energy associated with adsorption is similar in magnitude to that of a chemical reaction. For such cases, the regeneration may be achieved more effectively by shifting a chemical reaction equilibrium. Such an approach has been used for an iron oxide sorbent. The papers presented cover the spectrum of applications, adsorbents, and types of cycles.

Absorption is another unit operation that has many parallels to adsorption. Although the sorption media is liquid rather than solid, many of the underlying principles are the same. Most commercial applications for purification and bulk separation involve weak physical bonding of absorbate to absorbent. Again, regeneration of sorbent is accomplished by increasing the liquid temperature and/or by decreasing absorbate partial pressure. This volume contains a discussion of a process for recovering methane from hydrogen and carbon monoxide using liquid propane—a separation that might also have been attempted with a suitable solid adsorbent. Another state-of-the-art approach—the removal of acid gases (sulfur compounds and carbon dioxide)—is detailed; in this process the contaminant carbon dioxide becomes both an active adsorbent and a component of an absorptive fluid.

THADDEUS E. WHYTE, JR.
Catalytica Associates, Inc.
Santa Clara, CA

CARMEN M. YON
Union Carbide Corporation
Tarrytown, NY

EARL H. WAGENER
Dow Chemical Company
Walnut Creek, CA

February 28, 1983

Helium Recovery Using Semipermeable Membranes

F. E. MARTIN

Westinghouse Oceanic Division, Annapolis, MD 21404

T. S. SNYDER and E. J. LAHODA

Westinghouse Research & Development Center, Pittsburgh, PA 15235

A series of pure gas and gas mixture tests were performed, using a unique closed-circuit experimental loop. Based on data from continuous loop operations, a preliminary system design and economic evaluation were performed to recover helium from deep sea diving gas applications. This program was performed under Navy Contract N60921-79-C-A037 for the Naval Surface Weapons Center G-52. Membrane permeability was determined as a function of driving pressure and feed concentration for a single membrane element. Based on this data, a hypothetical design of a system to meet naval specifications was performed only as a contractual requirement with the Navy and is not intended as a specific Westinghouse system. Westinghouse at this time plans no such system for market. Projections based on the experimental data for the hypothetical system show that the least pure gas considered for the design, 58 mole % helium, could be enriched to better than 99.99% helium in five permeator stages. This gas could be enriched, hypothetically, to a physiologically acceptable quality in 3 stages. Carbon dioxide concentration in the gas is the design limiting parameter. This is a very conservative design estimate. The conservatism is necessary due to the limited nature of the design data.

The U. S. Navy, in pursuit of its many deep diving programs, must currently deal with exponentially rising costs and numerous supply difficulties concerning its prime diluent for breathing gas-helium. The logistics problems of providing large quantities of high pressure gas to remote diving sites over extended dive intervals, regardless of weather conditions, are difficult to quantify. However, provision for an indefinite supply of diluent via an on-board device that recycles expended gas, with relatively minor penalty to operational/maintenance costs and deck space,

0097-6156/83/0223-0001\$07.25/0

© 1983 American Chemical Society

In Industrial Gas Separations; Whyte, T., et al.;
ACS Symposium Series; American Chemical Society: Washington, DC, 1983.

would appear to be desirable. The benefit both to program contingency planning and to dive safety could be substantial, even if the device were relegated to a backup or supplemental mode of operation.

More amenable to quantitative and objective analysis is the economic incentive for developing a recycle system. It was predicted in 1974(1) that, for helium recovery at the well-head, a cost growth average of 17.9% per year could be anticipated for the decade succeeding that report. However, it is further predicted that natural gas fields bearing $\leq 0.3\%$ helium will be depleted by 1990-95, at which time fields bearing $\leq 0.1\%$ must be used. This would produce a sharp price escalation to wholesale prices five times then-current rates. Thereafter, projections are entirely dependent on how, whether, and when helium conservation and reserve storage policies are implemented, and on whether future air separation technology will enable competitive extraction of helium from the atmosphere.

The Navy, which, by our conservative estimate, (2) is a current user of some 2,800,000 std ft³ of helium per year, would benefit substantially from a shipboard system that could capture 90-95% of currently wasted helium and condition it to acceptable purity for re-use. The definition of acceptable purity is as shown in Table I, wherein the design goals and design requirements are set forth. The design goal reflects helium purity as found in bottle supplies meeting the referenced specification, Grade A, whereas the design requirement is derived from an assortment of analyses based on the practical, operational constraints on a diver's diluent gas. As per note 2 of Table I, the design requirement can allow as much as 1% O₂ and 1% N₂, and consequent drop of He to 97.8%, without impairing or jeopardizing the user; however, the design was to include sizing to the 99.995% design goal level to obtain an estimate for maximum design capacity needed.

Experimental System Description

Figure 1 is a schematic of the experimental loop constructed by the Westinghouse Oceanic Division to evaluate semipermeable gaseous membranes for helium recovery. The key system components in Figure 1 are the permeator modules, compressor, aftercooler, humidifier and the online gas chromatograph for sample analyses. This test system was unique in that it allowed closed circuit flow of multicomponent gas mixtures to the membrane for separation, followed by immediate recombination of the permeate and residual streams for recycle to the feed side. This arrangement permitted a constant volumetric feed rate to the membrane for prolonged periods without requiring prohibitive and costly gas inventory. Further, the experimental configuration provided complete monitoring and control capabilities over such parameters as back-pressure, split-stream flow rates, gas temperature, humidity and composition.

Table I. Helium Purity Goals and Requirements

Component	Design ⁽¹⁾ Goal	Design ⁽¹⁾ Requirement	Rationale for Requirements
Helium (minimum %)	99.995	99.8 ⁽²⁾	Federal Specification BB-H-11680, Type I, Grade B
Water Vapor (ppm)	10	200	30°F dew point at 1000 ft
Oxygen (ppm)	2	1%	$p_{O_2} = 0.3$ atm at 850 ft
Nitrogen (%)	0	1%	Results in same p_{N_2} at 850 ft as initially pressurizing chamber to 14 ft with air
Carbon Dioxide (ppm)	0	100	$p_{CO_2} = 0.003$ atm at 850 ft
Carbon Monoxide (ppm)	0	12	OSHA exposure limit
Gaseous Hydrocarbons measured as Methane (ppm)	1	1	Federal Specification BB-H-11686, Type I, Grade C
Oil (mg/liter)	0	0.001	OSHA exposure limit
All others (ppm)	37	37	Federal Specification BB-H-11680, Type I, Grade A
NOTES: (1) Maximum values by volume, unless otherwise indicated (2) May be further reduced by the amount of oxygen and nitrogen present			

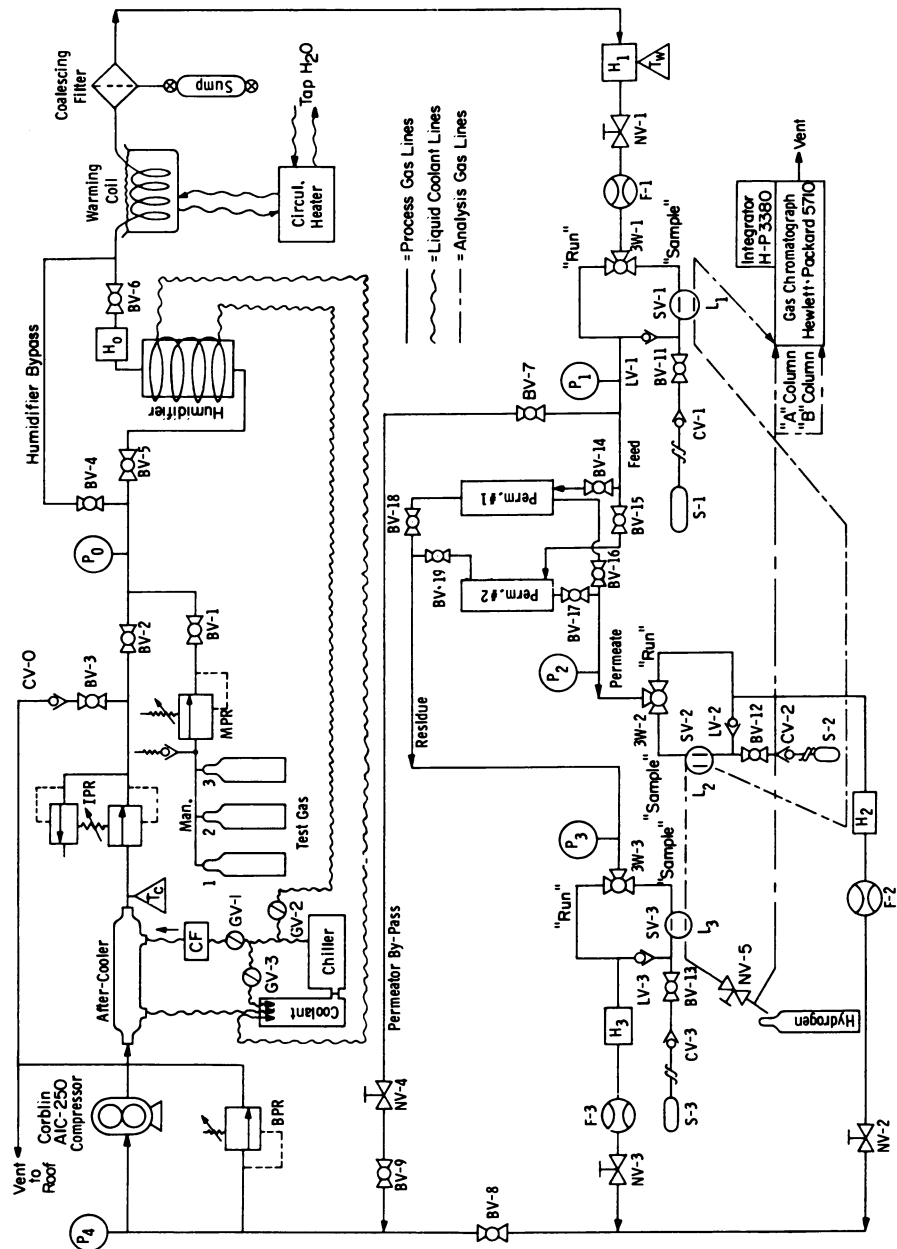





Figure 1. Helium reclaim test schematic.


PARAMETER EQUIPMENT


 F₁, F₂, F₃
Brooks Instruments' Model No. 5812 mass flow sensor and indicator/power supply model No. 5820, calibrated for 0-200 SLPM operation at 1000 psig. Helium, ±1% full-scale accuracy, < 1% linearity from 1000 to 200 psig, 1-2% from 200 * 0 psig


L₁, L₂, L₃
Hewlett-Packard 5700A gas chromatograph, featuring an H-P 3380A data integrator, and utilizing Alltech Assoc. No. 5680PC packed columns of Carbosphere 60/80. Samples injected via Valco Instruments' Model No. 4V6-HPaX valve with 100 µ liter loop into a hydrogen carrier gas stream.


 H₀, H₁, H₂, H₃
Panametries' hygrometer/thermistor probe No. M221RT for use with No. 2830 sample cells and model no. 2100-151(F)-161(B) multi-channel hygrometer (-60 to +60°C dewpoint and -30 to +70°C temperature range, electrical accuracy 1% of input, readability 0.5% of full scale)

 P₁, P₂, P₃
Matheson test gauge model 63-5613, 0-1400 psig, 0.25% accuracy

 P₄, P₀
Matheson standard gauge model 63-3123, 0-2000 psig, 2-3% accuracy

 CF
RCM Industries' liquid flowmeter, model 1/2 in.-7-1-R-2.

 T_c
Established via Dunham-Bush chiller, model no. CCP-45Q per dwg. no. C2-C03828, providing coolant flow to compressor after-cooler; sensed by Panametries M-2 thermister probe in no. 2830 cell.

 T_w
Established via Precision Scientific circulating heater, Model 200, cat. no. 66613, serial no. 20 AK-5; sensed at H₁.

Additional equipment includes the manifold pressure regulator (MPR), Matheson Model no. 3-580; the inlet pressure regulator (IPR), Matheson Model no. 3075-1/4; the back-pressure regulator (BPR), Grove Valve Co's model no. 155 per Figure no. 11410-F-P2-A; and the Corblin AIC-250 metal-diaphragm compressor, serial no. 1430.

Valving consists of the following.

TYPE	CODE	SOURCE	PART NO.
Ball Valves	BV-1 to BV-10 BV-14 to BV-19	Whitey	SS-43S4
Ball Valves	BV-11 to BV-13	Whitey	SS-41S2
Check Valves	LV-1 to LV-3	Nu Pro	SS-2C-1
Check Valves	CV-0 to CV-4	Nu Pro	SS-4CA-3
Needle Valves	NV-1 and NV-4	Whitey	SS-3 IRS4
Needle Valves	NV-2 and NV-3	Whitey	SS-2 IRS4
3-Way Valves	3W-1 to 3W-3	Whitey	SS-43XS4
Sampling Valves	SV-1 to SV-3	Valco	4V6-HPaX
1/2 in. Gate Valves	GV-1 to GV-3	Any	with 100 µl coil

Key to Figure 1.

Figure 2 describes the spiral-wound cellulose acetate membranes used in this testing series. Other types of permeators, e.g., hollow-fiber type of either polyamide or polysulfone, were considered, but could not be obtained within the time constraints of this program. Membrane operation and the final geometry of the loaded housing are described in Figure 2. The effective area for the cellulose acetate membrane used during the study was $\sim 1.7 \text{ ft}^2$. Membrane modules of other area sizes were either defective on receipt from the manufacturer or damaged during startup. This precluded obtaining scaling data for membrane area during the study.

Table II lists the feed gas compositions used for the study to determine the effects of feed composition on membrane performance. The different compositions are representative of diving gas mixtures used at various depths. Both the individual component permeabilities and the mixture permeabilities were evaluated at several different pressure drops up to 1200 psig feed pressure.

Table II
Feed Gas Composition

<u>Component</u>	<u>Mix #1</u>	<u>Mix #2</u>	<u>Mix #3</u>	<u>Mix #4</u>
	<u>By Volume Percent</u>			
Helium	79.7	92.5	95.4	(58.0)
Nitrogen	15.9	5.9	3.6	(11.5)
Oxygen	4.3	1.6	1.0	(30.0)
Carbon Dioxide	0.075	0.027	0.017	(0.526)
Representative Depth (ft)	200.	600.	1000.	0 to 200
Expt'l Run Numbers	201-204	181-184	191-194	

Note: Experimental difficulties pre-empted the experiments using Mix #4.

Calculations: Permeability Constants, Separation Factors and
Scaling of Results for System Design

The definition of a species' permeability in a given membrane is the product of its diffusivity and solubility in the membrane. It is this product which also results in the membrane's selectivity for one component of a mixture over another(9). However, since the permeability is actually a complicated function of the diffusivity and solubility, it is empirically measured and calculated by Equation 1.

$$q_i = k_i A \Delta p_i \quad (1)$$

where:

q_i = flow of component through the membrane
A = membrane area

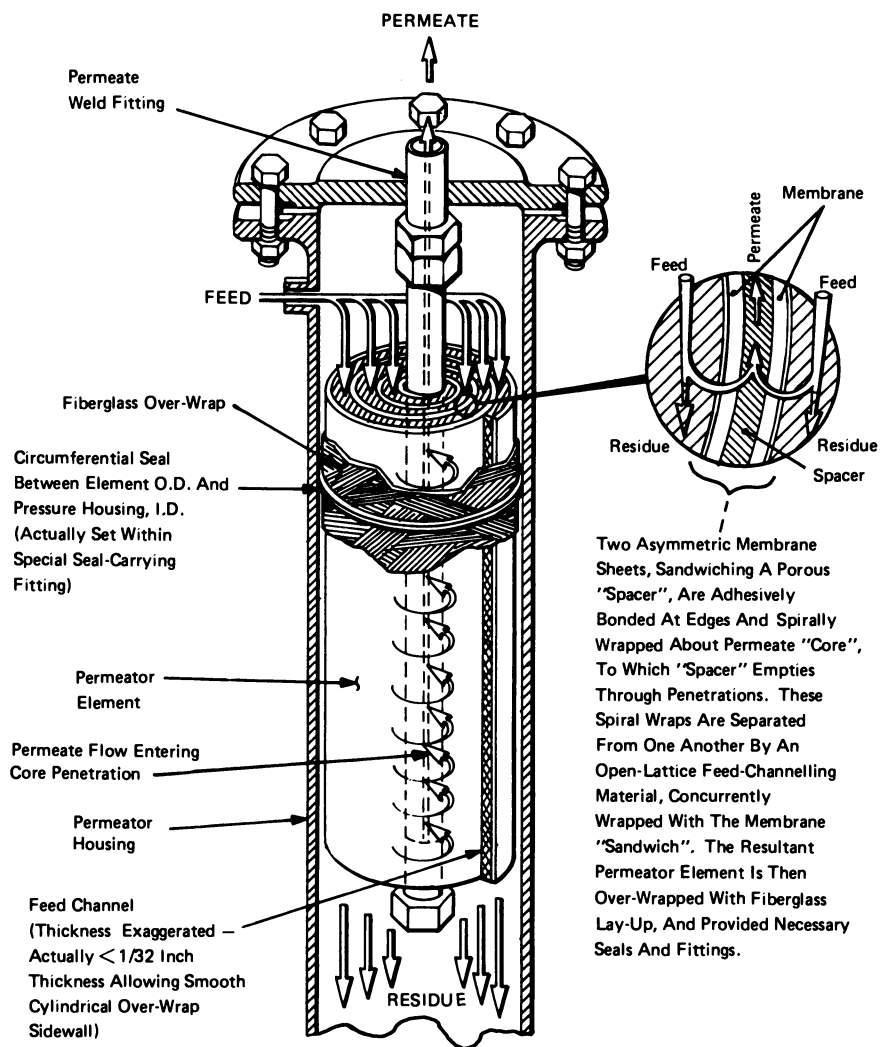


Figure 2. Spiral-wound permeator configuration.

p_i = partial pressure of component i
 k_i = permeability constant for component i

Table III describes the permeability constants as determined by this set of experiments.

As Figure 3 shows, strict application of Equation 1 results in 11 equations in 11 unknowns and an iterative solution for the design sequence. To circumvent this cumbersome calculation, the system permselectivity was used to estimate the number of stages required in the design sequence for the separation, and Equation (1) was then used to estimate the area requirements knowing the stage outlet compositions of the permeate and residual streams.

In addition, separation factors were selected as the method of scaling the data, rather than the permeability coefficients, because this method provides a more reliable fit of the limited data available. The data was limited because the 58% helium mixture in Table II was not studied experimentally due to plasticization by water vapor of the last workable membrane module. In addition to being the most common helium mixture which the prototype would encounter, this mixture represents lower values of the ratio $\beta = [\text{He}]/[\text{component } i]$ than studied experimentally. Using the separation factors, the values of $\beta_{\text{feed}}/\beta_{\text{permeate}}$ for the 58% helium mixture lie between the origin (0,0), a fixed boundary, and the existing data when plotting $\beta_{\text{feed}}/\beta_{\text{permeate}}$. Use of permeabilities would require extrapolation as opposed to separation factor interpolation. Therefore, the separation factor was selected for scaling.

The permselectivities, or separation factors, defined by Equation (3) were used to scale the experimental data for design purposes. The system permselectivity is analogous to the distillation separation factor

$$[\text{Sep. factor}]_{\chi}^{\text{He}} = \frac{(p_{\text{He}})_{\text{feed}}}{(p_{\chi})_{\text{feed}}} / \frac{(p_{\text{He}})_{\text{permeate}}}{(p_{\chi})_{\text{permeate}}} \quad (3)$$

discussed by McCabe & Smith(3) and by Treybal(5), defined by Equation (4), the relative volatility α_{ij} , for a binary system.

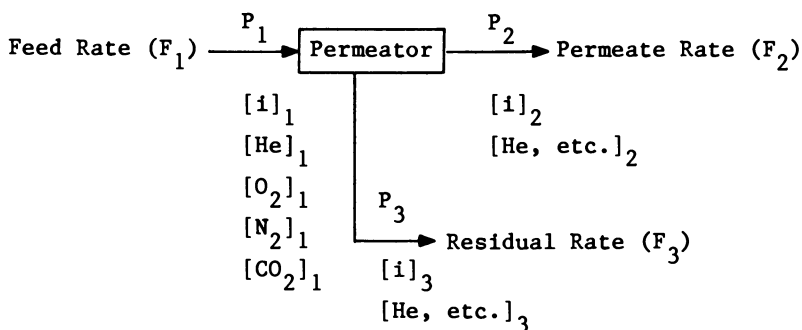
$$\alpha_{ij} = p_i^{\circ}/p_j^{\circ} = (p_A/p_B)_{\text{vapor}} / (p_A/p_B)_{\text{liquid}} \quad (4)$$

The permselectivity for membrane separations can also be calculated by substituting fugacities calculated from an equation of state, here using the Beattie-Bridgeman equation, into Equation (3) for the partial pressure values (4). The values of the permselectivities in Table IV are relatively constant at a fixed feed composition in agreement with the approximately linear behavior noted in Figures 9-11.

Table III. Permeability Results

Run No.	① Dalton		$K_{N_2} (\Delta p_{N_2})$	$\frac{K_{He} (\Delta p_{He})}{K_{N_2} (\Delta p_{N_2})}$ Q_1		③ Permeate Concentrations		$\frac{[He]}{[N_2]}$ Q_2	Comments
	$K_{He} (\Delta p_{He})$	$K_{N_2} (\Delta p_{N_2})$		% [He]	% [N ₂]				
181	8.25 (w) 164.8	0.44 (w) 20.4	151.6	99.21	0.66	150.3	92.8% He, 5.63% N ₂ feed gas		
182	8.01 (w) 337.5	0.59 (w) 31.4	145.9	99.20	0.68	145.9			
183	7.72 (w) 510.5	0.71 (w) 42.5	130.6	99.09	0.76	130.4			
184	7.43 (w) 682.9	1.25 (w) 52.5	77.3	98.44	1.27	77.5			
185	6.31 (w) 859.4	2.94 (w) 59.0	31.3	96.13	3.08	31.2			
191	8.03 (w) 169.5	(0.48) (w) (13.4)	(211.6)	99.50	(0.47)	(211.7)	() Inaccurate because of failure to separate [O ₂] from [N ₂] in analysis		
192	8.05 (w) 353	0.72 (w) 20.7	190.7	99.44	0.52	191.2			
193	7.7 (w) 529.7	0.78 (w) 28.0	186.8	99.37	0.53	187.5			
194	7.2 (w) 704.2	0.79 (w) 35.3	181.8	99.37	0.55	180.7			
201	5.75 (w) 266.4	0.46 (w) 86.0	38.4	95.77	2.54	37.7	80.0% He, 15.6% N ₂ feed gas		
202	5.9 (w) 417.1	0.56 (w) 116.8	37.6	95.86	2.56	37.4			
203	6.2 (w) 567.7	0.65 (w) 147.7	36.7	95.83	2.61	36.7			
204	6.08 (w) 715.5	0.85 (w) 176.8	28.9	94.87	3.28	28.9			

 Q_1 from Permeation Rates calculated by Dalton's Law Q_2 from ratio of Permeate Concentrations



where P_1, P_2, P_3 = Pressure of F_1, F_2 and F_3 streams, respectively
and $[i]_1, [i]_2, [i]_3$ = concentration of i -th component in respective streams

Overall Material Balance, $F_1 = F_2 + F_3$

Component Material Balances, $F_1 [i]_1 = F_2 [i]_2 + F_3 [i]_3$

Flux Equations, $F_2 [i]_2 = k_1 A \left(\frac{[i]_1 P_1 + [i]_3 P_3}{2} - [i]_2 P_2 \right)$

% Recovery = $\frac{[i]_2 F_2}{[i]_1 F_1} \times 100$

To perform design analysis for Helium Reclaimer:

<u>Solve for</u>	<u>Using</u>
4 Permeate Components	4 Flux Equations
4 Residual Components	4 Component Material Balances
1 Permeate Rate	1 Overall Balance
1 Residual Rate	1 Sum of Compositions
1 Membrane Area	1 Definition of Recovery
<hr/>	<hr/>
Total	
11 Unknowns	11 Equations

Figure 3. Single-stage schematic and material balances.

Experimental Results and Discussion

To verify the membrane integrity prior to attempting separations, pure gas permeation rates for nitrogen and helium were determined and compared to the vendor's data supplied with the membrane. Figure 4 and Table V verify the vendor's data reasonably well for the only membrane which survived shipment and startup. The agreement of the nitrogen values is particularly indicative of the membrane's integrity.

Table IV
Separation Factors

<u>Feed Composition</u>		<u>Values Calculated from Fugacity</u>	
		<u>Runs 181-184</u>	
He	92.83	mole %	$\Delta P = 189$ psi $\alpha = 9.59$
CO ₂	.051		$\Delta P = 380$ psi $\alpha = 9.48$
O ₂	1.49		$\Delta P = 566$ psi $\alpha = 8.34$
N ₂	5.63		$\Delta P = 751$ psi $\alpha = 4.87$
H ₂ O	.008		
<u>Feed Composition</u>		<u>Runs 191-194</u>	
He	95.23		$\Delta P = 187$ psi $\alpha = 9.86$
CO ₂	0.013		$\Delta P = 381$ psi $\alpha = 8.80$
O ₂	1.06		$\Delta P = 568$ psi $\alpha = 7.84$
N ₂	3.71		$\Delta P = 751$ psi $\alpha = 7.85$
H ₂ O	.014		
<u>Feed Composition</u>		<u>Runs 201-204</u>	
He	79.96		$\Delta P = 376$ psi $\alpha = 5.64$
CO ₂	.076		$\Delta P = 568$ psi $\alpha = 5.78$
O ₂	4.34		$\Delta P = 756$ psi $\alpha = 5.75$
N ₂	15.60		
H ₂ O	0.22		
<u>Permeate Composition</u>	<u>Runs 181-184</u>	<u>Runs 191-194</u>	<u>Runs 201-204</u>
<u>Ratios</u>	<u>92.8% He</u>	<u>95.2% He</u>	<u>80% He</u>
at $\Delta P = 380$ psi			
He/sum	124	178	23
He/CO ₂	5221	19888	1570
He/O ₂	992	1421	60
He/N ₂	144	191	38
$\Delta P =$ pressure range	189- 751	187- 751	376- 941
He/sum	126- 63	199- 158	23- 18
He/CO ₂ *	5221-3786	14214-11041	1570-1843
He/O ₂ ²	1044- 365	1421- 2481**	53- 60
He/N ₂	150- 78	212- 181	28- 38

* first value of 3543 at 189 ΔP is anomalously low

** α increases as ΔP increases

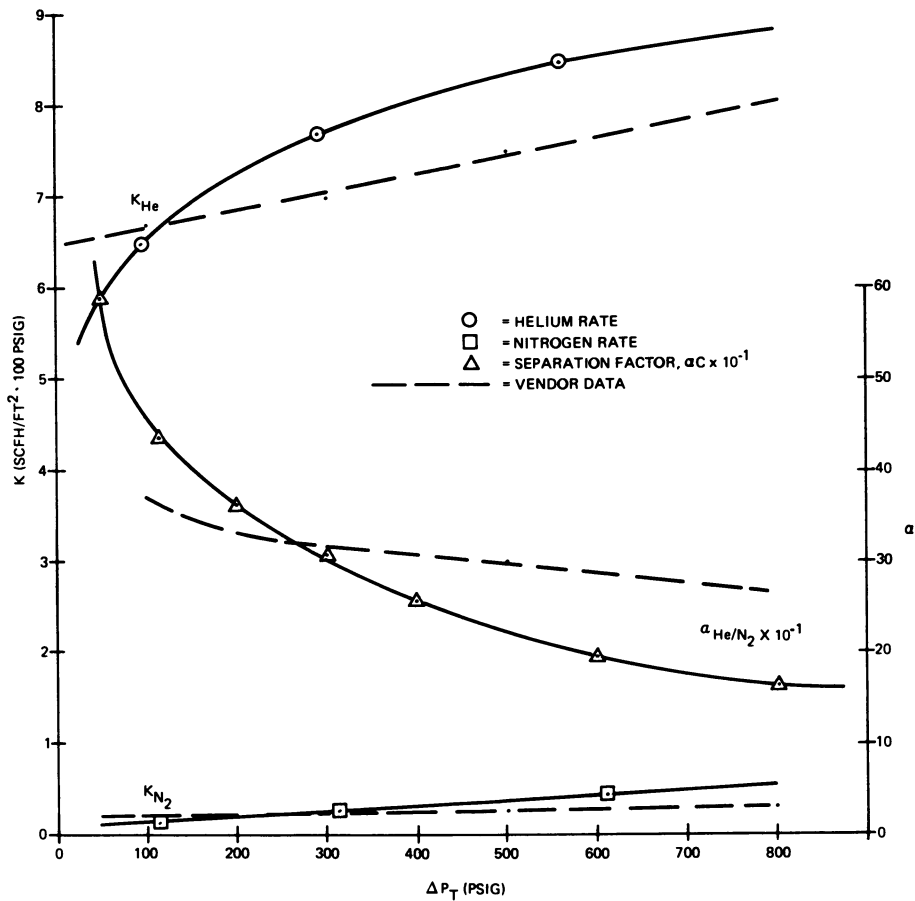


Figure 4. Pure gas permeation rates, Permeator Element No. 0003.

Table V. Comparative Permeability Rate Data - WEC Vs Vendor

Element	Run	Gas	WEC Data		Vendor Data		Ratios		Comments	
			ΔP	K_w	a_w	ΔP	K_y	a_y		K_w/K_y
No. 0003	171B	He	95	6.6	44.0	100	6.7	35.3	1.0	All ratios close to unity. Signifies intact membrane. Later confirmed by good He/N ₂ separation performance.
	161B	N ₂	115	0.15		100	0.19*		0.8	
	173B	He	557	8.5	19.8	575	7.6*	29.2	1.1	
	163B	N ₂	612	0.43		575	0.26*		1.6	

* = extrapolated value

Figure 5 shows that, during the experiments, helium recovery varied linearly with pressure drop for all three test mixtures. The 92% helium mixture, which was studied first, is displaced in the figure from its expected position (shown by the dotted line) except for the final data point. This final reading was taken at a pressure drop much higher than the vendor tests. This irreversibly compressed the membrane, altering its separation characteristics from the first four data points using 92% mixture, as verified by subsequent experiments on the 80% and 95% helium mixtures. Therefore, only the 80% and 95% mixture data were used for the design studies.

Helium Enrichment: Permeabilities and Separation Factors

Enrichment of the preferred gas, helium in this case, is most productively displayed as a plot of the feed concentration of this gas relative to the remainder gases (or to a less preferred gas in the mixture) versus the equivalent ratio in the permeate. This is thus a plot of feed ratio vs. flux ratio. If this is done for several feed compositions representing a significant preferred-gas composition range, enrichment curves can be generated, such as those displayed in Figures 6 and 7. Here it can be seen that the lower pressure differentials are more desirable from a permeate quality standpoint.

It can further be seen that helium is least efficiently enriched relative to carbon dioxide than to any other component. It is, therefore, enrichment with respect to CO_2 that becomes limiting and determines the number of stages necessary to achieve the purity levels set by Table I. In this respect, selection of a ~ 380 psi ΔP condition appears particularly favorable, since it yields the highest $[\text{He}]/[\text{CO}_2]$ enrichment.

Since these separation factors are the basis of the data scale-up procedure, Figures 8, 9, and 10 display the separation ratios for the 380 ΔP experimental data selected as the system design point.

In these experiments, the measured helium flux through the membrane was less than the flux predicted on the basis of the average bulk concentrations. Consequently, the helium permeability coefficients calculated from observed membrane flux and the bulk partial pressures are lower than the pure gas values obtained by the membrane supplier or independently by us. At the same time, observed nitrogen coefficients are higher than predicted.

Concentration polarization may be a possible explanation for this erratic permeability coefficient behavior; however, the influence of concentration polarization in gaseous exchange regimes such as the one herein reported is quite doubtful and subject to dispute(7). Alternative possibilities include (a) permeator functional loss due to on-going membrane compaction,

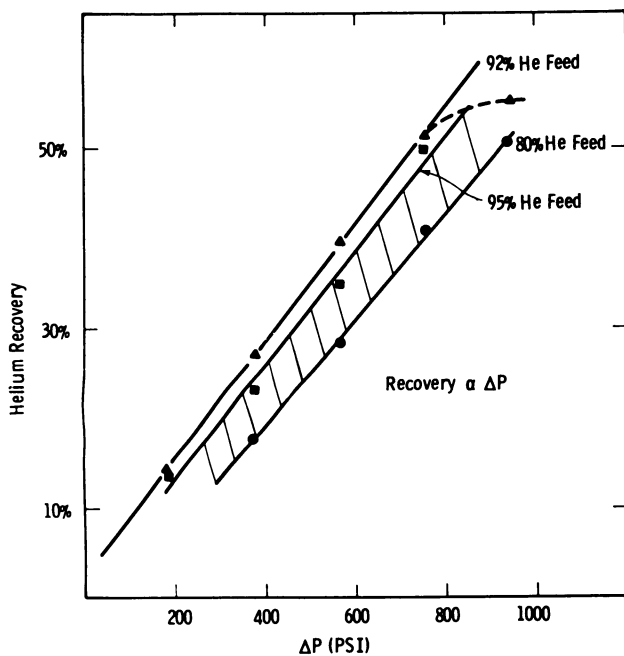


Figure 5. Recovery as a function of pressure drop.

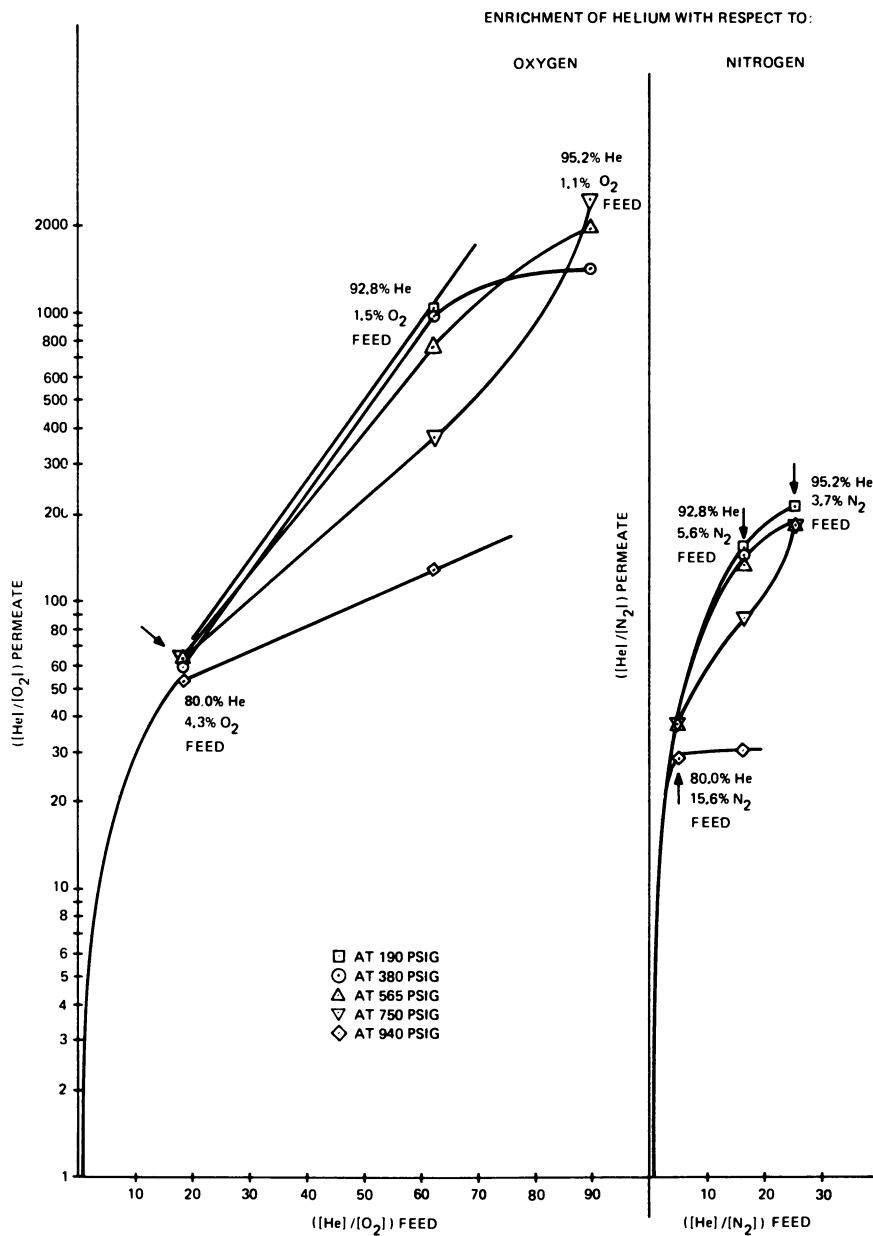


Figure 6. Enrichment of helium with respect to oxygen and nitrogen.

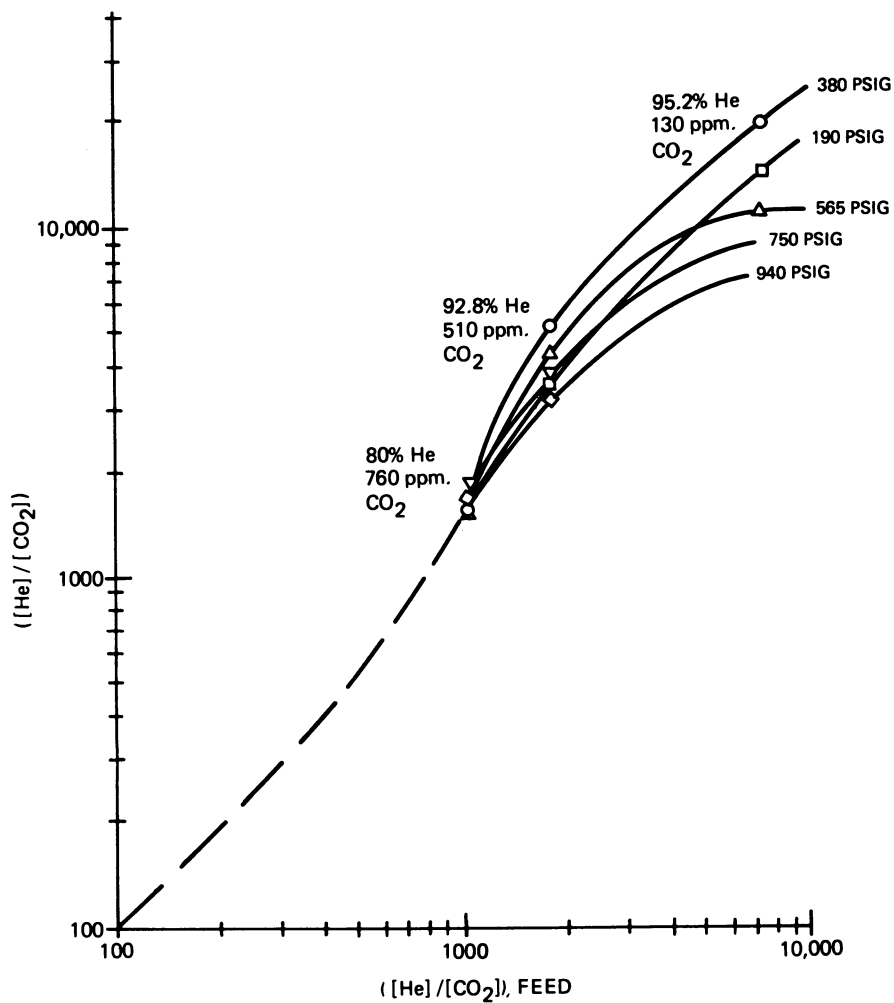


Figure 7. Enrichment of helium with respect to carbon dioxide.

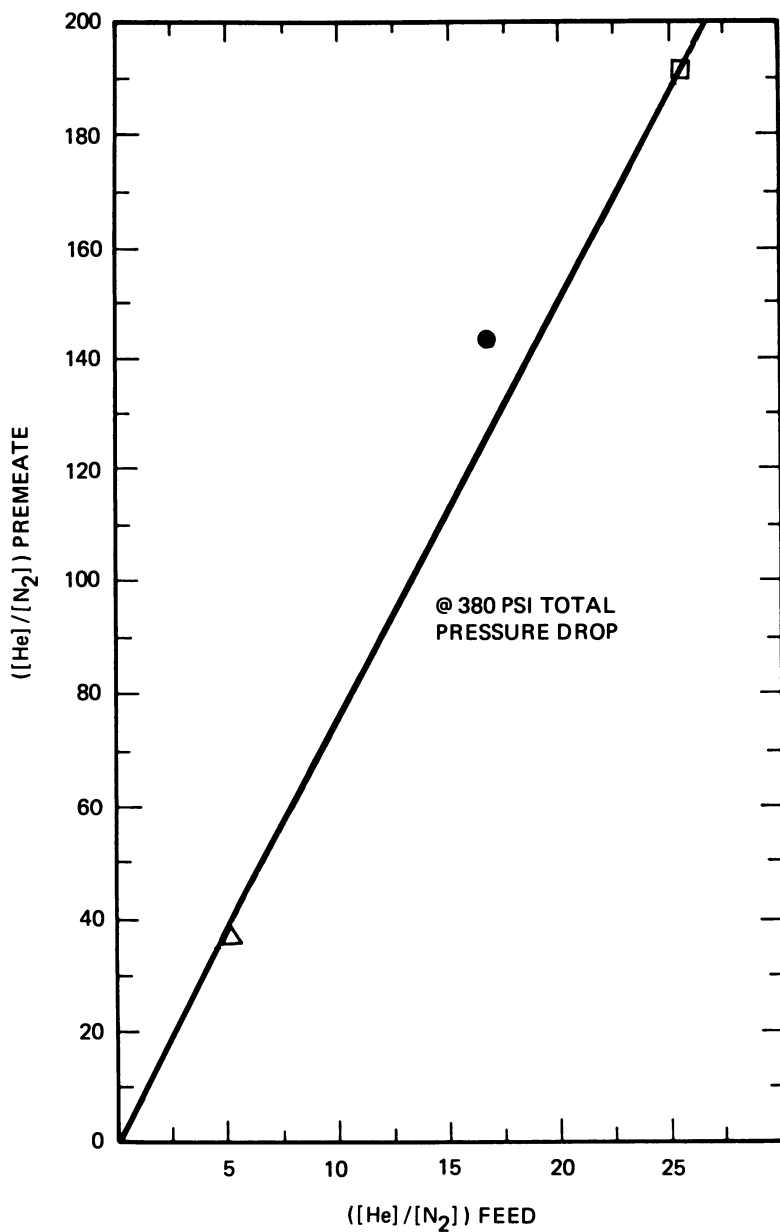


Figure 8. Enrichment of helium relative to nitrogen at 380 psig ΔP .

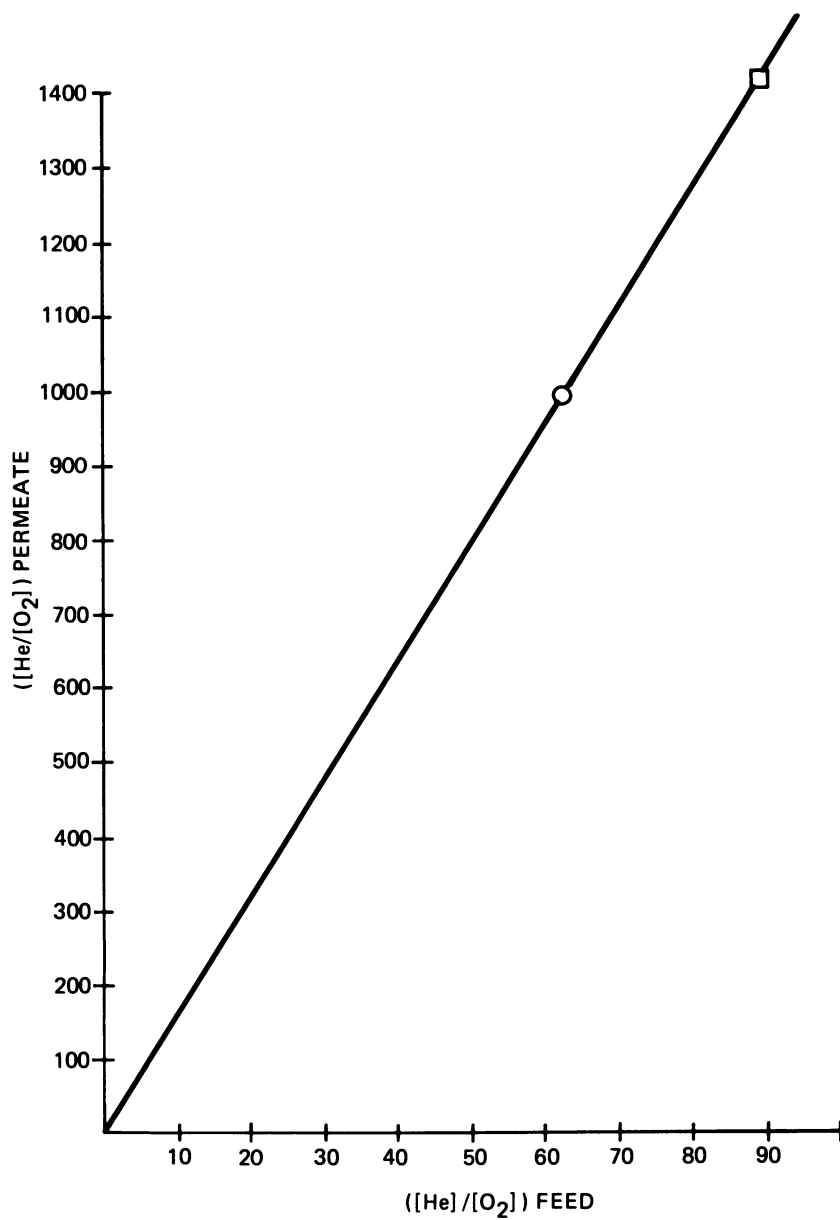


Figure 9. Enrichment of helium relative to oxygen at 380 psig ΔP .

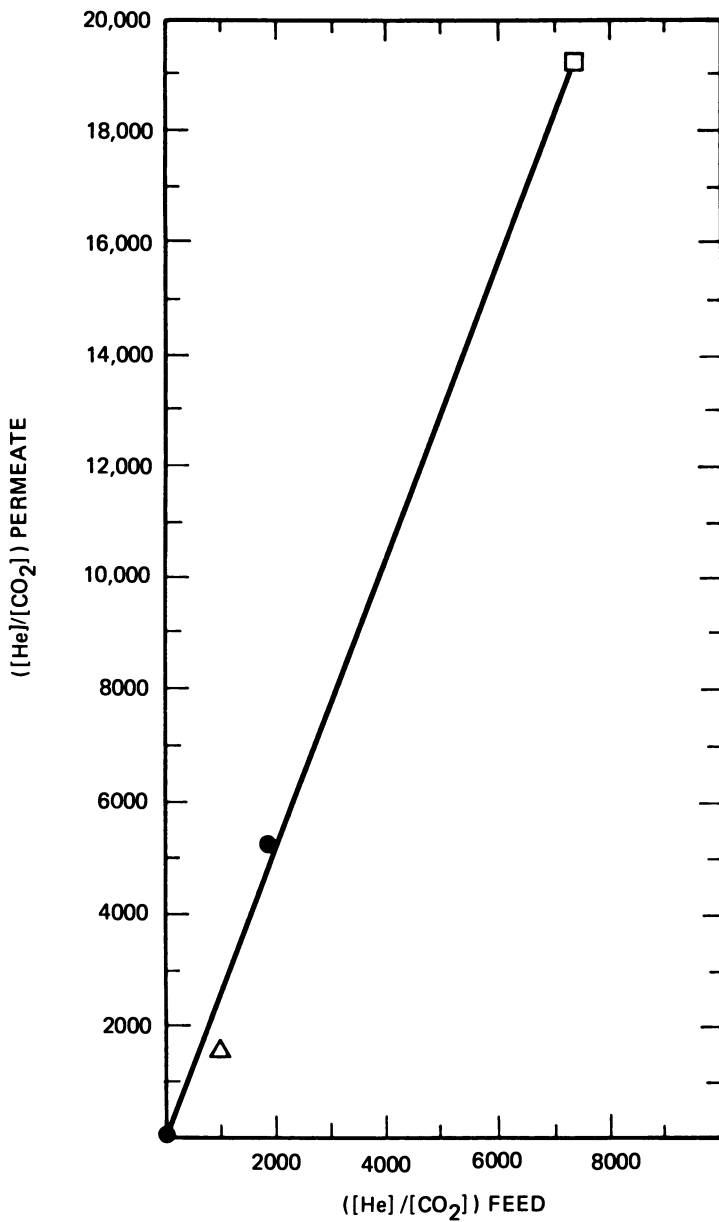


Figure 10. Enrichment of helium relative to carbon dioxide at 380 psig ΔP .

(b) loss due to some other factor such as gradual membrane plasticization by water vapor, or (c) non-ideality of mixtures especially at the higher pressures. The source of discrepancy remains an issue open to future evaluations.

Hypothetical System Design

Table VI
Design Assumptions for 58% Helium Mixtures

1. Recovery α Area
 $\alpha \Delta P$ (shown by data)
2. Linear Extrapolation of Permselectivities and Permeabilities
3. 50% Decrease in Flux due to Humidity Levels $\geq 80\%$ (see Reference 8).

In fulfillment of the contract requirements with the Navy, a hypothetical helium recovery system was designed based on the limited data available from the test program. These calculations were performed to put the test results in perspective. They are not, however, intended to describe a system that Westinghouse has for market. Westinghouse has no plans to market such a system.

Figure 11 and the accompanying material balances in Figure 12 show that five membrane separation stages are required in the hypothetical system to meet the specified levels in Table I for a 58% helium mixture.

Since the experimental data showed that the cellulose acetate membranes concentrate water, the water must be removed from the feed stream before it enters the permeation stages in twin zeolite absorption columns. The dewatering system would be backed up by high efficiency particulate filters rated to $\sim 0.3 \mu$. Since the final product is to be breathable, diaphragm compressors would be used throughout the system to prevent gaseous contamination by oil. A gas chromatograph would be used to monitor effluent quality, while the pressure, humidity and temperature taps check the system operation as the probes in Figure 11 indicate.

As Figure 12 shows, the fifth stage is required to meet the CO_2 spec when treating the 58% helium mixture, while only four stages are adequate to meet the target of $\geq 99.8\%$ He purity.

Conclusions

1. The design proposed here is a hypothetical preliminary design assembled to determine the technical feasibility of using semipermeable membranes to recover helium.
2. More detailed data concerning the effects of humidity, membrane area and lower helium concentrations in the feed stream on helium recovery must be obtained before a final design can be performed with confidence.

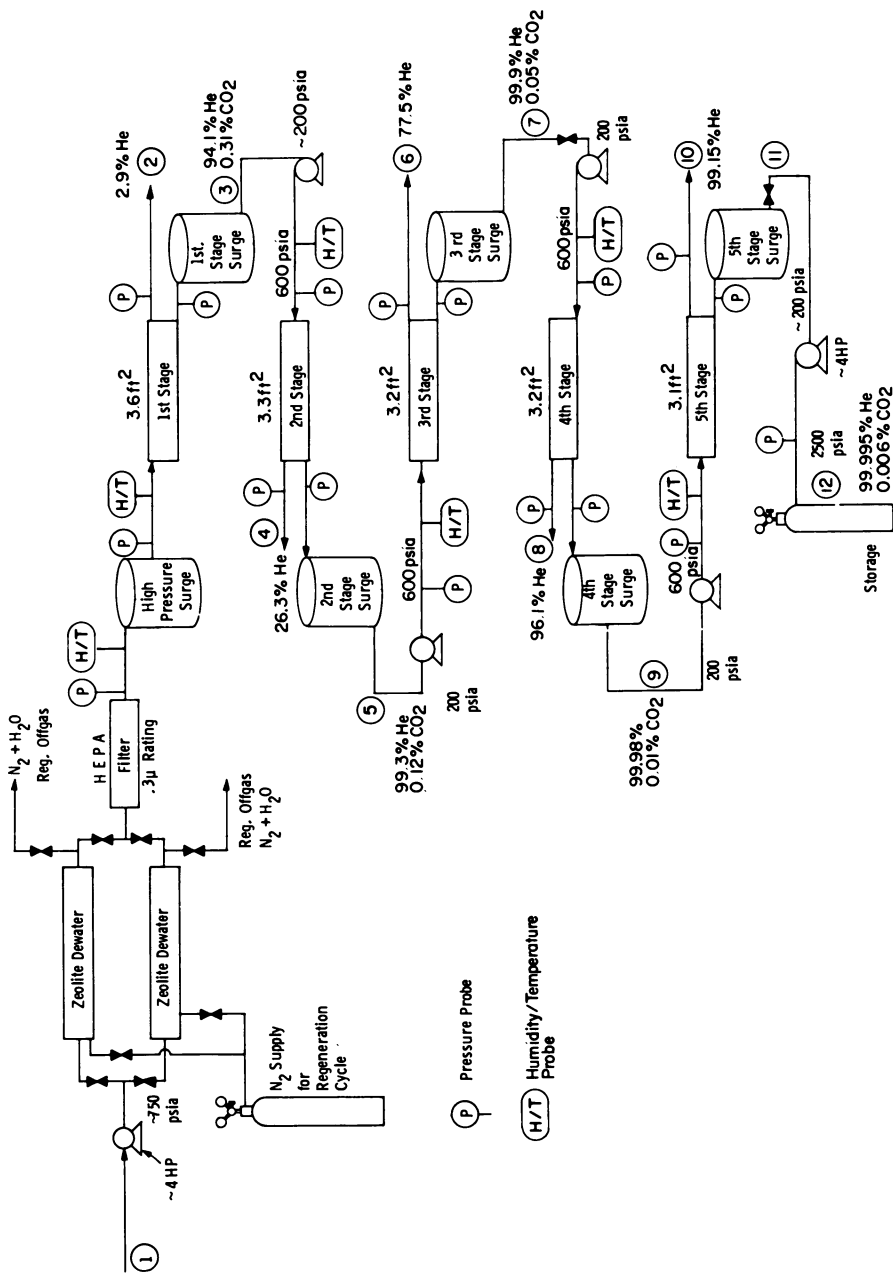


Figure 11. Helium reclaimer design.

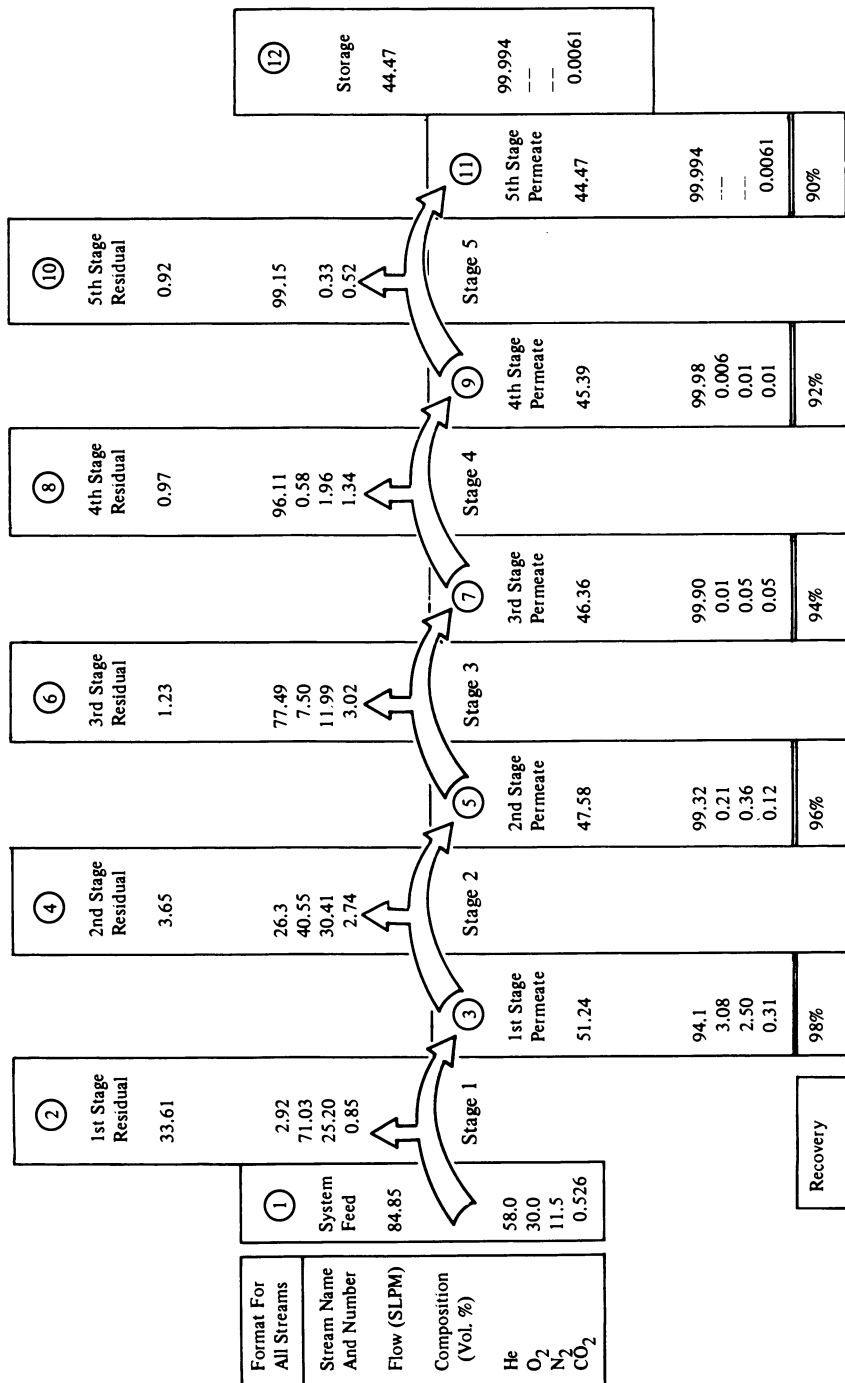


Figure 12. Helium reclaimer material balance.

3. For a hypothetical system design, based on the existing data, multistage systems are required to recover the helium from vented diving chamber gases in order to meet the design specifications outlined in Table I.

4. Five stages are required to achieve the helium purity goal and the carbon dioxide requirement in Table I.

5. Carbon dioxide is the limiting gas for the design as oxygen and nitrogen require only two stages to meet their design requirement levels.

Use of other membranes, having different properties, will, of course, result in a system different from that indicated above. Depending on the choice of membrane material, fewer or more, smaller or larger stages would be required for the system. The expected cost of reclaimed helium would be correspondingly affected.

Nomenclature

k	permeability coefficient (STD ft ³ /ft ² hr 100 psi)
p	pressure (atm)
T	temperature (°K except as noted)
ρ	density (g/cc)
L	some characteristic length (cm)
[i] ₂	permeate concentration mole %
[i] ₃	residual concentration mole %
[i] ₁	feed concentration mole %
A	area
F ₃	residual flow rate (SLPM)
F ₁	feed flow rate (SLPM)
F ₂	permeate flow rate (SLPM)
p _i ^o	vapor pressure of component i
x _{ij}	ideal separation for distillation = p _i ^o /p _j ^o
α _{ij}	separation factor or permselectivity

Literature Cited

1. Howland, H. R.; Hulm, J. K. The Economics of Helium Conservation, Final Report to Argonne National Laboratory, Contract No. 31-109-38-2820, December, 1974.
2. Helium Reclaimer Study, Westinghouse Electric Corporation, Proposal No. Y7420, April, 1978.
3. McCabe, W. G.; Smith, I.C. Unit Operations of Chemical Engineering, McGraw-Hill, 1967, Second Edition.
4. Balzhizer, R. W.; Samuels, M. R.; Eliassen, J. D. Chemical Engineering Thermodynamics, Prentice Hall, 1972.
5. Treybal, R.E. Mass Transfer Operations, McGraw-Hill, 1968.

6. Hwang, S. J.; Kemmermeyer, K. Membranes in Separation, Wiley & Sons, 1975.
7. Bird, R. B.; Stewart, W. E.; Lightfoot, E.M. Transport Phenomena, Wiley & Sons, 1960.
8. Schell, W. J. "Membrane Applications to Coal Conversion Processes," Envirogenics Systems Company, October, 1976, NTIS No. FE2000-4.
9. Li, N. N., Ed.; Recent Developments in Separation Science, Vol. II, CRC Press, Cleveland, Ohio, 1972.

RECEIVED January 18, 1983

A Low-Temperature Energy-Efficient Acid Gas Removal Process

R. E. HISE and L. G. MASSEY—Consolidated Natural Gas Research Company, Cleveland, OH 44106

R. J. ADLER, C. B. BROSILOW, and N. C. GARDNER—Case Western Reserve University, Cleveland, OH 44106

L. AUYANG, W. R. BROWN, W. J. COOK, and Y. C. LIU—Helipump Corporation, Cleveland, OH 44141

The CNG process removes sulfurous compounds, trace contaminants, and carbon dioxide from medium to high pressure gas streams containing substantial amounts of carbon dioxide. Process features include 1) absorption of sulfurous compounds and trace contaminants with pure liquid carbon dioxide, 2) regeneration of pure carbon dioxide with simultaneous concentration of hydrogen sulfide and trace contaminants by triple-point crystallization, and 3) absorption of carbon dioxide with a slurry of organic liquid containing solid carbon dioxide. These process features utilize unique properties of carbon dioxide, and enable small driving forces for heat and mass transfer, small absorbent flows, and relatively small process equipment.

Acid gas removal (AGR) refers to the separation of hydrogen sulfide and carbon dioxide from gas mixtures. The simultaneous removal of other trace sulfurous and nitrogenous compounds is also usually implied, e.g., carbonyl sulfide, carbon disulfide, mercaptans, hydrogen cyanide. A less emphasized but equally important function of acid gas removal is the separation of carbon dioxide from hydrogen sulfide and other trace contaminants. AGR thus serves to increase the market value of a gas by removing diluents and undesirable compounds, to cleanse a gas of compounds detrimental to downstream processing (catalyst poisons), to separate pollutant free carbon dioxide for by-product use or atmospheric venting, and to concentrate hydrogen sulfide for sulfur recovery.

The major applications of AGR appear to be: (1) treating natural gas containing sulfurous compounds and carbon dioxide, (2) treating shift gases in substitute natural gas production from coal, (3) treating synthesis gas made by partial oxidation

0097-6156/83/0223-0027\$06.00/0

© 1983 American Chemical Society

of sulfur-contaminated feedstocks, e.g., gasoline production from coal via synthesis gas (Fischer-Tropsch reaction or through the intermediates methanol or dimethyl ether), (4) acid gas removal in hydrogen production from coal or residual feedstocks for uses such as oil shale refining, and (5) treating synthesis gas made from methane and steam (production of ammonia, hydrogen, and oxo compounds). In short, acid gas removal is a key step in the up-grading of natural gas and synthesis gas made from natural gas, petroleum, or coal, and acid gas removal is an essential step in most envisioned fossil fuel energy conversion processes.

A proprietary acid gas removal process is under development by the CNG Research Company, a Subsidiary of the Consolidated Natural Gas Company; most of the research has been done by Helipump Corporation at Case Western Reserve University, Cleveland, Ohio. The goal is the development of a commercially attractive process. The process separates carbon dioxide, sulfurous molecules, and other trace contaminants from gas mixtures containing low molecular weight components such as hydrogen, carbon monoxide, methane, and nitrogen. The process operates at temperatures down to about -80°C , and is especially suited for medium to high pressure (300-1500 psia) gas mixtures containing substantial amounts of carbon dioxide. This paper provides background and motivation for alternative AGR technology, a description of the CNG process and its features, and reviews the present status of process development.

Background and Motivation for Alternative AGR Technology

There are two major types of acid gas removal processes, chemisorption and physical absorption. Typical chemisorption agents are amines and hot potassium carbonate; typical physical absorbents are dimethyl ether of tetraethylene glycol (Selexol) and cold methanol (Rectisol). At low acid gas partial pressure, less than about 200 psia, chemisorption is generally favored; at acid gas partial pressures above 200 psia, physical absorption is generally favored (1). The following discussion of AGR process characteristics is oriented primarily toward treatment of crude coal gasifier gases with pressure and composition favoring physical absorption AGR.

Existing AGR processes envisioned for use in the production of synthetic fuels from coal face unique challenges because these AGR processes were developed primarily in response to the needs of the petroleum and natural gas industries where crude gas mixtures are relatively well-defined. In contrast to crude gas mixtures in the petroleum and natural gas industries, crude coal gasifier gas generally contains much more carbon dioxide, a much higher ratio of carbon dioxide to hydrogen sulfide, and many trace contaminants. The AGR step in synthetic fuels production from coal must be capable of performing two tasks: (1) separation

of acid gases and the trace contaminants from the crude gas, and (2) separation of highly purified carbon dioxide from the hydrogen sulfide and trace contaminants. Capital and energy cost estimates for AGR in synfuels production are high because processing and environmental requirements demand that these separations be sharp. In fact, AGR is estimated to be the single most costly part of a substitute natural gas plant (excluding the oxygen plant), more costly than the gasification step or the methanation step (2).

Existing physical absorption AGR processes are relatively energy inefficient for application in coal gasification; they use substantial amounts of steam or stripping gas to regenerate lean solvent and power to pump lean solvent into the AGR absorber. In the treatment of crude gas with substantial carbon dioxide content, work available by expansion of separated carbon dioxide from its partial pressure in the crude gas, typically 100-300 psia, to atmospheric pressure, is not recovered. In theory, an AGR process could recover and utilize this potential energy.

Existing AGR processes have difficulty treating crude gases with high ratios of carbon dioxide to hydrogen sulfide to produce a sulfurous stream in sufficient concentration for conversion to elemental sulfur in a Claus plant. Although a Claus feed of 40% H₂S or greater is most desirable (3), AGR processes treating crude coal gasifier gases typically produce an acid gas stream containing 25% H₂S or less (4). Separation of pure carbon dioxide for by-product use or for rejection to the atmosphere (environmental restrictions are typically 200-250 ppm total sulfur, 10 ppm as H₂S) is also difficult to achieve with existing AGR processes. Attempting to increase the hydrogen sulfide concentration of the acid gas stream and to attain high purity carbon dioxide with existing AGR processes usually results in steeply rising capital and operating costs.

The many trace contaminants in gases produced from coal include sulfurous compounds such as carbonyl sulfide, carbon disulfide, mercaptans, thiophene, and nitrogen compounds such as ammonia and hydrogen cyanide, and aliphatic and aromatic hydrocarbons having a broad range of volatility. Existing AGR processes have difficulty removing all of these trace contaminants to the low levels desired for downstream processing and carbon dioxide venting. They also face potential technical and economic problems in solvent recovery and regeneration, e.g., solvent loss with treated or vent gases (methanol), and increased nitrogen or steam stripping for effective removal of contaminants. The problem of trace contaminant removal and rejection is receiving increased attention in the evaluation and selection of AGR processes for proposed coal gasification plants sited in the United States (5).

AGR Process Development Goals

The following goals were established at the start of efforts to develop an acid gas removal process more suited to gas cleaning in the production of synthetic fuels from coal, particularly medium BTU and substitute natural gases:

- Low energy consumption
- Reduced capital cost
- Concentrated hydrogen sulfide for conversion to sulfur
- Pure carbon dioxide by-product
- Non-polluting (pure carbon dioxide vent gas)
- Removal and rejection of trace contaminants
- Non-corrosive with ordinary materials of construction.

Theoretical analysis indicated that the first goal, reduced energy consumption, was realistic. A reversible acid gas removal process separating acid gases from a 1000 psia crude gas containing 30 mol % CO₂ would reject carbon dioxide at ambient temperature and pressure, and be a net energy producer.

Process Description and Features

The CNG acid gas removal process is distinguished from existing AGR processes by three features. The first feature is the use of pure liquid carbon dioxide as absorbent for sulfurous compounds; the second feature is the use of triple-point crystallization to separate pure carbon dioxide from sulfurous compounds; the third feature is the use of a liquid-solid slurry to absorb carbon dioxide below the triple point temperature of carbon dioxide. Pure liquid carbon dioxide is a uniquely effective absorbent for sulfurous compounds and trace contaminants; triple-point crystallization economically produces pure carbon dioxide and concentrated hydrogen sulfide; for bulk carbon dioxide absorption the slurry absorbent diminishes absorbent flow and limits the carbon dioxide absorber temperature rise to an acceptable low value. The sequence of gas treatment is shown in Figure 1, an overview of the CNG acid gas removal process.

Carbon dioxide plays a central role in the CNG process both as a pure component and in mixture with other compounds. The triple point of carbon dioxide is referred to frequently in the following discussion; it is the unique temperature and pressure at which solid, liquid, and vapor phases of carbon dioxide can exist at equilibrium (-56.6°C, 5.1 atm). The carbon dioxide triple point is shown in Figure 2, a phase diagram for carbon dioxide.

Precooling, Water Removal. The raw gas is cooled and residual water vapor is removed to prevent subsequent icing. The

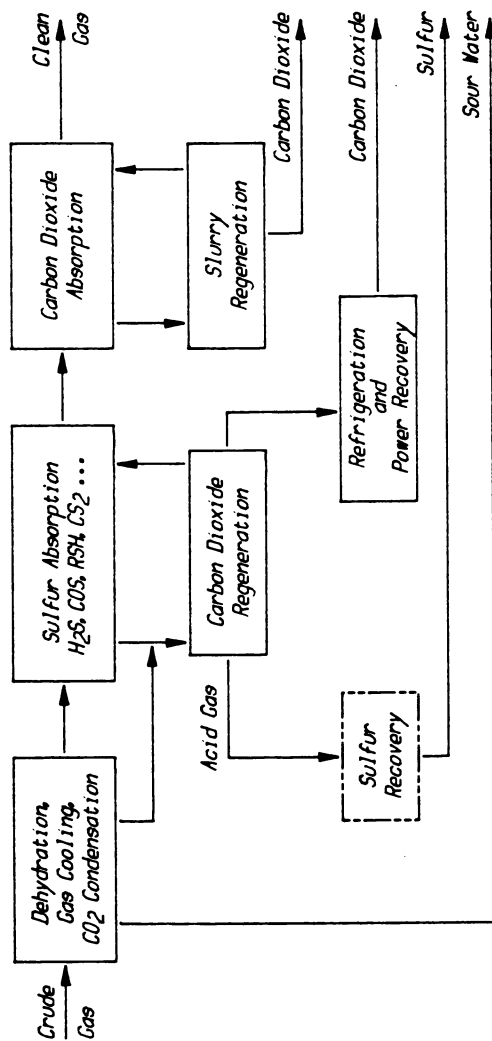


Figure 1. CNG process overview.

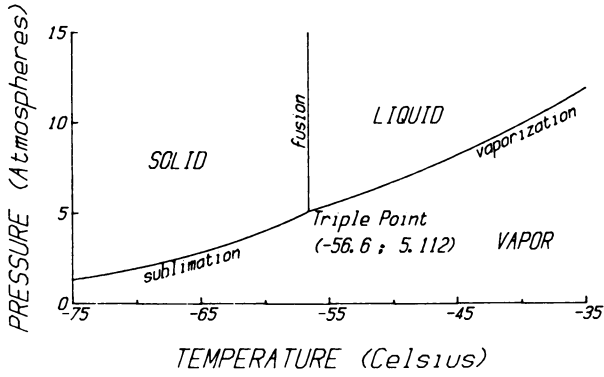


Figure 2. Carbon dioxide phase diagram.

method of water removal depends on the crude gas composition. If the crude gas is relatively free of C_2+ hydrocarbons, a regenerable molecular sieve can be used; otherwise, water can be removed by solvent washing, e.g., dimethyl formamide, with dry solvent regenerated by distillation. The economics of the two methods appear competitive. The water-free crude gas is further cooled to its carbon dioxide dew point by counter current heat exchange with return clean gas and separated carbon dioxide.

The dew point of the gas depends on the gas pressure and the carbon dioxide partial pressure. At fixed carbon dioxide composition, the dew point is lowered as total pressure decreases; at fixed total pressure, the dew point is lowered as carbon dioxide composition decreases. Calculated dew points for a synthesis gas with 30 mol % carbon dioxide, for both ideal and real gas behavior, are shown in Figure 3 for syn gas pressures up to 1500 psia.

The dew point must be warmer than -56.6°C to permit use of liquid carbon dioxide absorbent because pure liquid carbon dioxide cannot exist below the triple point. The carbon dioxide partial pressure, i.e., gas phase CO_2 mol fraction times total pressure, of synthesis gas mixtures with -56.6°C dew points is plotted versus synthesis gas pressure in Figure 4. Increasing the $\text{H}_2:\text{CO}$ ratio at fixed total pressure decreases the carbon dioxide partial pressure required for a -56.6°C dew point. Liquid carbon dioxide can be used to absorb sulfur molecules for any combination of gas pressure and carbon dioxide partial pressure which lies above the curves of Figure 4.

Carbon Dioxide Condensation, Sulfurous Compound Absorption.

Carbon dioxide is condensed by cooling the gas from its dew point to about -55°C ; the condensate is contaminated with sulfurous compounds. Substantial amounts of carbon dioxide can be condensed if the dew point is relatively warm. A synthesis gas at 1000 psia with 30 mol % carbon dioxide has a dew point of about -30°C , and approximately 65% of the carbon dioxide condenses to a liquid in cooling to -55°C . Removal of carbon dioxide by condensation reduces the amount which must be removed subsequently by absorption. Condensation is preferred over absorption because it is more reversible and hence is more energy efficient and less capital intensive.

The gas at -55°C is scrubbed clean of sulfurous compounds and remaining trace contaminants using pure liquid carbon dioxide. Liquid carbon dioxide has several desirable properties as an absorbing medium for sulfurous compounds. Surprisingly, liquid carbon dioxide absorbs carbonyl sulfide (COS) more effectively than it absorbs hydrogen sulfide as shown by their relative vaporization coefficients, i.e., $K_{\text{COS}} < K_{\text{H}_2\text{S}}$ ($K_i \equiv y_i/x_i$, y_i = vapor mole fraction component i , x_i = liquid mole fraction component i). Thus, an absorber for sulfurous compounds designed to remove hydrogen sulfide using liquid carbon dioxide will also

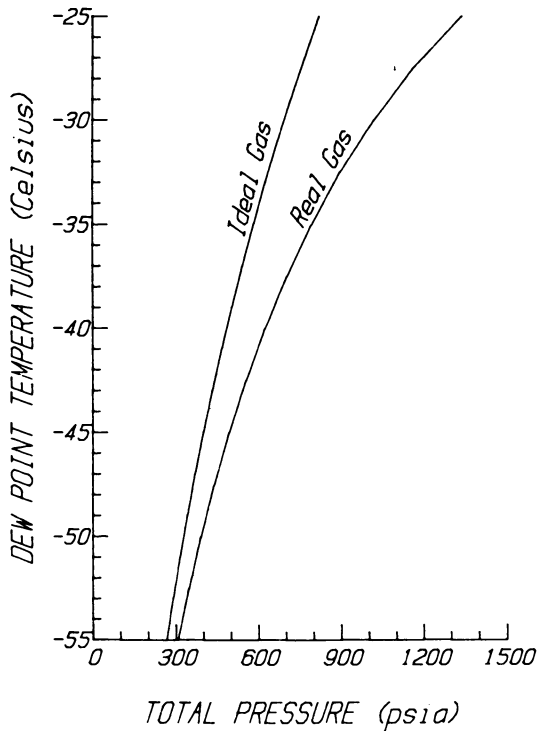


Figure 3. Dew point vs. pressure, synthesis gas with 30% CO_2 .

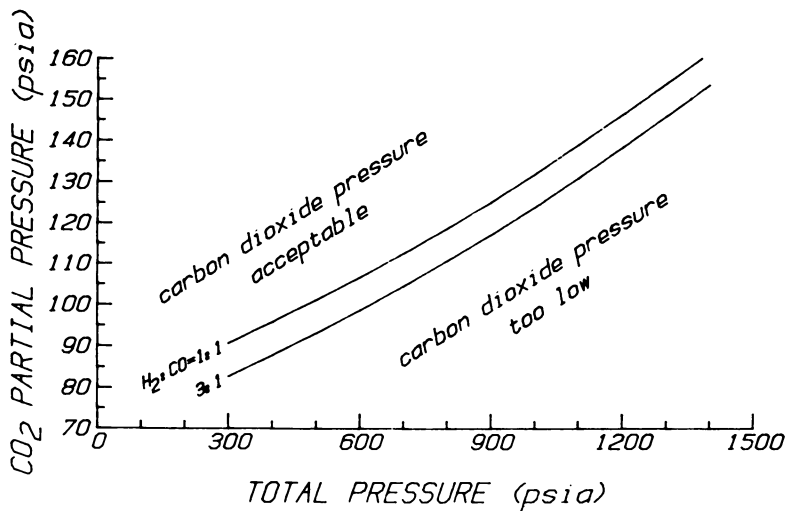


Figure 4. Carbon dioxide pressures required for sulfur compound absorption.

remove COS and all other less volatile sulfurous compounds in the gas. The opposite is true concerning COS for both cold methanol (Rectisol) and the dimethyl ether of polyethylene glycol (Selexol solvent). For comparison, the ratio $K_{H_2S}:K_{COS}$ is plotted in Figure 5 versus liquid phase composition from 100 mol% methanol to 100 mol% carbon dioxide. The ratio $K_{H_2S}:K_{COS}$ for Selexol solvent is even lower than for methanol.

The physical properties of liquid carbon dioxide also enhance its use as an absorbent in general. The low viscosity (about 0.35 centipoise at -55°C) and high density of liquid carbon dioxide promote high stage efficiency. For comparison, the viscosity of methanol is 7 to 8 times greater over the temperature range 0 to -55°C (Figure 6), and Selexol solvent's viscosity is 5 to 10 centipoise around room temperature. Liquid carbon dioxide is denser (specific gravity 1.17 at -55°C) than most absorbents which, together with its low viscosity, enables high liquid and gas flow rates in absorption and stripping towers. For comparison, methanol has a specific gravity of about 0.85 (-40°C), and Selexol solvent about 1.03 at room temperature. Carbon dioxide has a relatively low molecular weight of 44 compared to Selexol solvent's molecular weight of over 200 (6). Low molecular weight favors high gas solubility per unit volume of solvent. A comparison of physical properties for methanol, Selexol solvent, and liquid carbon dioxide is summarized in Table I. The liquid carbon dioxide used to absorb the sulfurous compounds and other trace impurities is not purchased but rather is obtained from the crude gas being treated.

The liquid carbon dioxide absorbent, with sulfurous compounds, other trace contaminants, and perhaps some co-absorbed light hydrocarbons such as methane and ethane, is combined with the contaminated liquid carbon dioxide condensed in precooling to -55°C . The combined carbon dioxide stream, typically 3 to 5 mol % hydrogen sulfide, is stripped of light hydrocarbons if necessary, and sent to the carbon dioxide regenerator. The treated gas, containing less than 1 ppm H_2S , leaves the sulfur absorber at essentially -55°C with carbon dioxide the only significant impurity yet to be removed.

Carbon Dioxide Regeneration by Triple Point Crystallization.

Crystallization of carbon dioxide produces pure carbon dioxide (less than 1 ppm sulfur) and concentrated hydrogen sulfide (up to 75 mol %). The great advantage of crystallization is that pure solid carbon dioxide crystals form from mother liquor containing sulfurous and various other trace compounds. In contrast, separation of pure carbon dioxide from hydrogen sulfide by distillation is difficult because of the very small relative volatility between carbon dioxide and hydrogen sulfide at low hydrogen sulfide concentrations (7). Solid carbon dioxide is not known to form solid solutions with any of the trace compounds likely to be absorbed by liquid carbon dioxide in the sulfurous

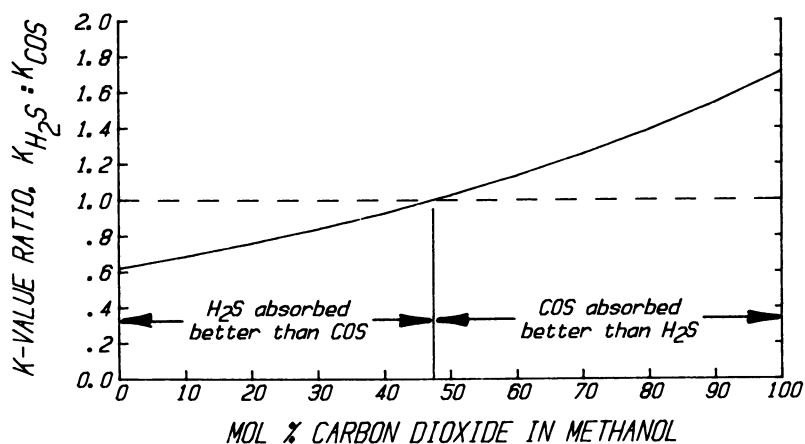


Figure 5. Equilibrium K ratios.

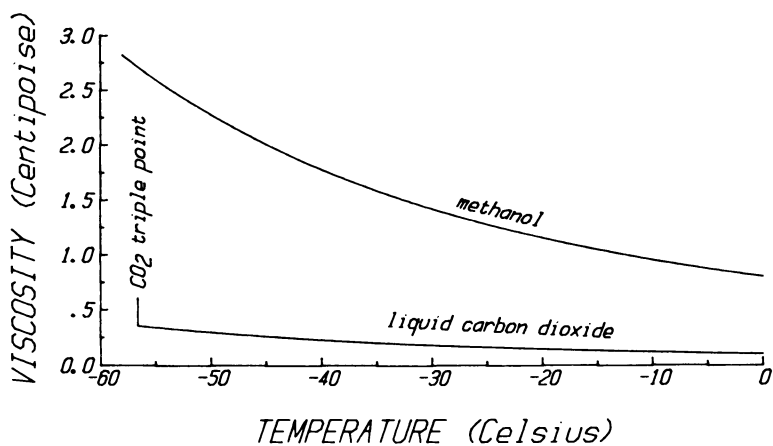


Figure 6. Viscosity, methanol, and liquid carbon dioxide.

Table I
Properties of Physical Absorbents

Solvent	MW	Sp.Gr. ^{T^oC}	μ (^o C) centipoise	BP, ^o C	FP, ^o C
methanol	32	0.85 ⁻⁴⁰	1.8(-40)	64.8	-97.5
dimethyl ether of polyethylene glycol	200	1.03	6.0(+25)	-	-20 to -30
liquid carbon dioxide	44	1.17 ⁻⁵⁵	0.35(-55)	-78.5 [†]	-56.6 [*]

[†]solid sublimation temperature

^{*}triple point, 75.1 psia

compound absorber. Consequently, the CNG process sharply rejects trace contaminants with the hydrogen sulfide rich acid gas stream.

The crystallization process employed is direct-contact triple-point crystallization with vapor compression. The crystallization process is a continuous separation cascade analogous to continuous distillation. The cascade operates at temperatures and pressures near the triple-point of carbon dioxide such that vapor, liquid, and solid phases coexist nearly in equilibrium. Solid carbon dioxide is formed by flashing; solid carbon dioxide is melted by direct contact with condensing carbon dioxide vapor. No heat exchange surfaces are necessary to transfer the latent heat involved. Crystal formation occurs at pressures slightly below the triple-point; crystal melting occurs at pressures slightly above the triple-point (several psi in each case). Carbon dioxide vapor is compressed from the crystal formation pressure to the crystal melting pressure. Only a few stages of recrystallization are required to achieve extremely pure carbon dioxide.

Pure carbon dioxide produced by triple-point crystallization is split into two streams, one is absorbent recycled to the sulfurous compound absorber, the other is sent back through the process for refrigeration and power recovery, and is delivered as a product stream or is vented to the atmosphere. The amount of excess liquid carbon dioxide produced at triple-point conditions can be substantial. For example, in treating a 1000 psia synthesis gas with 30 mol % carbon dioxide, nearly 40% of the total carbon dioxide to be removed from the syn gas is separated as pure triple-point liquid available for refrigeration and power recovery. The other product of triple-point crystallization, a concentrated hydrogen sulfide stream, also is recycled back through the process for refrigeration recovery before being sent to the sulfur recovery unit.

The triple-point crystallization of carbon dioxide is illustrated in Figure 7, which shows a schematic carbon dioxide phase diagram expanded about the triple-point and a closed-cycle triple-point crystallizer operating with pure carbon dioxide. The operation of this closed-cycle unit is identical to that of a unit in the stripping section of a continuous crystallizer cascade, except that in the cascade vapor would pass to the unit above, and liquid would pass to the unit below.

The adiabatic flash pressure P_f , maintained slightly below the triple-point pressure, causes liquid to spontaneously vaporize and solidify. The ratio of solid to vapor is determined by the heats of fusion and vaporization; for carbon dioxide about 1.7 moles of solid are formed for each mole vaporized. The solid, more dense than the liquid, falls through a liquid head and forms a loosely packed crystal bed at the bottom. The liquid head is about 10-12 feet, and increases the hydrostatic pressure on the solid to melter pressure P_m . The crystal bed depth is about two

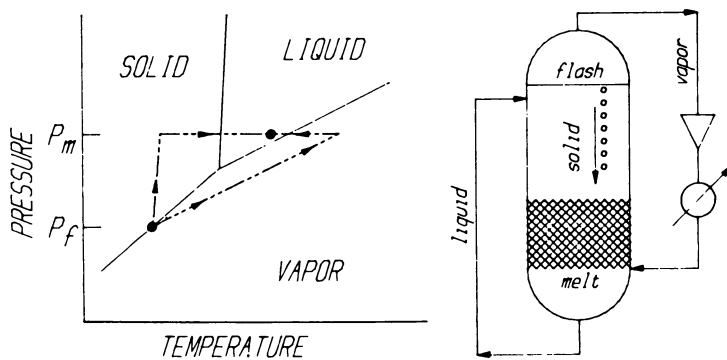


Figure 7. Carbon dioxide, triple point crystallization.

feet. In actual operation with sulfur compounds present, a small backwash flow is maintained upward through the bed to wash the crystals and prevent mother liquor from penetrating into the bed. The vapor is withdrawn from the flash zone, compressed to melter pressure P_m , sensibly cooled to near saturation, and dispersed under the solid bed where it condenses and causes solid to melt. The liquid is withdrawn and returned to the flash zone with a pump (not shown). The process cycle is traced on the phase diagram of Figure 7.

Concentration changes observed between mother liquor in the flash zone and liquid product in the melt zone of an experimental triple-point crystallizer have been dramatic. A qualitative concentration profile typical of those observed in the experimental unit is shown in Figure 8. The mother liquor concentration is relatively uniform above the packed bed, but a sharp drop in contaminant concentration occurs within the top several inches of the loosely packed crystal bed. Concentration changes of the order 500 to 5000 have been observed for representative sulfurous compounds and trace contaminants, including hydrogen sulfide, carbonyl sulfide, methyl mercaptan, ethane, and ethylene. Concentration profiles calculated for the packed bed of solid carbon dioxide using a conventional packed bed axial dispersion model agree very well with the observed experimental profiles.

Final Carbon Dioxide Removal. Carbon dioxide remaining in the gas after sulfurous compound absorption at -55°C is absorbed at temperatures below the carbon dioxide triple-point with a slurry absorbent. The slurry absorbent is a saturated solution of organic solvent and carbon dioxide containing suspended particles of solid carbon dioxide. The low carbon dioxide partial pressure of regenerated slurry absorbent, about one atmosphere, is considerably less than the carbon dioxide partial pressure of the entering raw gas, and provides the driving force for carbon dioxide absorption. As carbon dioxide is absorbed, the released latent heat warms the slurry and melts solid carbon dioxide. The direct refrigeration provided by the melting of solid carbon dioxide moderates the appreciable solvent temperature rise normally associated with bulk carbon dioxide absorption.

The large effective heat capacity of the liquid-solid slurry absorbent enables relatively small slurry flows to absorb the carbon dioxide heat of condensation with only modest absorber temperature rise. This contrasts with other acid gas removal processes in which solvent flows to the carbon dioxide absorber are considerably larger than flows determined by vapor-liquid equilibrium constraints. Large flows are required to provide sensible heat capacity for the large absorber heat effects. Small slurry absorbent flows permit smaller tower diameters because allowable vapor velocities generally increase with reduced liquid loading (8).

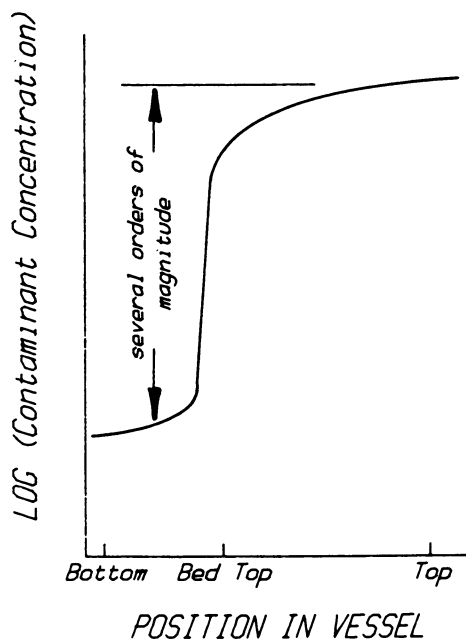


Figure 8. Concentration profile.

The liquid solvent of the slurry absorbent is the sink for absorbed carbon dioxide vapor and melted solid carbon dioxide. The carbon dioxide rich solvent exits the absorber near the triple-point temperature but containing no solid carbon dioxide, and is stripped of methane and lighter molecules if necessary. The carbon dioxide rich absorbent is next cooled by external refrigeration and flashed in stages at successively lower pressures to generate a cold slurry of liquid solvent and solid carbon dioxide. The carbon dioxide flash gas is recycled back through the process for refrigeration and power recovery, and is delivered as a product stream or is vented to the atmosphere. The regenerated slurry absorbent is recirculated to the carbon dioxide absorber.

The absorption of carbon dioxide with slurry and the regeneration of slurry by flashing carbon dioxide require small temperature and pressure driving forces. The small driving forces derive from the huge surface area of the solid carbon dioxide particles and the low viscosity of the slurry. Compared with other sub-ambient temperature carbon dioxide removal processes, the CNG process requires less refrigeration even though process temperatures are often lower.

The solubility of solid carbon dioxide in several solvents (9,10) is shown in Figure 9. A preferred range of carbon dioxide solubility for slurry absorption is defined qualitatively by the two dashed lines of Figure 9. The indicated preferred solubility range derives from computer simulations of slurry absorption based on experimental solubility data for various solvents, and of hypothetical slurry absorption based on constant carbon dioxide partial pressure driving force per stage. Solvents with preferred solubility include ethers and ketones (11), e.g., di-n-butyl ether and methyl ethyl ketone. These solvents have a relatively linear change in solubility with temperature (as compared with hexane or methanol), low viscosity when saturated with carbon dioxide, low melting points, and low vapor pressures. The thermodynamic ideal solubility is shown for reference.

Carbon dioxide removal by slurry absorption is attractive down to about -75°C , a temperature easily achieved by slurry regeneration to slightly above one atmosphere carbon dioxide pressure. For example, with a -75°C exit gas temperature, slurry absorption reduces the carbon dioxide content of a 1000 psia synthesis gas from about 13 to about 4 mole percent, a 70% reduction in carbon dioxide content. The exact level to which carbon dioxide can be removed from a treated gas by slurry absorption also depends on the solubility of solid carbon dioxide in the treated gas; the solubility of solid carbon dioxide in synthesis gas ($3\text{H}_2:\text{CO}$) is illustrated in Figure 10 for several synthesis gas pressures. Fine removal of carbon dioxide to lower levels is accomplished by conventional absorption into a slip stream of the slurry solvent which is regenerated to meet particular product gas carbon dioxide specifications.

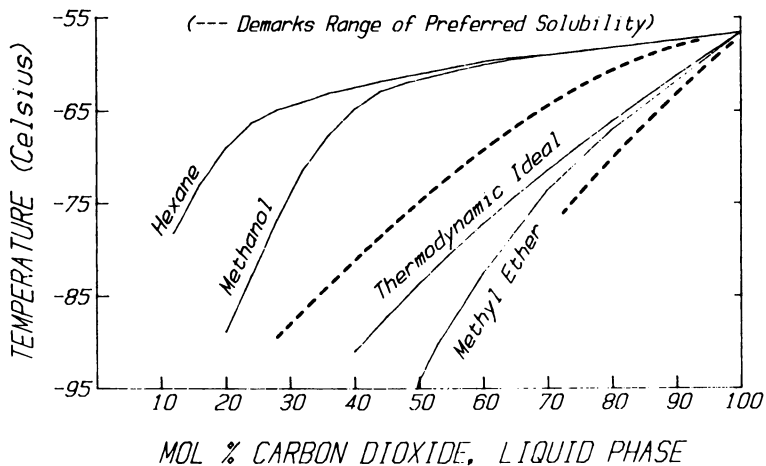


Figure 9. Solubility of solid carbon dioxide in selected solvents.

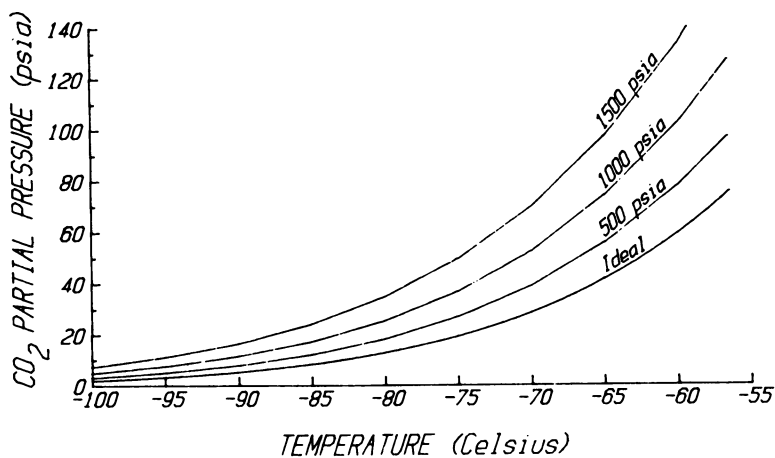


Figure 10. Solubility of solid carbon dioxide in synthesis gas.

Present Status

An extensive process data base has been accumulated which includes: (1) vapor-liquid-solid equilibrium data for binary systems of carbon dioxide with sulfurous compounds and with ethers and ketones, and multicomponent systems including hydrogen, carbon monoxide, methane, carbon dioxide, and hydrogen sulfide; (2) a bench-scale slurry formation and melting apparatus which provides data on slurry pumping, and on rates of slurry formation and melting, under various conditions of pressure driving force and agitation; and (3) a bench-scale closed-cycle triple-point crystallizer which provides data on rates of crystallization and melting, on the relation between these rates and the pressure driving forces applied, and on separation factors attainable in a single stage of crystallization.

The process features of carbon dioxide triple-point crystallization and slurry absorption of carbon dioxide have been demonstrated with the first generation bench-scale apparatus. Current efforts are focused on the design and construction of an improved version of the carbon dioxide triple-point crystallizer in cooperation with the U S Department of Energy. Future efforts are planned to design and construct absorption units to study multi-stage slurry absorption of carbon dioxide, and the more conventional gas-liquid absorption of sulfurous compounds with liquid carbon dioxide.

Summary

The CNG process meets three objectives commonly acknowledged by experts in gas purification to be highly desirable of acid gas removal in synthetic fuels production from coal:

- production of concentrated hydrogen sulfide for conversion to sulfur in a Claus plant
- production of pure carbon dioxide for atmospheric venting, for enhanced oil recovery, or other uses
- removal of trace contaminants from the treated gas, and easy solvent regeneration with respect to trace contaminants

Although the process requires the treated gas to have a certain minimum carbon dioxide partial pressure for removal of sulfurous compounds with liquid carbon dioxide, promising new SNG processes under development produce medium to high carbon dioxide content crude gases ideally suited for acid gas removal via the CNG process (12,13). The novel features of the CNG process have been demonstrated with bench-scale process development units; second generation process development units are in various stages of

planning, design, construction, and operation; readiness for commercial scale demonstration is anticipated in the time frame 1985-1987.

Literature Cited

1. Christensen, K.G., and W.J. Stupin, "Merits of Acid Gas Removal Processes," *Hydrocarbon Processing*, Feb. 1978, p. 125.
2. Factored Estimates for Western Coal Commercial Concepts, C.F. Braun and Company, Project 4568-NW, ERDA-AGA (1976).
3. Beavon, D.K., Kouzel, B., and Ward, J.W., "Claus Processing of Novel Acid Gas Streams," Symposium on Sulfur Recovery and Utilization, Division of Petroleum Chemistry, Inc., American Chemical Society, Atlanta Meeting, March 29-April 3, 1981.
4. Ghassemi, M., Strehler, D., Crawford, K., and Quinlivan, S., "Applicability of Petroleum Refinery Control Technologies to Coal Conversion," EPA Report No. EPA-600/7-78-190.
5. Rosseau, R.W., Kelly, R.M., and Ferrell, J.K., "Evaluation of Methanol as a Solvent for Acid Gas Removal in Coal Gasification Processes," Symposium on Gas Purification, AIChE Spring National Meeting, Houston, Texas, April 1981.
6. Sweny, J.W., "The Selexol Solvent Process in Fuel Gas Treating," paper presented at 81st National AIChE Meeting, Kansas City, Missouri, April 11-14, 1976.
7. Sobocinski, D.P., and Kurata, F., "Heterogeneous Phase Equilibria of the Hydrogen Sulfide - Carbon Dioxide System," *AIChE J.*, Vol. 5, No. 4, p. 545, 1959.
8. King, C.J., Separation Processes, McGraw-Hill, p. 547, 1971.
9. Kurata, F., "Solubility of Solid Carbon Dioxide in Pure Light Hydrocarbons and Mixtures of Pure Light Hydrocarbons," GPA Research Report RR-10, Feb. 1974.
10. Baume, G., and F.L. Perrot, *Recherches Quantitatives Sur Les Systemes Volatiles*, *Journal de Chimie Physique*, 12, (1914).
11. Adler, R.J., Brosilow, C.B., Brown, W.R., and Gardner, N.C., "Gas Separation Process," U.S. Patent 4,270,937, June 2, 1981.
12. "Direct methanation promises lower gas costs," *C & EN*, p. 30, April 5, 1982.
13. Kaplan, L.J., ed., "Methane from coal aided by use of potassium catalyst," *Chemical Engineering*, p. 64, March 22, 1982.

RECEIVED December 23, 1982

Implications of the Dual-Mode Sorption and Transport Models for Mixed Gas Permeation

R. T. CHERN, W. J. KOROS, E. S. SANDERS, S. H. CHEN, and
H. B. HOPFENBERG

North Carolina State University, Department of Chemical Engineering,
Raleigh, NC 27650

The concept of unrelaxed volume in glassy polymers is used to interpret sorption and transport data for pure and mixed penetrants. A review of recent sorption and permeation data for mixed penetrants indicates that competition for sorption sites associated with unrelaxed gaps between chain segments is a general feature of gas/glassy polymer systems. This observation provides convincing support for the use of the Langmuir isotherm to describe deviations from simple Henry's law sorption behavior.

The observed flux depressions of a component in a mixture, relative to its pure component value at an equivalent partial pressure driving force, derives from the above sorption competition mechanism which influences the effective concentration gradient driving diffusion across the membrane. The competition among penetrants for excess volume described above should be an important consideration for modeling essentially all permselective gas separation membranes. Significant plasticizing effects may mitigate flux reductions caused by the above competitive effects at high pressures in plasticization-prone polymers, but would also lead to selectivity losses which are highly undesirable. The permeation behavior of stiff-chain, plasticization-resistant polymers which are likely to comprise the next generation of gas separation polymers will be appropriately treated by the model discussed here.

0097-6156/83/0223-0047\$07.75/0

© 1983 American Chemical Society

American Chemical

Society Library

1155 16th St. N. W.

In Industry, Gas Separations: Why? ACS Symposium Series; ACS

Washington, D. C. 20036
ACS Symposium Series; American Chemical Society: Washington, DC, 1983.

High membrane permselectivity is generally associated with a rigid chain backbone of the constituent polymer, providing sieving on a molecular scale (1,2). At high upstream driving pressure (i.e., at high sorbed penetrant concentration), plasticization of the polymer may reduce the permselectivity of the membrane. Although plasticization will occur at sufficiently high sorbed concentrations for essentially all glassy materials, selection of a membrane material with a very high glass transition temperature and extraordinary inherent backbone rigidity should minimize effects associated with plasticization.

Often the ratio of pure component permeabilities at an arbitrary pressure for the components of interest is used as an indication of the potential selectivity of a candidate membrane. While this approach offers a useful approximation, the actual selectivity and productivity (flux) observed in the mixed gas case may be surprisingly different than predicted on the basis of the pure component data. As shown in Figure 1, prior to the onset of plasticizing, the presence of a second component B can depress the observed permeability of a component A relative to its pure component value at a given upstream driving pressure of component A. In the words of Pye et al. (3), the permeability of a membrane to a component A may be reduced due to the sorption of a second component B in the polymer which ". . . effectively reduces the microvoid content of the film and the available diffusion paths for the non reactive gases". The present paper will offer additional experimental and theoretical insight into this interesting effect that is characteristic of glassy polymers.

Unrelaxed Volume - Relation To Sorption And Transport Properties Of Glassy Polymers

The concept of "unrelaxed volume", $V_g - V_l$, illustrated in Figure 2 may be used to interpret sorption and transport data in glassy polymers exposed to pure and mixed penetrants. The extraordinarily long relaxation times for segmental motion in the glassy state lead to trapping of nonequilibrium chain conformations in quenched glasses, thereby permitting miniscule gaps to exist between chain segments. These gaps can be redistributed by penetrant in so-called "conditioning" treatments during the initial exposure of the polymer to high pressures of the penetrant (4). Following such initial exposure to penetrant, settled isotherms characterized by concavity to the pressure axis at low pressures and a tendency to approach linear high pressure limits are observed as shown in Figure 3. Reference to penetrant-induced conditioning effects have been made continuously since the very earliest investigations of penetrant/glassy polymer sorption

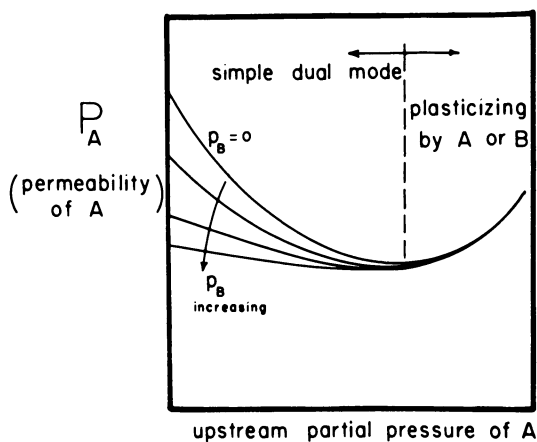


Figure 1. Permeability of a glassy polymer to penetrant A in the presence of varying partial pressures of penetrant B.

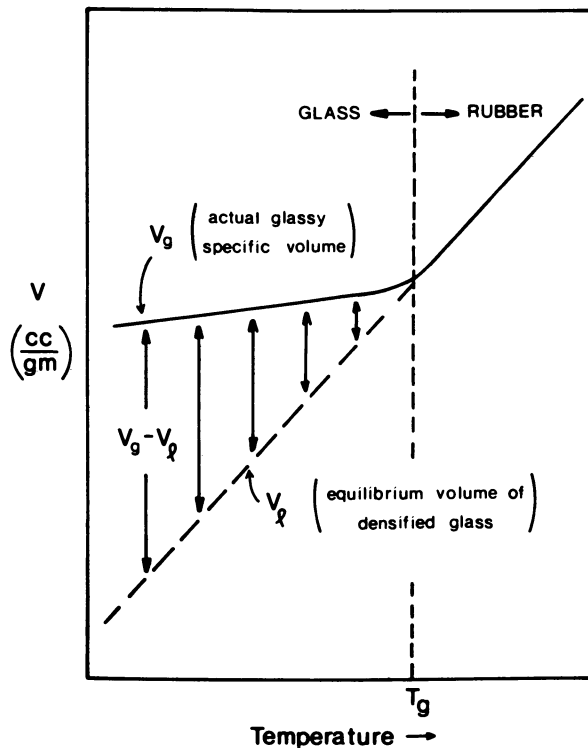


Figure 2. Schematic representation of the unrelaxed volume, $V_g - V_l$, in a glassy polymer. Note that the unrelaxed volume disappears at the glass transition temperature, T_g .

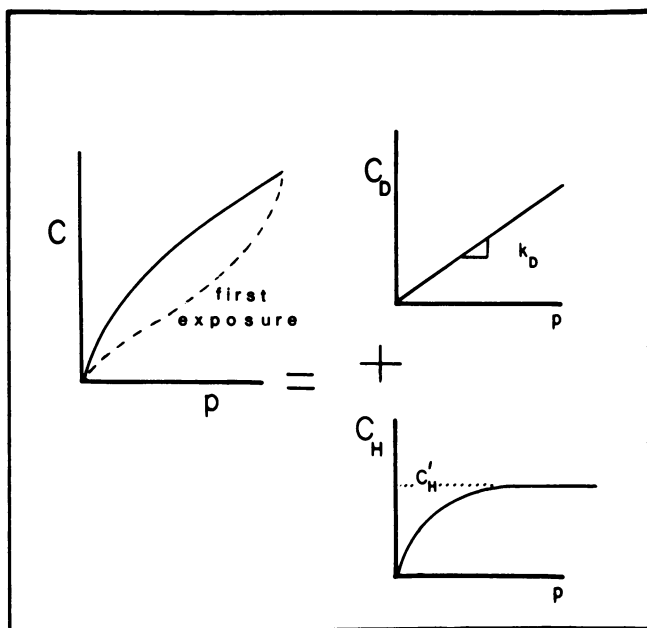


Figure 3. Schematic representation of the dual mode sorption concept.

behavior (2,4,5,6). If one "overswells" the polymer with a highly sorbing penetrant such as a high activity vapor and then removes the penetrant, the excess volume which is introduced will tend to relax quickly at first, followed by a very slow, long term approach toward equilibrium (6).

At extremely high gas conditioning pressures, substantial swelling of the polymer sample can occur with a resultant increase in the value of $V_g - V_l$ (5). For the case of conditioning with gases such as CO_2 at pressures less than 30 atm, however, consolidation in the absence of penetrant following the conditioning treatment is typically unmeasurable since penetrant sorption uptake is not very extensive (< 4-5% by weight) (4,5). As a result, in such cases redistribution of the originally present intersegmental gaps may be the primary process occurring during the first exposure of the polymer to high pressures of penetrant as shown in Figure 3 (4).

An interpretation of the observed conditioning behavior that occurs during the primary penetrant exposure in the absence of large swelling effects may be couched in terms of coalescence of packets of the original intersegmental gaps. Redistribution of chain conformations, consistent with optimal accommodation of the penetrant in the unrelaxed volume between chain segments may permit this process during the conditioning treatment. This rearrangement would tend to produce a more or less densified matrix with a small volume fraction of essentially uniformly distributed molecular scale gaps or "holes" throughout the matrix. In such a situation, one can appreciate the meaning of two slightly different molecular environments in the glass in which sorption of gas may occur. Consider first the limiting case in which a highly annealed, truly equilibrium densified glass characterized by " V_l " in Figure 2 is exposed to a given pressure of a penetrant. In this case, all gaps are missing, but there will clearly still be a certain characteristic sorption concentration (C_D) typical of true molecular dissolution in the densified glass, similar to that observed in low molecular weight liquids or rubbers (above T_g). Next, consider a corresponding conditioned nonequilibrium glass (illustrated by " V_g " in Figure 2) containing unrelaxed volume in which the surrounding matrix has been more or less densified by the coalescence of gaps to form molecular scale berths for penetrant. A local equilibrium requirement leads to an average local concentration of penetrant held in the uniformly distributed molecular scale gaps (C_H) in equilibrium with the "dissolved" concentration (C_D) at any given external penetrant pressure or activity. This simple physical model can be described analytically up to reasonably high pressures (generally for pressures less than or equal to the maximum conditioning pressure employed (4)) in terms of the sum of Henry's law for C_D and a Langmuir isotherm for C_H .

$$C = C_D + C_H \quad (1)$$

$$C = k_{DP} + \frac{C_H^{bp}}{1 + bp} \quad (2)$$

where k_D is the Henry's law constant that characterizes sorption of penetrant in the densified regions which comprise most of the matrix. The parameter b characterizes the affinity of the penetrant for the interchain gap regions in the polymer. The parameter C_H is the Langmuir sorption capacity of the glassy matrix and can be interpreted directly in terms of Figure 2 in which the unrelaxed volume, $V_g - V_\ell$, corresponds to the summation of all of the molecular scale gaps in the glass. As shown in Figure 4, the Langmuir capacity of glassy polymers tends to approach zero in the same way that $V_g - V_\ell$ approaches zero at the glass transition temperature (see Figure 2). This qualitative observation can be extended to a quantitative statement in cases for which the effective molecular volume of the penetrant in the sorbed state can be estimated. As a first approximation, one may assume that the effective molecular volume of a sorbed CO_2 molecule is 80 \AA^3 in the range of temperature from 25°C to 85°C . This molecular volume corresponds to an effective molar volume of 49 cc/mole of CO_2 molecules and is similar to the partial molar volume of CO_2 in various solvents, in several zeolite environments, and even as a pure subcritical liquid (See Table 1) (4,8). The implication here is not that more than one CO_2 molecule exists in each molecular scale gap, but rather that the effective volume occupied by a CO_2 molecule is roughly the same in the polymer sorbed state, in a saturated zeolite sorbed state and even in a dissolved or liquid-like state since all of these volume estimates tend to be similar for materials that are not too much above their critical temperatures. With the above approximation, the predictive expression given below for C_H^i can be compared to independently measured values for this parameter from sorption measurements.

$$C_H^i \left[= \frac{V_g - V_\ell}{V_g} \right] \rho^* \quad (3)$$

where ρ^* is the equivalent density of CO_2 ($\sim 1/49$ mole/cc) discussed above. The comparison of measured (4,9-11) and predicted C_H^i 's calculated from Eq (3) using reported dilatometric parameters (12-15) for the various glassy polymers is shown in Figure 5. The correlation is clearly impressive.

Application of Eq (3) to highly supercritical gases is somewhat ambiguous since the effective molecular volume of sorbed gases under these conditions is not easily estimated. A

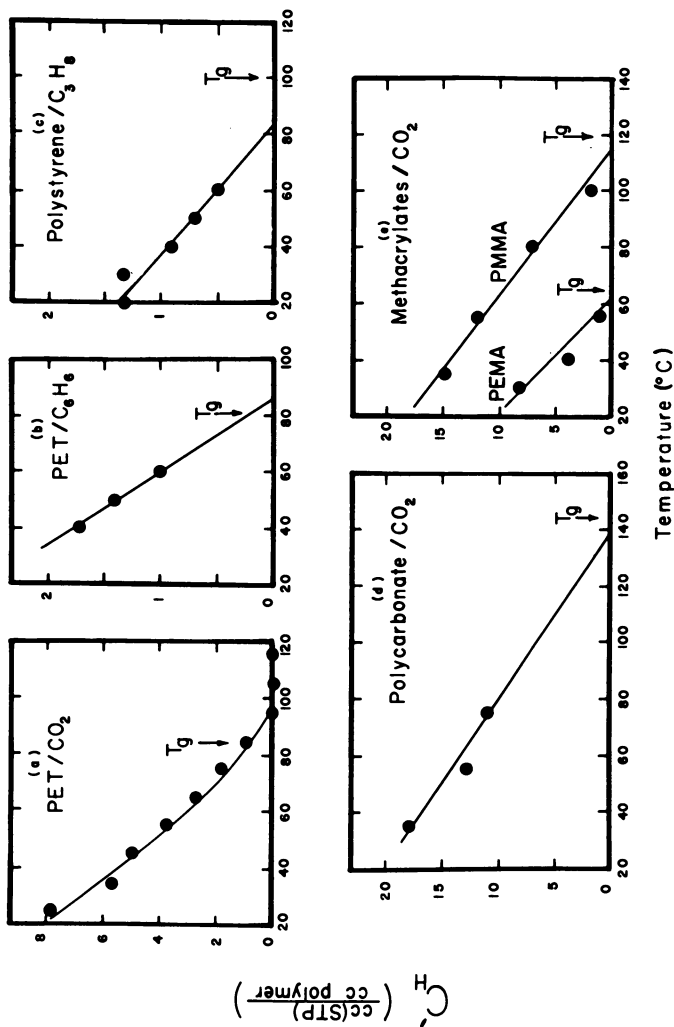


Figure 4. Langmuir sorption capacity, C_H , as a function of temperature for several polymer/penetrant systems. Note that C_H disappears near T_g . (Reproduced with permission from Ref. 7. Copyright John Wiley & Sons, 1981.)

Table 1: Effective Molar or Partial Molar Volume of CO₂ in Various Environments at 25°C.

Environment	Molar or Partial Molar Volume (cc/mole)	Ref
Carbon Tetrachloride	48.2	8
Chlorobenzene	44.6	8
Benzene	47.9	8
Acetone	44.7	8
Methyl Acetate	44.5	8
4A or 5A Zeolite at saturation of capacity	52.4	4

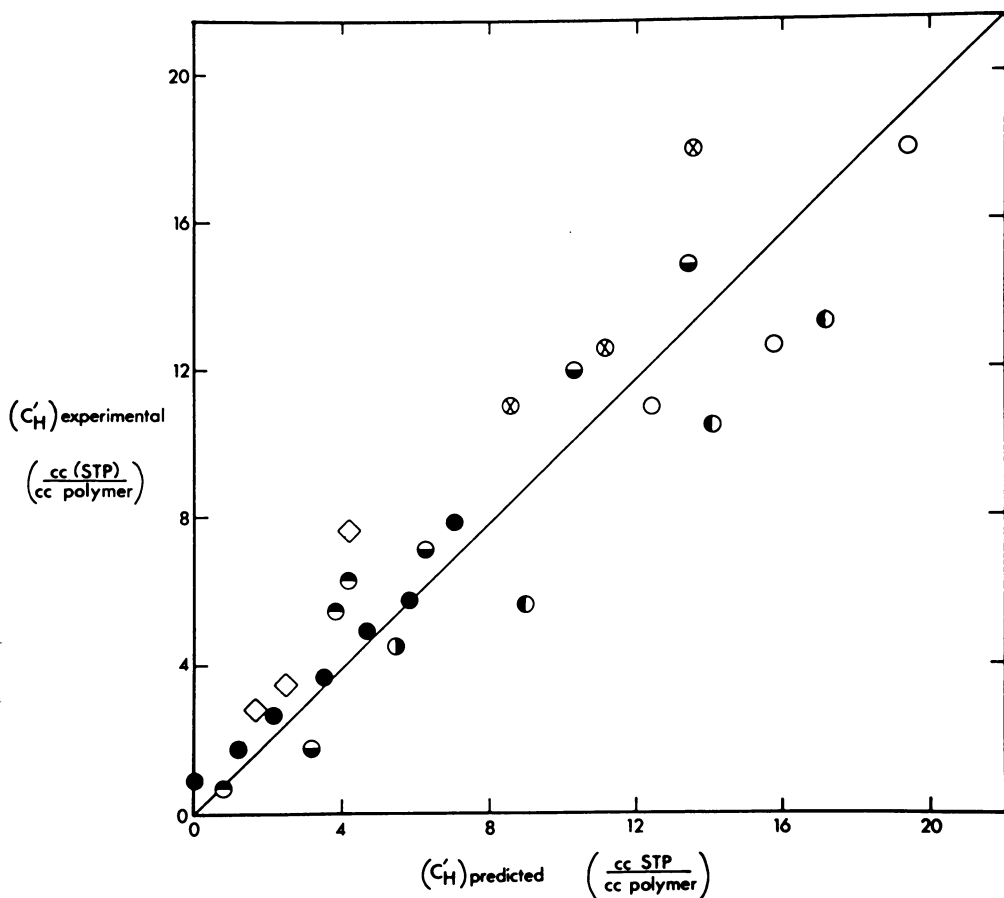


Figure 5. Quantitative comparison of experimentally measured values of C_H' for CO_2 in various polymers with the predictions of Equation 3. [\bullet , poly(ethylene terephthalate) at 25, 35, 45, 55, 65, 75, and 85 $^\circ\text{C}$], [\bullet , poly(benzyl methacrylate) at 30 $^\circ\text{C}$], [\bullet , poly(phenyl methacrylate) at 35, 50, and 75 $^\circ\text{C}$], [\diamond , poly(acrylonitrile) at 35, 55, and 65 $^\circ\text{C}$], [\circ , \odot polycarbonate at 35, 55, and 75 $^\circ\text{C}$: the \circ symbols refer to predictions using dilatometric coefficients from Ref. 14; the \odot symbols refer to predictions using coefficients from Ref. 15]. [\bullet , poly(ethyl methacrylate) at 30, 40, and 55 $^\circ\text{C}$], [\bullet , poly(methyl methacrylate) at 35, 55, 80 and 100 $^\circ\text{C}$].

similar problem exists in a priori estimates of partial molar volumes of supercritical components even in low molecular weight liquids (16). The principle upon which Eq (3) is based remains valid, however, and while the total amount of unrelaxed volume may be available for a penetrant, the magnitude of C_H' depends strongly on how condensible the penetrant is, since this factor determines the relative efficiency with which the component can utilize the available volume.

Transport. A companion transport model that also acknowledges the fact that penetrant may execute diffusive jumps into and out of the two sorption environments expresses the local flux, N , at any point in the polymer in terms of a two part contribution (17-20):

$$N = -D_D \frac{\partial C_D}{\partial x} - D_H \frac{\partial C_H}{\partial x} \quad (4)$$

where D_D and D_H refer to the mobility of the dissolved and Langmuir sorbed components, respectively. It is typically found that D_D is considerably larger than D_H except for non condensible gases such as helium (14). The above expression can be written in terms of Fick's law with an effective diffusion coefficient, $D_{eff}(C)$, that is dependent on local concentration:

$$N = -D_{eff}(C) \frac{\partial C}{\partial x} \quad (5)$$

The dual mobility model expresses the concentration dependency of $D_{eff}(C)$ in terms of the local concentration of dissolved penetrant, C_D , as shown in Eq (6):

$$D_{eff}(C) = D_D \left[\frac{1 + \frac{FK}{(1 + \alpha C_D)^2}}{1 + \frac{K}{(1 + \alpha C_D)^2}} \right] \quad (6)$$

where $F \equiv D_H/D_D$, $K \equiv C_H' b/k_D$ and $\alpha \equiv b/k_D$. This model explains concentration dependency of the local diffusion coefficient such as that shown for CO_2 in poly(ethylene terephthalate) (PET) in Figure 6 (21) in terms of a progressive increase in the fraction of the local concentration present in the higher mobility Henry's law environment as the local Langmuir capacity saturates at increasingly higher pressures.

The points in Figure 6 were evaluated from the phenomenological permeability and sorption concentration data

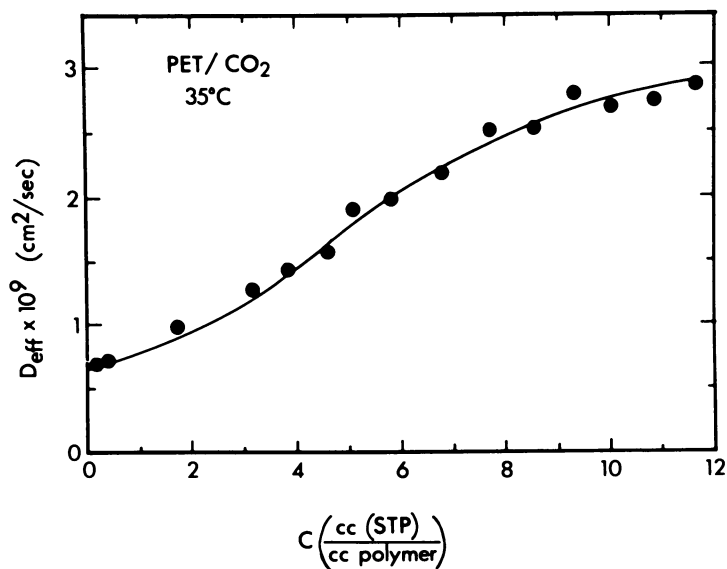


Figure 6. Local effective diffusion coefficient, $D_{eff}(C)$, for carbon dioxide in poly(terephthalate) at 35 °C.

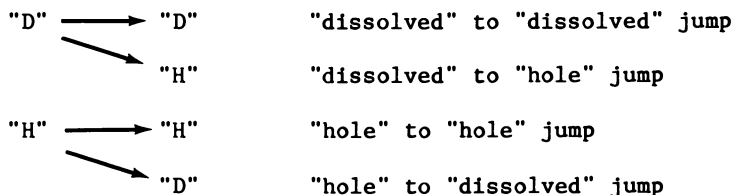
using a method that does not depend on the dual mode model in any way (22). Interestingly, however, the line through the data points corresponds to the predictions of $D_{\text{eff}}(C)$ using Eq (6) along with the independently determined dual mode parameters for this system (21,23). It is also important to note that the form of data in this plot which exhibits a tendency to asymptote at high pressures is not typical of plasticization. Finally, if one considers the low concentration region of Figure 6, it is clear that the diffusion coefficient is surprisingly concentration dependent. For example, $D_{\text{eff}}(C)$ increases by more than 35% as the local sorbed concentration rises from 0.142 cc(STP)/cc polymer (or 0.00020 wt. fraction) at 50 mm Hg to 1.7 cc(STP)/cc polymer (or 0.0025 wt. fraction) at 760 mm Hg. The above concentrations are extremely dilute, corresponding to less than 1 $\text{CO}_2/1200$ PET repeat units and 1 $\text{CO}_2/98$ repeat units respectively (4).

An even more dramatic case corresponds to CO_2 in PVC in which $D_{\text{eff}}(C)$ rises by 86% as the local concentration increases from 1 $\text{CO}_2/4400$ repeat units at 100 mm Hg to 1 $\text{CO}_2/1300$ repeat units at 500 mm Hg at 40°C (24). The above values of CO_2 solubility are based on measurements by Toi (24) and Tikhomorov et al. (25) which are in good agreement.

At such extraordinarily low penetrant concentrations, plasticization of the overall matrix is certainly not anticipated. Motions involving relatively few repeat units are believed to give rise to most short term glassy state properties. In rubbery polymers, on the other hand, longer chain concerted motions occur over relatively short time scales, and one expects plasticization to be easier to induce in these materials. Interestingly, no known transport studies in rubbers have indicated plasticization at the low sorption levels noted above for PVC and PET.

The discussion directly following Eq (6) provides a simple, physically reasonable explanation for the preceding observations of marked concentration dependence of $D_{\text{eff}}(C)$ at relatively low concentrations. Clearly, at some point, the assumption of concentration independence of D_D and D_H in Eq (6) will fail; however, for our work with "conditioned" polymers at CO_2 pressures below 300 psi, such effects appear to be negligible. Due to the concave shape of the sorption isotherm, even at a CO_2 pressure of 10 atm, there will still be less than one CO_2 molecule per twenty PET repeat units at 35°C. Stern (26) has described a generalized form of the dual mode transport model that permits handling situations in which non-constancy of D_D and D_H manifest themselves. It is reasonable to assume that the next generation of gas separation membrane polymers will be even more resistant to plasticization than polysulfone, and cellulose acetate, so the assumption of constancy of these transport parameters will be even more firmly justified.

Although not necessary in terms of phenomenological applications, it is interesting to consider possible molecular meanings of the coefficients, D_D and D_H . If two penetrants exist in a polymer in the two respective modes designated by "D" and "H" to indicate the "dissolved" (Henry's law) and the "hole" (Langmuir) environments, then the molecules can execute diffusive movements within their respective modes or they may execute intermode jumps.



Clearly, the true character (activation energy, entropy and jump length) of the phenomenologically observed D_D will be a weighted average of the relative frequency of "D"→"D" and "D"→"H" jumps, and likewise for D_H in terms of "H"→"H" and "H"→"D" jumps. Given the relatively dilute overall volume fraction associated with the non equilibrium gaps which comprise the "H" environment (< 4 to 5% on a volume basis), one may to a first approximation assume that most diffusive jumps of a penetrant from a "D" environment result in movement to another "D" environment and most diffusive jumps from "H" environments result in movement to a "D" environment. The observed activation energies, entropies and jump lengths, therefore, have fairly well-defined meanings on a molecular scale.

One can easily show that the appropriate equation derived from the dual mode sorption and transport models for the steady state permeability of a pure component in a glassy polymer is given by Eq (7) (18) when the downstream receiving pressure is effectively zero and the upstream driving pressure is p .

$$P = k_D D_D \left[1 + \frac{FK}{1 + bp} \right] \quad (7)$$

The first term in Eq (7) describes transport related to the Henry's law environment, while the second term is related to the Langmuir environment. The tendency for the permeability to asymptotically approach the limiting value of $k_D D_D$ at high pressures derives from the fact that after saturation of the upstream Langmuir capacity at high pressures, additional pressure increases result in additional flux contributions only from the term related to Henry's law which continues to increase as upstream pressure increases.

The remarkable efficacy of the dual mode sorption and

transport model for description of pure component data has been illustrated by plots of the linearized forms of Eq (2) and Eq (7) for a wide number of polymer/penetrant systems (4,5,9,10,22,24). These linearized plots are stringent tests of the ability of the proposed functional forms to describe the phenomenological data. Assink (27) has also investigated the dual mode model using a pulsed NMR technique and concluded that:

"We have been able to demonstrate the basic validity of the assumptions on which the dual mode model is based and we have shown the usefulness of NMR relaxation techniques in the study of this model."

Whereas the dual sorption and transport model described above unifies independent dilatometric, sorption and transport experiments characterizing the glassy state, an alternate model offered recently by Raucher and Sefcik provides an empirical and fundamentally contradictory fit of sorption, diffusion and single component permeation data in terms of parameters with ambiguous physical meanings (28). The detailed exposition of the dual mode model and the demonstration of the physical significance and consistency of the various equilibrium and transport parameters in the model in the present paper provide a back drop for several brief comments presented in the Appendix regarding the model of Raucher and Sefcik.

Mixed Component Sorption and Transport

Arguments similar to those presented above for pure components have been extended to generalize the expressions given in Equations 2 and 7 to account for the case of mixed penetrants (29,30). The appropriate expressions are given below:

$$C_A = k_{DA}P_A + \frac{C_{HA}^i b_{APA}}{1 + b_{APA} + b_{BPB}} \quad (8)$$

$$P_A = k_{DA}D_{DA} \left[1 + \frac{F_A K_A}{1 + b_{APA} + b_{BPB}} \right] \quad (9)$$

In the above expressions, "A" refers to the component of primary interest while "B" refers to a second "competing" component.

The permeability of a polymer to a penetrant depends on the multiplicative contribution of a solubility and a mobility term. These two factors may be functions of local penetrant concentration in the general case as indicated by the dual mode model. Robeson (31) has presented data for CO₂ permeation in

polycarbonate in which both solubility and diffusivity are reduced due to antiplasticization caused by the presence of the strongly interacting 4-4' dichloro diphenyl sulfone. On the other hand, sorption of a less strongly interacting penetrant, such as a hydrocarbon, may affect primarily only the solubility factor without significantly changing the inherent mobility of the penetrant in either of the two modes. Flux reduction in this latter context occurs simply because the concentration driving force of penetrant A is reduced. This results from the exclusion of A by component B from Langmuir sorption sites which were previously available to penetrant A in the absence of penetrant B.

Consistent with the preceding discussion concerning sorption and flux reductions by relatively non interacting penetrants, the data shown in Figure 7 clearly illustrate the progressive exclusion of CO₂ from Langmuir sorption sites in poly(methyl methacrylate) (PMMA) as ethylene partial pressure (p_B) is increased in the presence of an essentially constant CO₂ partial pressure of $p_A = 1.53 \pm 0.04$ atm (32). The tendency of the CO₂ sorption shown in Figure 7 to decrease monotonically with ethylene pressure provides impressive support for the "competition" concept on which Eq (8) and Eq (9) are based. Permeation data are not available for this system to determine if changes in the value of D_D and D_H occur in the mixed penetrant situation; however, for the case of the relatively non interacting ethylene at the pressures studied, any such effects are expected to be minor.

The data shown in Figure 8 illustrate the reduction in permeability of polycarbonate to CO₂ caused by competition between isopentane and CO₂ for Langmuir sorption sites (33). The flux depression shown in Figure 8 was found to be reversible, with the permeability returning to the pure CO₂ level after sufficient evacuation of the isopentane-contaminated membrane. Even at the low isopentane partial pressure considered (117 mm Hg) the tendency is clear for the CO₂ permeability to be depressed from its pure component level toward the limiting value ($P_A = k_{DA} D_{DA}$) corresponding to complete exclusion of CO₂ from the Langmuir environment. Further increases in the isopentane partial pressure in the feed should eventually complete the depression of CO₂ permeability to its limiting value of 4.57 Barrers unless plasticizing effects set in at the higher isopentane levels. This suggests, for example, that the effective CO₂ permeability at a CO₂ partial pressure of 2 atm could be reduced by as much as 36% due to small amounts of such hydrocarbons in the feed stream.

The lines drawn through the data in Figure 8 were calculated from Eq (7) and Eq (9) for the pure and mixed penetrant feed situations, respectively, using the same CO₂ model parameters in both cases. The affinity constant of

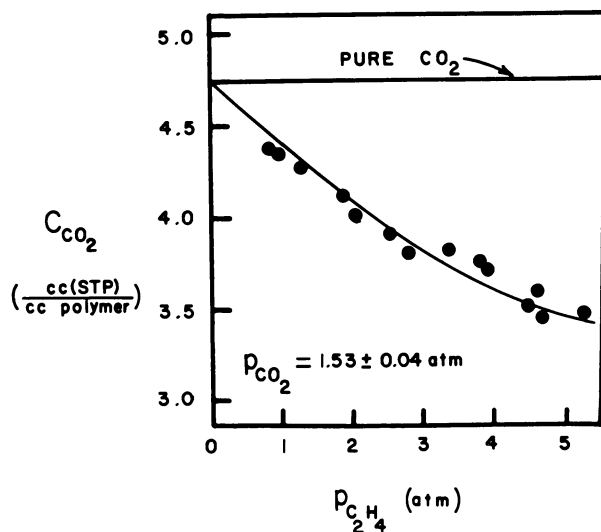


Figure 7. The effect of ethylene on the sorption level of carbon dioxide in poly(methyl methacrylate) at 35 °C.

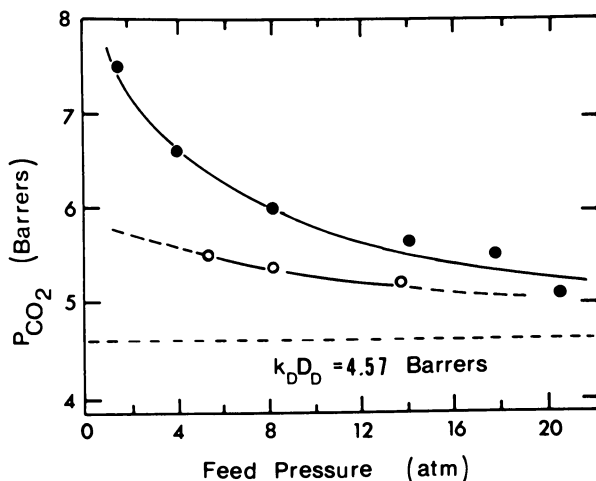


Figure 8. Permeability of Lexan polycarbonate to carbon dioxide at 35 °C as a function of CO_2 partial pressure. [○, in the presence of 117 mm. Hg of isopentane in the feed; ●, pure CO_2 .]

isopentane was estimated for use in Eq (9) to be 13.8 atm^{-1} (33). The excellent fit of the data suggests that D_D and D_H for CO_2 in the mixed feed case are not affected measurably by the presence of the relatively non-interacting isopentane. The sorption and transport parameters for CO_2 in the polycarbonate sample used in the above study are reported in Table 2.

Conclusions

The confluence of current views of the glassy state with recent data for sorption and transport of mixed penetrants in glassy polymers provides a complementary framework useful in both areas. Specifically, the concept of "unrelaxed volume" invoked to explain concavity in the sorption isotherm may eventually be valuable in rationalizing different creep, impact strength and physical aging behavior of glassy polymers. The dual mode sorption and transport model provides a valuable basis for both qualitative and quantitative analysis of gas separator operation in the preplasticizing regime. Although plasticizing effects are likely to be of considerable importance at high pressures in gas separators with the present generation of membrane materials, one might anticipate that the next generation of materials based on very high T_g , highly rigid backbone polymers will minimize sensitivity to such deleterious effects. If such stiff-chain materials can be formulated into useful membranes, phenomena associated with dual mode sorption and transport will be of primary importance over the full range of operating pressures, since the transition to plasticizing behavior shown in Figure 1 would presumably require very high sorbed concentration levels. Such plasticization-resistant membranes might even maintain reasonable selectivity in liquid/liquid permeation separations such as pervaporation.

Appendix: Comments Concerning The "Matrix" Model For Sorption and Diffusion in Glassy Polymers

In the preceding discussion we have presented a model with physically interpretable parameters to explain sorption data for penetrants in glassy polymers. The basis of the model, the concept of "unrelaxed volume" is also useful in understanding many other properties of glassy polymers such as impact strength, physical aging and creep, which are related to the non equilibrium nature of these materials. Moreover, this model yields a physically consistent expression for the local effective diffusion coefficient, $D_{eff}(C)$, which shows concentration dependence at sorbed concentrations well below the point at which substantial interaction of one penetrant with the matrix is generally expected to significantly facilitate the movement of another penetrant.

Table 2

Sorption and transport parameters of CO₂ in
Lexan polycarbonate at 35°C

k_D $\frac{\text{cc(STP)}}{\text{cc-atm}}$	0.6751
b atm^{-1}	0.2563
C_H' $\frac{\text{cc(STP)}}{\text{cc polymer}}$	17.61
D_D cm^2/sec	5.1484×10^{-8}
D_H cm^2/sec	5.8266×10^{-9}

The dual mode model assumes that the heterogeneity that characterizes the glassy polymer state can be treated in a physically reasonable fashion using the concept of two basically different environments in the polymer. One environment corresponds to that in which a penetrant molecule is sorbed between chain segments that have achieved essentially their equilibrium conformations and interchain distances (perhaps with the aid of the invading penetrant during the "conditioning" step shown in Figure 3). A second environment corresponds to that in which a penetrant molecule finds itself sorbed in a region of localized lower density (perhaps due to local chain kinks or other impediments to rapid relaxation). The model requires, however, that the local concentrations of C_D and C_H in Eq (1) adjust themselves consistent with the requirement that there is only one chemical potential applicable to the penetrant, and at sorption equilibrium this chemical potential is also identical to that of the penetrant in the external gas phase. Any significant energetic heterogeneity associated with sorption in the nonequilibrium gaps regions should manifest itself as a failure in the Langmuir form to fit the deviation from the simple Henry's law model, since the Langmuir form assumes a uniform site affinity. Repeated tests of the linearized form of the Langmuir contribution to sorption have shown excellent conformity to the model. Any such energetic heterogeneity is, therefore, of negligible importance with respect to sorption modeling. In their recent paper, Raucher and Sefcik interpret Dr. R. Assink's pulsed NMR study of ammonia sorption in polystyrene (27) and indicate that: "Spectroscopic analyses of gas molecules within polymer matrices are consistent with all of the gas molecules being in a single state" (28). One is given the indirect and erroneous impression from Raucher's and Sefcik's reference to Assink's work that the Assink study did not support the concepts of the dual mode model. On the contrary, the conclusions of Dr. Assink with regard to this issue completely support the dual mode model premises as shown below in a direct quote of the complete conclusions from the Assink paper (27):

"We have been able to critically examine the dual mode model by pulsed NMR relaxation techniques. The pressure dependence of the concentration of sorbed gas was consistent with the dual mode model while the relaxation data addressed itself to the validity of the assumptions made by the model. The assumption of rapid interchange was found to be valid for this system while the assumption of an immobile adsorbed phase could introduce a small error in the analysis. It should be possible to reduce this error by more exact measurements of the concentration of sorbed gas as classical pressure experiments could

provide. We have been able to demonstrate the basic validity of the assumption on which the dual mode model is based and we have shown the usefulness of NMR relaxation techniques in the study of this model."

The only "small error", suggested in Assink's statement concerning the dual mode model's assumptions, deals with the earlier approximation by Vieth and Sladek (34) that D_H was equal to zero. The work of Assink was performed prior to the formulation of the dual mobility model which eliminates this approximation and accomodates values of $D_H > 0$ (17,18).

In the present symposium, Dr. Raucher argued that the observed curvature in gas sorption isotherms does not arise from a site saturation mechanism such as we have described in the preceding discussion. The form of the sorption isotherm and local concentration dependent diffusion coefficient proposed by Raucher and Sefcik are given below:

$$C = \frac{\sigma_0 P}{1 + \alpha C} \quad (A-1)$$

$$D_{eff}(C) = D_0 [1 + \beta C] \quad (A-2)$$

where D_0 was identified as the zero concentration limit of the diffusion coefficient and β was identified as a plasticization-related parameter which indicates the relative sensitivity of the local diffusion coefficient, $D_{eff}(C)$ to the presence of other penetrants in the vicinity. While no physical interpretation was given to the sorption parameters, the σ_0 parameter is clearly equal to the limiting slope of the concentration versus pressure isotherm. During a question and answer period following his presentation, Dr. Raucher explicitly ruled out an interpretation of the parameter α in terms of a site saturation mechanism similar to the Langmuir model.

Drs. Raucher and Sefcik have stated: "The apparent concentration dependence of the sorption capacity in the matrix model results from a decrease in a Henry's law-like constant as the polymer adjusts to the sorbate" (28). The extent of the interpretation of α offered by these authors is that: " α is a parameter indicating the magnitude of the change in solubility arising from changes in the gas-polymer matrix". Specifically, what is missing from their discussion is a statement as to what the nature of the hypothetical polymer/penetrant interactions are that cause the concavity in the isotherm. In other words, what change is induced in the nature of the polymer in the presence of the penetrant? The "model" comprised of Eq (A-1) and (A-2) has a strictly empirical basis. It seems incumbent upon these authors to explain how the change in the polymer matrix makes it more difficult to insert another penetrant

[Eq (A-1)], but at the same time makes it easier for the penetrant to move through the matrix [Eq (A-2)]. The dual mode model offers the physical interpretation that concavity in the isotherm arises from a site saturation mechanism related to filling of unrelaxed gaps--a phenomenon which is not only easily visualized and understood, but also has been tested explicitly with independently obtained dilatometric data (See Figure 5).

In an attempt to justify the assumption of plasticization put forth in their interpretation of β in Eq (A-2), Raucher and Sefcik compare transport data and ^{13}C NMR data for the CO_2/PVC system. This comparison has several questionable aspects. To relate local molecular chain motions to the diffusion coefficient of a penetrant, one should use the so-called local effective coefficient, $D_{\text{eff}}(\text{C})$, such as shown in Figure 5 rather than an average or "apparent" diffusion coefficient as was employed by these authors. $D_{\text{eff}}(\text{C})$ describes the effects of the local sorbed concentration on the ability of the average penetrant to respond to a concentration or chemical potential gradient in that region.

Raucher and Sefcik, on the other hand, base their comparisons between NMR data and transport data on the so-called "apparent" diffusion coefficient defined by:

$$D_a = l^2/\theta \quad (\text{A-3})$$

where θ is the observed time lag and l is the membrane thickness. D_a does not have a simple meaning equivalent to a true molecular mobility unless both the time lag and permeability are independent of upstream pressure. Since this situation is not typically observed in glassy polymers, one must use $D_{\text{eff}}(\text{C})$ for comparison with complementary techniques that probe molecular motion.

The seriousness of this oversight is apparent in Sefcik and Schaefer's analysis of Toi's transport data (24) in terms of their NMR results (28). The value of the so-called "apparent" diffusion coefficient calculated from Toi's time lag data increases by ~25% for an upstream pressure range between 100 mm Hg and 500 mm Hg. On the other hand, the value of $D_{\text{eff}}(\text{C})$ calculated from Toi's data changes by 86% over the concentration range from 100 to 500 mm Hg. The difference in the two above coefficients arises from the fact that D_a is an average of values corresponding to a range of concentrations from the upstream value to the essentially zero concentration downstream value in a time lag measurement. $D_{\text{eff}}(\text{C})$, on the other hand, has a well-defined point value at each specified concentration and is typically evaluated (independent of any specific model other than Fick's law) by differentiation of solubility and permeability data (22).

A second issue clouding the NMR interpretation of Toi's

40°C transport data lies in the fact that the cited NMR data were collected at 26°C rather than 40°C. If one neglects this fact, Sefcik and Schaefer suggest that the 5.7% increase in the average rotating frame relaxation rate, $\langle R_{1\rho}(C) \rangle$ over the pressure range (100 mm Hg to 500 mm Hg) corresponding to T_{01} 's measurements validate their claims concerning plasticization. This suggestion neglects the fact that the 25% increase in D_a does not match the 5.7% increase in $\langle R_{1\rho}(C) \rangle$. Moreover, recall that D_a is actually not even the correct coefficient to compare with $\langle R_{1\rho}(C) \rangle$. The observed 86% increase in $D_{\text{eff}}(C)$ is in poor agreement with the 5.7% increase in the NMR parameter over the range of pressures where both types of data are available.

The considerable discrepancy between the changes in the two parameters $D_{\text{eff}}(C)$ and $\langle R_{1\rho}(C) \rangle$ is not impressive proof for plasticization at such low concentrations. This observation is especially true since part of the observed 5.7% increase in $\langle R_{1\rho}(C) \rangle$ may be accounted for by spin-spin effects. The value of $\langle R_{1\rho}(C) \rangle$ requires cautious interpretation in terms of bulk polymer properties such as the effective diffusion coefficient; especially in light of the preceding discussion concerning T_{01} 's data. It is important to remember that even at 500 mm Hg, there is only one CO_2 molecule for every 1300 PVC repeat units in the above situation and yet an increase of 86% occurs in the value of $D_{\text{eff}}(C)$ between 100 mm Hg and 500 mm Hg. These conditions are extraordinarily dilute, and the observed concentration dependence of $D_{\text{eff}}(C)$ is perfectly consistent with a site saturation type behavior inherent in the dual mode model. We have always acknowledged that concentration dependence of D_D and D_H may become important factors at elevated pressures for plasticization prone polymers. Such effects, if present have been of second order importance in our work which is generally performed on "conditioned" polymers at CO_2 pressures no greater than 300 psi. Eventual concentration dependence of D_D and D_H is, however, not related to the views of Raucher and Sefcik summarized by Eq (A-1) and Eq (A-2). These equations require that the seemingly mutually exclusive processes of antiplasticization (Eq A-1) and plasticization (Eq A-2) occur simultaneously.

Finally, it was suggested by Raucher and Sefcik that the equations derived from their analysis were essentially as effective as the dual mode model for describing existing data. This statement requires some strong qualification, since no linear equation can describe the inflected form of the $D_{\text{eff}}(C)$ plot shown in Figure 6 which was evaluated by graphical differentiation of the permeability and solubility data without reference to any particular model other than Fick's law (21,22). The curve through the data, nevertheless, corresponds to the dual mode model and provides a very good description of the data. The form of these data is not at all consistent with

plasticization. This same argument will apply for essentially all of the cases in which the dual mode model has been shown to fit the form of the local diffusivity. The data points can at best be made to "snake" around the linear fit of the expression in Eq (A-2) and the linear model becomes seriously in error as D_{eff} begins to asymptote. Limited data for two gas/polymer systems were shown by Dr. Raucher which indicated that the descriptions of permeabilities and time lags using the dual mode and matrix models is not very different for the systems checked. If this is true, it is surprising since the different forms of $D_{\text{eff}}(C)$ would be expected to give rise to somewhat different time lag results when integrated according to Frisch's method (35). A similar conclusion pertains to the permeability, since even if the solubility data were perfectly described, the misfit of $D_{\text{eff}}(C)$ suggests that there should be a misfit in permeability as well. It is possible that a misfit of $D_{\text{eff}}(C)$ versus C and of C versus p could offset each other.

In one of their comparisons between the matrix model and the dual mode model, a somewhat misleading presentation of data is unintentionally offered in Figure 4 of the Raucher and Sefcik paper: "Matrix Model of Gas Sorption and Diffusion in Glassy Polymers" (28). What should be compared in the left hand side of this plot is the dual mode model with refitted parameters over the same pressure range as the "Matrix model" parameters were refitted over. Clearly, a detailed statistical comparison of the permeability and time lag predictions arising from Eq (A-1) and Eq (A-2) must be made with the large body of experimental data available for glassy systems before a conclusion can be reached regarding the efficacy of the "matrix" model for phenomenologically describing such data in general.

On a more basic level, since the matrix model implicitly requires a somewhat inconsistent interpretation for the various model parameters in Eq (A-1) and Eq (A-2), it becomes primarily an empirical means of reproducing the observed pure component data with no fundamental basis for generalization to mixtures. One could, of course envision several extensions based on additional α terms in the denominator of Eq (A-1) and additional β terms in Eq (A-2). Such an approach to mixture permeation analyses would be completely empirical and mimic the generalization of Eq (2) and Eq (7); however, without any physical justification. The generalizations of Eq (2) and Eq (7) were natural outgrowths of the fundamental physical basis of the Langmuir isotherm. The fact that the mixture data are so consistent with Eq (7) and Eq (9) provides strong support for the physical basis of the dual mode model.

An important value of a permeation model is not simply its ability to correlate experimental data, but rather to provide a framework for understanding the principal factors controlling membrane performance. The dual mode model is derived from

consistent, physical descriptions of the glassy state and yields parameters which make unambiguous molecular scale statements regarding the general nature of glassy, amorphous materials.

In summary, the two expressions offered in Eq (A-1) and Eq (A-2) provide empirical forms for correlating the general trends in pure component sorption and transport data. These expressions are not offered in terms of internally consistent physical arguments and appear to offer no fundamental basis for understanding general glassy state behavior. Furthermore, no fundamental approach is apparent for the treatment of the critically important mixed penetrant problem using the model, since the various parameters in the model lack the well-defined significance provided by the dual mode model.

Nomenclature

- b_i Affinity constant of component i for the polymer (atm^{-1})
 D_D Diffusion coefficient of the Henry's law species (cm^2/sec)
 D_H Diffusion coefficient of the Langmuir species (cm^2/sec)
 F Ratio of Langmuir and Henry's law diffusion coefficients
 k_D Henry's law constant ($\text{cm}^3 \text{ gas (STP)}/\text{cm}^3 \text{ polymer-atm}$)
 K C_H^i/k_D where C_H^i is the capacity of Langmuir mode ($\text{cm}^3 \text{ gas (STP)}/\text{cm}^3 \text{ polymer}$)
 p_i Upstream driving pressure for penetrant i (atm)
 P_i Permeability of i ($\text{cm}^3 \text{ gas(STP)-cm}/\text{cm}^2\text{-sec-cmHg}$)
 V_g Specific volume of the glassy polymer (cm^3/g)
 V_g^d Specific volume of the densified glassy polymer (cm^3/g)

Acknowledgments

The authors gratefully acknowledge support of this work under NSF Grant No. CPE-79-18200 and ARO Contract No. DAAG29-81-K-0039. Also the assistance of Mrs. Leslie Edgerton in typing the manuscript is acknowledged.

Literature Cited

1. Stannett, V. T.; Koros, W. J.; Paul, D. R.; Lonsdale, H. K. and Baker, R. W.; Adv. in Polymer Sci., 1979, 32, 69.
2. Barrer, R. M. and Barrie, J. A.; J. Polym. Sci., 1957, 23, 331.
3. Pye, D. G.; Hoehn, H. H. and Panar, M.; J. Appl. Polym. Sci., 1976, 20, 287.
4. Koros, W. J. and Paul, D. R.; J. Polym. Sci.-Polym. Phys. Ed., 1978, 16, 1947.
5. Wonders, A. G. and Paul, D. R.; J. Membr. Sci., 1979, 5, 63.
6. Fechter, J. M.; Hopfenberg, H. B. and Koros, W. J.; Polym. Engr. and Sci., 1981, 21, 925.

7. Koros, W. J. and Paul, D. R.; J. Polym. Sci., Polym. Phys. Ed., 1981, 19, 1655.
8. Horiuti, J.; Sci. Papers of the Inst. of Phy. and Chem. Res. (Tokyo); 1931, 17, 126.
9. Chan, A. H. and Paul, D. R., Polym. Engr. and Sci., 1980, 20, 87.
10. Huvard, G. S.; Stannett, V. T.; Koros, W. J. and Hopfenberg, H. B., J. Membr. Sci., 1980, 6, 185.
11. Chen, S. H., M.S. Thesis, North Carolina State University, 1982.
12. Lewis, O. G.; "Physical Constants of Linear Homopolymers," Springer Verlag, New York (1968).
13. Kolb, H. J. and Izard, E.; J. Appl. Phys., 1949, 20, 564.
14. Matuska, S. and Ishida, Y.; J. Polym. Sci., Pt. C., 1960, 14, 247.
15. Mercier, J. P.; Aklonis, J. J.; Litt, M.; and Tobolsky, A. V.; J. Appl. Polym. Sci., 1965, 9, 447.
16. Sandler, Stanley I.; "Chemical and Engineering Thermodynamics," J. Wiley and Sons, New York, 1977, pg. 435.
17. Petropoulos, J. H.; J. Polym. Sci., Pt. 2-A, 1970, 8, 1797.
18. Paul, D. R. and Koros, W. J.; J. Polym. Sci.-Polym. Phys. Ed., 1976, 14, 675.
19. Koros, W. J.; Chan, A. H. and Paul, D. R.; J. Membr. Sci., 1977, 2 165.
20. Barrie, J. A.; Williams, M. L. and Munday, K.; Polym. Engr. and Sci., 1980, 20, 20.
21. Koros, W. J., Ph.D. Dissertation; "Sorptions and Transport of Gases in Glassy Polymers," The University of Texas (Austin), 1977.
22. Koros, W. J.; Paul, D. R. and Rocha, A. A.; J. Polym. Sci., Polym. Phys. Ed., 1976, 14, 687.
23. Koros, W. J. and Paul, D. R.; J. Polym. Sci., Polym. Phys. Ed., 1978, 16, 2171.
24. Toi, K.; Polym. Engr. and Sci., 1980, 20, 30.
25. Tikhomorov, B. P.; Hopfenberg, H. B.; Stannett, V. T. and Williams, J. L.; Macromol. Chem., 1968, 118, 177.
26. Stern, S. A. and Saxena, V.; J. Membr. Sci., 1980, 7, 47.
27. Assink, R. A.; J. Polym. Sci.-Polym. Phys. Ed., 1975, 13, 1665.
28. Raucher, D. and Sefcik, M.; Paper presented in this symposium.
29. Koros, W. J.; J. Polym. Sci.-Polym. Phys. Ed., 1980, 18, 981.
30. Koros, W. J.; Chern, R. T.; Stannett, V. T. and Hopfenberg, H. B.; J. Polym. Sci.-Polym. Phys. Ed., 1981, 19, 1513.
31. Robeson, L. M.; Polym. Engr. and Sci., 1969, 9, 277.

32. Sanders, E. S.; Koros, W. J.; Hopfenberg, H. B. and Stannett, V. T.; "Mixed Gas Sorption in Glassy Polymers: Equipment Design and Considerations and Preliminary Results," Submitted for Publication, J. Polym. Sci.- Phys. Ed.
33. Chern, R. T.; Koros, W. J.; Hopfenberg, H. B. and Stannett, V. T.; "The Effects of Low Partial Pressures of Isopentane on the Permeability of Polycarbonate to CO₂," accepted by J. Polym. Sci.- Phys. Ed.
34. Vieth, W. R. and Sladek, K. J.; J. Coll. Sci., 1965, 20, 1014.
35. Frisch, H. L.; J. Phys. Chem., 1957, 61, 93.
36. Smith, G. N.; M.S. Thesis, North Carolina State University, 1980.

RECEIVED December 27, 1982

Standard Reference Materials for Gas Transmission Measurements

JOHN D. BARNES

National Bureau of Standards, Polymer Science and Standards Division,
Washington, DC 20234

Standard Reference Material 1470 is a 23 micrometer thick polyester film whose gas transmission characteristics with respect to helium, carbon dioxide, oxygen, and nitrogen have been carefully measured. A completely computerized manometric permeation measuring facility developed at NBS was used for the measurements. The steps taken to characterize the gas transmission rate of this material over the range of pressures from 67.5 kPa to 135 kPa and over the range of temperatures from 18 °C to 31 °C are described. The results obtained in these measurements are compared with those in the literature. The role of Standard Reference Material 1470 in improving the repeatability and reproducibility of gas transmission measurements employing other instrumentation is discussed.

A Standard Reference Material (SRM) can be defined as "a material (not necessarily a pure substance) having given properties with numerically assessed values, within certain tolerances, certified by an appropriate technical body" (1). An SRM for oxygen gas transmission measurements has been available since 1978 from the National Bureau of Standards (NBS) (2). This material has recently been certified for its permeance with respect to carbon dioxide, helium, and nitrogen as well as oxygen. This was done to make the material available to a larger community of users. The work on oxygen was repeated in order to determine whether the existing stock of material had aged to any appreciable extent and to ensure that all results were reported on a common basis. The present paper describes the experiments that were done to characterize the gas transmission properties of the material over a range of conditions that the user can expect to experience and the manner in which the results on the SRM certificate are to be interpreted by the user.

This chapter not subject to U.S. copyright
Published 1983, American Chemical Society

SRM's exist because of the widely perceived need to achieve agreement among measurement results obtained from a measurement system. In order for such materials to be useful, the property of interest must be stable in the chosen material, the property must be measured by a method that is free of bias, and the property must be homogeneous across all possible specimens of the material.

The typical user of an SRM performs a measurement of the certified property using the apparatus in his laboratory. He compares his result with the certificate value and, if his measurement fails to reproduce the certified value within acceptable limits of precision he investigates his measurement system to remove sources of bias. There are numerous examples of measurement systems in which the level of agreement among measured results by employing SRM's in this way, and the statistical assessment of the performance of measurement systems employing SRM's is a well-established science (3).

NBS's involvement in SRM's for gas transmission studies arose out of activities within ASTM Committees D-20 (Plastics) and F-2 (Flexible Barrier Materials) that were aimed at standardizing a new instrumental method employing a coulometric oxygen detector for the measurement of oxygen gas transmission rates in materials used for various kinds of packaging (4). A subsequent reevaluation of the precision data for the classical manometric and volumetric methods (5) for gas transmission measurements showed that there are serious problems with the reproducibility and repeatability these methods. The use of SRM 1470 to verify the calibration is currently being written into ASTM standards D-3985 and D-1434.

Approach

The effort being described here is a simple extension of the work that was done earlier to characterize the gas transmission properties of SRM 1470 with respect to oxygen alone (2). The material that is used for this SRM is a poly(ethylene terephthalate) (PET) film approximately 23 micrometers thick that is used commercially as a base for magnetic tape. This material appeared to be suitable from the standpoint of homogeneity and long term stability and its oxygen transmission rate was in the desired range. Similar material was already in use as a de facto SRM provided by a manufacturer of coulometric oxygen transmission measuring equipment. Specimens for the recertification measurements were obtained by random sampling from the existing stock of material.

We chose to use a modernized version of the manometric measuring technique both in our earlier work and in the present experiments. This approach offered good flexibility in that the electronic manometers used to monitor the gas flux respond to a wide variety of gases. It is also possible to calibrate the apparatus reliably using existing standards. By completely computerizing the measurement process (6) we were able to provide

for unattended operation as well as enhanced reliability and safety.

In the time-lag technique (7) for measuring permeation gas passes through a well defined area of a film from a reservoir at an elevated pressure into a receiving chamber. The film is devoid of permeant to begin with. In the manometric realization of this method the accumulation of permeant in the receiving chamber is measured by monitoring the pressure of the gas in the chamber. In our system we begin by connecting both chambers to vacuum pumps to remove any sorbed gases. We then monitor the small pressure rise that occurs when the receiving chamber is isolated from the pump but the upstream chamber is still being evacuated. We assign this pressure rise to a background flux. At a chosen instant the upstream chamber is supplied with gas at a controlled pressure. Gas does not appear in the downstream chamber until enough of it diffuses into the film to establish a finite concentration gradient at the downstream boundary. After a while the pressure in the downstream chamber rises at a steady rate. Once we are satisfied that we have enough data to precisely estimate the steady-state flux we terminate the pressure monitoring and reevacuate both sides of the film in preparation for the next experiment.

Calibration

The calibration problem for our measurement system can be discussed in the light of the following relationship:

$$n = pV/RT = AF_{\infty}[t - \tau + q(t/\tau)] \quad (1)$$

where n is the number of moles of permeant accumulated in the receiving chamber after a time t , p is the pressure in the receiving chamber at time t , V is the volume (in liters) of the receiving chamber, T is the temperature of the system (in kelvins), R is the ideal gas constant (8.3144 kPa-l/mol-K) and A is the area (in m^2) of film through which permeation takes place. F_{∞} is the permeant flux (in $mol/m^2 \cdot s$) for steady-state permeation, τ is the time-lag and $q(t/\tau)$ is a function that accounts for the transient response of the system. F_{∞} is the product of the upstream gas pressure, p_u , and the permeance, P , of the film being tested. The functional form of $q(t/\tau)$ for the case of ideal diffusion can be obtained by rearranging the equations from the standard texts (8,9). In our case the receiving volume, V , is large enough and the final pressure is low enough so that we can neglect the effects due to the finite volume of the receiving chamber. Under these conditions there is a substantial period of time during which q is essentially equal to unity and the pressure vs time trace may be treated as a straight line with slope $s = F_{\infty}ART/V$ and intercept $y_0 = -\tau AF_{\infty}RT/V$, a circumstance that our computer programs make use of to perform data reduction by least squares.

The calibration characteristics of the pressure transducer are described by the following relationship:

$$P_{\text{true}} = P_{\text{app}} \times [1 + a(T)] \quad (2)$$

The subscript "true" denotes the corrected pressure values while "app" refers to the observed values after they have been corrected for contributions from the background flux. The function $a(T)$ is a small correction that is obtained by intercomparing each cell manometer with a well-calibrated manometer that is always evacuated and maintained at a fixed temperature. Differentiating equation 2 gives

$$s = [1 + a(T)] dp_{\text{app}}/dt = [1 + a(T)] s_{\text{app}} \quad (3)$$

where s_{app} is the slope derived from fitting a straight line to the apparent pressure vs time trace.

In extracting s_{app} from our experimental data we use only data for long times ($t \gg \tau$) and we use an iterative process to correct for the small contribution from the time-lag.

Using equations 1, 2, and 3 together with the definition of the permeance we obtain

$$P = V [1 + a(T)] s_{\text{app}} / ART p_u \quad (4)$$

as an expression linking measured quantities with the quantity we wish to determine. The quantity $V[1 + a(T)]/ART$ can be regarded as a temperature dependent "cell constant" whose value is fixed by the design of the apparatus. Our studies indicate that this cell constant is accurate to within 2 percent of its measured value and that there is a random error of approximately 1 percent attributable to the calibration instability of the pressure sensors. More detailed studies of the calibration errors are currently in progress.

Potential sources of interference that can bias the observed results include leakage into the cell from extraneous sources and outgassing of the film being tested. A guard ring is built into the cell to minimize the former problem and we correct for the latter effect by monitoring the pressure rise in the cell while the upstream chamber is under a vacuum. If the resulting leakage flux is too large the computer postpones the experiment until the flux drops to an acceptable level. We perform the carbon dioxide measurements separately precisely because the outgassing in this case is so protracted as to interfere with the other measurements.

If the leakage flux falls within the acceptable range we merely measure its value for use as a baseline correction to the pressure vs time data taken when the upstream chamber is pressurized. The presence of this background flux tends to degrade the signal to noise ratio of the data for the less permeable species. Experiments using a solid aluminum plate in place of the film demonstrate that this leakage flux arises mainly from the polymer.

Experimental Design

Nine sheets of material were selected at random from the entire batch of SRM 1470 that was on hand. Our apparatus subjects three specimens to the same treatment at the same time, where a "treatment" is a measurement using a specified combination of gas, temperature, and upstream pressure. Measurements were made at 5 different temperatures ranging from 18 °C to 31 °C in order to allow the user some flexibility in his choice of measurement temperature. Measurements were also made at 4 different pressures ranging from 67.5 kPa to 135 kPa in order to determine if the material behaved non-ideally. Since we used a complete factorial design the total number of treatments was 80 (4 gases x 5 temperatures x 4 pressures). Each specimen was subjected to the complete set of treatments before being replaced by a new specimen. All measurements involving nitrogen, helium, and oxygen at a given temperature were made before the temperature was changed. The treatments involving carbon dioxide were applied last because of the prolonged outgassing required between experiments using this gas. Except for the restrictions described above the treatments were applied in random order. We found no evidence that the previous sample history affected the measurement results as long as as care was taken to ensure proper outgassing before applying the next treatment.

The order in which the treatments were to be applied was programmed into the computer, and the apparatus then operated unattended until it was time to insert a fresh data recording disc or to change the specimens. A complete series of treatments on a group of three specimens required about 6 weeks.

The processing of the data consisted of extracting the steady state slopes and the time lags from the pressure versus time traces, converting the slopes to permeances using the equations given above, and tabulating the results for subsequent statistical analysis.

Results

The complete set of experiments described above produced approximately 720 values of the permeance and 540 values of the time-lag (the time-lag for helium was too short to measure). We used the following fixed effects statistical model to study the data from each of the gases:

$$\ln Q = \mu_a + S_i + \theta_j + \rho_k + \epsilon_{ijk} \quad (6)$$

Q represents either the time-lag or the permeance as required, the S_i term accounts for the effect of selecting a particular one of the nine specimens, the θ_j term accounts for the effect

of choosing a particular one of the five temperatures, and ρ_k accounts for the pressure effect. The pressure effect was significant only when dealing with the time-lag data for carbon dioxide (see discussion below). We did not find any significant interaction terms between the main effects shown in equation 6. The ϵ_{ijk} term accounts for random errors of measurement.

Over the narrow (13 °C) range of temperatures in our experiments the temperature effect is linear and a temperature coefficient can be derived by fitting the θ values to the following model:

$$\theta_j = \alpha + \beta (T_j - 23) \quad (7)$$

The value of 23 °C was chosen so that the certificate values would be correct for the standard laboratory atmosphere (10).

Using equation 7 and taking the exponential function of both sides of equation 6 yields:

$$\hat{Q}(T) = \hat{Q}(23) e^{\beta(T-23)} \quad (8)$$

where the " $\hat{}$ " denotes that the quantity is an estimated value. Note that $\hat{Q}(23) = e^{\mu} Q + \alpha$. A measurement on an individual specimen can be expected to deviate from this estimate because of measurement error, and because of the specimen effect embodied in the S_i . Values of $\hat{Q}(23)$ and β obtained from the analysis of the permeance and the time-lag data are given in Tables I and II respectively. Since the time-lag for carbon dioxide depends upon the upstream pressure it is necessary to multiply the estimates obtained from equation 8 by a term of the form:

$$e^{a_1(p_u - 101.32) + a_2(p_u - 101.32)^2} \quad (9)$$

where the upstream pressure is expressed in kPa. Estimates derived from equations 8 and 9 are valid only for pressures between 67.5 and 135 kPa and for temperatures between 18 °C and 31 °C.

Tables I and II provide additional statistical data that can be used to qualify the estimates derived from the fitting process. C_μ is the standard deviation of μ , its numerical value is largely determined by the sampling error arising from the selection of test specimens. C_S is the standard deviation of the S_i 's, which is a measure of the inhomogeneity of the lot of SRM material. C_R is the standard deviation of the residuals from the fit, which is a measure of the extent to which individual data values depart from the model in equation 6. We have chosen not to construct the usual confidence or tolerance intervals because we do not have enough data on the distribution of the S_i 's.

The individual values of the S_i are plotted as a function of gas in Figures 1 and 2. If the factor that is giving rise to this variability influences all gases equally we would expect the lines in Figures 1 and 2 to be parallel. Parallel straight lines

Table I - Summary of fit results for Permeance data

Parameter	Gas				Units
	N2	O2	CO2	He	
$\hat{P}(23)$.042	.35	1.72	13.8	pmol/m ² .s.Pa
β	.0521	.0376	.0309	.0287	1/K
C_{μ}	.023	.014	.018	.012	
C_s	.057	.045	.056	.037	
C_r	.050	.017	.010	.009	

Table II - Summary of fit results for Time-lag data

Parameter	Gas			Units
	O2	N2	CO2	
$\tau(23)$	388.	1792.	2160.	sec.
β	-.0597	-.0763	-.0624	1/K
C_{μ}	.013	.022	.014	
C_s	.039	.067	.042	
C_r	.024	.094	.016	
a_1	--	--	-1.873×10^{-3}	1/kPa.
a_2	--	--	09.11×10^{-6}	1/(kPa.) ²

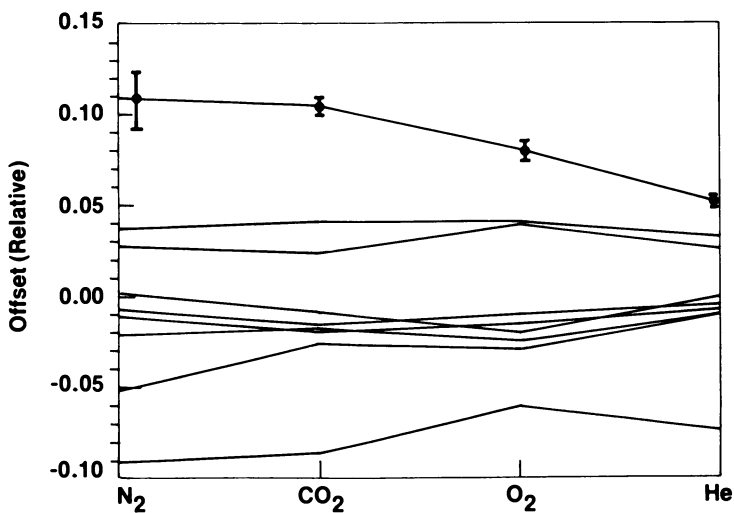


Figure 1. Specimen effect for the permeance plotted as a function of gas.

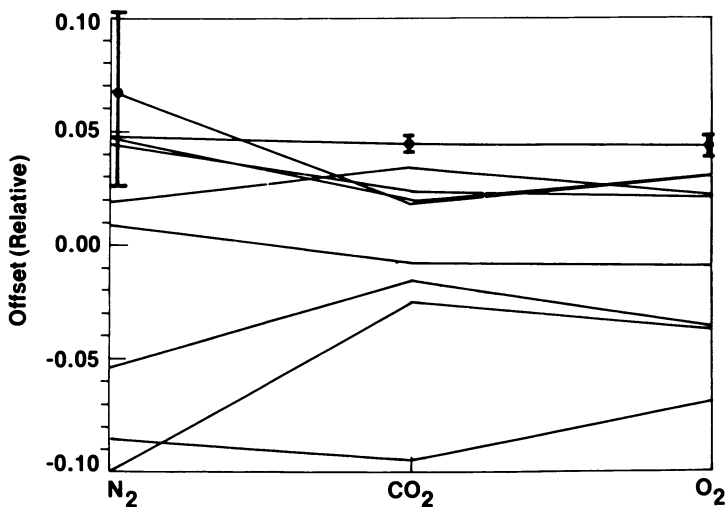


Figure 2. Specimen effect for the time lag plotted as a function of gas.

account for most of the variation but the scatter shown in the figures is significant. We are studying additional specimens to better define the structure and distribution of these specimen effects.

We are also seeking simple auxiliary measurements such as the specimen thickness or the density that can be used to define correction factors for reducing the measured values to a common basis. In the absence of such a scheme the specimen-to-specimen variability is the dominant factor limiting the precision that can be expected when comparing measurements among different stations in a measurement system.

In some instances where SRM's have been found to be inhomogeneous it is possible to individually certify each specimen. Aside from the fact that such a procedure would lead to intolerably costly standards, it is impractical because we have found that specimens that have been removed from the measuring apparatus cannot be reused. Thus a unit of SRM 1470 contains about 15 sheets of material, which last the average user quite a long time.

The observed decrease of the ρ values for the time-lag of carbon dioxide with increasing pressure is consistent with published data that have been interpreted using a "partial immobilization" model (11,12). It is somewhat surprising that we do not observe a concomitant decrease in the permeance; perhaps the pressures used are too low or the pressure range is not broad enough.

The residuals from the fits to the short time part of the pressure versus time traces provide additional evidence that the transport process of carbon dioxide in SRM 1470 is different from that of the other gases. The trace for carbon dioxide departs from the background trend line much more slowly than do the traces for the other gases. This is qualitatively reasonable in terms of the partial immobilization model, but we hope to develop appropriate solutions to the transport equations to verify this effect.

The effects of partial immobilization are small in the range of conditions covered in our experiments. Users who wish to carry out measurements at much higher pressures and temperatures should realize that they may have to take explicit account of this phenomenon.

We are modifying our apparatus to operate at higher pressures and at temperatures encompassing the glass transition of PET.

Assuming a specimen thickness of 23 micrometers we calculated permeabilities and diffusion coefficients for comparison with literature values. Our data and the data used for comparison are listed in Table III, which is organized along the same lines as Yasuda's compilation (13). Our values compare well with the limited data available (14-18) when one makes allowance for the differences in film morphology that are likely to exist.

The gas transmission properties of PET films similar to SRM 1470 are near the low end of the range commonly associated with

Table III - Literature values of Transport Parameters

Gas	Ref.	$\underline{P}(25)$	E_p	$D(25)$	E_D	Comment
N2		1.074	38.0	5.73	55.6	SRM 1470
	14	2.01				
	17	2.18	32.7	14.	44.0	crystalline
	15	3.23				
	17	4.35	26.4	20.	47.7	amorphous
O2	4	7.7				
	18	8.6				ASTM D-3985
		8.73	27.4	25.6	43.5	SRM 1470
	18	8.8				ASTM D-1434
	17	11.7	32.3	35.	46.1	crystalline
	15	12.6				
CO2	17	19.7	37.6	50.	48.5	amorphous
	18	22.7				ASTM D-1434
	16	39.4				
	12	40.6	24.8	3.5	49.7	
		42.1	22.6	4.62	45.5	SRM 1470
	17	56.9	18.4	6.	50.2	crystalline
	17	100.4	27.6	8.5	52.3	amorphous
HE	16	324.				
	14	335.				
		336.	20.9			SRM 1470
	17	442.	19.7	20000	20.	crystalline
	17	1098.	21.3	30000	19.3	amorphous

Explanation of selected column headings:

Ref.	- See Literature cited for source of data
$\underline{P}(25)$	- permeability at 25 °C expressed in amol/m . s. Pa (1 amol = 10^{-18} mole)
E_p	- Activation energy for Permeation, kJ/mol
$D(25)$	- Diffusion coefficient as calculated from $D=l^2/6\tau$ expressed in $10^{-14} m^2/s$ ($10^{-10} cm^2/s$)
E_D	- Activation energy for Diffusion, kJ/mol

homopolymer films (13,19). Persons interested in good gas barriers would like to see SRM's of lower transmission rate. In other cases (notably including separation membranes) one desires a poor barrier to certain gases. NBS is working to identify needs for new standard materials and improved measurement methods in these areas.

Since it is difficult to control processes for making plastic films in order to limit variability in their physical properties to one percent or less we find that material inhomogeneity is an obstacle to the development of better SRM's. It is also difficult to use such materials as transfer standards because their characteristics often drift with time and test specimens often do not tolerate abuse suffered during the measuring process.

Needs for improved measurement methods differ depending on whether one is considering low or high transmission rate materials. In the former case one needs very sensitive detectors. Selectivity is also desirable so that interferences from extraneous species can be avoided. In the case of high transmission rate materials instrumental time constants and saturation effects need to be better understood. In all cases there is a need for more convenient instruments and a better knowledge of their operating principles.

The existence of biases between labs is a clear indication that the operating principles that are used to describe a measurement process are not being realized in practice. In some cases the operator's technique fails to account for a factor that influences the measurement. In other cases the model that is used to describe the measurement process contains approximations that are violated in using the method. Examples include the back pressure correction, which can be important in situations where the gas is highly soluble in the polymer, the correction for the volume increase in manometric measurements using mercury columns 5, 20, or the influence of humidity on permeability in systems using moist test gases or carrier gases (4,21). If SRM 1470 is exposed to a carrier gas near 100 percent humidity its transmission rate decreases by about 20 percent (21). For this reason ASTM D-3985 specifies that calibration and referee measurements must be made with dry gases (4) even though the coulometric apparatus normally uses moist gases. Biases in measurement systems often depend upon the level of the property being measured. It is, therefore, desirable to cover a broad range of levels when checking calibration.

The main purpose of our work is to provide a material that is easily available to anyone who wishes to evaluate the performance of a permeation measuring system. Users whose equipment can accept any of the gases we used can cover a 350-fold range of transmission rates with the values on the SRM certificate. Interlaboratory comparisons that have been conducted to date (22) reveal that the repeatability (level of agreement for results obtained within individual laboratories) is much better than the re-

producibility (level of agreement between laboratories). This situation is common in measurement systems that have been operating without benefit of standards.

The resolution of an experiment to detect differences between laboratories will depend upon the statistical design that is used. Given the specimen to specimen variability that exists in SRM 1470, differences of less than 5 percent of the measured value will be difficult to detect using this material. Since differences between labs of 30 percent are common in the existing measurement system, there is considerable room for improvement. Individual laboratories may be able to achieve good agreement by regularly exchanging check samples of materials other than an SRM, but their results could well contain systematic errors if they fail to check their measurements against others in which bias has been carefully eliminated.

Literature Cited

1. Milazzo, G. "Standard Reference Materials and Meaningful Measurements", National Bureau of Standards Special Publication 408; Seward, R., Ed.; U. S. Govt. Printing Office, Washington, 1975, p. 127.
2. Barnes, J.D.; Martin, G.M.; "Standard Reference Materials: SRM 1470: Polyester Film for Oxygen Gas Transmission Measurements", National Bureau of Standards Special Publication 260-58; U.S. Govt. Printing Office, Washington, 1979.
3. Mandel, J. "Standard Reference Materials and Meaningful Measurements", National Bureau of Standards Special Publication 408; Seward, R., Ed.; U. S. Govt. Printing Office, Washington, 1975, P. 146.
4. ASTM Standard D-3985, "Standard Test Method for Oxygen Gas Transmission Rate through Plastic Film and Sheeting Using a Coulometric Sensor"; in Part 35 of Annual Book of ASTM Standards, American Society for Testing and Materials, Philadelphia, Revised Annually.
5. ASTM Standard D-1434, "Standard Test Methods for Gas Transmission of Plastic Film and Sheeting"; in Part 35 of Annual Book of ASTM Standards, American Society for Testing and Materials, Philadelphia, Revised Annually.
6. Barnes, J. D., Technical Papers Volume XXVIII, Society of Plastics Engineers, Inc.; Fairfield, CT; 1982, p. 19.
7. Daynes, H. A. Proc. Phil. Soc. London, 1920, 97A, 286-307.
8. Crank, J.; Park, G.S.; "Diffusion in Polymers"; Crank, J. and Park, G. S., Eds.; Academic Press; New York, 1968, p. 6.
9. Crank, J.; "Mathematics of Diffusion", 2nd ed.; Clarendon Press, Oxford, 1975 p. 49.
10. ASTM Standard E-171, "Standard Specification for Standard Atmospheres for Conditioning and Testing Materials"; in Part 35 of Annual Book of ASTM Standards, American Society for Testing and Materials, Philadelphia, Revised Annually.

11. Koros, W.J.; Paul, D.R.; Fujii, M.; Hopfenberg, H.B.; Stannett, V. - *J. Appl. Polymer. Sci.*, 1977, 21, 2899-904.
12. Koros, W.J., and Paul, D.R. - *J. Polym. Sci.* - 1978, 16, 217-87.
13. Yasuda, H.; Stannett, V.; "Polymer Handbook"; J. Brandrup and E.H. Immergut, Eds.; Wiley- Interscience, New York, 1975 pp. III-299-240.
14. Stern, S. A. "Membrane Processes for Industry, Proceedings of the Symposium", Southern Res. Inst., 1966, p. 196.
15. Tajar, T. G.; Miller, I. F. *Amer. Inst. Chem. Eng. J.*, 1972, 18, p. 78.
16. Brubaker, D. W.; Kammermeyer, K. *Ind. Eng. Chem.*, 45, 1148 (1953).
17. Michaels, A. S.; Vieth, W. R.; Barrie, J. A. *J. Appl. Phys.* 34(1), 1963, p. 13.
18. Fenelon, P. J.; "Polymer Science and Technology, Vol 6; Permeability of Plastics Films and Coatings to Gases, Vapors, and Liquids"; H. B. Hopfenberg, Ed.; Plenum Press, New York, pp. 285-299.
19. Hwang, S.T.; Choi, C. K.; Kammermeyer, K. - *Separation Sci.*, 9(6), p. 461-78.
20. Evans, R. E. *J. Testing and Evaluation*, 1974, 2, 529-32.
21. Brown, C. N.; personal communication
22. Pike, L.; personal communication
23. "The International System of Units (SI)", National Bureau of Standards Special Publication 330; U.S. Govt. Printing Office, Washington, 1977.

Appendix - A Word About Units

The system of units used to express our results is completely in accordance with the prescriptions of the SI system (23). This scheme differs from the various systems in use in industry and academia in that it uses the mole instead of the cc(STP) to express the quantity of matter being transported, the pascal rather than the atmosphere or the cm. Hg. to express pressure, the meter rather than the mil, the inch, or the centimeter to express length, and the second rather than the day to express time. Our experience indicates that the existing variety of unit systems leads to confusion and that calculations of related physical properties such as permeabilities, diffusion coefficients, and solubilities are easier using the SI units. More modern measurement systems which detect permeants by means of the electrical currents generated by individual atoms are easier to analyze when one uses moles rather than cc(STP) to express the amount of matter undergoing transport. Applications involving the transport of mixed permeant species are also easier to deal with on a molar basis. Conversion tables between the SI units and customary units are provided on the SRM certificate and in the appropriate standards documents (4,5).

We have chosen to express our results as permeances rather than permeabilities because we are presently unable to justify the assumption that the properties of the material are uniform throughout the film. We suspect that normalizing the results to unit thickness would introduce additional scatter. The SRM certificate gives instructions for calculating gas transmission rates, which are the quantities that are measured directly.

RECEIVED January 12, 1983

Gas Transport and Cooperative Main-Chain Motions in Glassy Polymers

DANIEL RAUCHER and MICHAEL D. SEFCIK

Monsanto Company, St. Louis, MO 63167

Carbon-13 rotating-frame relaxation rate measurements are used to elucidate the mechanism of gas transport in glassy polymers. The nmr relaxation measurements show that antiplasticization-plasticization of a glassy polymer by a low molecular weight additive effects the cooperative main-chain motions of the polymer. The correlation of the diffusion coefficients of gases with the main-chain motions in the polymer-additive blends shows that the diffusion of gases in polymers is controlled by the cooperative motions, thus providing experimental verification of the molecular theory of diffusion. Carbon-13 nmr relaxation measurements also show that the presence of a permanent gas alters the cooperative motions of the polymeric chains. These changes in main-chain molecular motions correlate with changes in the diffusion coefficient of the gas in the polymer, thus providing evidence that the diffusion coefficient is dependent on the gas-polymer-matrix composition.

Experimental results show that sorbed gases interact with polymeric chains, inducing changes in the structural and dynamic properties of the polymer. These properties and the interchain forces controlling them determine many of the physical characteristics of the matrix, including the solubility and diffusion coefficients. These results are inconsistent with the assumptions and the physical interpretations implicit in the dual-mode sorption and transport model, and strongly suggest that the sorption and transport of gases in glassy polymers should be represented by concentration (composition) dependent solubility and diffusion coefficients.

0097-6156/83/0223-0089\$06.50/0

© 1983 American Chemical Society

The transport of gas in polymers has been studied for over 150 years (1). Many of the concepts developed in 1866 by Graham (2) are still accepted today. Graham postulated that the mechanism of the permeation process involves the solution of the gas in the upstream surface of the membrane, diffusion through the membrane followed by evaporation from the downstream membrane surface. This is the basis for the "solution-diffusion" model which is used even today in analyzing gas transport phenomena in polymeric membranes.

In 1879, von Wroblewski (3) showed that sorption and transport of gases in polymers followed Henry's and Fick's laws, respectively,

$$C = \sigma_0 p \quad (1)$$

$$J = -D_0 (dC/dx) \quad (2)$$

where C is the equilibrium gas concentration in the polymer, J is the permeation flux, σ_0 and D_0 are the solubility and diffusion coefficients, respectively, and p is the gas pressure. By assuming that D_0 is constant, von Wroblewski showed that the steady state flux is given by,

$$J = \sigma_0 D_0 (p/\ell) = P_0 (p/\ell) \quad (3)$$

where p is the pressure difference across the membrane (for simplicity, the downstream pressure has been assumed to be zero), and ℓ is the thickness of the membrane. The permeability coefficient at steady state, P_0 , is defined by eq. (3) as,

$$P_0 = \sigma_0 D_0 \quad (4)$$

Daynes (4) (1920) showed that a transient permeation experiment, under the boundary conditions $C(x;t) = 0$ for $t < 0$, $C(0;t) = C$ and $C(\ell;t) = 0$ for $t > 0$ gives two characteristic parameters, the permeability, P_0 , and the time-lag, θ_0 . Daynes showed that the solution of Fick's law under these boundary conditions yields,

$$D_0 = \ell^2/6\theta_0 \quad (5)$$

Thus, P_0 , D_0 , and σ_0 [by eq. (4)] could be measured in a single time-lag experiment.

Eqs. (1)-(5) are still the basic sorption and transport equations used today for "ideal" systems, penetrant-polymer systems in which both σ_0 and D_0 are pressure and concentration independent. This "ideal" behavior is observed in sorption and transport of permanent and inert gases in polymers well above their T_g .

Barrer (6) (1937) showed that diffusion is an activated process and that the diffusion coefficient had an Arrhenius form,

$$D_0 = D_0^* \exp(-E_d/RT) \quad (6)$$

where E_d is the activation energy of diffusion and D_0^* is the frequency or pre-exponential factor. A number of attempts have been made to explain the temperature dependence of the diffusion coefficient. The zone-theory of Barrer (7), the free volume theories (8, 9), and the molecular theories of diffusion (10, 11, 12), although differing in many aspects, have in common the connotation that the activation energy of diffusion is the energy needed for chain separation, through cooperative motions, of sufficient size to allow the penetrant to execute a diffusional jump.

Section IA summarizes the molecular model of diffusion of Pace and Datyner (12) which proposes that the diffusion of gases in a polymeric matrix is determined by the cooperative main-chain motions of the polymer. In Section IB we report carbon-13 nmr relaxation measurement which show that the diffusion of gases in poly(vinyl chloride) (PVC) - tricresyl phosphate (TCP) systems is controlled by the cooperative motions of the polymer chains. The correlation of the phenomenological diffusion coefficients with the cooperative main-chain motions of the polymer provides an experimental verification for the molecular diffusion model.

Section IIA summarizes the physical assumptions and the resulting mathematical descriptions of the "concentration-dependent" (5) and "dual-mode" (13) sorption and transport models which describe the behavior of "non-ideal" penetrant-polymer systems, systems which exhibit nonlinear, pressure-dependent sorption and transport. In Section IIB we elucidate the mechanism of the "non-ideal" diffusion in glassy polymers by correlating the phenomenological diffusion coefficient of CO_2 in PVC with the cooperative main-chain motions of the polymer in the presence of the penetrant. We report carbon-13 relaxation measurements which demonstrate that CO_2 alters the cooperative main-chain motions of PVC. These changes correlate with changes in the diffusion coefficient of CO_2 in the polymer, thus providing experimental evidence that the diffusion coefficient is concentration dependent.

I. DIFFUSION AND COOPERATIVE MAIN-CHAIN MOTIONS

A. Diffusion Theory

Recently Pace and Datyner (12) advanced a molecular theory of diffusion that correlates the diffusion of gases in a polymeric matrix with the cooperative motions of the polymer chains. The theory proposes that the diffusant molecule can move

through the polymer matrix in two distinct ways: (a) sliding along the axis of interchain channels or bundles formed by adjacent polymer chains, or (b) jumping at right angles to the polymer chains whenever adjacent chains are sufficiently separated. The first process has a smaller activation energy than the second and therefore occurs much more rapidly. This is true because only limited main-chain motions are necessary to create interchain channels of molecular dimensions in disordered glasses. The penetrant diffuses freely within these interchain channels, which may be bounded by regions of dense local packing. The diffusant can proceed to the next region of facile diffusion only when two adjacent polymer chains undergo sufficient cooperative motions to cause an interchain separation greater than the molecular dimensions of the diffusant. Thus, process (b) is the rate determining step in diffusion and the activation energy of diffusion is the activation energy of the chain separation. In other words, the phenomenological diffusion process is the result of two dynamic events: the first, high-frequency motions ($>10^{10}$ Hz) of the diffusant within interchain channels; and the second, low-frequency, cooperative motions (10^4 - 10^8 Hz) of the polymer chains to allow the diffusant to enter another interchain channel. The former motions have been observed experimentally in diffusion experiments (14, 15), the latter are reported here.

The activation energy for a symmetrical separation of polymer chain centers by a distance of z over a length x is given by (12),

$$\Delta E = \int_{-\infty}^{\infty} \left[f(z) - f(\rho) + \frac{\beta}{2} \left[\frac{d^2 z}{dx^2} \right]^2 \right] dx \quad (7)$$

where $f(z)$ is the average interchain potential per unit length, β is the average effective single chain-bending modulus per unit length, and ρ is the equilibrium chain separation. Solution of eq. (7) for $z = d$, where d is the minimum chain separation which will allow transverse passage of a penetrant, gives the activation energy of diffusion,

$$Ed = \Delta E = 3.11 \Gamma^{3/4} \beta^{1/4} d^{5/4} \quad (8)$$

where Γ and β are parameters which characterize the interchain cohesion and chain stiffness, respectively. The value of Γ can be estimated from polymer density and cohesive energy density, and β can be approximated from the polymer chain backbone geometry and bond rotation potentials. The theory makes the unique prediction that the activation energy of diffusion depends nearly linearly on the penetrant diameter. This prediction has been recently confirmed experimentally by Berens and Hopfenberg (16).

From this molecular theory, we see that the diffusion coefficient depends on the frequency of cooperative main-chain motions of the polymer, ν , which cause chain separations equal to or greater than the penetrant diameter. Pace and Datyner were able to estimate ν by adopting an Arrhenius rate expression in which the pre-exponential factor, A , is a function of both ΔE and T . The diffusion coefficient is given by,

$$D_0 = \frac{1}{6} \bar{L}^2 \nu = \frac{1}{6} \bar{L}^2 A \exp(-\Delta E/RT) \quad (9)$$

where \bar{L}^2 is the mean-square jump displacement. The characteristic frequency of the diffusion process establishes a time scale ($\tau = 1/\nu$) for jumps of the diffusant molecule in the polymeric matrix. Hence, \bar{L} is the mean displacement in the average position of the gas molecule following an activated jump. (The average position of a penetrant molecule is determined by its random motion within the region of facile diffusion, process (a), and averaged over time τ .) The average jump distance, \bar{L} , is not predictable within the limits of the theory.

B. Diffusion Mechanism in Polymers - Experimental Evidence

1. Cooperative Main-Chain Motions in PVC-TCP

It is now well established that TCP acts as an antiplasticizer of PVC at low concentrations and as a plasticizer at high concentrations. The observed variations in tensile modulus, tensile strength, impact strength, ultimate elongation, and thermal expansion coefficient of PVC with additive concentration have been attributed to the antiplasticization-plasticization phenomenon (17, 18, 19). Antiplasticization of PVC also results in a decrease in gas permeability, and plasticization in an increase in gas permeability (17).

Based on changes of secondary-loss transitions of antiplasticized polymers, Robeson (20) speculated that additives altered the cooperative motions of the polymer chains, and these alterations were responsible for the observed changes in diffusivity. In particular, Robeson suggested that the addition of antiplasticizers to polymers restricted molecular flexibility of chains thereby restricting diffusion of penetrants. Kinjo (18) attributed the antiplasticization effect of several polar low-molecular weight additives in PVC to cohesion of the additive to the polymer chain by dipole-dipole interactions. He proposed that motions of the cohering parts of the PVC would be extremely hindered, reducing the mechanical β -dispersion and increasing tensile strength. It was suggested in the literature (21) that high concentrations of TCP in PVC decrease the interchain

interactions in the polymer, thus enhancing the main-chain motions, resulting in plasticization of the polymeric matrix.

We have been interested in the nature of cooperative motions in polymers for some time and have used carbon-13 nuclear magnetic resonance for examining main-chain motions in solids (22-27). Carbon-13 nmr with cross-polarization and magic-angle sample spinning is a high-resolution, high-sensitivity technique for solids (Figure 1). The cooperative main-chain motions in glassy polymers can be evaluated from carbon-13 rotating-frame relaxation rates, $[R_1\rho(C)]$. Details of the nmr experiment are reported elsewhere (28).

The average relaxation rate of the methylene- and methine-carbons in PVC decreases with the addition of TCP up to about 15 weight % (Table I). Based on standard relaxation rate theory (29), reduced relaxation rates are indicative of a shift in the average cooperative motions to lower frequencies. These results prove that antiplasticization is associated with reduced cooperative motions of the polymer chains. As the concentration of TCP in PVC is increased above 15 weight %, the average relaxation rate of the methylene- and methine-carbons in PVC increases (Table I), showing that plasticization leads to increased cooperative motions in the glass.

Our results show for the first time the effect of antiplasticization-plasticization on polymer properties at the molecular level. These results provide experimental evidence for the assumptions of Robeson (20) and Kinjo (18) that attributed the changes in polymer properties with antiplasticization-plasticization to changes in the interchain cohesion of the polymer.

2. Transport in PVC-TCP

Hydrogen and carbon monoxide permeability data for films of PVC and PVC containing TCP are given in Table I. The permeability coefficients, of both gases, decrease as TCP concentration is increased to about 15 weight %, and then increase sharply with additive concentration. Similar results have been reported for CO₂ and H₂O permeabilities in the PVC-TCP system (17).

Table I lists also the apparent diffusion coefficients, D_a , calculated from the time lag, θ . The dependence of the apparent diffusion coefficients on additive concentration is similar to the dependence of the permeability coefficients on this concentration. We will show later that the diffusion coefficients in PVC are dependent on the gas concentration in the polymer, and we emphasize here that the values quoted in Table I are the apparent diffusion coefficients and are not the values of either the real or effective diffusion coefficients, D and \bar{D} , respectively. We recognize that D_a actually underestimates both D and \bar{D} , but we can still use the apparent diffusion coefficients to show the

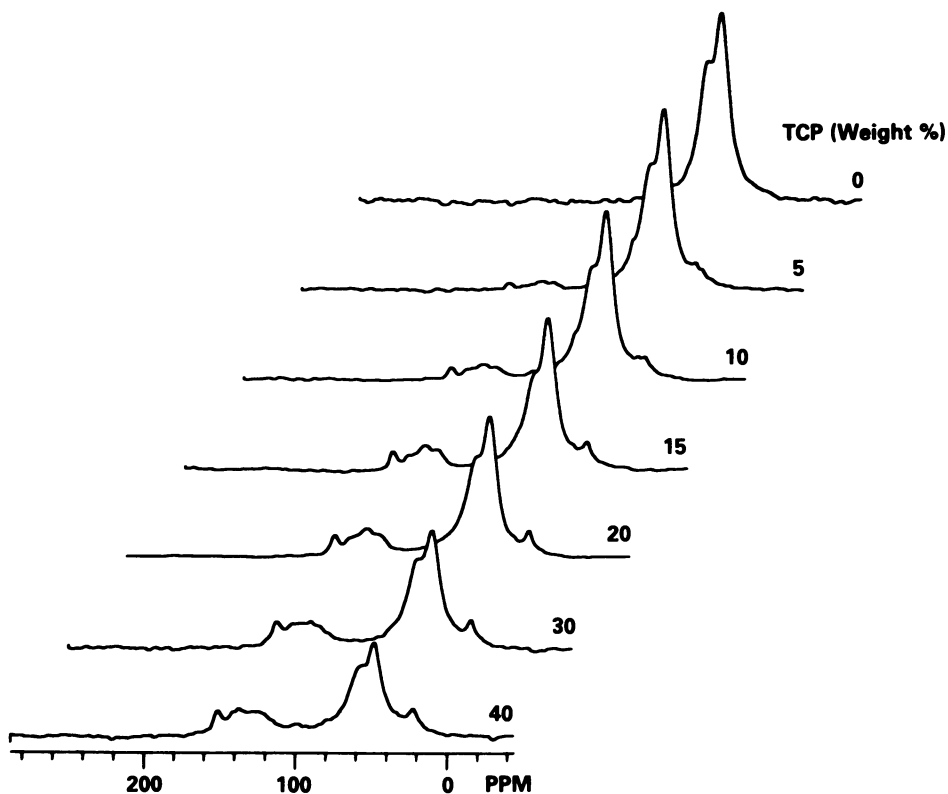


Figure 1. Cross-polarization and magic-angle spinning ^{13}C -NMR spectra of PVC-TCP systems. The 15.08 MHz spectra were obtained with 1 msec contact time and 1800 Hz spinning speed.

TABLE I
GAS TRANSPORT AND C-13 NMR PARAMETERS FOR PVC-TCP

TCP	Additive (weight %)	$P \times 10^{10} \text{ CC(STP)} \cdot \text{cm} / \text{cm}^2 \cdot \text{sec} \cdot \text{cmHg}^a$		$D_a \times 10^7 \text{ cm}^2 \cdot \text{sec}^{-1} a$		$\langle R_{1\rho}(C) \rangle \times \text{sec}^{-1} b$
		H ₂	CO	H ₂	CO	
0		2.38 ± .06	.0248 ± .0004	4.80 ± .20	.0229 ± .0012	235
5.0		1.91 ± .06	.0154 ± .0015	4.56 ± .37	.0210 ± .0006	170
10.2		1.77 ± .01	.0178 ± .0003	4.22 ± .33	.0157 ± .0001	140
15.0		1.69 ± .01	.0180 ± .0002	4.44 ± .23	.0251 ± .0002	120
20.1		2.16 ± .04	.0274 ± .0016	4.73 ± .58	.0293 ± .0004	155
30.8		2.86 ± .02	.01050 ± .0010	15.6 ± 2.20	.0535 ± .0023	250
40.0		3.61 ± .01	.3740 ± .0030	22.5 ± 1.40	.2880 ± .0100	430

a. At 270 cmHg and 27°C.

b. Measured at 34 kHz and 26°C. Average relaxation rate for methylene and methine carbons.

relative changes in these diffusion coefficients as the changes in D and \bar{D} are proportional to the changes in D_a . Further, both Barrer (30) and Florianczyk (31) have shown that the solubility of gases in PVC is only weakly dependent on TCP concentration. Thus, the changes in the permeabilities must be due mainly to changes in the effective diffusion coefficients [see eq. (12)].

3. Diffusion and Cooperative Main-Chain Motions in PVC-TCP

The molecular theory of Pace and Datyner (12) predicts that the frequency of polymer motions important to diffusion of CO and H_2 in PVC is in the range of 10^5 - 10^8 Hz. We can expect $R_1\rho(C)$ measurements performed between 10^4 to 10^5 Hz to be sensitive to alterations in ν by additives. The dependence of $\langle R_1\rho(C) \rangle$ on the rotating-frame Larmor frequency observed for the PVC-TCP system (28) means that a general change in main-chain motions (restriction or enhancement) will result in a change (decrease or increase, respectively) in $\langle R_1\rho(C) \rangle$ measured at 34 kHz (29).

When the concentration of additive is low we observe that the D_a of both gases decrease and parallel the decrease in $\langle R_1\rho(C) \rangle$ (Fig. 2). The addition of low levels of TCP increases the average interchain potential in PVC and results in a decrease in ν , and in lower diffusion coefficients. At high concentrations of TCP both $\langle R_1\rho(C) \rangle$ and D_a increase (Fig. 2). The dilution of the chains by the low molecular weight additive decreases the interchain potential, thereby increasing the frequency of main-chain motions, and increasing the diffusion coefficients.

In conclusion, the average rotating-frame relaxation rate of the methylene- and methine-carbons correlate with the apparent diffusion coefficients for H_2 and CO in PVC when the main-chain molecular motions of the polymer are altered by an additive. (Fig. 2). These results provide experimental evidence that main-chain cooperative motions control the diffusion of gases through polymers. In Section IIB we will show that perturbation of polymeric cooperative motions is not restricted to classical plasticizing additives.

II. SORPTION AND TRANSPORT IN GLASSY POLYMERS

Nonlinear, pressure-dependent solubility and permeability in polymers have been observed for over 40 years. Meyer, Gee and their co-workers (5) reported pressure-dependent solubility and diffusion coefficients in rubber-vapor systems. Crank, Park, Long, Barrer, and their co-workers (5) observed pressure-dependent sorption and transport in glassy polymer-vapor systems. Sorption and transport measurements of gases in glassy polymers show that these penetrant-polymer systems do not obey the "ideal" sorption and transport eqs. (1)-(5). The observable variables,

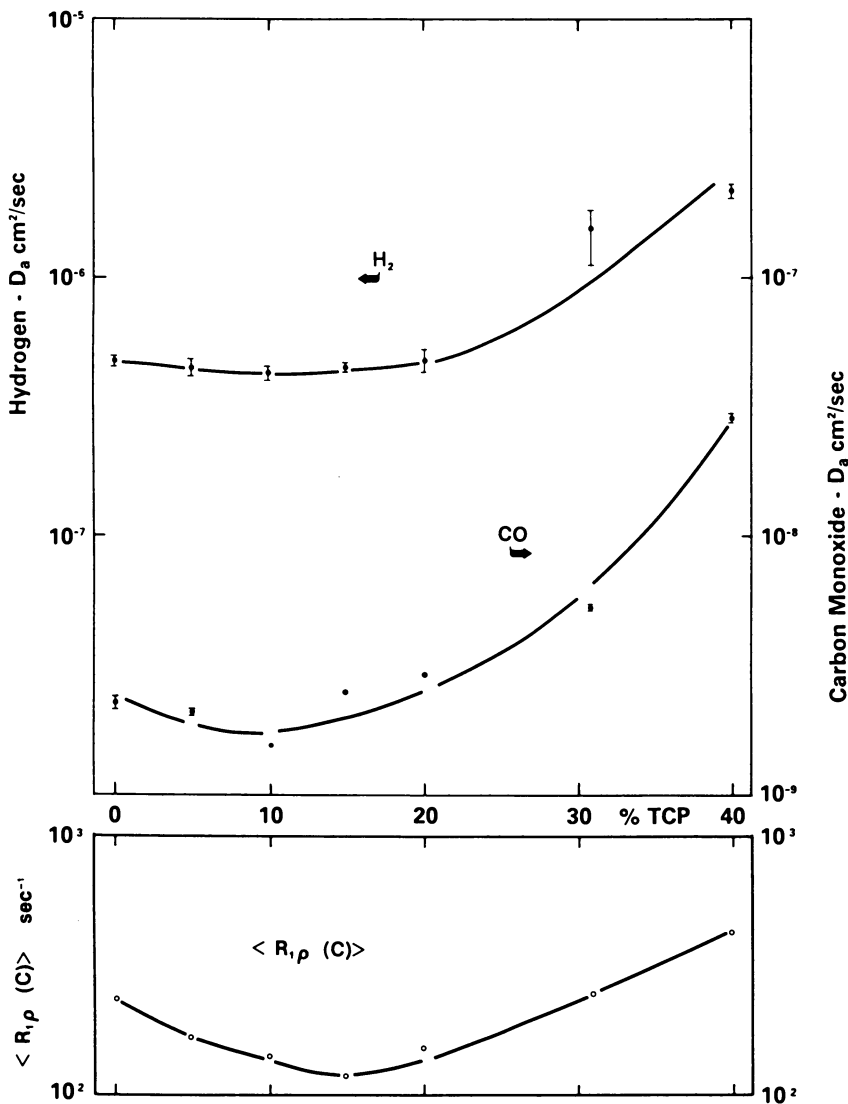


Figure 2. The dependence of the main-chain rotating-frame relaxation rate, and apparent diffusion coefficients of H_2 and CO , on the concentration of TCP in PVC. The relaxation rates were measured at 34 kHz and 26 °C. The diffusion coefficients were measured at 270 cm-Hg and 27 °C.

solubility coefficient, permeability, and diffusion time-lag are pressure dependent (13).

A number of attempts have been made to explain the nonlinear, pressure-dependent sorption and transport in polymers. These explanations may be classified as "concentration-dependent" (5) and "dual-mode"(13) sorption and transport models. These models differ in their physical assumptions and in their mathematical descriptions of the sorption and transport in penetrant-polymer systems.

A. Sorption and Transport Models

1. Concentration-Dependent Sorption and Transport Model

Pressure-dependent sorption and transport properties in polymers can be attributed to the presence of the penetrant in the polymer. Crank (32) suggested in 1953 that the "non-ideal" behavior of penetrant-polymer systems could arise from structural and dynamic changes of the polymer in response to the penetrant. As the properties of the polymer are dependent on the nature and concentration of the penetrant, the solubility and diffusion coefficient are also concentration-dependent. The concentration-dependent sorption and transport model suggests that "non-ideal" penetrant-polymer systems still obey Henry's and Fick's laws, and differ from the "ideal" systems only by the fact that σ and D are concentration dependent,

$$C = \sigma p = \sigma_0 [1 + g(C)] p \quad (10)$$

$$J = -D (dC/dx) = -D_0 [1 + f(C)] (dC/dx) \quad (11)$$

where $g(C)$ and $f(C)$ are functions describing the concentration dependence of σ and D , respectively. Solution of eq. (11) under the boundary conditions of the transient permeation experiment yields,

$$\begin{aligned} P &= \bar{D} \sigma = D_0 [1 + f'(C)] \sigma_0 [1 + g(C)] \\ &= P_0 [1 + f'(C)] [1 + g(C)] \end{aligned} \quad (12)$$

$$\theta = (\ell^2/6D_0) [1 + F(C)] = \theta_0 [1 + F(C)] \quad (13)$$

where \bar{D} , the effective diffusion coefficient, is defined by $\bar{D} = (1/C) \int D dC$, and the functions $f'(C)$ and $F(C)$ describe the concentration dependence of \bar{D} and θ , respectively.

Crank, Park, Long, Barrer and their co-workers (5) have shown that \bar{D} and D can be represented as exponential functions of penetrant concentration. Aitken and Barrer (33) used successfully a linear expression to describe the concentration

dependence of D . Frisch (34) developed explicit expressions for θ for cases where D is concentration-dependent.

2. Dual-Mode Sorption and Transport Model

Barrer, Barrie, and Slater (35) suggested in 1958 that nonlinear sorption isotherms of gases and vapors in glassy polymers could be explained by invoking two distinct mechanisms of sorption. They described this dual-mode sorption as arising from ordinary dissolution (Henry's law mode) plus absorption in pre-existing "holes" (Langmuir's mode). Michaels, Vieth, and Barrie (36) suggested in 1963 that only the dissolved gas (Henry's population) was involved in the transport process. Vieth and Sladek (37) extended this idea and developed the total-immobilization model of gas transport. The transport model, assuming complete immobilization of the absorbed gas (Langmuir's population), was modified by Petropoulos (38) and later by Paul and Koros (39). They suggested that the Langmuir population was not immobilized but had a finite mobility. The dual-mode sorption and transport model describes the sorption of a gas in a glassy polymer by a combination of Henry's and Langmuir's isotherms, eq. (14), and the gas transport by Fick's law, eq. (15),

$$C = C_D + C_H = k_D P + \frac{C_H' b p}{1 + b p} \quad (14)$$

$$J = -D_D \frac{dC_D}{dx} - D_H \frac{dC_H}{dx} \quad (15)$$

where C_D and C_H are the concentrations of Henry's and Langmuir's populations, respectively, D_D and D_H are the respective diffusion coefficients of the two populations, C_H' and b are the capacity and affinity parameters of the Langmuir sorption, respectively, and k_D is Henry's law solubility coefficient. Solution of eq. (15) for the boundary conditions of the transient permeation experiment yields (39),

$$P = k_D D_D \left(1 + \frac{KF}{1 + b p} \right) \quad (16)$$

$$\theta = \frac{q^2}{6D_D} [1 + f(K, F, b p)] \quad (17)$$

where $K = C_H' b / k_D$, $F = D_H / D_D$, and the function symbolized is too cumbersome to reproduce here.

In summary, the dual-mode sorption and transport model assumes (13):

- (a) Two modes of sorption - normal Henry's mode dissolution, and Langmuir's mode absorption into unrelaxed-volume frozen in the glassy state.
- (b) The two gas populations are in a dynamic equilibrium with each other.
- (c) The two gas populations have constant but different diffusion coefficients. Langmuir's population generally has considerably less diffusional mobility than Henry's population.
- (d) Gases, particularly permanent gases, do not interact with the polymer matrix, thus Henry's law solubility coefficient, k_D , and the diffusion coefficients of both Henry's population, D_D , and Langmuir's population, D_H , are pressure and concentration-independent.

In the dual-mode sorption and transport model the pressure-dependence of σ ($= C/p$), P and θ in gas-glassy polymer systems arises from the pressure-dependent distribution of the sorbed gas molecules between Langmuir sites and Henry's law dissolution. Although k_D , D_D and D_H are assumed to be constant, the average or effective solubility and diffusion coefficients of the entire ensemble of gas molecules change with pressure as the ratio of Henry's to Langmuir's population, C_D/C_H , changes continuously with pressure [eq. (14)].

B. Diffusion Mechanism in Glassy Polymers - Experimental Evidence

1. Cooperative Main-Chain Motions in PVC-CO₂

In Section IB we showed that carbon-13 rotating-frame relaxation measurements can be used to measure cooperative main-chain motions in polymers (28). We report here the effect of CO₂ on the main-chain motions of PVC.

Carbon-13 rotating-frame relaxation rates $\langle R_{1\rho}(C) \rangle$, were determined on static samples using cross-polarization techniques (40). Without magic-angle sample spinning, the methylene- and methine-carbon resonances are unresolved, so the relaxation rates reported here are the average relaxation rates for the combination line. The $\langle R_{1\rho}(C) \rangle$, at 37 kHz, for PVC in vacuo and in the presence of CO₂ are given in Table II. Two major effects are observed; the presence of relatively small amounts of CO₂ increases the $\langle R_{1\rho}(C) \rangle$ of PVC, and exposure of PVC to CO₂ causes a long-term increase in $\langle R_{1\rho}(C) \rangle$. The first phenomena will be discussed in terms of its effect on transport properties, and the second in terms of history-dependent properties.

The $\langle R_{1\rho}(C) \rangle$ for "conditioned" PVC in vacuo is 154 sec^{-1} . The presence of CO₂ leads to noticeable increases in $\langle R_{1\rho}(C) \rangle$. At 100 torr the $\langle R_{1\rho}(C) \rangle$ of PVC is increased to 158 sec^{-1} .

TABLE II

Relaxation Rates in PVC-CO₂

Sequence of Experiment	Sample Description	Relaxation Rate ^a <R _{1ρ} (C)> sec ⁻¹
1	in vacuo	138 ± 3
3	degassing ^b after first exposure to 800 torr CO ₂ -in vacuo	151 ± 4
7	degassing after repeated exposure to CO ₂ -in vacuo	154 ± 3
5	100 torr CO ₂ ^c	158 ± 5
6	200 torr CO ₂	163 ± 8
4	400 torr CO ₂	166 ± 3
2	800 torr CO ₂	183 ± 4

a) Least-squares fit of relaxation data collected for times between 0.05 and 1 msec; error limits are one standard deviation; H₁(C) = 37 kHz. Average for methylene and methine carbons.

b) All samples were degassed for 24 hours at 10⁻³ torr.

c) Measured after 12 hours equilibration at stated pressure. The concentration of CO₂ ranges from about 1 CO₂ molecule per 1200 repeat units at 100 mmHg to about 1 CO₂ per 200 repeat units at 800 mmHg (19).

Higher pressures of CO_2 cause correspondingly larger increases in $\langle R_1\rho(\text{C}) \rangle$. At 800 torr an increase of 19% to 183 sec^{-1} is observed. Based on standard relaxation rate theory (29), increased relaxation rates are indicative of a shift in the average cooperative main-chain motions to higher frequencies. Conversely, this means that even small amounts of CO_2 increase the cooperative motions of the polymer chains.

Gravimetric measurements by Berens (41) show that CO_2 sorption by PVC ranges from about 0.5 mg CO_2/gram of PVC at 100 torr to about 3.5 mg CO_2/gram of PVC at 800 torr of CO_2 . The reason that such small amounts of CO_2 are so effective in altering the cooperative motions of PVC results from the fact that gases have very high molecular mobilities in glassy polymers (correlation time between 10^{-10} - 10^{-12} sec) and can sample extended areas of the polymer on the time scale of the cooperative motions of the polymer (10^{-5} - 10^{-8} sec).

The experimental data in Table II shows that $\langle R_1\rho(\text{C}) \rangle$ of PVC becomes longer after successive exposures of the sample to CO_2 . This indicates that exposure to carbon dioxide causes a change in the molecular packing of PVC which allows more main-chain motions. There is now abundant evidence that exposure of polymers to gases results in changes which persist long after the gases are removed. These changes are reflected in altered physical properties of the polymer (42-46). The "conditioning" of a polymer by exposure to a gas can be thought of in the same terms as annealing. In annealing, the increased thermal energy allows the polymer sufficient segmental mobility to eliminate energetically unfavorable conformations which were frozen into the solid on rapid cooling from the melt (47). Exposure to a gas can have the opposite effect. Since the polymer must swell to accommodate the sorbed gas molecules, the polymer becomes stressed and ultimately reaches a new equilibrium condition determined by the presence of the penetrant. The concentration and the nature of the penetrant determine the rate of relaxation just as temperature determines the rate of relaxation in the annealing experiment.

Since the penetrant enhances cooperative motions of the polymer, the rate of structural change in the polymer, measured by various relaxation experiments, will be greater during sorption, or in the presence of the penetrant, than it will be during desorption, or in the absence of the penetrant (32). Because of this, "conditioning" of a polymer results in long-term or "permanent" changes in the polymer. The results of sorption and transport experiments therefore depend on the static and dynamic state of the polymer, which are determined by the thermal history of the sample and by the pressure and duration of previous exposures to sorbents. Wonders and Paul (42) have described these phenomenological effects in detail for the CO_2 -polycarbonate system.

2. Diffusion and Cooperative Main-Chain Motions in PVC-CO₂

In Section IB we presented experimental evidence that diffusion coefficients correlate with PVC main-chain polymer motions. This relationship has also been justified theoretically (12). In the previous section we demonstrated that the presence of CO₂ effects the cooperative main-chain motions of the polymer. The increase in $\langle R_1\rho(C) \rangle$ with increasing gas concentration means that the real diffusion coefficient [D in eq. (11)] must also increase with concentration. The nmr results reflect the real diffusion coefficients, since the gas concentration is uniform throughout the polymer sample under the static gas pressures and equilibrium conditions of the nmr measurements. Unfortunately, the real diffusion coefficient, the diffusion coefficient in the absence of a concentration gradient, cannot be determined from classical sorption and transport data without the aid of a transport model. Without prejudice to any particular model, we can only use the relative change in the real diffusion coefficient to indicate the relative change in the apparent diffusion coefficient.

Apparent diffusion coefficients of CO₂ in PVC have been reported by Toi (48). Semilog plots of both the apparent diffusion coefficient, D_a , and the relaxation rate, $\langle R_1\rho(C) \rangle$, as a function of CO₂ pressure in the range of 0-800 torr are shown in Figure 3. Of course, there is no reason to expect the magnitude of the change in the rotating-frame relaxation rate to be equal to the magnitude of the change in D or D_a . Both the relaxation rate and the diffusion coefficient depend on the frequency of the main-chain cooperative motions but in different ways (28, 29, 49). Nevertheless, the similarity in the dependence of both the relaxation rate and the apparent diffusion coefficient on CO₂ pressure supports the observation that main-chain molecular motions play a major role in determining the diffusion coefficient of a gas through a polymer matrix (28).

The experimental evidence presented here and in the literature (15) show that the real diffusion coefficient depends on concentration. These results are incompatible with the notion of concentration-independent diffusion coefficients for the dissolved and Langmuir sorbed molecules [D_D and D_H in equation (15)] as proposed by the dual-mode sorption and transport model (13).

C. Concentration-Dependent Sorption and Transport in Glassy Polymers

The basic difference between "concentration-dependent" and "dual-mode" models is in their assumption about penetrant-polymer interactions. Concentration-dependent sorption and transport models are based on the assumption that the concentration-dependence of the solubility and diffusion coefficients arises

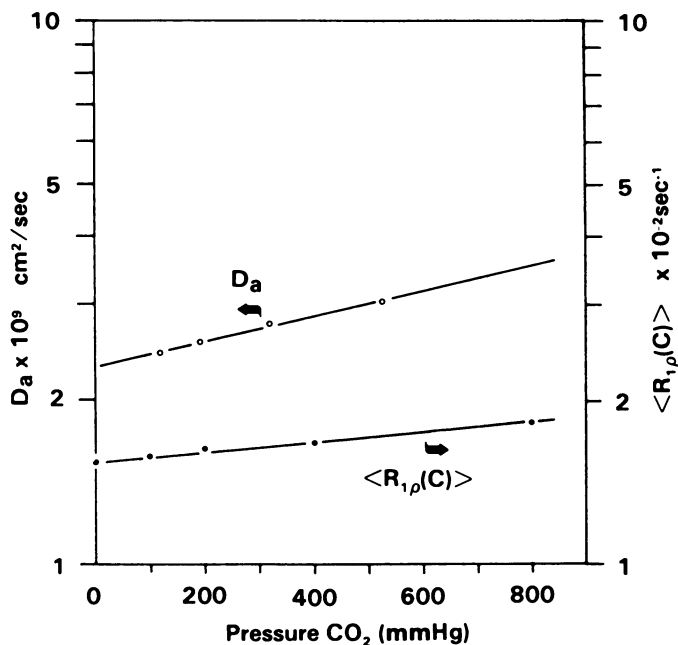


Figure 3. The dependence of relaxation rate and apparent diffusion coefficient on CO₂ pressure in PVC. The relaxation rates were measured at 37 kHz and 26 °C. The diffusion coefficients, measured at 40 °C, are from Ref. 48.

from penetrant-polymer interactions. On the other hand, the dual-mode sorption and transport model assumes that there are no gas-polymer interactions, thus assuming concentration-independent solubility and diffusion coefficients - k_D , D_D and D_H , respectively.

Experimental results presented in this work and in the literature are inconsistent with the assumptions and the physical interpretations implicit in the dual-mode sorption and transport model, and strongly suggest that the sorption and transport in gas-glassy polymer systems should be presented by a concentration-dependent model:

- (a) Evidence for gas-glassy polymer interactions is abundant. The results presented in Table II show that even small amounts of gas affect the cooperative main-chain molecular motions of glassy polymers. Evidence that the presence of gases in polymer cause structural and dynamic changes can be seen in the depression of the T_g (42, 43, 44), and in the increased viscoelastic relaxation rates (43, 44) of polymer-gas systems. Further, "conditioning" of polymers, the gas-induced structural changes in polymers by exposure to penetrant, was shown by Wonders and Paul (42), as well as by our work (40) (Table II).
- (b) The effect of gas on the cooperative main-chain motions of glassy polymers (Table II) shows that the molecular level diffusion process is concentration dependent, as must be the phenomenological diffusion coefficient.
- (c) There is only one population of sorbed gas in a glassy polymer at any given pressure. All spectroscopic analyses (15, 22), including the work of Assink (14), are consistent with all of the sorbed gas molecules being in a single state. Nuclear magnetic spin-spin and spin-lattice relaxation measurements of sorbed gases consistently show single exponential decays indicating that all of the gas molecules are relaxed by the same mechanism. These studies also show that the relaxation times increase with increasing equilibrium gas pressure. There are at least two possible explanations for these results: 1) there is a single population of gas molecules which interact with the polymer matrix; or 2) there are two populations with different mobilities in rapid exchange and whose relative populations vary with pressure. The results presented in Section IIB are consistent only with the first explanation (40). The work of Assink (14) has been frequently cited as proof for the existence of two distinct sorption modes in glassy polymers (50). This is not the case. Measuring the spin-spin relaxation time (T_2) of ammonia in polystyrene, Assink showed that the ammonia is relaxed by a single exponential process and that T_2 increases with increasing concentration of sorbed ammonia. Assink eliminated the

obvious interpretation of gas-polymer interactions by assuming that at the experimental pressures of up to 6 atm. "the concentration of dissolved gas was not sufficient to appreciably plasticize the polymer". He proceeded to analyze his experimental results in terms of the dual-mode sorption theory by attributing different mobilities and therefore different T_2 's to Henry's and Langmuir's populations. Assink plotted T_2 as a function of the mole fraction of the gas in the Langmuir sites, as determined from the dual-mode model, so the slope of the line should give $1/T_2$ for the Langmuir fraction of the ammonia and the intercept would be the $1/T_2$ for the dissolved or Henry's fraction of the gas. A least-squares analysis of the data gave a slope of 235 sec^{-1} and an intercept of -5.2 sec^{-1} . A negative relaxation rate is physically impossible. Rather than abandoning the attempt to represent the data by dual-sorption-mobility model, Assink arbitrarily assigned a value of 12 sec^{-1} for $1/T_2$ of the dissolved molecules making the mobility of the Langmuir molecules 1/20th that of the dissolved molecules.

The results of Zupančič, et.al. (15), are also relevant here. Zupančič investigated diffusion of butane in linear polyethylene using pulsed magnetic field gradient experiments to measure directly the real diffusion coefficient at 23°C . They showed that the real diffusion coefficient increased with equilibrium butane pressure as did the spin-spin relaxation time. As the polyethylene was above its T_g , these results cannot be attributed to dual mode behavior (13). A single population of butane interacting with the polyethylene accounts for both the change in the diffusion coefficient and the change in spin-spin relaxation.

The only exception to a single population of sorbent in a glassy polymer was observed in the water-cellulose acetate system (51, 52). In this system two resonance frequencies and two relaxation rates for water were observed. However, the two dynamic states of the water in this system are due to specific hydrogen bonding interactions rather than sorption in Langmuir type holes.

- (d) There is no model-independent or physical evidence for the existence of Langmuir or other sorption sites in glassy polymers which could account for multiple-site sorption. The interpretation of free volume as molecular-size voids responsible for Langmuir sorption are only partially successful. While free volume has been equated with the Langmuir capacity, C_H' , in CO_2 -glassy polymer systems (13, 46, 50, 53) the correlation fails to hold for other gases (54, 55). Koros et. al. (50) explain the equivalence of the "unrelaxed volume" to the Langmuir capacity by

suggesting that the total "unrelaxed volume" is uniformly distributed as molecular scale gaps and that these gaps are Langmuir sorption sites for single CO_2 molecules. This physical model implies that the average Langmuir site has the same molecular volume as the effective molecular volume of CO_2 molecules when sorbed on zeolites or in liquids (80 \AA^3) (50, 54). Methane is slightly larger than CO_2 so it is reasonable that not all sites accessible to CO_2 would be accessible to CH_4 . Indeed, the Langmuir saturation capacities of polycarbonate (54) and polysulfone (55) for CH_4 are about 1/2 the C'_H of CO_2 capacities. However, argon and nitrogen are both slightly smaller than CO_2 , so it should be possible to sorb one of these molecules into each Langmuir site under saturation conditions, but the C'_H 's for Ar and N_2 in polycarbonate (54) and polysulfone (55) are again less than 1/2 the C'_H for CO_2 in the same polymers. To accept the physical rational of the dual-mode model would imply that CO_2 is unique among all penetrants in probing the "unrelaxed volume" of polymers. The discrepancy in the values of C'_H for different gases cannot be attributed to the condensibility of the penetrants, since condensibility determines the relative efficiency with which the penetrant can utilize the available volume and so would effect only the value of the Langmuir affinity parameter, b (13).

- (e) Dilatometric measurements (56) of the swelling of "conditioned" polycarbonate by CO_2 show that the relative swelling of the polymer drops dramatically as the CO_2 pressure is increased. These results cannot be reconciled with the dual-mode sorption model, which assumes preferential sorption into pre-existing sorption sites at low pressures (sorption that should have little effect on the polymer dimensions) and mainly Henry's type dissolution at high pressures (dissolution that should result in the swelling of the polymer).

The dual-mode sorption and transport model provides an adequate mathematical description of the phenomenological sorption and transport in glassy polymers (13). However, the results presented here invalidate the physical assumptions implicit to the dual-mode model regarding no penetrant-polymer interactions and the existence of two distinct populations of sorbed gas molecules. In the initial formulation of the dual-sorption-mobility model, the authors cautioned against attaching physical significance to the mathematical parameters (39, 57). Since that time no physical evidence has appeared to support the existence of Langmuir sorption sites or concentration-independent diffusion and solubility coefficients in glassy polymers. Nevertheless, the mathematical parameters describing these two states have taken on a physical significance out of proportion with reality.

In the following chapter we present the matrix model of gas sorption and diffusion in glassy polymers which is based on the observation that gas molecules interact with the polymer, thereby altering the solubility and diffusion coefficients of the polymer matrix.

Literature Cited

1. Barr, G. "Dictionary of Applied Physics"; R. Glazerbrook, Ed.; MacMillan: London, 1923; Vol. 5.
2. Graham, T. Phil. Mag. 1866, 32, 401.
3. Von Wroblewski, S. Wiedemanns Ann. Physik. 1979, 8, 29.
4. Daynes, H. A. Proc. Roy. Soc. (London) A. 1920, 97, 286.
5. Barrer, R. M. J. Phys. Chem. 1957, 61, 178, and references therein.
6. Barrer, R. M. Nature 1937, 140, 106.
7. Barrer, R. M. Trans. Faraday Soc. 1939, 35, 644.
8. Bueche, F. J. Chem. Phys. 1953, 21, 1850.
9. Cohen M. H.; Turnbull, D. J. Chem. Phys. 1959, 31, 1164.
10. Brandt, W. W. J. Phys. Chem. 1959, 63, 1080.
11. DiBenedetto, A. T. J. Polym. Sci. A 1963, 1, 3477.
12. Pace, R. J.; Datyner, A. J. Polym. Sci., Polym. Phys. Ed. 1979, 17, 437.
13. Paul, D. R. Ber. Bunsenges Phys. Chem. 1979, 83, 294.
14. Assink, R. A. J. Polym. Sci., Polym. Phys. Ed. 1975, 13, 1665.
15. Zupančič, I.; Lahajnar, G.; Blinc, R.; Reneker, D. H.; Peterlin, A. J. Polym. Sci., Polym. Phys. Ed. 1978, 16, 1399.
16. Berens, A. R.; Hopfenberg, H. B. J. Membrane Sci. 1982, 10, 283.
17. Kinjo, N. Japan Plastics 1973, 7(4), 6.
18. Kinjo, N.; Nakagawa, T. Polymer Journal 1973, 4, 143.
19. Jacobson, U. British Plastics 1959, 32, 152.
20. Robeson, L. M. Polym. Eng. Sci. 1969, 9, 277.
21. Gardon, J. L. J. Colloid Interface Sci. 1977, 59, 582.
22. Schaefer, J.; Sefcik, M. D.; Stejskal, E. O.; McKay, R. A. Macromolecules, in press.
23. Schaefer, J.; Stejskal, E. O.; Buchdahl, R. Macromolecules 1977, 10, 384.
24. Steger, T. R.; Schaefer, J.; Stejskal, E. O.; McKay, R. M. Macromolecules 1980, 13, 1127.
25. Schaefer, J.; Stejskal, E. O.; Steger, T. R.; Sefcik M. D.; McKay, R. M. Macromolecules 1980, 13, 1121.
26. Sefcik, M. D.; Schaefer, J.; Stejskal, E. O.; McKay, R. A. Macromolecules 1980, 13, 1132.
27. Stejskal, E. O.; Schaefer, J.; Steger, T. R. Symp. Faraday Soc. 1979, 13, 56.
28. Sefcik, M. D.; Schaefer, J.; May, F. L.; Raucher, D.; Dub. S. J. Polym. Phys., Polym. Phys. Ed. in press.

29. Bloombergen, N.; Purcell, E. M.; Pound, R. V. Phys. Rev. 1948, 74, 679.
30. Barrer, R. M.; Mallinder, R.; Wong, P. S-L. Polymer 1967, 8, 321.
31. Florianczyk, T. Polimery 1978, 23, 431.
32. Crank, J. J. Polym. Sci. 1953, 11, 151.
33. Aitken, A.; Barrer, R. M. Trans. Faraday Soc. 1955, 51, 116.
34. Frisch, H. L. J. Phys. Chem. 1957, 61, 93.
35. Barrer, R. M.; Barrie, J. A.; Slater, J. J. Polym. Sci. 1958, 27, 177.
36. Michaels, A. S.; Vieth, W. R.; Barrie, J. A. J. Appl. Phys. 1963, 34, 13.
37. Vieth, W. R.; Sladek, K. J. J. Coll. Sci. 1965, 20, 1014.
38. Petropoulos, J. H. J. Polym. Sci. A 1970, 2, 1797.
39. Paul, D. R.; Koros, W. J. J. Polym. Sci., Polym. Phys. Ed. 1976, 14, 675.
40. Sefcik, M. D.; Schaefer, J. J. Polym. Phys., Polym. Phys. Ed. in press.
41. Berens, A. R. Polym. Eng. Sci. 1980, 20, 95.
42. Wonders, A. G.; Paul, D. R. J. Membrane Sci. 1979, 5, 63.
43. Wang, W. C.; Sachse, W.; Kramer, E. J. Bull. Am. Phys. Soc. 1981, 26, 367.
44. Wang, W. C.; Sachse, W.; Kramer, E. J. J. Polym. Sci., Polym. Phys. Ed. 1982, 20, 1371.
45. Robinson, C. Trans. Faraday Soc. 1946, 42B, 12.
46. Chan, A. H.; Paul, D. R. Polym. Eng. Sci. 1980, 20, 87.
47. Dunn, C. M. R.; Turner, S. Polymer 1974, 15, 451.
48. Toi, K. Polym. Engr. Sci. 1980, 20, 30.
49. Pace, R. J.; Datyner, A. J. Polym. Sci., Polym. Phys. Ed. 1980, 18, 1169.
50. Chern, R. T.; Koros, W. J.; Sanders, E. S.; Chen, S. H.; Hopfenberg, H. B. Chapter in this book.
51. Belfort, G.; Scherfig, J.; Seevers, D. O. J. Coll. Interface Sci. 1974, 47, 106.
52. Almagor, E.; Belfort, G. J. Coll. Interface Sci. 1978, 66, 146.
53. Koros, W. J.; Paul, D. R. J. Polym. Sci., Polym. Phys. Ed. 1978, 16, 1947.
54. Koros, W. J.; Chan, A. H.; Paul, D. R. J. Membrane Sci. 1977, 2, 165.
55. Erb, A. J.; Paul, D. R. J. Membrane Sci. 1981, 8, 11.
56. Sefcik, M. D.; Andrady, A. L.; Schaefer, J.; Desa, E. Polym. Prepr., Am. Chem. Soc., Div. Polym. Chem. in press.
57. Koros, W. J.; Paul, D. R.; Rocha, A. A. J. Polym. Sci., Polym Phys. Ed. 1976, 14, 687.

RECEIVED January 12, 1983

Sorption and Transport in Glassy Polymers

Gas-Polymer-Matrix Model

DANIEL RAUCHER and MICHAEL D. SEFCIK

Monsanto Company, St. Louis, MO 63167

The gas-polymer-matrix model for sorption and transport of gases in polymers is consistent with the physical evidence that; 1) there is only one population of sorbed gas molecules in polymers at any pressure, 2) the physical properties of polymers are perturbed by the presence of sorbed gas, and 3) the perturbation of the polymer matrix arises from gas-polymer interactions. Rather than treating the gas and polymer separately, as in previous theories, the present model treats sorption and transport as occurring through a gas-polymer matrix whose properties change with composition. Simple expressions for sorption, diffusion, permeation and time lag are developed and used to analyze carbon dioxide sorption and transport in polycarbonate.

Nonlinear, pressure-dependent sorption and transport of gases and vapors in glassy polymers have been observed frequently. The effect of pressure on the observable variables, solubility coefficient, permeability coefficient and diffusion timelag, is well documented (1, 2). Previous attempts to explain the pressure-dependent sorption and transport properties in glassy polymers can be classified as "concentration-dependent" and "dual-mode" models. While the former deal mainly with vapor-polymer systems (1) the latter are unique for gas-glassy polymer systems (2).

The concentration-dependent models attribute the observed pressure dependence of the solubility and diffusion coefficients to the fact that the presence of sorbed gas in a polymer affects the structural and dynamic properties of the polymer, thus affecting the sorption and transport characteristics of the system (3). On the other hand, in the dual-mode model, the pressure-dependent sorption and transport properties arise from a

0097-6156/83/0223-0111\$06.00/0

© 1983 American Chemical Society

unique mechanism which assumes two distinct modes of sorption (2, 4). The dual-mode model assumes that the diffusant gas does not interact with the polymer matrix and does not induce changes in the polymer characteristics, thus the diffusion coefficients of both populations are assumed to be independent of gas pressure or concentration (4, 5, 6).

In the preceding chapter (7) we elucidated the mechanism of gas diffusion in glassy polymers by presenting evidence that the diffusion of gases through polymer matrices is controlled by the cooperative main-chain motions of the polymer (8), and that these motions are altered by the presence of penetrants (9). These results mean that sorbed gases alter the structure and dynamics of the polymer matrix, thus altering the sorption and transport characteristics of the system. We proposed that gas-polymer interactions reduce the interchain potential of the polymer, thus decreasing the activation energy of polymer chain separation, and therefore the activation energy of diffusion. The decrease in the activation energies results in higher frequencies of cooperative main-chain motions and in higher diffusion coefficients. The heat of sorption, and ultimately the solubility of gases, depend on similar interactions (12). Since the gas-polymer interactions alter the interchain energies, solubility coefficients also vary as the structure and dynamics of the polymer matrix change (10).

The experimental results presented in the preceding chapter and in the literature are inconsistent with the assumptions and the physical interpretation implicit in the dual-mode model and strongly suggest that the sorption and transport in gas-glassy polymer systems should be represented by a concentration-dependent type model.

In Section I we introduce the gas-polymer-matrix model for gas sorption and transport in polymers (10, 11), which is based on the experimental evidence that even permanent gases interact with the polymeric chains, resulting in changes in the solubility and diffusion coefficients. Just as the dynamic properties of the matrix depend on gas-polymer-matrix composition, the matrix model predicts that the solubility and diffusion coefficients depend on gas concentration in the polymer. We present a mathematical description of the sorption and transport of gases in polymers (10, 11) that is based on the thermodynamic analysis of solubility (12), on the statistical mechanical model of diffusion (13), and on the theory of corresponding states (14). In Section II we use the matrix model to analyze the sorption, permeability and time-lag data for carbon dioxide in polycarbonate, and compare this analysis with the dual-mode model analysis (15). In Section III we comment on the physical implication of the gas-polymer-matrix model.

I. GAS-POLYMER-MATRIX MODEL

A model for sorption and transport of gases in polymers has to specifically account for the fact that the presence of sorbed gases in the polymer modifies the matrix (7, 9). In developing the matrix model we are guided by the physical evidence relating to the mechanism of sorption and transport. The matrix model is consistent with the following observations and assumptions:

- (a) There is only one population of sorbed gas molecules in a polymer at any given pressure. Spectroscopic analyses of gas molecules within polymer matrices are consistent with all of the gas molecules being in a single state (16, 17, 18). Further, there is no physical evidence for the existence of Langmuir or other sorption sites in glassy polymers which could account for multiple sorption sites.
- (b) The physical properties of a polymer matrix are perturbed by the presence of a sorbed gas. In addition to the observed changes in cooperative main-chain motions of the polymer in the presence of a sorbed gas (7, 9), changes in viscoelastic relaxation (19, 21, 22), and T_g (15, 20, 21, 22) have also been reported.
- (c) Based on the effect of sorbed gas on the main-chain motions of the polymer (7, 9) we propose that the perturbation of the polymer matrix arises from interactions between the gas molecules and polymer chains.

The matrix model ascribes the apparent concentration dependence of polymer properties to gas-polymer interactions, which affect the interchain potential energy of the polymer. The thermodynamic analysis of solubility of gases in polymers (10) shows that the gas-polymer interactions affect the free energy of solution of gases in polymers, thus controlling the solubility coefficient. Pace and Datyner proposed in their statistical mechanical model of diffusion of gases in polymers (13) that the interchain potential energy controls the activation energy of chain separation, the activation energy of diffusion, and the diffusion coefficients. Chow (23) showed by classical and statistical thermodynamics that gas-polymer interactions are manifested in the depression of the glass-transition temperature of the polymer.

It is possible to gain some insight into the effect of sorbed gas on the interchain potential energy, by analogy to the effect of temperature on interchain cohesion forces. Raising the temperature of the polymer, like increasing the sorbed gas concentration in the polymer, reduces the interchain potential, resulting in higher diffusion coefficient and in lower solubility coefficient.

A. Matrix Model Expressions for Sorption and Transport

1. Solubility Coefficient

The solubility coefficients of gases in glassy polymers are not constant, but decrease with increasing concentration of the gas in the polymers (2). Calculations of the isosteric enthalpy of sorption in several gas-polymer systems confirm that the gas-polymer affinity is reduced with increasing sorbed gas concentrations (24, 25, 26). The change in the isosteric enthalpy of sorption is a result of the changes in the polymer matrix induced by the presence of the sorbed gas.

We have shown previously (10) that based on Gee's thermodynamic analysis of gas solubility in polymers (12) and the theory of corresponding states (14), the solubility coefficient, σ , can be expressed as,

$$\sigma = \sigma_0 \exp(-\alpha^* \kappa) \quad (1)$$

where σ_0 is the solubility coefficient in the zero-concentration limit, α^* is a constant relating the excess free energy of mixing to the depression of the glass-transition temperature of the polymer by the gas and κ is defined as,

$$\kappa = [T_g(o) - T_g(C)]/T \quad (2)$$

where $T_g(o)$ and $T_g(C)$ are the glass-transition temperatures of the pure polymer and the polymer-gas mixture, respectively. Chow (23) derived an explicit expression for the depression of the glass-transition temperature of polymers by diluents. To a first approximation, $[T_g(o) - T_g(C)]$ may be regarded as proportional to the gas concentration in the matrix (11). Thus, eq. (1) can be rewritten as,

$$\sigma = \sigma_0 \exp(-\alpha C) \quad (3)$$

where α is a constant relating $\alpha^* \kappa$ to the concentration, C . Eq. (3) can be simplified by expanding the exponential as a power series and neglecting the higher order-terms,

$$\sigma = \frac{\sigma_0}{1 + \alpha C} \quad (4)$$

2. Diffusion Coefficient

We have shown in the preceding chapter (7) that the presence of gas increases the cooperative main-chain motions of glassy polymers (9). The diffusion model of Pace and Datyner (13)

suggests that increased frequency of the cooperative motions results in an increased diffusion coefficient.

Based on the diffusion model of Pace and Datyner (13) and the theory of corresponding states (14) the diffusion coefficient, D , can be represented by (10),

$$D = D_0 (1 + \beta^* \kappa) \exp(\beta^* \kappa) \quad (5)$$

where D_0 is the diffusion coefficient in the zero-concentration limit, and β^* is a constant relating the excess activation energy of chain separation to the depression of the glass-transition temperature of the polymer by the gas. As the diffusion coefficient changes with concentration (or κ), the diffusivity of the gas, in a steady-state transport experiment, changes continuously through the membrane. Experimentally determined diffusion coefficients reflect the continuous change of the diffusivity and are therefore called effective diffusion coefficients (27). The effective diffusion coefficient can be expressed as a function of κ by,

$$\bar{D} = (1/\kappa) \int D d\kappa \quad (6)$$

Substituting eq. (5) into eq. (6) and integrating between the boundary conditions of a steady-state experiment yields,

$$\bar{D} = D_0 \exp(\beta^* \kappa) \quad (7)$$

As before, by assuming linearity between κ and C , eq. (7) can be rewritten as,

$$\bar{D} = D_0 \exp(\beta C) \quad (8)$$

where β is a constant relating $\beta^* \kappa$ to C . Eq. (8) can be simplified by expanding the exponential as a power series and neglecting the higher-order terms,

$$\bar{D} = D_0 (1 + \beta C) \quad (9)$$

B. Matrix Model Parameters of Sorption and Transport

1. Constants σ_0 and D_0 - Sorption and Transport in the Zero Concentration Limit.

In the limit of zero-concentration, gas-glassy polymer systems behave "ideally." As the gas concentration in the membrane approaches zero the solubility coefficient becomes constant with the value σ_0 [eqs. (1), (3) and (4)]. In the same limit, the diffusion coefficients are constant and equal to the diffusion coefficient D_0 , [eqs. (5), (7), (8) and (9)]. As typical of limiting values, σ_0 and D_0 have no correspondence to

reality, but merely describe the behavior of the gas-polymer system as if there were no induced changes in the polymer matrix.

It should be kept in mind that σ_0 and D_0 are really mean values, recognizing the fact that glassy polymers are heterogeneous and contain a distribution of structural and dynamic states (28). As such, these parameters are dependent on the nature of the penetrant and of the polymer (13), as well as the distribution of properties in the polymer.

2. Parameter α and β - Concentration Dependence of Sorption and Transport

The matrix model ascribes the apparent concentration dependence of the solubility and diffusion coefficients to gas-polymer interactions. The parameters α and β are proportionality constants, indicating the effectiveness of gas-polymer interaction in inducing changes in the solubility and diffusion coefficients. The explicit expressions for σ and D describe them as functions of the excess free energy of solution and the change in the activation energy of chain separation, respectively (10). As our understanding of the effect of the gas-polymer matrix composition on these excess energies increases we may find it possible to explicitly determine these energy parameters and thus σ and D without having to resort to empirically determined proportionality constants.

II. ANALYSIS OF SORPTION AND TRANSPORT DATA BY THE MATRIX MODEL

We show elsewhere (10) that sorption and transport expressions derived from eqs. (1) and (5) represent experimental sorption and transport data well. Nevertheless, the calculations are cumbersome and require additional polymer parameters. These disadvantages might hinder the broad use of these expressions; thus, we will base our following discussions on the simplified expressions, eqs. (4) and (9), exclusively.

In the derivation of the simplified expressions for solubility and diffusion coefficients, eqs. (4) and (9), C was assumed to be small. This fact does not limit the usefulness of these expressions for high concentrations. We show below that sorption and transport expressions, eqs. (11) and (14), respectively, derived from the simplified equations retain the proper functional form for describing experimental data without being needlessly cumbersome. Of course, the values of the parameters in eqs. (4) and (9) will differ from the corresponding parameters in eqs. (3) and (8), to compensate for the fact that the truncated power series used in eqs. (4) and (9) poorly represent the exponentials when $\alpha C > 1$ or $\beta C > 1$. Nevertheless, this does not hinder the use of the simplified equations for making correlation between gas-polymer systems.

A. Sorption of Gases in Glassy Polymers

The concentration of sorbed gas in the polymer is the product of the solubility coefficient and the gas pressure p ,

$$C = \sigma p \quad (10)$$

When σ is given by eq. (4)

$$C = \frac{\sigma_0 p}{1 + \alpha C} \quad (11)$$

The expression for the solubility, eq. (11), can be easily rearranged by solution of the quadratic equation to give a simple dependence of C on p ,

$$C = \frac{(1 + 4\alpha \sigma_0 p)^{\frac{1}{2}} - 1}{2\alpha} \quad (12)$$

The solid line in Fig. 1 represents the sorption isotherm of carbon dioxide in polycarbonate calculated by fitting the solubility expression, eq. (11), to experimental data of Wonders and Paul (15). The best fit to the experimental data was achieved with the parameters $\sigma_0 = 7.33 \text{ cm}^3(\text{STP})/\text{cm}^3(\text{polymer}) \cdot \text{atm}$ and $\alpha = 0.161 \text{ cm}^3(\text{polymer})/\text{cm}^3(\text{STP})$. As can be seen in Fig. 1, eq. (11) describes the experimental data over the entire pressure range. The algorithm used to fit eq. (11) to the experimental data is described elsewhere (11).

The broken line in Fig. 1 was calculated following a non-linear least-squares fit of the dual-mode expression for the equilibrium gas concentration [eq. (14) in the preceding chapter] to the experimental points, with $k_D = 0.758 \text{ cm}^3(\text{STP})/\text{cm}^3(\text{polymer}) \cdot \text{atm}$, $C_H' = 14.58 \text{ cm}^3(\text{STP})/\text{cm}^3(\text{polymer})$, and $b = 0.2835 \text{ atm}^{-1}$ (15).

Both the matrix-model and the dual-model represent the experimental data satisfactory (Fig. 1). After modeling sorption measurements in several gas-polymer systems we have observed no systematic differences between the mathematical descriptions of the two models.

B. Transport of Gases in Glassy Polymers

1. Steady-State Transport

Solution of Fick's first law under the boundary conditions of a steady state permeation experiment yields an expression for the permeability constant, P (27),

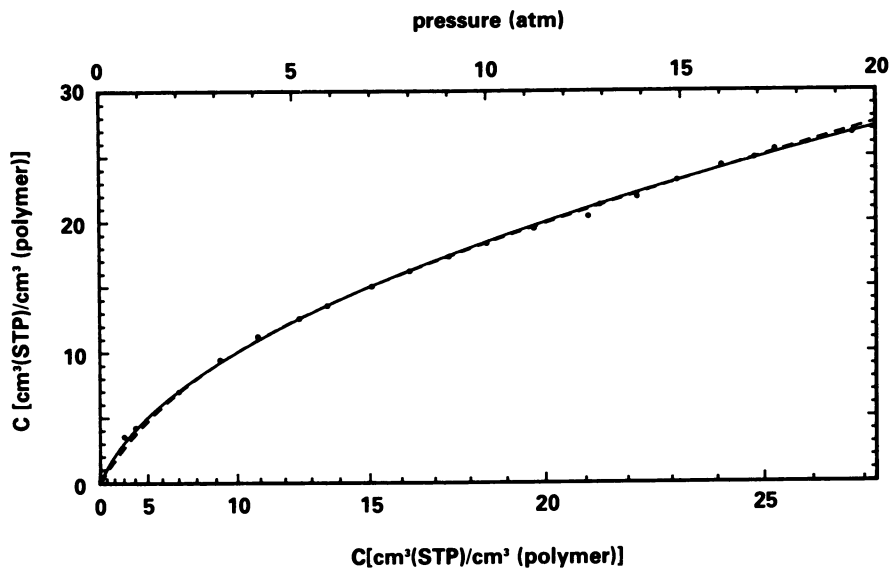


Figure 1. Sorption isotherm at 35 °C for CO₂ in polycarbonate conditioned by exposure to 20 atm CO₂. The experimental data are from Ref. 15. The curves, based on the matrix model (solid line) and the dual-mode model (broken line), are calculated using the parameters given in the text.

$$P = \bar{D} \sigma \quad (13)$$

When σ is given by eq. (4) and \bar{D} by eq. (9) we have,

$$P = D_0 \sigma_0 \frac{1 + \beta C}{1 + \alpha C} \quad (14)$$

The solid line in Fig. 2 shows the permeability-pressure curve of CO₂ in polycarbonate calculated by fitting the simplified permeability expression, eq. (14), to experimental data of Wonders and Paul (15). The data fitting procedure, described elsewhere (11), gives $D_0 = 1.09 \times 10^{-8}$ cm²/sec and $\beta = 0.065$ cm³(polymer)/cm³(STP). Fig. 2 shows a good agreement between the experimental data and eq. (14) over the entire pressure range.

Wonders and Paul (15) report that a nonlinear least-squares fit of the dual-mode expression [eq. (16) in the preceding chapter] to the permeability versus pressure data, for CO₂ in polycarbonate, gives D_D and D_H values of 4.78×10^{-8} and 7.11×10^{-9} cm²/sec, respectively. The broken curve in Fig. 2 was calculated from the dual-mode sorption coefficients of Fig. 1 and the values of the diffusion coefficients given above.

Comparing the curves in Fig. 2 shows that representing the permeability versus pressure data by either model provides a satisfactory fit to the data over the pressure range of 1 to 20 atm. However, at pressures less than 1 atm. the two models differ in their prediction regarding the behavior of the permeability-pressure curve [Fig. 2]. While the matrix model predicts a strong apparent pressure dependence of the permeability in this range (solid line), the dual-mode model predicts only a weak dependence (broken line).

2. Transient Transport

Transient-transport measurements are a powerful tool for evaluating the validity of any sorption-transport model. The ability of a model to predict diffusion time lags is a test for its validity, as all the parameters are fixed by the equilibrium sorption and steady state transport, and because the time lag depends on the specific form of the concentration and diffusion gradients developed during the transient-state experiments.

Frisch has developed explicit expressions for the time lag in diffusion of a gas across a planar membrane when the diffusion coefficient is concentration dependent (29). Using his generalized method of solution,

$$\theta = \frac{l^2}{6D_0} \cdot \frac{10 + 25 \beta C + 16(\beta C)^2}{10(1 + \beta C)^3} \quad (15)$$

when \bar{D} is given by eq. (9).

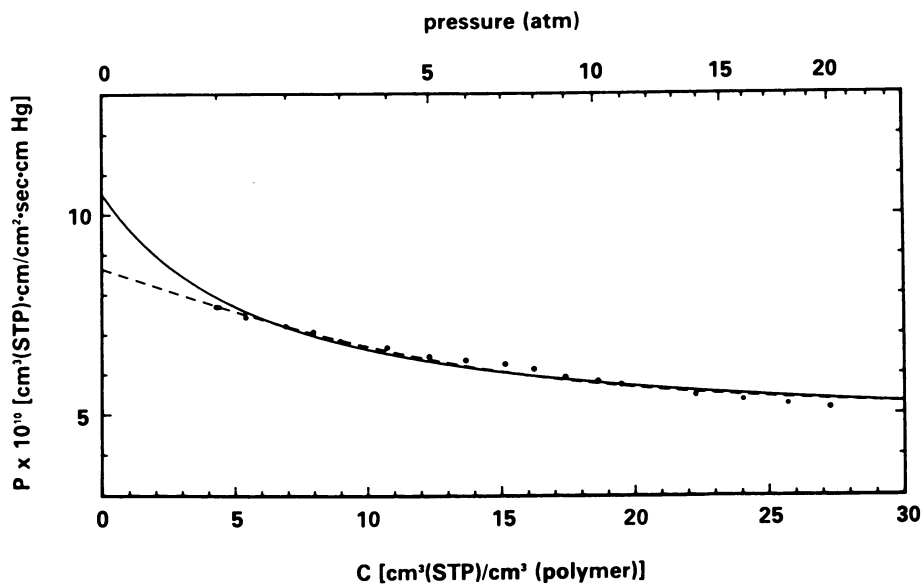


Figure 2. Permeability of CO_2 in conditioned polycarbonate at 35°C . The experimental data are from Ref. 15. The solid curve is the calculated permeability based on the matrix model and the broken curve is calculated from the dual-mode model. Parameters used in the curves are given in the text.

Fig. 3 shows the calculated time lags (solid line) and the experimental time lags reported by Wonders and Paul (15) for CO₂ in polycarbonate. The time lags predicted by eq. (15) are in excellent agreement with the experimental results at both low and high pressures. The broken line in Fig. 3 results from calculations using the dual-mode model [eq. (17) in the previous chapter].

Using the dual-mode parameter values determined from sorption and permeation experiments, calculated time lags agree with the experimental data only at gas pressures above 5 atm. At lower pressures, dual-mode time lags are appreciably shorter than the observed ones, whereas time lags calculated from the matrix model by eq. (15) agree with the experimental data over the entire pressure range.

III. THE MATRIX AND DUAL-MODE MODELS AS PHYSICAL MODELS

The matrix model of gas sorption and transport ascribes the apparent concentration dependence of the structural and dynamic properties of the polymer to gas-polymer interactions. These interactions affect the interchain potential energy of the polymer, thus affecting the sorption and transport characteristics of the matrix. The matrix model is consistent with experimental evidence that the presence of gases causes changes in the structure, dynamics, glass-transition temperature, and viscoelastic relaxations of glassy polymers (7). The formalism developed here describes gas sorption and transport results and may also prove useful in quantifying these other changes.

In contrast, the dual-mode sorption and transport model assumes that the diffusant gas does not interact with the polymer (2, 4). In the dual-mode model the concentration dependence of the sorption and transport characteristics arises from the pressure-dependent distribution of the sorbed gas between Langmuir sites and Henry's law dissolution. Experimental results presented in the preceding chapter (7) are inconsistent with the assumptions and the physical interpretations implicit in the dual-mode model. Although the dual-mode model provides a fairly adequate mathematical description of the phenomenological sorption and transport of gases in glassy polymers (2, 4), the physical assumption of the model regarding no penetrant-polymer interactions and the existence of two distinct populations of sorbed gas molecules seems to be invalid in light of the experimental data (7).

A model for sorption and transport of gases in polymers should serve two purposes. First, the model should convey an understanding of the molecular interactions which are responsible for the macroscopic processes, and second, the model should

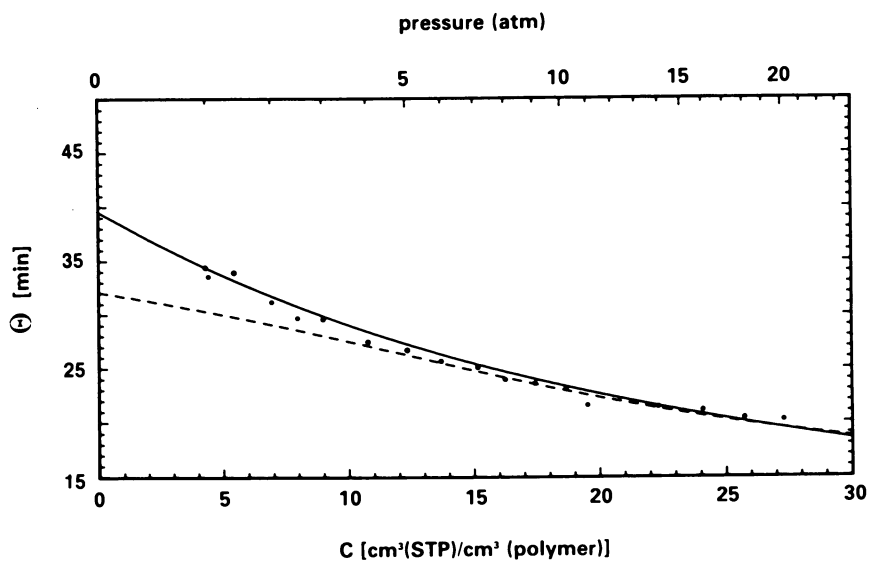


Figure 3. Time lag for diffusion of CO_2 at 35°C in a 4.9 mil thick polycarbonate film conditioned by prior exposure to CO_2 . The data are from Ref. 15. Calculated time lags based on the matrix model (solid line) and the dual-mode model (broken line) use parameters determined from fitting the sorption and permeation data.

enable correlative predictions of the macroscopic processes. Different mathematical expressions can be used for the modeling of the macroscopic sorption and transport phenomena. The dual-mode model proved to be extremely useful in this area (2). However, it is just as important to gain insight into the molecular processes in the gas-polymer matrix. It is mainly for this reason that we have introduced the matrix model and promoted its use in modeling macroscopic sorption and transport of gases in polymers. We believe that continued refinement of the formalism of the matrix model will lead to better understanding of gas-polymer systems.

Literature Cited

1. Barrer, R. M. J. Phys. Chem. 1957 **61**, 178, and references therein.
2. Paul, D. R. Ber. Bunsenges Phys. Chem. 1979, **83**, 294, and references therein.
3. Crank, J. J. Polym. Sci. 1953, **11**, 151.
4. Paul, D. R.; Koros, W. J. J. Polym. Sci., Polym. Phys. Ed. 1976, **14**, 675.
5. Koros, W. J.; Paul, D. R.; Rocha, A. A. J. Polym. Sci., Polym. Phys. Ed. 1976, **14**, 687.
6. Chern, R. T.; Koros, W. J.; Sanders, E. S.; Chen, S. H.; Hopfenberg, H. B., Chapter in this book.
7. Raucher, D.; Sefcik, M.D., Chapter in this book, and references therein.
8. Sefcik, M. D.; Schaefer, J.; May, F. L.; Raucher, D.; Dub, S. M. J. Polym. Sci., Polym. Phys. Ed. in press.
9. Sefcik, M. D.; Schaefer, J. J. Polym. Sci., Polym. Phys. Ed. in press.
10. Sefcik, M. D.; Raucher, D. J. Polym. Sci., Polym. Phys. Ed. in press.
11. Sefcik, M. D.; Raucher, D. J. Polym. Sci., Polym. Phys. Ed. in press.
12. Gee, G. Quart. Rev. Chem. Soc. 1947, **1**, 265.
13. Pace, R. J.; Datyner, A. J. Polym. Sci., Polym. Phys. Ed. 1979, **17**, 437.
14. Prigogine, I. "The Molecular Theory of Solutions"; North-Holland Publishing Co.: Amsterdam, 1957; Ch. 6.
15. Wonders, A. G.; Paul, D. R. J. Membrane Sci. 1979, **5**, 63.
16. Assink, R. A. J. Polym. Sci., Polym. Phys. Ed. 1975, **13**, 1665.
17. Zupančič, I.; Lahajnar, G.; Blink, R.; Reneker, D. H.; Peterlin, A. J. Polym. Sci., Polym. Phys. Ed. 1978, **16**, 1339.
18. Schaefer, J.; Sefcik, M. D.; Stejskal, E. O.; McKay, R. A. Macromolecules in press.
19. Sefcik, M. D.; Andrady, A. L.; Schaefer, J.; Desa, E. Polym. Prepr., Am. Chem. Soc., Div. Polym. Chem. in press.

20. Assink, R. A. J. Polym. Sci. A-2, 1974, 12.
21. Wang, W. C.; Kramer, E. J. Bull. Am. Phys. Soc. 1981, 26, 367.
22. Wang, W. C.; Sachse, W.; Kramer, E. J. J. Polym. Sci. Polym. Phys. Ed., 1982, 20, 1371.
23. Chow, T. S. Macromolecules 1980, 13, 362.
24. Koros, W. J.; Paul, D. R.; Huvard, G. S. Polymer 1979, 20, 956.
25. Barrie, J. A.; Williams, M. J. L.; Munday, K. Polym. Eng. Sci. 1980, 20, 20.
26. Ranade, G.; Stannett, V.; Koros, W. J. J. Appl. Polym. Sci. 1980, 25, 2179.
27. Crank, J. "Mathematics of Diffusion", 2nd Ed.: Oxford Univ., 1975.
28. Ferry, J.D. "Viscoelastic Properties of Polymers," Wiley & Sons: New York, 1980, Ch. 15.
29. Frisch, H. L. J. Phys. Chem. 1957, 61, 93.

RECEIVED January 12, 1983

Membrane Gas Separations for Chemical Processes and Energy Applications

WILLIAM J. SCHELL

Separex Corporation, Spectrum Separations Division, Anaheim, CA 92806

C. DOUGLAS HOUSTON

Separex Corporation, DGH, Inc. Division, Tyler, TX 75703

Membranes have been used commercially for many years for water desalination by the reverse osmosis process. These membranes consist of a microporous substructure of cellulose acetate and a thin layer of dense cellulose acetate (active layer) on the upper surface, cast onto a supporting cloth for added mechanical strength. The active layer serves as the separating barrier, and due to its thinness, provides very high transport rates. It has been determined that these membranes, when dried, are also suitable for gas separation. As certain gases permeate more rapidly than others a gas mixture of two or more gases of varying permeability may be separated into two streams, one enriched in the more permeable components and the other enriched in the less permeable components. The membrane system to be described consists of spiral-wound elements connected in series and contained within pressure vessels. A rubber U-cup attached to the element serves to seal the element with the inner diameter of the pressure vessel, thereby forcing the feed gas to flow through the element. The pressure vessels usually contain six elements each and are mounted in racks on a skid. Applications that will be discussed include recovery of hydrogen from refinery process streams and tail gases, carbon dioxide removal and sweetening of natural gas, dehydration of natural gas on offshore platforms and production of carbon dioxide for enhanced oil recovery. The advantages of membrane separation over conventional processes typically include greatly reduced capital costs, lower energy consumption, smaller size and weight, lower installation costs due to its modular design, and simplified operation.

0097-6156/83/0223-0125\$06.00/0

© 1983 American Chemical Society

It has been recognized for many years that nonporous polymer films exhibit a higher permeability toward some gases than toward others. As early as 1831, investigations were reported on the phenomenon of enrichment of air with rubber membranes (Ref. 1); however, not until 1950 had the practical possibility of this and other gas separations with permselective membranes been seriously studied. Weller and Steiner in their classic papers, demonstrated the feasibility of separating oxygen from air and described practical processes for separation of hydrogen and helium from methane (Ref. 2,3). Although their results were highly valuable in the development of the science of membrane separation, the calculated membrane area requirements for industrial processes were enormous, due to the very low permeation rates of the gases through these dense films.

The technical breakthrough in the application of membranes to gas separation came with the development of a process for preparing cellulose acetate in a state which retains its permselective characteristics but at greatly increased permeation rates (Ref. 4,5). These flat-sheet cellulose acetate membranes, which were originally developed for reverse-osmosis water desalination (Ref. 6), are prepared from a solution of the polymer which is cast on a supporting cloth, partially dried then set or gelled in a water bath. At this state the membranes are heated in water to improve their selectivity characteristics, followed by drying with a solvent-exchange technique. These membranes have vastly increased permeation rates, while retaining the permselective characteristics of films of cellulose acetate, due to the formation of a thin, dense layer on the air-dried surface of the membrane. This so-called "active" layer has characteristics similar to those of cellulose acetate films but with a thickness of the order of 0.1 micrometer (μm) or less, whereas the total membrane thickness may range from approximately 75 to 125 μm (see Figure 1). The major portion of the membrane is an open-pore sponge-like support structure through which the gases flow without restriction. The permeability and selectivity characteristics of these asymmetric membranes are functions of casting solution composition, film casting conditions and post-treatment, and are relatively independent of total membrane thickness.

Methods were developed later to incorporate this asymmetric membrane structure for gas separation in a hollow fiber configuration rather than the flat-sheet (Ref. 7). Hollow fibers have a greater packing density (membrane area per packaging volume) than flat sheets, but typically have lower permeation rates. The mechanism for gas separation is independent of membrane configuration, however, and is based on the principle that certain gases permeate more rapidly than others. This is due to a combination of diffusion and solubility differences, whereby a gas mixture of two or more gases of varying permeability may be separated into two streams, one enriched in the more permeable components and the other enriched in the less permeable components.

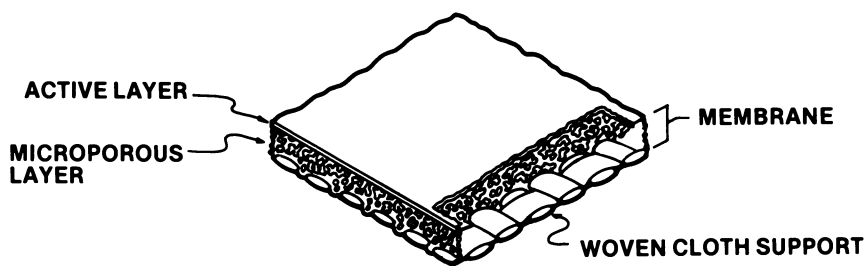


Figure 1. Cross section of asymmetric cellulose acetate membrane.

Membrane Element Configuration

In order for membranes to be used in a commercial separation system they must be packaged in a manner that supports the membrane and facilitates handling of the two product gas streams. These packages are generally referred to as elements or bundles. The most common types of membrane elements in use today include the spiral-wound, hollow fiber, tubular, and plate and frame configurations. The systems currently being marketed for gas separation are of the spiral-wound type, such as the SEPAREX and Delsep processes, and the hollow-fiber type such as the Prism separator and the Cynara Company process.

Spiral-wound elements, as shown in Figure 2, consist primarily of one or more membrane "leaves," each leaf containing two membrane layers separated by a rigid, porous, fluid-conductive material known as the "permeate channel spacer." The permeate channel spacer facilitates the flow of the "permeate", an end product of the separation. Another channel spacer known as the "high pressure channel spacer" separates one membrane leaf from another and facilitates the flow of the high pressure stream through the element. The membrane leaves are wound around a perforated hollow tube, known as the "permeate tube", through which the permeate is removed. The membrane leaves are sealed with an adhesive on three sides to separate the feed gas from the permeate gas, while the fourth side is open to the permeate tube.

The operation of the spiral-wound element can best be explained by means of an example. In order to separate carbon dioxide and/or hydrogen sulfide (acid gases) from a mixture of these acid gases and hydrocarbon gases, the gaseous mixture enters the pressure tube at high pressure and is introduced into the element via the "high pressure channel spacer." The more permeable acid gases rapidly pass through the membrane into the "permeate channel spacer" where they are concentrated as a low pressure gas stream. This low pressure acid gas stream flows through the element in the "permeate channel spacer" and is continuously enriched by additional acid gas entering from other sections of the membrane. When the low pressure acid gas stream reaches the permeate tube at the center of the element, the acid gas "permeate" is removed. The high pressure "residual gas" mixture remains in the high pressure channel spacer, losing more and more of its acid gas and being enriched in hydrocarbon gas as it flows through the element, and exits at the opposite end of the element.

The membrane system consists of membrane elements connected in series and contained within pressure tubes as shown in Figure 3. A rubber U-cup attached to the element serves to seal the element with the inner diameter of the pressure tube, thereby forcing the feed gas to flow through the element. The pressure tubes usually contain six elements each and are mounted in racks on a skid. Commercial size elements are typically 8 inches in diameter by 40 inches long and contain from 150 to 275 square feet of membrane area.

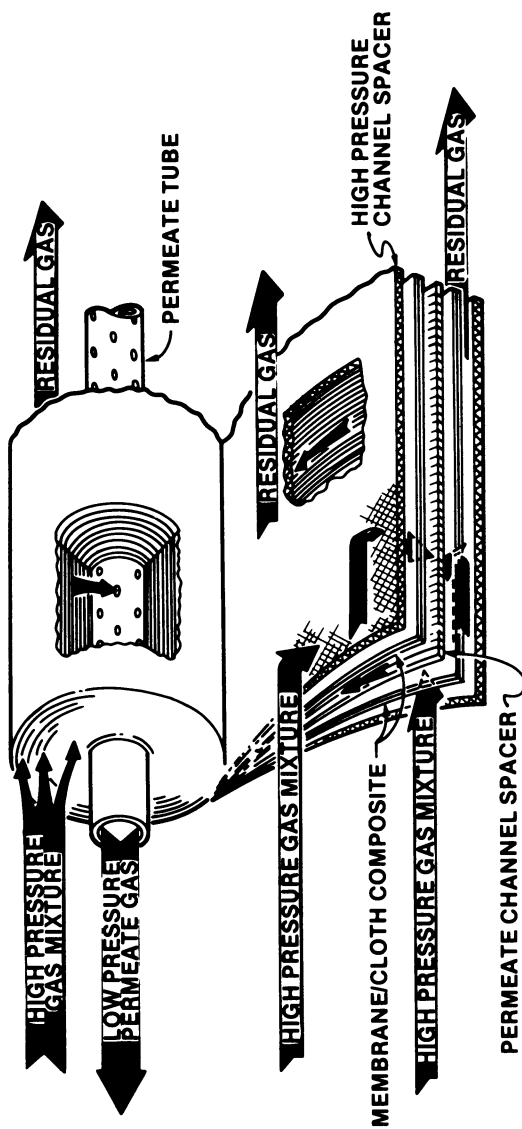


Figure 2. Spiral-wound element construction.

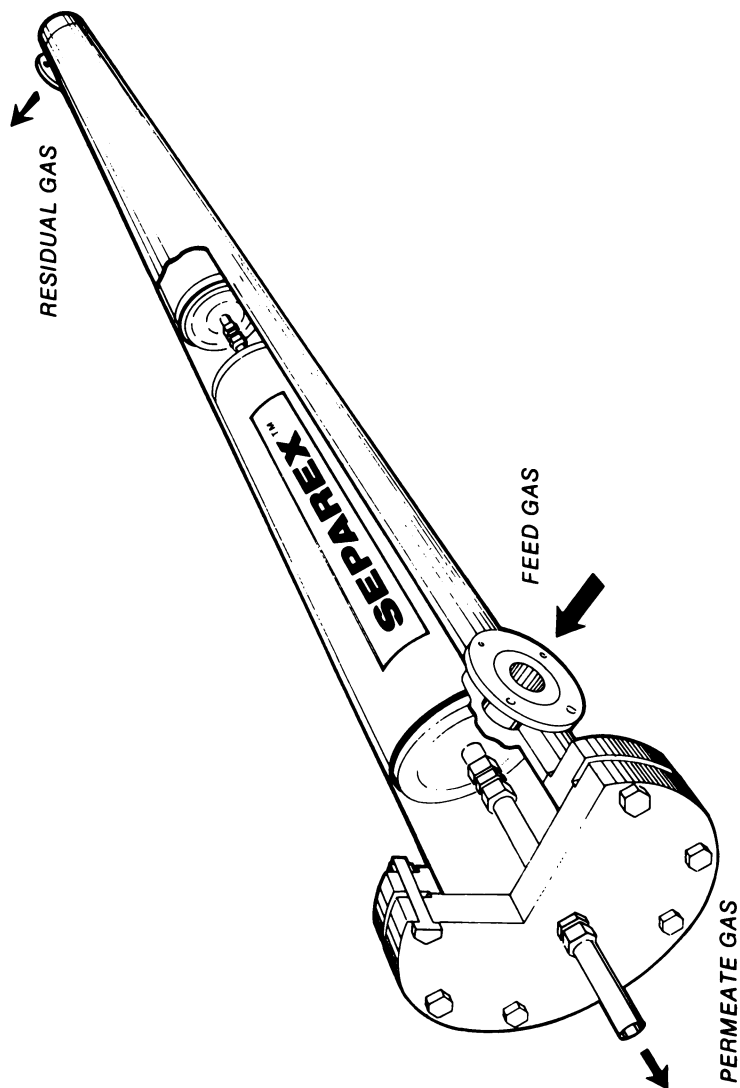


Figure 3. Separex spiral-wound element assembly.

Typical operating parameters for the SEPAREX process are a temperature range of 32°F to 140°F, pressure differentials up to 1200 psig and feed flow rates from 50 MSCFD to more than 100 MMSCFD. The cellulose acetate membrane system is capable of processing mixtures containing a wide range of concentrations of hydrogen, carbon dioxide, hydrogen sulfide, water vapor, hydrocarbons and oxygen. Minor amounts of aromatic hydrocarbons, chlorinated hydrocarbons, olefins and heavy hydrocarbons do not appear to effect the membrane performance. Elements have actually been operated on liquid hydrocarbons without any detrimental effect.

Basic Equations Affecting Separation

The steady state mass flux (J_i) of component i through a homogeneous film of uniform thickness separating two gaseous phases is given by Fick's "First Law" of diffusion:

$$J_i = D_i \frac{dC_i}{dx} = \text{constant} \quad 1)$$

where

D_i = local diffusivity (cm²/sec)

C_i = local concentration of component i

x = the distance through the film

This relationship can be simplified when the gases do not chemically associate with each other and when the gases are sparingly soluble in the membrane material. In such cases, the diffusivity of the permeating gas is constant through the film and the solubility of the gas at the membrane surface is essentially directly proportional to its partial pressure in the gas phase adjacent to that surface, i.e., Henry's Law applies:

$$C_i = k_i P_i \quad 2)$$

where k_i is the solubility parameter and P_i is the partial pressure.

If we let superscript I refer to the high pressure of the upstream side of the membrane and superscript II refer to the low pressure or downstream side of the membrane, Equation 1, after integration between C_i^I at $x = 0$ and C_i^{II} at $x = l$, becomes:

$$J_i = \frac{k_i D_i (P_i^I - P_i^{II})}{l}$$

The product $k_i D_i$ is termed the permeability coefficient of the membrane for component i . This coefficient is independent of membrane thickness and pressure differential and the frequently used units are, cc(STP) - cm/cm²-sec-cm Hg. Another parameter of

interest is the permeation rate, \bar{P}_i , defined as $k_i D_i / \ell$, which is a measured characteristic of a given membrane, with units cc(STP) / cm²-sec-cm Hg or SCFH/ft²·100 psi. The total pressures, P^I and P^{II} , are given by the sums, $P_i^I + P_j^I$ and $P_i^{II} + P_j^{II}$, respectively. The ratio \bar{P}_i / \bar{P}_j is defined as the ideal separation factor for component i with respect to component j in the membrane and is written $\alpha_{i/j}$.

From the previous discussion it can be seen that, if component i is the more permeable, increasing P_i^I , either by increasing the total pressure or the concentration of component i , will result in a higher membrane permeability rate. In addition, higher values for $\alpha_{i/j}$ result in greater efficiency in gas separation.

It can be shown that the composition of the permeate gas, P_i^{II} , for permeation of a binary gas mixture is given by the following quadratic equation:

$$\frac{P_i^{II}}{(P^{II} - P_i^{II})} = \frac{\alpha_{i/j} (P_i^I - P_i^{II})}{(P^I - P^{II}) - (P_i^I - P_i^{II})}$$

Parameters Affecting The Process

The separation efficiency for a given membrane with a particular binary gas mixture will be dependent mainly upon three factors: gas composition, the pressure ratio between feed and permeate gas, and the separation factor for the two components. A higher separation factor gives a more selective membrane, resulting in a greater separation efficiency. This parameter is a function of the membrane material and is determined by the individual gas permeation rates.

The gas composition and pressure ratio are interrelated in terms of their effect on separation efficiency. Their interaction is pronounced when the feed gas has a low concentration of the more permeable gas, with the result that the effective separation is small at low pressure ratios, irrespective of the $\alpha_{i/j}$ value of the membrane. This behavior is shown in Figure 4. This phenomenon is due to the fact that the partial pressure of the more permeable component on the permeate (low pressure) side cannot exceed its partial pressure on the feed (high pressure) side. For high concentration gases the pressure ratio has only a small influence, as shown in Figure 5. Hence, if compression energy is an important factor in the economics of a particular separation, lower pressure ratios may be used with little or no loss in separation efficiency. By contrast (see Figure 4), the pressure ratio is a very important consideration in achieving efficient separation of low concentration gas mixtures.

Another important factor in membrane gas separation is the pressure differential, $P^I - P^{II}$; the greater this difference the less membrane area required. The membrane area is exactly proportional to the inverse of the pressure differential, i.e., $\text{Area} = \text{constant} (P^I - P^{II})^{-1}$. The effective separation factor is

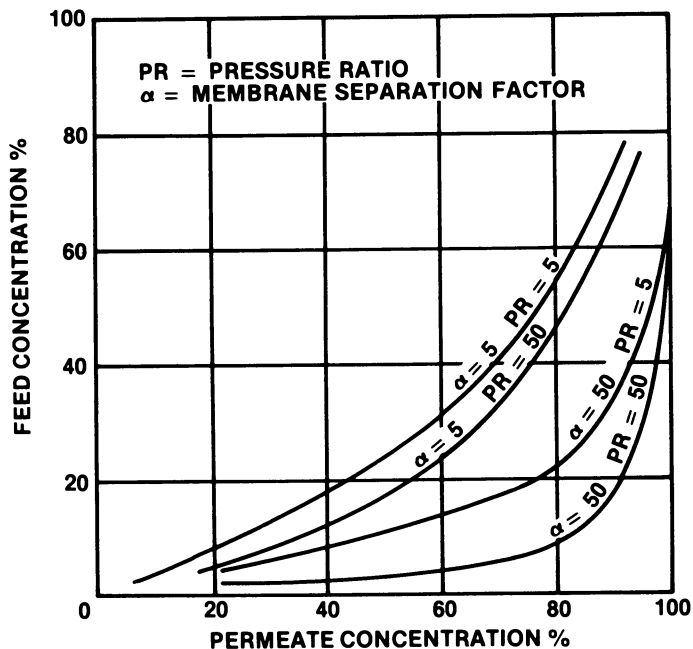


Figure 4. Effect of feed composition on permeate enrichment.

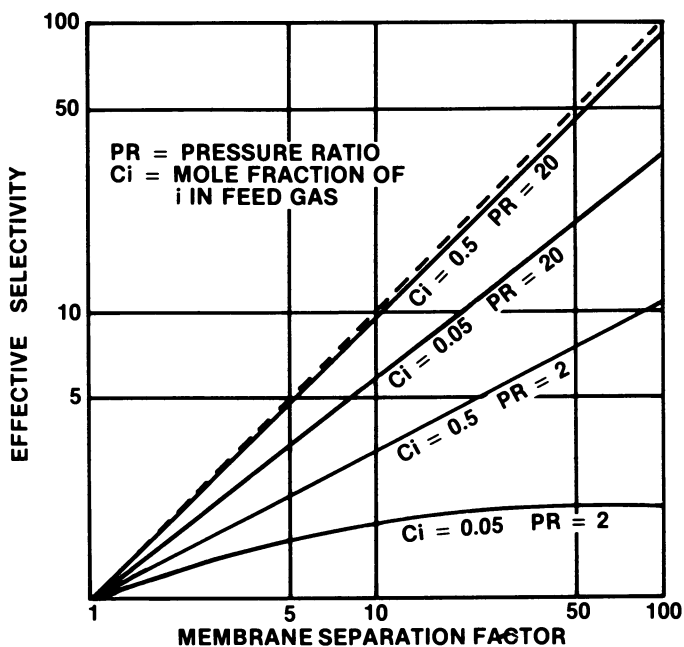


Figure 5. Effect of pressure ratio and membrane separation factor on effective selectivity.

unaffected by the pressure differential as long as the pressure ratio is unchanged.

Other system variables that will have an effect on the separation process are temperature and relative humidity of the gas. Increasing the temperature raises most permeabilities by about 10 to 15% per 10°C and has little effect on separation factors. The effect of relative humidity is variable depending upon the membrane used. High relative humidities, greater than 95%, are generally detrimental due to membrane plasticization. Contamination with liquid water has been found to dramatically reduce membrane performance for cellulose acetate.

The flow dynamics of the permeate stream through the product channel spacer material, or through the fiber bore in the case of hollow fiber systems, may also adversely affect the system performance. If the permeate flow is sufficiently high, a back pressure will be observed in the permeate stream. It can be seen from Figures 4 and 5 that this would result in a lower enrichment due to a lowering of the effective pressure ratio. It has been found that in spiral-wound elements the permeate flow behaves as if it were under laminar conditions. Gas viscosity is therefore the determining factor in comparing the relative back pressure of various gases flowing at the same rates. This effect may be essentially eliminated by proper construction of the membrane element.

Cellulose Acetate Membrane Data

Membranes manufactured by Spectrum Separations, Inc., a subsidiary of SEPAREX CORPORATION, are of the cellulose acetate type. They are similar to those made for reverse osmosis except they must be dried for gas separation use. A proprietary process is used to accomplish this so that the membrane does not collapse and lose its asymmetric character upon removal of the water.

The permeation rates are measured at various pressures for the gases of interest in order to characterize the membranes. Permeation rates for water vapor, helium, hydrogen, hydrogen sulfide and carbon dioxide are the highest with N_2 , CH_4 , CO and C_2H_6 being the lowest. The high rate for H_2O , H_2S and CO_2 is due to the high solubility of these gases in the membrane. Gas permeation and selectivity data for SEPAREXTM spiral-wound elements are shown in Table I. It may be noted that the oxygen/nitrogen selectivity is of an order of magnitude less than the other gas couples, due to the very small difference in molecular size and solubility of O_2 and N_2 . This low separation factor makes oxygen enrichment the most difficult to accomplish, both technically and economically, of the major gas separations of interest. The selectivity and permeation rates achieved in finished elements are somewhat lower than the membrane due to boundary layer problems, permeate back pressure, problems with imperfect seals, defects in the membrane and contaminants found in gas mixture in the field.

Table I

ELEMENT PERFORMANCE

<u>Gas Couple</u>	<u>Separation Factor, α</u>
H ₂ O (Vapor)/CH ₄	200 - 400
H ₂ /CH ₄	45 - 55
CO ₂ /CH ₄	20 - 30
H ₂ S/C ₃ H ₈	75 - 110
He/CH ₄	60 - 85
O ₂ /N ₂	4 - 5

Permeation Rate at 500 psig, SCFH

<u>Gas</u>	<u>4-in. Dia.</u>	<u>8-in. Dia.</u>
He	3,300	14,000
H ₂	2,800	12,000
CO ₂	1,400	6,000
O ₂	200	850

Applications

There are many commercial applications for membrane gas separations, some of which are currently being marketed, and others being tested.

Several field test studies have been undertaken utilizing the SEPAREX process in a 2-in. diameter element size. Due to the modular configuration of membrane systems, a full size system can be directly designed from the test results with a small pilot plant. Although the flow rates for a pilot unit are considerably lower than might be encountered in a full-size system, all process parameters such as product purities, pressure drop, product recoveries, optimum pressure and temperature, membrane area required and series/parallel arrangement of the elements can be directly determined.

Acid Gas Separation from Methane. Removal of hydrogen sulfide (H₂S) and carbon dioxide (CO₂) from natural gas is an ideal application for membranes in that H₂S and CO₂ permeate through the membrane approximately 30 times faster than methane, enabling a high recovery of the acid gases without significant loss of pressure in the methane pipeline product gas (Ref. 5,8). The membrane system would be considered a bulk removal process in this case and has the greatest economic advantage over conventional technology when the acid gas content is over 10%.

The most obvious place for membrane systems in this application is in the retrofitting of existing sour gas processing plants. This would increase the capacity and reduce the energy load of the existing system or eliminate the need for expanding the existing plant when wellhead pressure loss or increased acid gas content occurs.

Another application for membrane systems related to sour gas processing is the recovery of carbon dioxide for use as a miscible flood for enhanced oil recovery (EOR) from depleted oil fields (Ref. 9). It has been found that CO₂ at concentrations above 90% will solubilize oil absorbed in the substrata, allowing for secondary and tertiary recovery. There are many gas wells containing about 40% to 80% CO₂ that could be processed with a membrane system, providing a high purity CO₂ for EOR and a fuel gas by-product. In EOR production, CO₂ injected into the formation eventually appears with light hydrocarbon gases associated with the crude oil. A membrane system can again be used to recover CO₂ for reinjection and recover light hydrocarbons for sale as pipeline gas. For example, a typical associated gas contains 70-85% CO₂ at 100°F and 40 psig (Ref. 10). If such gas is sent through a two-stage SEPAREX process at 300 psig, CO₂ would be recovered in the permeate stream at a concentration of 95% and a recovery of 98%, along with a residual high pressure light hydrocarbon pipeline gas containing 3% or less CO₂.

A CO₂-CH₄ methane process gas stream, similar to a typical high CO₂ natural gas has been under test by SEPAREX for CO₂ removal in a 2-in. diameter element pilot plant since September 1981. The feed gas contains 30% CO₂ and is delivered to the membrane test unit at 250-450 psig under ambient temperature conditions. The objective of the system is to reduce the CO₂ level of the methane to less than 3.5%. The membrane system consists of 5 pressure tubes in series, each tube containing three 40-in. long elements. The gas is conditioned to maintain it at a minimum of 20°F above the dewpoint. The system was operated at a variety of flow rates, pressures, recoveries and temperatures. Selected data are presented in Figures 6 through 8.

A plot of the feed and residual gas flow rates as a function of stage cut is shown in Figure 6. Stage cut is defined as the fraction of feed gas that permeates through the membrane for a given number of elements (single stage). In this case a stage consists of fifteen elements in series. It can be seen that at a feed flow rate of about 180 SCFH all of the gas would permeate the membrane, resulting in no enrichment. This is further demonstrated in Figure 7, where the permeate gas composition at zero residual gas flow is equal to the feed composition.

By combining Figures 6 and 7 it is possible to relate stage cut to the residual and permeate gas stream compositions. These calculations are useful in determining recoveries and in designing series/parallel flow arrangements in large systems. The dashed portions of the curves in the low flow rate region of Figure 7 represents predicted CO₂ compositions under uniform flow conditions, whereas the solid lines represent actual obtained data. The deviation between predicted and actual performance is most likely due to feed gas channeling in the elements or the development of stagnant flow regions as a result of the low pressure difference across the high pressure side (feed to residual) of the elements.

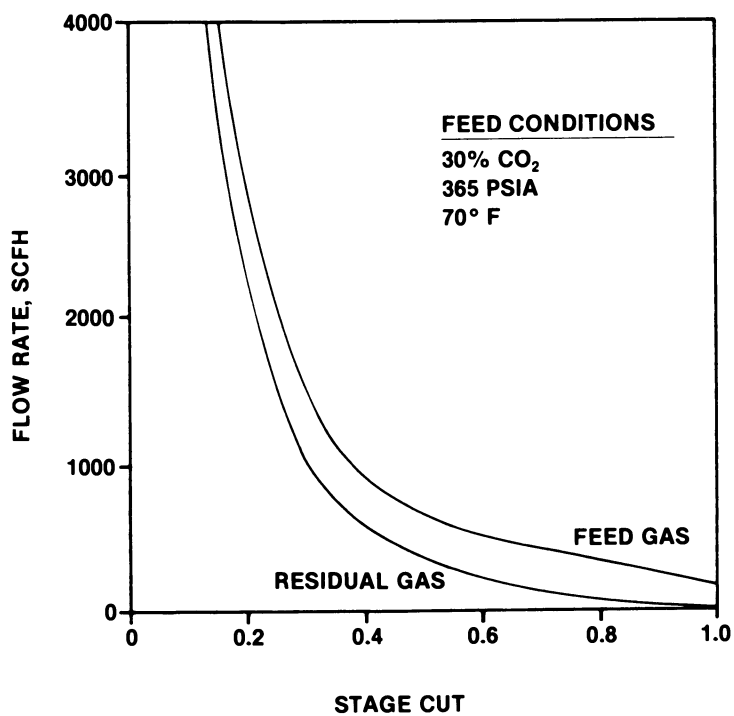


Figure 6. Stage cut as function of flow rate.

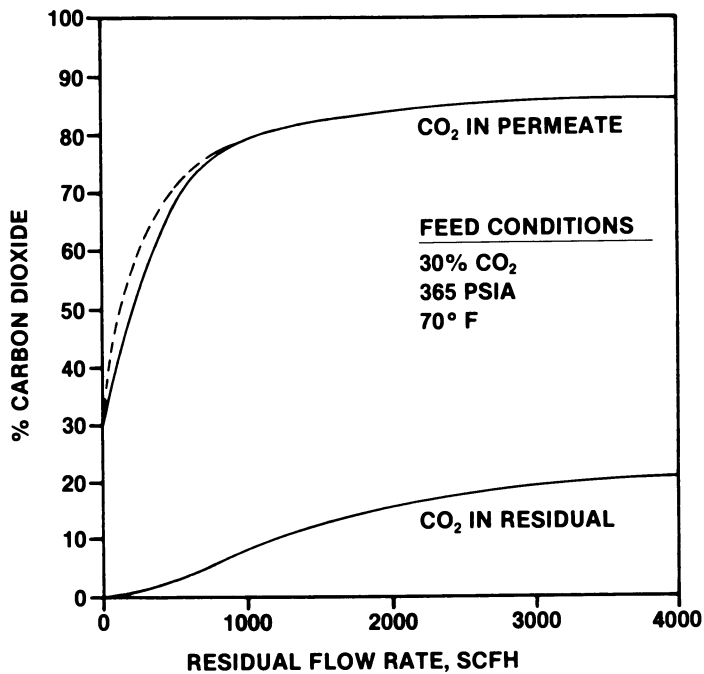


Figure 7. Effect of flow rate on enrichment.

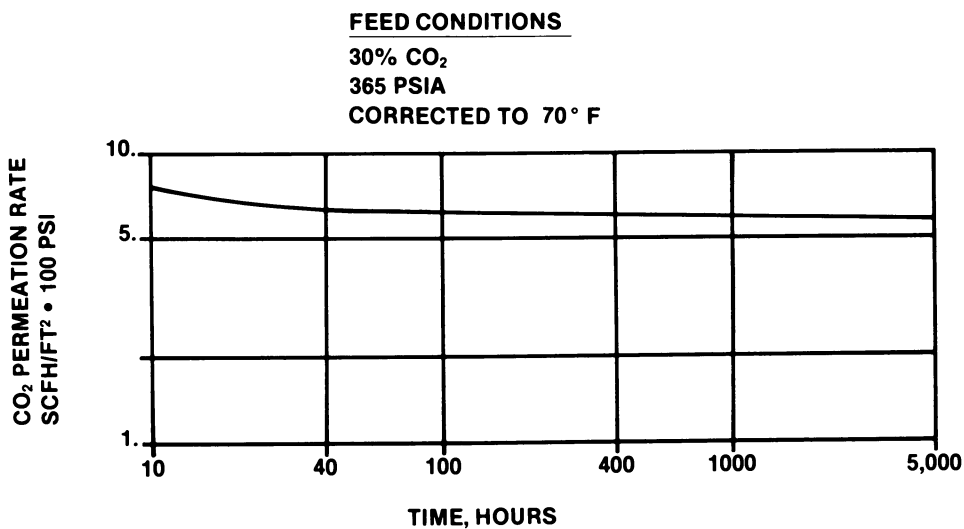


Figure 8. Time-dependent flux decline (log/log).

Under the particular feed conditions and element arrangement for this test, the criteria of less than 3.5% CO₂ in the residual stream could not be reached without experiencing some loss in separation efficiency. This goal could be achieved, however, by operating at higher flow rates with more elements in series. The conclusion arrived at from these data, therefore, is that there is a critical minimum flow rate for given feed gas conditions and element array. In order to maximize system performance this parameter must be taken into consideration when designing a full size system.

Time-dependent flux decline is plotted in Figure 8. The CO₂ permeation rate, in units of SCFH/ft².100 psi, was calculated from performance data for the fifteen elements in series. This rate corresponds to that which would be obtained for pure CO₂ under similar partial pressure differences. After an initial (40 hrs) nonlinear flux decline, the CO₂ rate experienced a 10% loss over the next 1,000 hours (40 days). As this flux decline is a log/log relationship, only 6% more would be lost over the next three years, the minimum expected element lifetime. Membrane systems can be easily designed to adapt to a changing permeation rate by adjusting the feed flow rates and/or pressure, by allowing for addition of more elements in series after a period of time, and by using a progressive element replacement schedule.

Gas Dehydration. It has been found that water vapor permeates cellulose acetate membranes at a rate approximately 500 times that of methane (Ref. 2). This exceptionally high selectivity for water vapor make cellulose acetate membrane systems attractive for dehydration of hydrocarbon gas streams to pipeline specifications on either a pure gas stream or while simultaneously removing contaminating acid gases. For these applications the small size, low weight and low maintenance of the SEPAREX™ system is particularly advantageous for offshore installations.

Liquid water is detrimental to the performance of the membrane, however, so that the feed gas is delivered to the membrane system at less than 90% relative humidity. This can be accomplished by either heating the saturated gas 10-20°F or by dropping the pressure slightly.

The previously described pilot plant test was operated with gases containing water vapor for some period of time during the test program. The feed gas was saturated at 450 psig in a range of temperatures from 80-95°F, corresponding to water contents of 62-100 lbs/MMSCF. The feed gas pressure was dropped from 450 psig prior to entering the membrane unit. Two pressures were studied; 250 psig (57% relative humidity) and 350 psig (78% relative humidity). The membrane unit was operated for 2 months under these conditions with no deterioration of the carbon dioxide permeation rate or change in membrane selectivity. The feed gas under all conditions was dehydrated to a dew point below -55°F (<5 lbs

water/MMSCF), or greater than 97% water removal. The water vapor measuring device used was not suitable below -55°F so that an accurate measurement of the dew point was not obtainable. The measurement was further complicated by the presence of traces of heavy hydrocarbons interfering with the water dew point. It was concluded from this study, however, that Spectrum Separations' cellulose acetate membranes are suitable for dehydration even in the presence of high CO₂ concentrations.

Hydrogen Recovery. Hydrogen is consumed in petroleum refining, in the manufacture of ammonia and methanol, for hydrogenation of fats and oils and in the electronics industry, at an annual rate of approximately 7 million tons (Ref. 11). In many of these processes hydrogen is lost as an off-gas that could be purified and recycled to the point of use. Most of these off-gases are mixtures of hydrogen and carbon monoxide, methane and/or nitrogen and offer an excellent application for membrane systems due to a high hydrogen permeation rate and the high selectivity of hydrogen relative to these gases.

An additional application for membranes might be realized if coal gasification and coal liquefaction processes continue to develop to a commercial level. The membrane system could be utilized to recover hydrogen from the hydrogasifier off-gas and be recycled to the gasifier or sold as a chemical feedstock. In other coal gasification schemes, the product gas could be upgraded or separated into a hydrogen product and a fuel gas product.

SEPAREX delivered a hydrogen recovery system, utilizing 4-in. diameter spiral-wound elements, in early 1982. The system will recover hydrogen from the off-gas of a unit utilizing UOP's Butamer^R process in a LPG processing complex.

In UOP's Butamer process normal butane is catalytically isomerized to produce high-purity iso-butane. N-butane is charged into a fixed-bed vapor phase reactor and hydrogen is added with small amounts of an organic chloride compound. The unit yields iso-butane and a hydrogen stream contaminated with hydrocarbons and traces of HCl. The hydrogen stream is fractionated, leaving an off-gas containing about 70% hydrogen. This gas, which normally is sent to fuel, is processed with the SEPAREX membrane system to recover the hydrogen for recycle to feed make-up. A simplified process schematic is shown in Figure 9.

The SEPAREX system will recover over 90% of the hydrogen at a purity of 96+% for recycle, while increasing the heating value of the fuel gas from ~550 BTU/SCF to ~950 BTU/SCF. The projected flow rates and gas purities for the membrane separation are shown in Table II. Under the bone-dry feed conditions the cellulose acetate membrane is not affected by HCl. Special materials of construction and adhesives have been used in the fabrication of the spiral-wound elements to ensure their resistance to HCl in the gas streams.

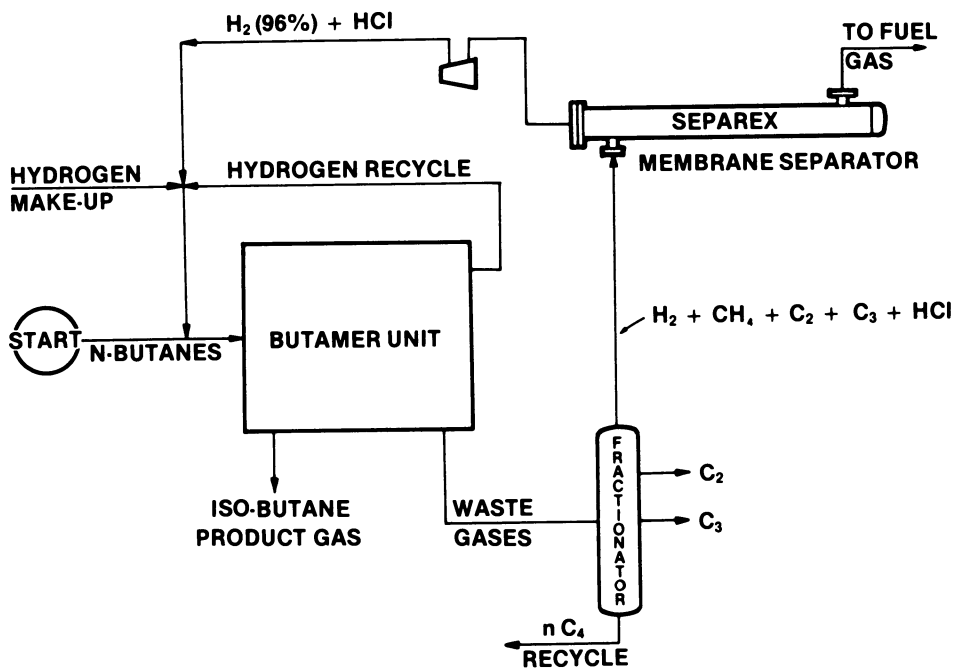


Figure 9. Hydrogen recovery schematic.

Table II

HYDROGEN RECOVERY FROM
A UOP'S BUTAMER^R PROCESS

	<u>Feed Gas</u>	<u>Residual Gas</u>	<u>Permeate Gas</u>
Pressure, psia	265	240	15
Flow Rate, MSCFH	47.8	16.8	31.0
Temperature, °F	110	100	100
Mol% H ₂	68.9	17.8	96.4
Mol% CH ₄	23.7	63.0	2.6
Mol% C ₂ ⁺	6.8	19.0	0.2
Mol% HCl	0.6	0.2	0.8

Oxygen Enrichment of Air. The U.S. produces approximately 15 million tons of oxygen from air each year (Ref. 12). Most of this production is accomplished cryogenically, and in large plants the cost is very low. Uses of oxygen in quantities of less than 10 tons per day, however, constitute a substantial share of this market. It is thought that membrane systems could economically enrich air at these smaller plant sizes.

One area of particular interest is in secondary sewage treatment utilizing oxygen instead of air (Ref. 13). There are approximately 5,000 air-treatment sewage plants in this country that each consume 5 tons of atmospheric oxygen per day. Many of these plants suffer seasonal overloads (for example in farming communities) and many others are reaching capacity and will require new construction for expansion. The use of enriched oxygen in place of air could increase the capacity of these existing plants without the addition of space-consuming conventional treatment processes.

Five major U.S. chemical firms are now producing oxygenation systems for sewage wastewater treatment, in what the industry feels could become oxygen's largest market (Ref. 12). Membrane systems could economically compete with conventional technologies in the smaller plants.

Literature Cited

1. Mitchell, J. V. J. Roy. Inst. 1831, 2, 101, 307.
2. Weller, S.; Steiner, W. A. J. Appl. Physics 1950, 21, 279.
3. Weller, S.; Steiner, W. A. Chem. Eng. Prog. 1950, 46, (11), 585.
4. Gantzel, P. K.; Merten, U. Ind. Eng. Chem. 1970, 9, (2), 331.
5. Schell, W. J.; Lawrence, R. W.; King, W. M. Membrane Applications to Coal Conversion Processes, Final Report to the Energy Research and Development Administration, Report No. FE-2000-4, 1976.
6. Reid, C. E.; Breton, E. J. J. Appl. Poly. Sci. 1959, 1, 133.
7. Gardner, R. J.; Crane, R. A.; Hannon, J. F. Chem. Eng. Prog. October 1977, 76.
8. Cooley, T. E.; Coady, A. B. U. S. Patent 4,130,403 1978.

9. Goddin, C. S. Comparison of Processes Treating Gases with High CO₂ Content, presented at the 61st Annual GPA Convention, March 1982.
10. Meissner, R. E. Hydrocarbon Processing, April 1980, 113.
11. Kelley, J. H.; Escher, W. J. D.; vanDeelen, W. Chem. Eng. Prog. January 1982, 58.
12. Fallwell, W. F. Chem. & Eng. News, July 15, 1974, 7.
13. Gross, R. W. Chem. Eng. Prog. October 1976, 51.

RECEIVED January 12, 1983

Gas-Adsorption Processes: State of the Art

GEORGE E. KELLER, II

Union Carbide Corporation, Ethylene Oxide and Glycol Division,
Technical Center, South Charleston, WV 25303

Gas-adsorption processes are used for a wide variety of separations throughout the chemical and other industries. But to effect various separations, quite different process embodiments are necessary. These differences are primarily concerned with the method by which the adsorbent is regenerated. This choice is influenced by the percentage of adsorbate in the feed, ease of desorption and degree of separation required. In this paper, we discuss temperature-swing, inert-purge, displacement-purge, pressure-swing, parametric-pumping, chromatographic and other cycles; the separations for which they are best suited; and their limitations. Commercial examples are given. Finally, predictions are made as to future improvements in various technologies as well as to what new separations will be amenable to adsorption separation.

Gas-adsorption processes involve the selective concentration (adsorption) of one or more components (adsorbates) of a gas (or vapor) at the surface of a microporous solid (adsorbent). The attractive forces causing the adsorption are generally weaker than those of chemical bonds and are such that, by increasing the temperature of the adsorbent or reducing an adsorbate's partial pressure, the adsorbate can be desorbed. The desorption step is quite important in the overall process. First, desorption allows recovery of adsorbates in those separations where they are valuable, and second, it permits reuse of the adsorbent for further cycles.

This paper is concerned with a broad range of gas-adsorption processes as practiced in the organic-chemical, petroleum, natural-gas and allied industries. Emphasis will be on a description of processes rather than a review of adsorber design

0097-6156/83/0223-0145\$07.25/0
© 1983 American Chemical Society

procedures, which have been covered in other publications (1-6), or a discussion of traditional adsorbents, which have also been covered elsewhere (7-15). The objectives of this paper are (i) to review those situations in which adsorption can be an economically viable process, (ii) to provide a description of present-day adsorption technology, and (iii) to indicate the likely directions that new adsorption technology and uses will take.

Criteria for When to Use Gas Adsorption

Distillation and related vapor-liquid processes are by far the most common means of separating homogeneous mixtures in the industries mentioned above. The reasons for this are the basic process simplicity and scalability of distillation (which helps promote low investment per annual unit of feed) and the ability to achieve many theoretical stages (which effects high degrees of separation) in many systems. On the other hand, distillation is fundamentally a high-energy-usage process. In most distillations the energy usage is at least one and frequently two orders of magnitude greater than the minimum thermodynamic work of separation.

We can use the following as rough criteria to decide whether gas adsorption might be a viable alternative for distillation for a given separation.

1. The relative volatility between the key components to be separated is in the order of 1.2 to 1.5 or less.
2. The bulk of the feed is a relatively low-value, more-volatile product, and the product of interest is in relatively low concentration (about 10 weight percent or less). In such situations large reflux ratios can be required, resulting in high energy costs.
3. One set of components whose boiling range overlaps that of a second set of chemically or geometrically dissimilar components must be separated from the second set. To make such a separation, even though various relative volatilities may be reasonably large, several distillation columns would be required.
4. Separation by distillation requires cryogenic operation or pressures above about 20 atmospheres.

Gas adsorption should be considered for a given separation when one or more of the above criteria apply to distillation and when a suitable adsorbent exists. In general a suitable adsorbent is one which shows adequate selectivity (greater than two for the key components) and capacity, can be regenerated easily and causes no damage to the products by promoting byproduct-forming reactions. It is also usually desirable that the adsorbent selectively adsorb the component(s) in lower concentrations in the feed to minimize the amount of adsorbent required per unit of feed processed.

Separations and Processes

Commercial gas-adsorption processes (see Table I) can be divided into bulk separations, in which about 10 weight percent or more of a stream must be adsorbed, and purifications, in which usually considerably less than 10 weight percent of a stream must be adsorbed. Such a differentiation is desirable to make because in general different process cycles are used for the different categories, as will be discussed later. Below, four basic process cycles and two combinations are described in their simplest forms. In other sections, recent uses and modifications of these cycles, as well as other new process cycles, are described.

Temperature-Swing Cycle. In this cycle, a stream containing a small amount of an adsorbate is passed through the adsorbent bed at a relatively low temperature. After equilibrium between adsorbate in the feed and on the adsorbent is reached, the bed temperature is raised to a higher value, and more feed is passed through the bed. Desorption occurs and a new, lower equilibrium loading is established. The net bed removal capacity, called the delta loading, is the difference between these two loadings. (This value is actually an upper limit, since equilibrium loadings in practical operation are not attained.) When the bed is subsequently cooled and feed is again passed through the bed, purification will occur down to a concentration in equilibrium with the residual loading on the adsorbent.

The time required to heat, desorb and cool a bed is usually in the range of a few hours to over a day. Because during this long regeneration time the bed is not productively separating, temperature-swing processes are used almost exclusively to remove small concentrations of adsorbates from feeds. Only in such situations can the on-stream time be a significant fraction of the total cycle time of the process.

Inert-Purge Cycle. In this cycle, the adsorbate, instead of being removed by temperature increase, is removed by passing a non-adsorbing gas containing no adsorbate through the bed. This has the effect of lowering the partial pressure of the adsorbate around the particles, and desorption occurs. If enough purge gas is passed through the bed, the adsorbate will be completely removed, and the maximum delta loading will equal the equilibrium loading. As in the temperature-swing cycle and all others, actual delta loadings will be less than the equilibrium delta loading. During the subsequent adsorption step, removal of adsorbate from the feed would be essentially complete until the adsorbent becomes nearly fully loaded and breakthrough occurs.

**American Chemical
Society Library**

1455 16th St. N. W.

In Industrial Gas Separations: Whyte, T. et al.;
ACS Symposium Series; American Chemical Society: Washington, DC, 1983.

TABLE I
 REPRESENTATIVE COMMERCIAL GAS-ADSORPTION SEPARATIONS

Separation*	Adsorbent
I. Gas Bulk Separations	
Normal Paraffins/Isoparaffins, Aromatics	Zeolite
N ₂ /O ₂	Zeolite
O ₂ /N ₂	Carbon Molecular Sieve
CO, CH ₄ , CO ₂ , N ₂ , A, NH ₃ /H ₂	Zeolite, Activated C
Acetone/Vent Streams	Activated C
C ₂ H ₄ /Vent Streams	Activated C
Separation of Perfume Components	---
II. Gas Purification	
H ₂ O/Olefin-Containing Cracked Gas, Natural Gas, Air, Synthesis Gas, Etc.	Silica, Alumina, Zeolite
CO ₂ /C ₂ H ₄ , Natural Gas, Etc.	Zeolite
Organics/Vent Streams	Activated C, Others
Sulfur Compounds/Natural Gas, Hydrogen, Liquified Petroleum Gas (LPG), Etc.	Zeolite
Solvents/Air	Activated C
Odors/Air	Activated C
NO _x /N ₂	Zeolite
SO ₂ /Vent Streams	Zeolite
Hg/Chlor-Alkali Cell Gas Effluent	Zeolite

*Adsorbates are listed first.

Displacement-Purge Cycle. This cycle, which is somewhat similar to the previous one, differs from it in that a gas or vapor which adsorbs about as strongly as the adsorbate is used to remove the adsorbate (see Figure 1). Removal is thus facilitated both by adsorbate partial-pressure reduction in the fluid around the particles and by competitive adsorption of the displacement medium. As with the inert-purge cycle, the maximum delta loading is the equilibrium loading.

The use of the two different types of purge fluids causes two major differences in the processes. First, since the displacement-purge fluid is actually adsorbed, it is present when the adsorption part of the cycle begins and therefore contaminates the less-adsorbed product. (In the inert-purge cycle this contamination is usually much smaller.) In practical terms this means that the displacement-purge fluid must be recovered from both product streams. Second, since the heat of adsorption of the displacement-purge fluid is approximately equal to that of the adsorbate, as the two exchange on the adsorbent, the heat generated (or consumed) is virtually zero, and the adsorbent's temperature remains unchanged. When an inert-purge gas is used, a temperature rise occurs in the region where adsorption occurs, and this temperature rise can severely limit the adsorption capacity of the bed in some cases.

Pressure-Swing Cycle. In a gas-adsorption cycle, the partial pressure of an adsorbate can be reduced by reducing the total pressure of the gas. This change can be used to effect a desorption. The lower the total pressure of the desorbing step, the greater the maximum delta loading will be.

The time required to load, depressurize, desorb and repressurize a bed is usually a few minutes and can in some cases be only a few seconds. Thus, even though practical delta loadings are substantially less than the maximum delta loadings to minimize thermal-gradient problems, the very short cycle times make a pressure-swing cycle quite attractive for bulk-gas separations.

Combined Cycles. Often a temperature-swing cycle is combined with an inert-purge to further facilitate desorption. Several possibilities are shown in Figure 2. The inert-purge stream can be a fraction of the less-adsorbed product, or a separate purge stream can be used. If the feed is at super-atmospheric pressure, many times the desorption step will be carried out at atmospheric pressure.

In pressure-swing processes, it is quite common to use a fraction of the less-adsorbed gas product as a low-pressure purge gas, as shown in Figure 2. Often the purge flow is in the opposite direction from the feed flow. Rules for the minimum fraction of less-adsorbed gas product for displacing

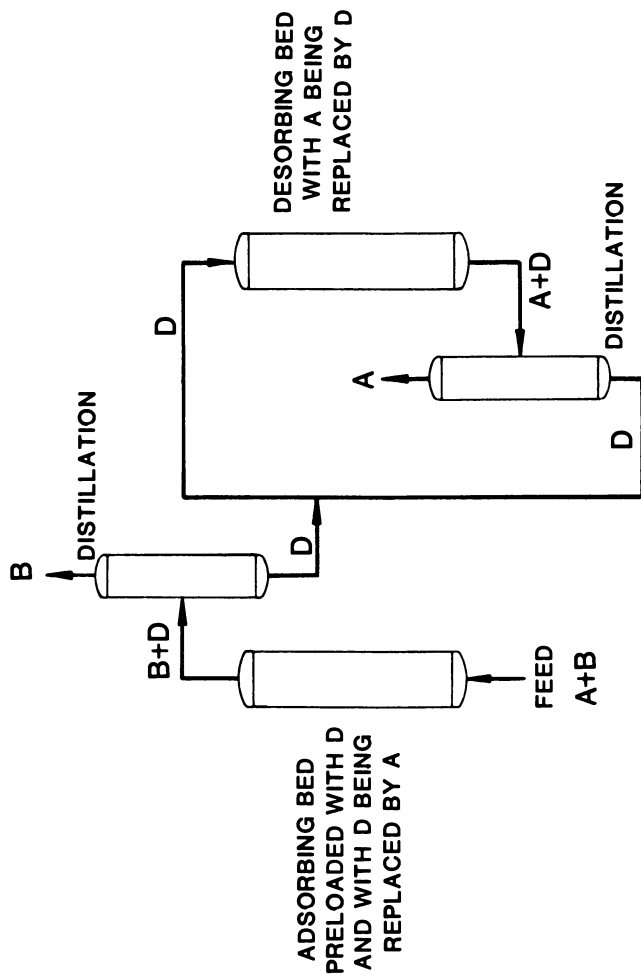


Figure 1. Displacement-purge cycle. A, adsorbate; B, less-adsorbed component; and D, displacement agent.

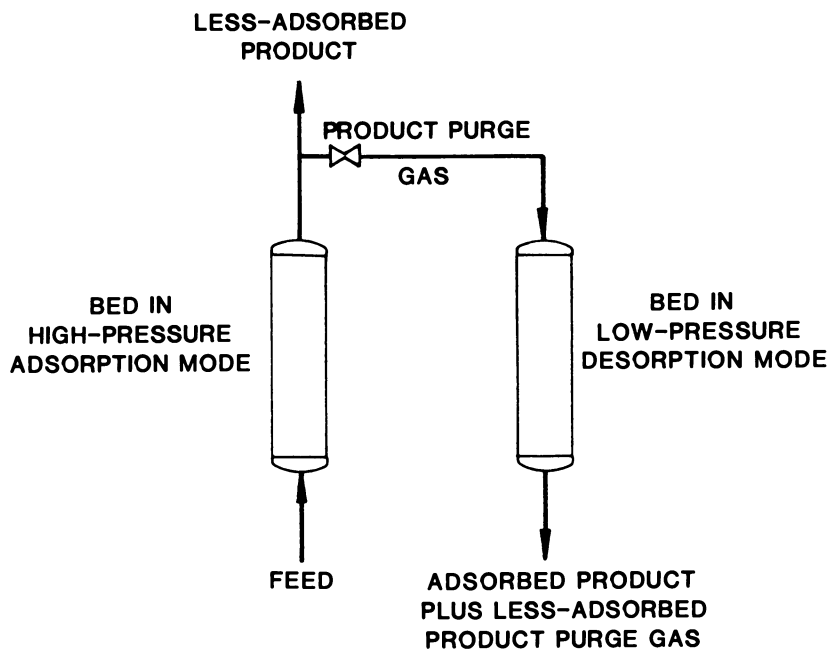


Figure 2. Combined pressure-swing, non-adsorbed-product-purge cycle (pressure-swing adsorption).

the adsorbate have been given by Skarstrom (16). This process has been called heatless fractionation or, more commonly, pressure-swing adsorption (PSA). The latter name will be used in this paper.

Gas Bulk-Separation Processes

Gas bulk-separation processes consist mostly of pressure-swing adsorption (PSA) variations and displacement-purge and inert-purge processes. Recently, however, a chromatographic cycle has been commercialized. Below, these cycles will be discussed.

PSA. As mentioned earlier, PSA processes use a fraction of the less-adsorbed product to aid in purging the adsorbate from the adsorbent. Thus an inevitable feature of present-day PSA processes is the loss of part of the less-adsorbed product to the purge stream. This has the additional implication that the purge stream cannot be of high purity, and as a result PSA is limited at present to those applications where only one pure product is desired: oxygen and nitrogen (but not both simultaneously) from air, hydrogen recovery in cases in which complete recovery is not required, and chemical process purge-stream treatment in which the less-adsorbed product is removed from the process and the adsorbate-enriched stream is recycled to the process.

Most often, PSA processes use three or more beds in parallel. The advantages are (i) energy savings, which accrue from using gas from a high-pressure bed to partially repressurize a low-pressure bed following desorption, and (ii) higher product recoveries, which accrue from using a combination of purging steps in the cycle.

Recently two widely divergent process variations of PSA have been commercialized by Union Carbide Corporation. The first of these is called POLYBED PSA, which is used for hydrogen recovery (17-21). Plants with capacities of up to about 1.2×10^6 NM³/day of hydrogen have been built. Hydrogen recoveries of 86 percent vs 70-75 percent for other PSA processes have been demonstrated, as well as purities of 99.999 mole percent (20). POLYBED PSA involves the use of five or more beds, with extensive gas interchanges and pressure equalizations between the beds. One process embodiment (17) is shown in Figure 3.

Thus POLYBED PSA can be thought of as a process which aims for maximum recovery of the less-adsorbed component in very high purity at the expense of a complex flowsheet. Its growing commercial acceptance suggests that it competes quite successfully with cryogenic separation in many cases.

The second process, called pressure-swing parametric pumping (PSPP), was developed to minimize process complexity

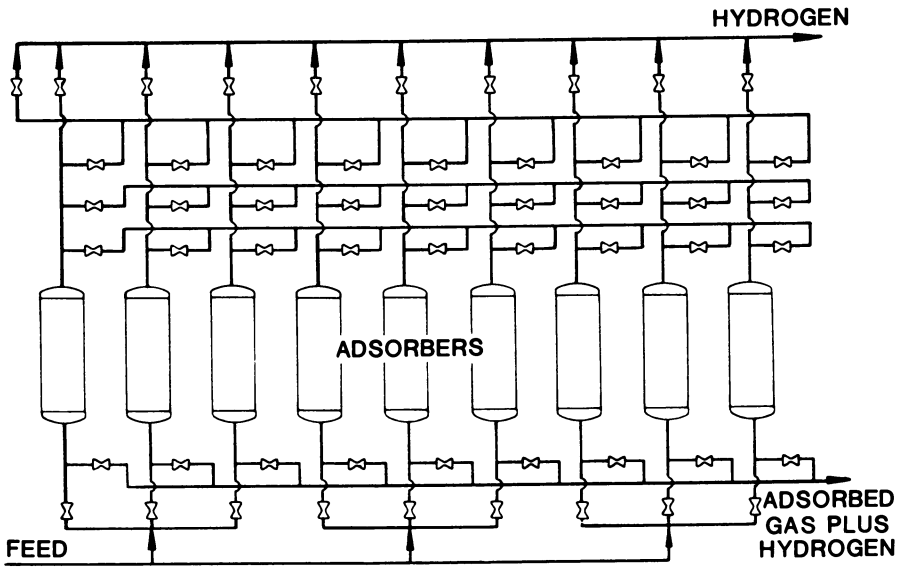


Figure 3. Polybed PSA process.

and investment at the expense of product recovery. The name parametric pumping was coined by Wilhelm (22), who described an adsorption-based separation process involving reversing flows. When the flow is in one direction a parameter, such as temperature, which influences adsorptivity, is at one value, while the parameter is changed to another value when the flow is in the opposite direction. Such a process will create a separation between components with different adsorptivities. Chen (23) has correctly pointed out that PSA processes constitute a subset of parametric pumping, in which pressure is the parameter used to influence adsorptivity.

Because of its highly unusual nature, PSPP will be described in some detail. PSPP exists in both single-bed (24-26) and multiple-bed (27) embodiments. Schematic diagrams of both are shown in Figure 4. The single-bed process will be described first. The bed can vary from about 0.3 to 1.3 or more meters in length and contains adsorbent particles with diameters in the range of 177 to 420 μm . Feed gas under pressure is supplied in pulses of up to about a second in length from a compressor and a surge tank. The pulse is controlled by a solenoid valve and a timer. During this feed pulse the exhaust solenoid valve is closed. Following the feed pulse both valves at the feed end are closed for about 0.5 to three seconds; this period is called the delay. Next the solenoid valve on the exhaust or purge line opens for a period of about five to twenty seconds. Since the pressure in this line is maintained below that in the feed line, reverse flow of gas from the bed occurs. And finally another delay period with both solenoid valves closed is used in some cases. Its length is generally less than one second.

However, while pressures and flow directions are fluctuating substantially at the feed end of the bed, a continuous flow emerges from the product end and through a small surge tank. This flow is enriched in less-adsorbed components; in the case of air separation, the product consists typically of 90 to 95 percent oxygen, with the balance argon and a small amount of nitrogen. Conversely the exhaust stream is somewhat depleted in oxygen and argon.

The net effect of this process is to produce, using a single adsorbing bed and two surge tanks, a constant flow of less-adsorbed product - primarily oxygen in this case - from a constant flow of air from a compressor.

The multiple-bed process uses essentially the same range of bed lengths and adsorbent particle sizes. The time cycles of the three beds can be sequenced in such a way that compressed feed is always flowing to the process. This reduces the size of the feed surge tank or completely eliminates the need for it. In general the fraction of the overall cycle devoted to the feed pulse in the multiple-bed process is much greater - about

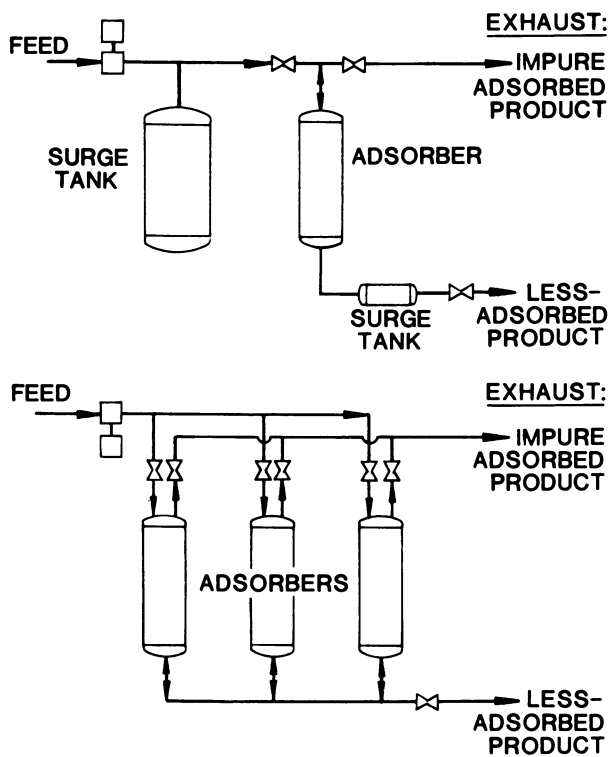


Figure 4. One-bed and three-bed pressure-swing parametric pumps.

one-third - than the fraction in the single-bed process - in the order of one-tenth. The multiple-bed process usually produces somewhat higher less-adsorbed product pressures and slightly higher less-adsorbed product recoveries compared to the single-bed process.

The most unusual feature of PSPP is the continuously changing axial pressure profile. Whereas all other processes operate with virtually a constant pressure through the bed at any given time, the fast cycle of PSPP and the flow resistance caused by the use of very small adsorbent particles create substantial pressure drops in the bed, as shown in Figure 5. These pressure profiles are highly critical to the performance of the process. For example, the unusual profile during the exhaust part of the cycle, which shows a maximum pressure somewhere inside the bed, simultaneously permits purging of part of the bed while less-adsorbed products are continually produced at the opposite end of the bed.

PSPP has been commercialized for the production of oxygen and for the recovery and recycle of ethylene and a small amount of chlorocarbons (the adsorbed stream) to an ethylene-chlorination process while purging nitrogen (the less-adsorbed component) from the process.

As mentioned before, POLYBED PSA and PSPP represent quite different approaches to improving the basic PSA process. Table II shows the pluses and minuses of these approaches compared to a basic PSA process.

A new PSA process has been developed by Bergbau Forschung GmbH for the production of nitrogen from air (28,29). The process uses a unique carbon-based molecular sieve as the adsorbent. The adsorbent's micro-geometry is such that, even though the adsorption isotherms of oxygen and nitrogen are almost identical, oxygen diffuses many times more rapidly into the pores. This creates an oxygen-depleted gas phase until both gases equilibrate, which requires over an hour. By operating the process with a time cycle considerably less than the equilibrium time, the adsorbent becomes oxygen-selective and produces a high-nitrogen product. Nitrogen purities of up to 99.9 percent can be produced. The process, depicted in Figure 6, uses a vacuum desorption step to facilitate production of high-purity nitrogen.

Nitrogen production using carbon molecular sieves is the only known commercial process using differences in intraparticle diffusivity, rather than inherent adsorbent selectivity or selective molecular exclusion, as the basis for the separation.

Another method of using PSA to obtain nitrogen from air has recently been revealed by Toray Industries, Inc. (30). The standard PSA process has been modified to produce an impure (33 percent oxygen) less-adsorbed gas and a relatively pure (up to 99.9 percent) purge stream of nitrogen. A diagram is shown

TABLE II
COMPARISON OF THE PERFORMANCES OF POLYBED PSA
AND PRESSURE-SWING PARAMETRIC PUMPING
WITH BASIC PSA

	<u>Polybed PSA</u>	<u>Pressure-Swing Parametric Pumping</u>
Compression Cost	Less	Same or Greater
Productivity	About the Same	Much Greater
Degree of Separation	Greater	Same or Less
Process Complexity	Greater	Less
Adaptability to Large Flows	Greater	Less
Cycle Time	About the Same (Several Minutes)	Much Less (Several Seconds)
Non-Adsorbed Product Pressure	Same	Lower

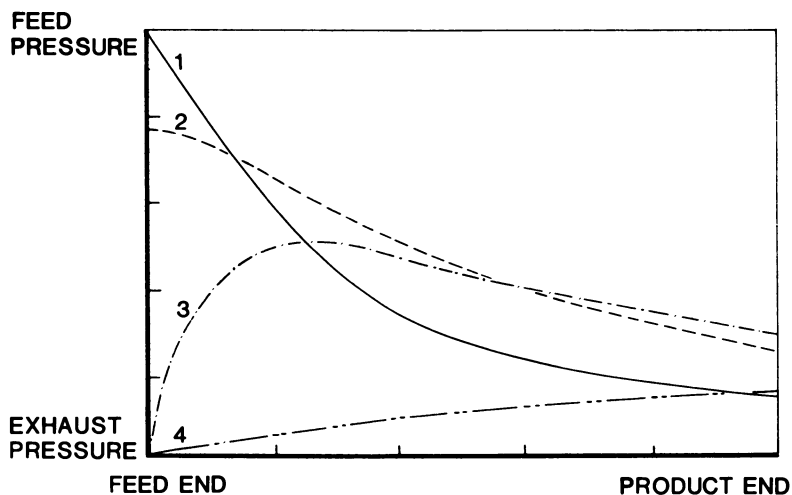


Figure 5. Pressure profiles in an adsorbent bed producing 90 mole percent oxygen. 1, middle of feed; 2, middle of delay; 3, early in exhaust; and 4, late in exhaust.

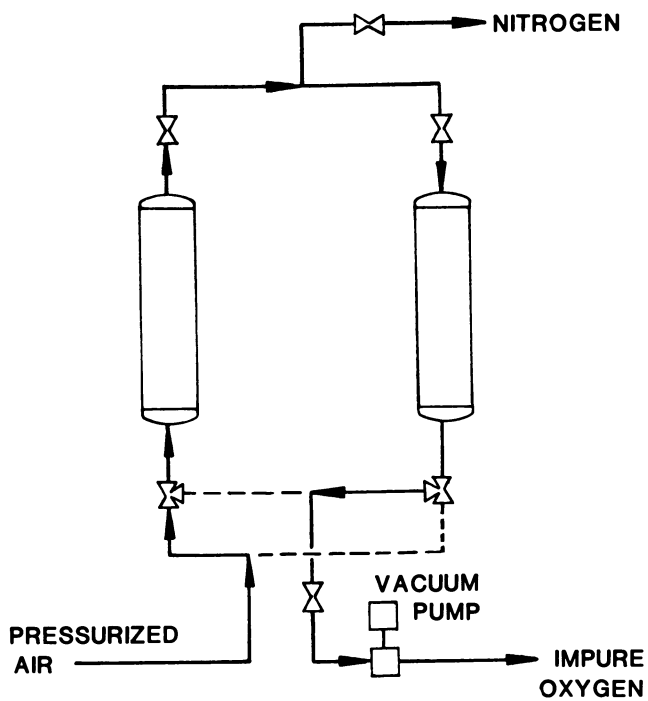


Figure 6. Bergbau Forschung nitrogen-production process.

in Figure 7. Dried air is passed through the adsorber at super-atmospheric pressure; nitrogen is preferentially adsorbed. Part of the nitrogen product from previous cycles is then passed into the bed to desorb small amounts of oxygen, after which the bed is reduced to atmospheric pressure to desorb nitrogen. Finally more nitrogen is recovered by vacuum desorption. The adsorbent used in this process is apparently the same - zeolite molecular sieves - as that used in oxygen PSA processes.

This process has been demonstrated in pilot-scale. Its commercial status is unknown.

Displacement-Purge and Inert-Purge Cycles. By far the most widespread embodiment of these cycles is the separation of normal and iso-paraffins in a variety of petroleum fractions. These fractions in general contain several carbon numbers and can include molecules from about C₅ to about C₁₈. All of these separations use 5A molecular sieve as the adsorbent. Its 0.5 nm pore diameter is such that normal paraffins can enter but iso-paraffins are excluded; this constitutes the basis for separation.

A recent review (13) lists six different commercial vapor-phase processes. These processes use either displacement-purge or inert-purge cycles. The former are used when higher-molecular-weight fractions are being processed. In such cases, the adsorbates are held so tightly by the adsorbent that the use of an adsorbing displacement agent is necessary to effect desorption. In turn, however, two distillation columns are required to recover the displacement fluid from the product streams. When lower-molecular-weight fractions are being processed, the simpler inert-purge cycles suffice. With these cycles, coolers followed by vapor-liquid separators can be used to recover products from the purge gas.

The normal/iso-paraffin separation process used most often is Union Carbide's IsoSiv process. IsoSiv units with feed capacities up to 3600 metric tons per day have been built. In the mid-1970s IsoSiv was combined with the Hysomer paraffin-isomerization process developed by Shell Research B.V. (31,32); this combination is called the Total Isomerization Process (TIP) and can produce a completely iso-paraffin product from a normal or mixed paraffin feed. A schematic diagram is shown in Figure 8. Hydrogen, which is required in the isomerization step, also serves as the purge gas for desorbing the normal paraffins, which are recycled to the Hysomer unit. The process is carried out in the vapor phase, and utility requirements are considerably below those of distillation (32). Product from a TIP unit has a Research Octane Number of 88 to 92, compared to a RON of 79 to 82 for the product from a Hysomer unit alone.

The close-coupling of reaction and separation units for driving equilibrium reactions to complete conversion, though

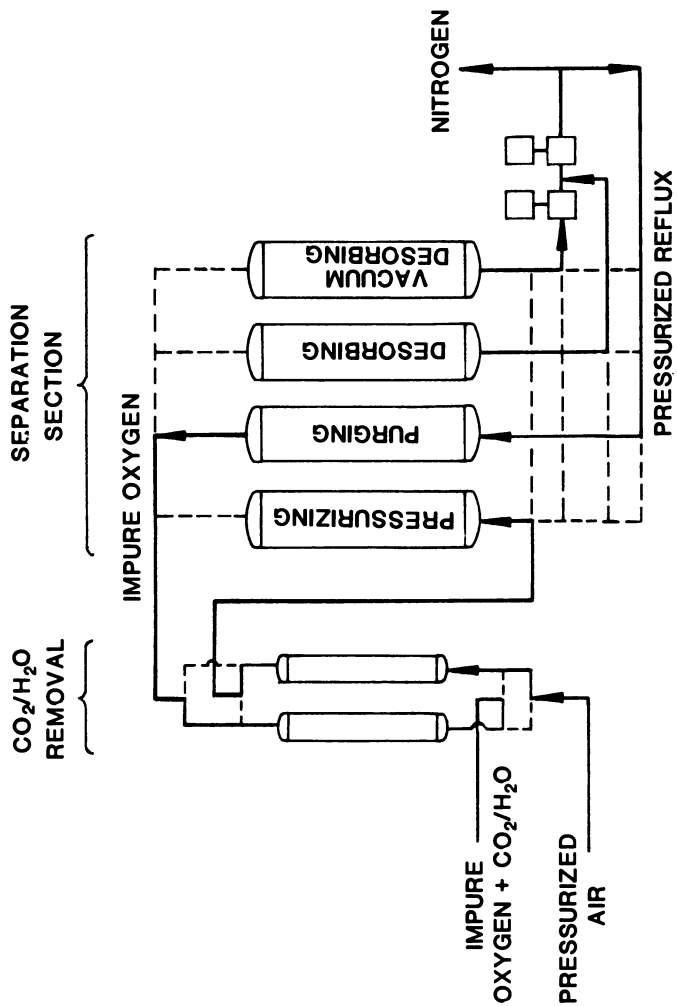


Figure 7. Toray reverse PSA nitrogen-production process.

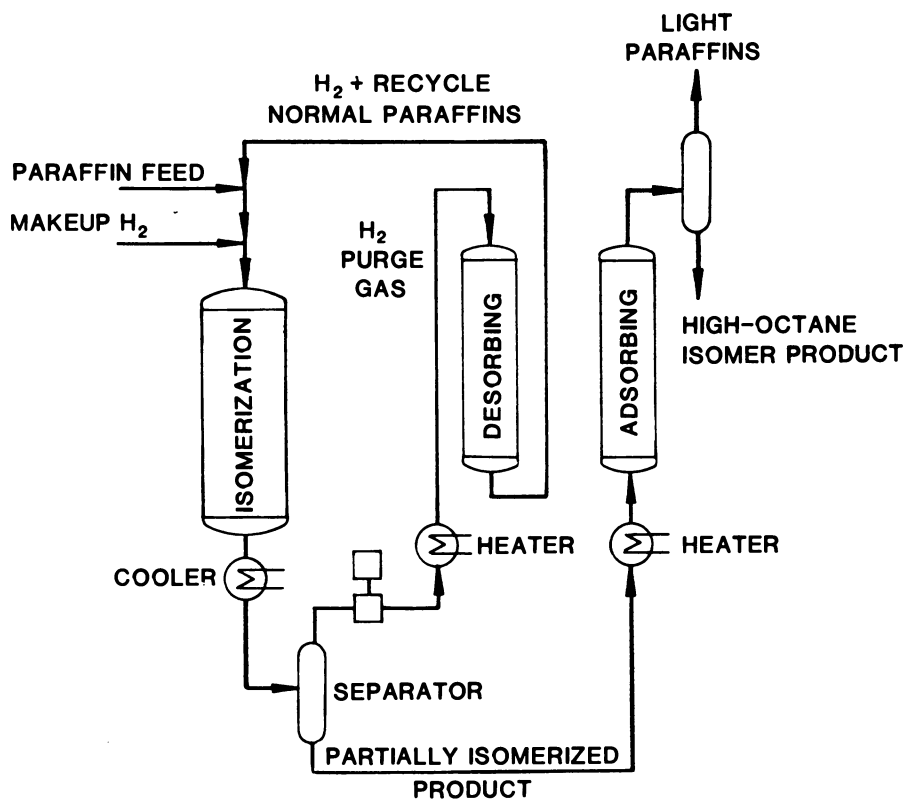


Figure 8. Total isomerization process.

not new, is probably an underutilized concept. Adsorption, which can sometimes separate materials easily which distillation can separate only with difficulty, represents an extra degree of freedom in conceiving of such processes.

Another isomer-separation process which has been announced is called OlefinSiv (13). This process separates iso-butene from normal butenes in a manner similar to IsoSiv.

Chromatography. The laboratory analytical technique of gas chromatography has been an appealing model for a commercial separation process for many years. In spite of numerous attempts at scale-up, only recently has this effort apparently been successful. The Societe Nationale Elf Aquitaine and Societe de Recherches Techniques et Industrielles (SRTI) have announced a process for separating mixtures difficult to separate by distillation (33-35). Hydrogen is used as the carrier gas. The Elf-SRTI process is presently commercially separating 100 metric tons per year of perfume ingredients. More recently Elf Aquitaine has announced a 100,000 metric tons per year demonstration unit for separating C₄-C₁₀ normal and iso-paraffins (35). A schematic diagram is shown in Figure 9. This process uses several beds in parallel to produce a constant flow of products.

As mentioned earlier, the use of a non-condensable, non-adsorbing carrier gas simplifies the task of recovery of products compared to that task in displacement-purge adsorption. At the same time, the scale-up of this process means that the effects of separation-inhibiting thermal gradients accompanying adsorption and desorption have been dealt with successfully.

Gas-Purification Processes

Compared to adsorption's use in bulk-gas separations, its use in gas purifications is much more frequent (see Table I and references 13, 36 and 37), and the technology is, for the most part, more conventional. Temperature-swing adsorption, often combined with inert-purge stripping, is by far the most common process used. Two or more fixed beds operated in parallel, typically with one adsorbing and one or more regenerating, constitute the standard flowsheet.

Temperature-swing cycles are inherently energy-intensive per unit of material adsorbed; regeneration energy usage is usually several times the heat of condensation of the adsorbate. However, if the amount of adsorbate per unit of feed is small, the regeneration energy usage per unit of feed can reduce to a reasonable value. A second advantage is that a combined temperature-swing/inert-purge cycle can provide very high degrees of desorption during regeneration, leading to very high degrees of adsorbate removal from the feed. Removals down to

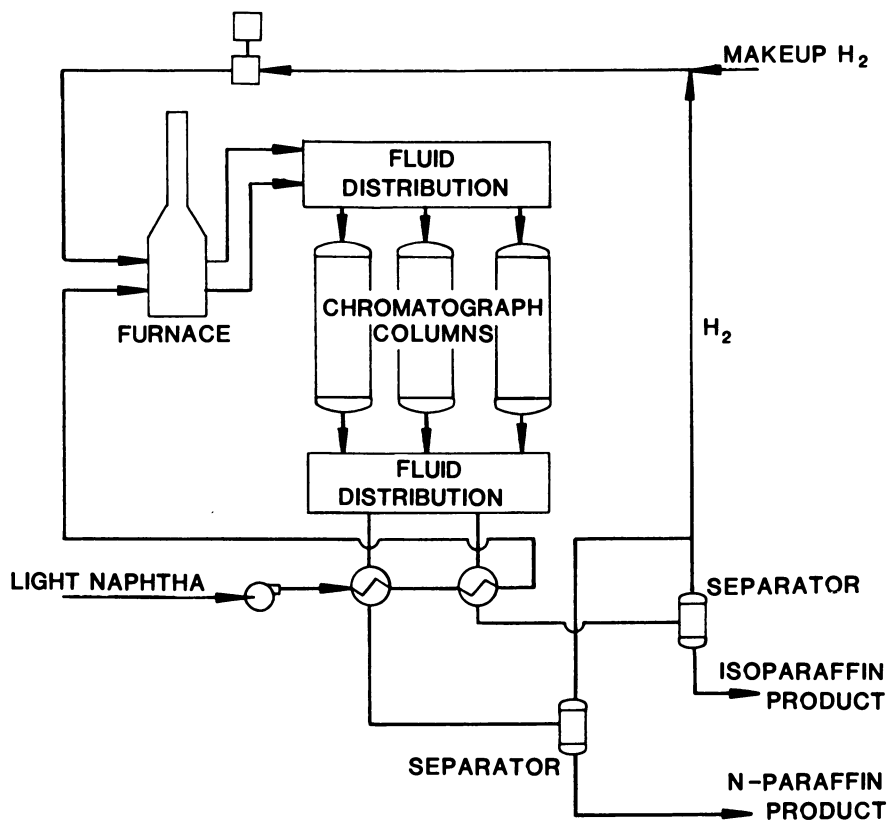


Figure 9. Elf Aquitaine chromatographic separator.

one volume part per million or less of adsorbate in the less-adsorbed product are not uncommon.

The development of a very hard, microspherical activated carbon called bead activated carbon (BAC), by Kureha Chemical Co., Ltd. of Japan has made possible the commercialization of a new fluidized-bed/moving-bed process (38). This process was called GASTAK by Taiyo Kaken Co., Ltd. (now a part of Kureha) and is licensed by Union Carbide Corporation for sale in the United States and Canada under the name PURASIV HR (39). A diagram is shown in Figure 10. This process is used primarily for removal of solvent vapors from air streams. Feed gas is contacted countercurrently by fluidized adsorbent on trays similar to those in distillation columns. The loaded adsorbent then drops into a heated, moving-bed regeneration zone where the adsorbate is desorbed and recovered. Stripped adsorbent is then gas-lifted to the top tray in the upper section. Adsorbate reductions in the less-adsorbed gas can range from 90 to well over 99 percent (40). The advantages claimed for this process over fixed-bed processes include energy reductions of 70 to 75 percent, improved quality of recovered adsorbate, mechanical simplicity and compact size.

The PURASIV HR process is not the first circulating-adsorbent process to be commercialized. As early as the 1930s moving-bed processes were proposed. About 1950, Union Oil Company developed the Hypersorption moving-bed process for various light-hydrocarbon separations (41,42), and in the mid-1960s, Cortaulds, Ltd. developed a fluidized-bed process for carbon disulfide recovery from air (43). These processes were plagued by attrition and loss of the activated carbon adsorbent, however, and were shut down. BAC apparently eliminates that problem, raising the possibility of applying fluidized-bed and moving-bed adsorption technology to a number of other separations.

Future Directions

As stated earlier, distillation and related vapor-liquid operations are by far the most common separation processes in the organic-chemical, petroleum and allied industries. It is unlikely that adsorption will ever rival distillation in frequency of use, but adsorption's share of the separation task should grow substantially. The purpose of this section is to indicate the likely areas of growth in existing and new applications, as well as the technological innovations which would foster this growth.

Gas Bulk Separations. Recovery of oxygen and nitrogen by various pressure-swing processes will continue to grow. Oxygen from these processes is already being produced for waste-treatment plants, for welding shops and for in-home care of

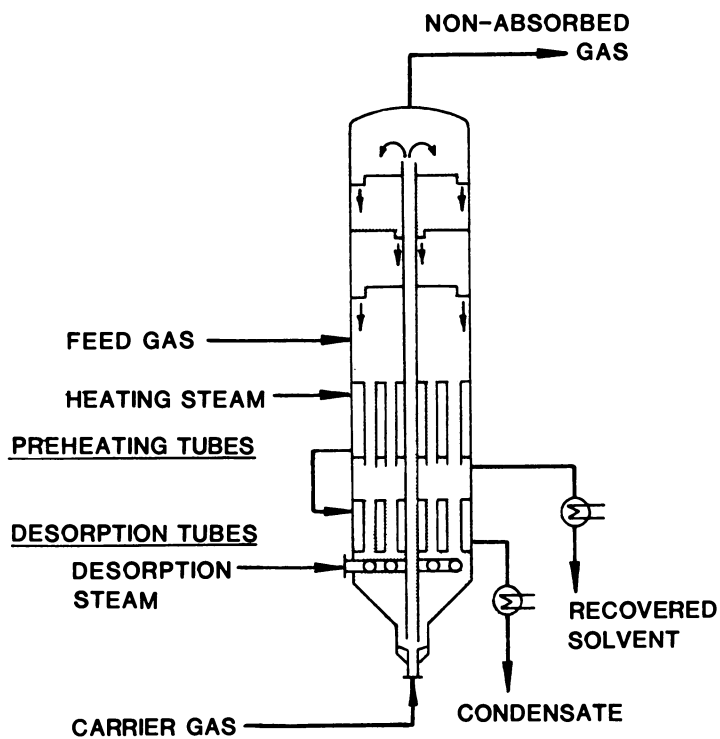


Figure 10. PURASIV HR fluidized-bed/moving-bed process.

lung-disease patients. Recently it was announced that units to supply oxygen on board aircraft will be built (44). Nitrogen will be produced for inerting of storage tanks, purging of process lines and vessels, creating modified atmospheres to prolong storage life in food-storage areas, etc.

It can also be predicted that, as further process improvements are made, PSA oxygen will compete successfully with cryogenically-produced oxygen in quantities considerably above 10 to 20 metric tons per day.

PSA hydrogen recovery will also compete more favorably with cryogenic alternatives in the future. Streams of 50 to 100 thousand cubic meters per hour will be processed at pressures up to about 70 atmospheres. In addition, as hydrogen becomes more valuable in chemical processes, high-purity hydrogen via PSA will be used more frequently to minimize vent-stream losses. Conversely impure hydrogen in other vent streams will be a candidate for recovery and cleanup via PSA.

But pressure-swing processes will not compete with distillation for many gas separations requiring the production of two nearly pure products (examples: ethane/ethylene, removal of inerts from natural gas) without a technological breakthrough. That breakthrough would be the ability to perform such separations in a relatively mechanically simple, i.e., low-investment, fashion, and with energy requirements less than those of comparable distillations. Though these are formidable goals, they should not be considered impossible to attain.

Displacement-purge cycles will not find many new uses, primarily because of their inherent complexity (see Figure 1). This complexity prevents these cycles from competing with distillation from an investment standpoint except in cases where key-component relative volatilities are well below 1.5. Inert-purge cycles will find additional uses if the problem of dissipating or coping with the heat of adsorption, which can cause large temperature rises during adsorption and thereby limit adsorption capacity, can be solved.

Moving-bed and fluidized-bed processes should be reinvestigated for economic viability, given the existence of Kureha's BAC and the possibility of producing other adsorbents in a tough, microspheroidal form. Also, the recent work of Szirmay (45) certainly gives impetus to moving-bed processes by showing that quite sharp separations can be made between key components in very short lengths of bed. A major problem of such processes is the same as that of the fixed-bed, inert-purge cycles: the large temperature rise accompanying adsorption, such as was found in the Hypersorption process (41).

Finally, there may be a few opportunities for close-coupling of reaction and adsorption systems to overcome thermodynamic-equilibrium limitations or to enhance selectivity by operating with low conversions per pass. Reaction types

include hydrogenation/dehydrogenation, isomerization and esterification/deesterification, among others, with boiling points of the species low enough to be amenable to vapor-phase processing.

Gas Purifications. Few if any major process innovations are likely to occur in this area. Fixed-bed, temperature-swing processes will continue to dominate, with some extension of PURASIV HR technology into new areas. Applications of adsorption will grow, however. A major area for growth is the recovery of small amounts of organics from chemical-process, storage-tank and other gaseous vents, as well as from solvent-painting, purging and cleaning operations. This area will grow in direct relation to the concern over air-pollution problems. Other major-use areas - gas dehydration, removal of sulfur compounds and carbon dioxide, and various specialty separations (37) - will grow in proportion to the growth in the industries they serve.

Acknowledgment

The author gratefully acknowledges helpful discussions with and sharing of information by Messrs. R. A. Anderson, R. T. Cassidy, M. S. Clancy, R. L. Drahushuk, and M. F. Symoniak, all of Union Carbide Corporation.

Literature Cited

1. Lukchis, G. M. Chemical Engineering June 11, 1973, 111.
2. Lukchis, G. M. Chemical Engineering July 9, 1973, 83.
3. Lukchis, G. M. Chemical Engineering August 6, 1973, 83.
4. Vermeulen, T.; Klein, G.; Hiester, N. K. "Adsorption and Ion Exchange," in "Chemical Engineers' Handbook," Perry, R. H.; Chilton, C. H., Eds., 5th edition, McGraw-Hill, New York, 1973.
5. Vermeulen, T. "Adsorptive Separation," in "Kirk-Othmer Encyclopedia of Chemical Technology," 3rd edition, vol. 1, Wiley-Interscience, New York, 1978.
6. Kovach, J. L. "Gas-Phase Adsorption," in "Handbook of Separation Techniques for Chemical Engineers," Schweitzer, P. A., Ed., McGraw-Hill, New York, 1979.
7. Deitz, V. R. "Bibliography of Solid Adsorbents," N.B.S. Circular 566, National Bureau of Standards, Washington, DC, 1956.
8. "Adsorption Handbook," Pittsburgh Chemical Co., Pittsburgh, PA, 1961.
9. Young, D. M.; Crowell, A. D. "Physical Adsorption of Gases," Butterworths, London, 1962.
10. Ross, S.; Olivier, J. P. "On Physical Adsorption," Wiley-Interscience, New York, 1964.

11. Breck, D. W. "Zeolite Molecular Sieves," Wiley-Interscience, New York, 1974.
12. Ponc, V.; Knor, Z.; Cerny, S. "Adsorption on Solids," Butterworths, London, 1974.
13. Chi, C. W.; Cummings, W. P. "Adsorptive Separation (Gases)," in "Kirk-Othmer Encyclopedia of Chemical Technology," 3rd edition, vol. 1, Wiley-Interscience, New York, 1978.
14. Flanigen, E. M. "Molecular Sieve Technology - The First Twenty-Five Years," in "Proceedings of the Fifth International Conference on Zeolites, Naples, Italy, 2-6, June, 1980," Heyden, London, 1980.
15. Breck, D. W.; Anderson, R. A. "Molecular Sieve Zeolites," in "Kirk-Othmer Encyclopedia of Chemical Technology," 3rd edition, vol. 15, Wiley-Interscience, New York, 1981.
16. Skarstrom, C. W. "Heatless Fractionation of Gases over Solid Adsorbents," in "Recent Developments in Separation Science," Li, N. N., Ed., vol. 2, CRC Press, Cleveland, OH, 1972.
17. Fuderer, A.; Rudelstorfer, E. "Selective Adsorption Process," United States Patent 3,986,849, October 19, 1976.
18. Heck, J. L. Hydrocarbon Processing January, 1978, 175.
19. Corr, F.; Dropp, F.; Rudelstorfer, E. Hydrocarbon Processing March, 1979, 119.
20. Cassidy, R. T. "Polybed Pressure-Swing Adsorption Hydrogen Processing," in "Adsorption and Ion Exchange With Synthetic Zeolites," Flank, W. H., Ed., American Chemical Society Symposium Series 135, 1980.
21. Heck, J. L. Oil and Gas Journal February 11, 1980, 122.
22. Wilhelm, R. H. Ind. Eng. Chem. Fund. 1966, 5, 141.
23. Chen, H. T. "Parametric Pumping," in "Handbook of Separation Techniques for Chemical Engineers," Schweitzer, P. A. (Ed.), McGraw-Hill, New York, 1979.
24. Jones, R. L.; Keller, G. E.; Wells, R. C. "Rapid Pressure-Swing Adsorption With High Enrichment Factor," United States Patent 4,194,892, March 25, 1980.
25. Keller, G. E.; Jones, R. L. "A New Process for Adsorption Separation of Gas Streams," in "Adsorption and Ion Exchange With Synthetic Zeolites," Flank, W. H., Ed., American Chemical Society Symposium Series 135, 1980.
26. Jones, R. L.; Keller, G. E. Journal of Separation Process Technology 1981, 2 (3), 17.
27. Earls, D. E.; Long, G. N. "Multiple Bed Rapid Pressure Swing Adsorption for Oxygen," United States Patent 4,194,891, March 25, 1980.
28. Knoblauch, K. Chemical Engineering November 6, 1978, 87.
29. "Pure Nitrogen Generator," Gas Services International, Ltd., Enfield, Middlesex, England.
30. Miwa, K.; Inoue, T. Chemical Economy and Engineering Review 1980, 12 (11), 40.

31. Symoniak, M. F.; Reber, R. A.; Victory, R. M. Hydrocarbon Processing May, 1973, 101.
32. Symoniak, M. F. Hydrocarbon Processing May, 1980, 110.
33. Bonmati, R. G., Chapelet-Letourneux, G., and Margulis, J. R. Chemical Engineering March 24, 1980, 70.
34. Anon. Analytical Chemistry 1980, 52, 481A.
35. Bernard, J. R.; Gourlia, J. P.; Guttierrez, M. J. Chemical Engineering May 18, 1981, 92.
36. Lee, M. N. Y. "Novel Separation With Molecular Sieves Adsorption," in "Recent Developments in Separation Science," Li, N. N., Ed., vol. 1, CRC Press, Cleveland, OH, 1972.
37. Anderson, R. A., "Molecular Sieve Adsorbent Applications State of the Art," American Chemical Society Symposium Series 40, 1977.
38. Sakaguchi, Y. Chemical Economy and Engineering Review 1976, 8 (12), 36.
39. Anon. Chemical Engineering August 29, 1977, 39.
40. "PURASIV HR for Hydrocarbon Recovery," Union Carbide Corporation, Danbury, CT.
41. Berg, C. Petroleum Refiner 1951, 30 (9), 241.
42. Treybal, R. E. "Mass Transfer Operations," McGraw-Hill, New York, 1955.
43. Avery, D. A.; Tracey, D. H. "The Application of Fluidized Beds of Activated Carbon to Solvent Recovery from Air or Gas Streams," Institution of Chemical Engineers Symposium Series, No. 30, 1968.
44. Anon. Science News 1981, 120, 346.
45. Szirmay, L. "Design Aspects of MAB (Moving Adsorbent Bed) Units for Continuous Chromatography-Like Sharp Separation," presented at the A.I.Ch.E. National Meeting, Orlando, FL, February 29, 1982.

RECEIVED January 25, 1983

Nonisothermal Gas Sorption Kinetics

SHIVAJI SIRCAR and RAVI KUMAR

Air Products and Chemicals, Inc., Allentown, PA 18105

Analytical equations for adsorbate uptake and radial adsorbent temperature profiles during a differential kinetic test are derived. The model assumes that the mass transfer into the adsorbent can be described by a linear driving force model or the surface barrier model. Heat transfer by Fourier conduction inside the adsorbent mass in conjunction with external film resistance is considered.

Experimental uptake data for sorption of *i*-octane on 13X zeolite and *n*-pentane on 5A zeolite were quantitatively described by the model. The results show that internal thermal resistance of the adsorbent mass plays a significant role during the uptake for these systems even though the adsorbent temperature changes are small.

The model shows that the non-isothermal uptake curve for an adsorbent mass which has low effective thermal conductivity (k) is identical in form to that of the isothermal Fickian diffusion model for mass transport. It is shown that k can be significantly low for an assemblage of microparticles at low pressure and high temperatures.

A parametric study of the effects of the equilibrium and the transport properties of the adsorption system on sorption kinetics is carried out. Complex interactions between these properties in determining the shape of the uptake curve are observed.

0097-6156/83/0223-0171\$07.00/0
© 1983 American Chemical Society

The importance of adsorbent non-isothermality during the measurement of sorption kinetics has been recognized in recent years. Several mathematical models to describe the non-isothermal sorption kinetics have been formulated [1-9]. Of particular interest are the models describing the uptake during a differential sorption test because they provide relatively simple analytical solutions for data analysis [6-9]. These models assume that mass transfer can be described by the Fickian diffusion model and heat transfer from the solid is controlled by a film resistance outside the adsorbent particle. Diffusion of adsorbed molecules inside the adsorbent and gas diffusion in the interparticle voids have been considered as the controlling mechanism for mass transfer.

Comparisons of estimated diffusivity values on zeolites from sorption uptake measurements and those obtained from direct measurements by nuclear magnetic resonance field gradient techniques have indicated large discrepancies between the two for many systems [10]. In addition, the former method has often resulted in an adsorbate diffusivity directly proportional to the adsorbent crystal size [11]. This led some researchers to believe that the resistance to mass transfer may be confined in a skin at the surface of the adsorbent crystal or pellet (surface barrier) [10,11]. The isothermal surface barrier model, however, failed to describe experimental uptake data quantitatively [10,12].

Measurement of radial temperature gradient inside the adsorbent particle during the sorption test showed that the internal resistance to heat transfer may not be negligible in comparison with the external film [13-16].

In view of these observations, we propose a non-isothermal sorption kinetics model with the following assumptions:

- (a) Sorbate mass transfer can be described by a linear driving force model (LDF) using a "lumped-up" mass transfer coefficient k_s [17].
- (b) Fourier conduction inside the adsorbent mass in conjunction with an external film resistance describes the heat transfer from the adsorbent.

The LDF model is a realistic representation of the system with a surface barrier. Otherwise, k_s can be treated as an apparent mass transfer coefficient irrespective of the true transport mechanism which can be directly used in the design and optimization of adsorbers. This concept has been successfully used to analyze column breakthrough data for practical non-isothermal systems [18-20]. It substantially

simplifies the mathematical modelling of the behavior of adsorbent columns in comparison with the use of Fickian diffusion models [22,23].

Non-isothermal LDF Model

We assume that the adsorbent mass used in the kinetic test consists of a sphere of radius R . It may be composed of several microsize particles (such as zeolite crystals) bonded together as in a commercial zeolite bead or simply an assemblage of the microparticles. It may also be composed of a noncrystalline material such as gels or aluminas or activated carbons. The resistance to mass transfer may occur at the surface of the sphere or at the surface of each microparticle. The heat transfer inside the adsorbent mass is controlled by its effective thermal conductivity. Each microparticle is at a uniform temperature dependent on time and its position in the sphere.

We assume that the adsorbent mass is initially in equilibrium with the adsorbate at pressure P_0 and temperature T_0 , and a differential step change in the gas phase pressure to P_∞ is applied at time $t = 0$. The pressure inside the adsorbent mass (or the microparticles), $P(t)$, increases with time, which is given by:

$$\frac{dP(t)}{dt} = k_s [P_\infty - P(t)] \quad (1)$$

k_s is the "lumped-up" mass transfer coefficient.

The heat balance for the adsorbent in the region $0 \leq r < R$ may be written as:

$$\rho c \left. \frac{\partial T}{\partial t} \right|_r = \frac{1}{r^2} \cdot \frac{\partial}{\partial r} [k_e r^2 \cdot \frac{\partial T}{\partial r}] + \rho q \left. \frac{\partial n}{\partial t} \right|_r \quad (2)$$

Where T is the temperature of the adsorbent mass at radius r and time t . n is the adsorbate loading per unit weight of the adsorbent at radius r and time t . q is the isosteric heat of adsorption. ρ , c and k_e are, respectively, the density, the heat capacity and the effective thermal conductivity of the adsorbent mass.

The adsorbent is at equilibrium under local conditions of P and T . Thus for a differential test where the changes in the adsorbent temperature and the adsorbate loading are small, one may write:

$$[n(t,r) - n_\infty] = a [P - P_\infty] + b [T(t,r) - T_0] \quad (3)$$

$$a = \frac{\partial n^*}{\partial P} \text{ at } T_o, P_\infty \quad (4)$$

$$b = \frac{\partial n^*}{\partial T} \text{ at } T_o, P_\infty \quad (5)$$

The asterick indicates that the quantities are evaluated under equilibrium conditions. n_o and n_∞ are, respectively, the initial and the final equilibrium adsorbate loadings during the test.

The boundary conditions for equations (1) and (2) are:

$$\begin{aligned} P(o) &= P_o \\ P(\infty) &= P_\infty \\ T(r,o) &= T_o \\ T(r,\infty) &= T_o \\ \frac{\partial T}{\partial r} \bigg|_{r=0} &= 0 \\ \frac{\partial T}{\partial r} \bigg|_{r=R} &= -\frac{h}{k_e} \cdot [T - T_o] \end{aligned}$$

The last boundary condition accounts for the external heat transfer from the adsorbent mass. h is the effective external heat transfer coefficient. a , b , c , ρ , q , k_e , k_s and h can be assumed to be constants for a differential test.

The average adsorbate loading in the adsorbent mass, $\bar{n}(t)$, can be obtained by:

$$\bar{n}(t) = \frac{3}{R^3} \int_0^R n(r,t) \cdot r^2 \cdot dr \quad (6)$$

Equations (1) - (3) and (6) were simultaneously solved using the above boundary conditions by Laplace transformation and inversion by the method of residues to obtain the following analytical equations:

$$F = 1 - e^{-\eta\tau} + \frac{6\beta}{1-\beta} \frac{\eta}{\eta - p_n^2} \frac{s^2}{p_n^2 \{p_n^2 - s(1-s)\}} (e^{-p_n^2\tau} - e^{-\eta\tau}) \quad (7)$$

$$\theta = 2 \frac{\sin p_n x}{(x) \sin p_n} \frac{\eta}{\eta - p_n^2} \frac{s}{\{p_n^2 - s(1-s)\}} \frac{1}{(e^{-p_n^2 \tau} - e^{-\eta \tau})} \quad (8)$$

where

$$\begin{aligned} x &= r/R \\ \tau &= \frac{\alpha t}{R^2} \\ \beta &= \frac{bq}{c} \\ s &= \frac{h R}{k_e} \\ \alpha &= \frac{k_e}{\rho c(1-\beta)} \end{aligned} \quad (9)$$

$$\eta = \frac{k_s R^2}{\alpha}$$

$$F = \frac{\bar{n} - n_o}{n_\infty - n_o}$$

$$\theta = \frac{T(x,t) - T_o}{T^* - T_o}$$

$$(T^* - T_o) = \frac{q (n_\infty - n_o)}{c (1 - \beta)}$$

p_n 's are the positive roots of the transcendental equation:

$$p_n \cot p_n - 1 = -s \quad n = 1, 2, 3, \dots \quad (10)$$

It can be shown from adsorption thermodynamics that:

$$\beta = - \frac{q^2 (n_o + \eta_\infty)/2}{c R T_o^2} \left. \frac{\partial \ln n}{\partial \ln P} \right|_{\text{at } T_o, (P_o + P_\infty)/2}^* \quad (11)$$

a, q and β can be calculated from the equilibrium adsorption isotherms at various temperatures. R_g is the gas constant.

Equation (7) gives the dimensionless uptake, F, for the differential test in terms of dimensionless time (τ). Equation (8) describes the dimensionless adsorbent temperature θ as a function of dimensionless time and radius (x). The parameters of these two equations are dimensionless groups, η [reciprocal of modified Lewis number], s [Biot number] and the equilibrium parameter β .

Equations (7) and (8) have nine variables, viz. a, q, b, c, ρ , R, k_s , and h. Of these variables, the equilibrium properties [a, q, β] can be evaluated by independent measurement of adsorption isotherms at two or more temperatures. The physical properties of the adsorbent mass [c, ρ , R] can also be independently measured. The remaining three transport properties [k_s , k_e , h] can then be evaluated from the experimental uptake data and the temperature-time profiles in the adsorbent at two different radial positions using equations (7) and (8). However, measurement of $T(x,t)$ may be difficult in a differential test.

For moderately fast adsorption ($\eta \gg p_1^2$), it can be shown from equation (7) that a plot of $\ln [1-F(t)]$ against t yields a straight line at large t. Such behavior has been experimentally observed for many systems [7,8,24]. The slope (m) and intercept (I) at $t = 0$ of the linear curve are given by:

$$m = - \frac{\alpha p_1^2}{R^2} \quad (12)$$

$$I = - \frac{6\beta}{1-\beta} \frac{\eta}{\eta - p_1^2} \frac{s^2}{p_1^2 \{p_1^2 - s(1-s)\}} \quad (13)$$

where p_1 is the first root of equation (10)

$$p_1 \cot p_1 - 1 = -s \quad (14)$$

Equation (7) shows that the slope (m_o) of $\ln[1-F(t)]$ against t at $t = 0$ is:

$$m_o = - \frac{\eta \alpha}{R^2(1-\beta)} \quad (15)$$

Equations (12)-(15) provide four independent equations relating the parameters η , p_1 , α/R^2 and s . Thus a unique solution is possible. However, m_0 may be difficult to measure for systems with relatively fast adsorption. In that case, the problem reduces to a single variable search to best fit the uptake curve using equations (12)-(14).

Special Cases

For isothermal adsorption [$q \rightarrow 0$], equation (7) reduces to

$$F = 1 - e^{-k_s t} \quad (16)$$

For very rapid adsorption [$k_s \rightarrow \infty$], equations (7) and (8) become:

$$F = 1 + \frac{6\beta}{1-\beta} \sum \frac{s^2}{p_n^2 \{p_n^2 - s(1-s)\}} e^{-p_n^2 \tau} \quad (17)$$

$$\theta = 2 \sum \frac{\sin p_n x}{(x) \sin p_n} \frac{s}{\{p_n^2 - s(1-s)\}} e^{-p_n^2 \tau} \quad (18)$$

Equation (17) represents the general case of uptake under complete heat transfer control and equation (18) gives the corresponding adsorbent temperature profile. Furthermore, if k_e is large compared to h , ($s \ll 1$), equation (10) can be approximated as $p_n^2 \sim 3s$ and equations (17) and (18) reduce to

$$F = 1 + \frac{\beta}{1-\beta} e^{-\frac{3ht}{R\rho c(1-\beta)}} \quad (19)$$

$$\theta = e^{-\frac{3ht}{R\rho c(1-\beta)}} \quad (20)$$

Equations (19) and (20) correspond to the familiar case of uptake controlled by external heat transfer resistance derived earlier by King and Cassie [25]. Equation (20) shows that $(T^* - T_0)$ is the maximum temperature rise in the adsorbent for this case, and it occurs at $t = 0$.

For the case where k_e is very small, as compared with k_s and h , ($\eta \gg 1$, $s \gg 1$), the roots of equation (10) are given by $p_n \simeq n\pi$, and equations (7) and (8) transform to:

$$F = 1 + \frac{6\beta}{1-\beta} \sum \frac{1}{(n\pi)^2} e^{-\frac{\alpha (n\pi)^2 t}{R^2}} \quad (21)$$

$$\theta = \sum \frac{\sin n\pi x}{n\pi x} e^{-\frac{\alpha (n\pi)^2 t}{R^2}} \quad (22)$$

The form of equation (21) is interesting. It shows that the uptake curve for a system controlled by heat transfer within the adsorbent mass has an equivalent mathematical form to that of the isothermal uptake by the Fickian diffusion model for mass transfer [26]. The isothermal model has mass diffusivity (D/R^2) instead of thermal diffusivity (α/R^2) in the exponential terms of equation (21). According to equation (21), uptake will be proportional to \sqrt{t} at the early stages of the process which is usually accepted as evidence of intraparticle diffusion [27]. This study shows that such behavior may also be caused by heat transfer resistance inside the adsorbent mass. Equation (22) shows that the surface temperature of the adsorbent particle will remain at T_0 at all t and the maximum temperature rise of the adsorbent is T^* at the center of the particle at $t = 0$. The magnitude of T^* depends on $(n_\infty - n_0)$, q , c and β , and can be very small in a differential test.

Experimental Verification

The proposed model was used to fit the uptake data for sorption of *i*-octane on 13X zeolite [8] and *n*-pentane on 5A zeolite [7]. These experiments were carried out using an assemblage of microsize crystals and satisfied the criteria for a differential test.

Figure 1 shows the uptake of *i*-octane on 13X zeolite at 403 K measured under a mean pressure level of 0.048 torr. The solid line (curve a) is the best fit of the data by equation (7) which shows that the data can be quantitatively described by the model. β for the system was evaluated using the equilibrium data [8]. A heat of adsorption of 19.5 kcal/mole was calculated for the system. c and ρ were taken to be 0.25 cal/gm/K and 0.8 g/cc, respectively. Curve b in Figure 1 shows the uptake curve for the same k_s as in curve a but with only the external film resistance s controlling the heat transfer. Curve c shows the corresponding isothermal uptake. These curves clearly

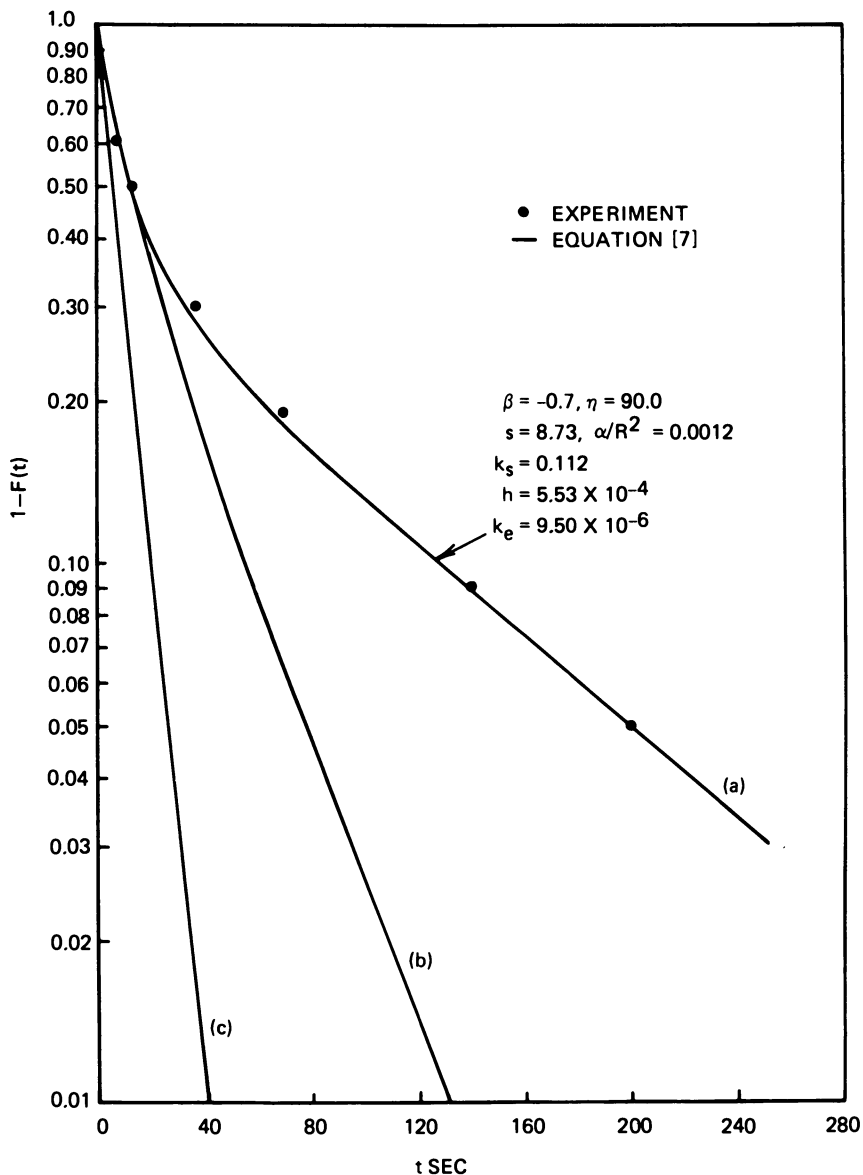


Figure 1. Sorption of *i*-octane on 13X at 403 K: (a) comparison of the experimental uptake with the best fit obtained by the present model; (b) uptake with no internal heat transfer resistance; and (c) uptake for an isothermal case.

demonstrate the importance and effects of various heat transfer resistances on the shapes of the uptake curves. They also show that ignoring any of these thermal resistances in a model may yield a lower value of the mass transfer coefficient.

Figure 2 shows the corresponding temperature profiles at the center and the surface of the adsorbent mass calculated by equation (8). The maximum temperature rises at the center and the surface are, respectively, only 0.64°C and 0.23°C. Figure 2 also shows that the maximum temperature rise occurs much earlier at the surface than at the center and the surface temperature quickly approaches that of the surrounding.

Figure 3 shows the uptake of n-pentane on 5A zeolite [7] at 523 K (13 mg sample) measured under a mean pressure level of 24 torr. This system exhibits much faster uptake than the previous one. The data can again be quantitatively described by the model as shown by curve a in the figure. The equilibrium data [28] was used to evaluate β for the system. A heat of adsorption of 14.9 kcal/mole was estimated for the system. Curves b and c, respectively, show the corresponding uptakes for external film heat transfer control and isothermal sorption using the same k_s as in curve a.

Figure 4 shows the calculated temperature profiles for this system. The maximum temperature rises at the center and the surface are, respectively, 2.3°C and 0.7°C and it occurs earlier at the surface. The surface cools down to near ambient temperature quicker than the center.

Effective Thermal Conductivity

No experimental data on the effective thermal conductivity of an assemblage of micron size zeolite crystals under the conditions of sorption tests used in the examples above could be found in the literature. However, several methods are available for the calculation of k for an assemblage of particles with void fraction f . The thermal conductivities of the solid phase (k_s) and the gas phase (k_g) in the voids are needed [29]. We used the method developed by Maxwell.

k_g at low pressures can be significantly lower than the gas thermal conductivity at atmospheric pressure (k_g^0) due to the formation of Knudsen regime in the void space [30,31]. This is expected to happen when the mean free path (λ) of the gas becomes comparable to the space between the particles (l) of the assemblage. Since the true size of the space between the particles is not known, we assume it to be equal to the diameter of the microparticle (d_p) as a first approximation. The Knudsen effect has, however, been observed at much higher pressures where $\lambda \ll d_p$ [32].

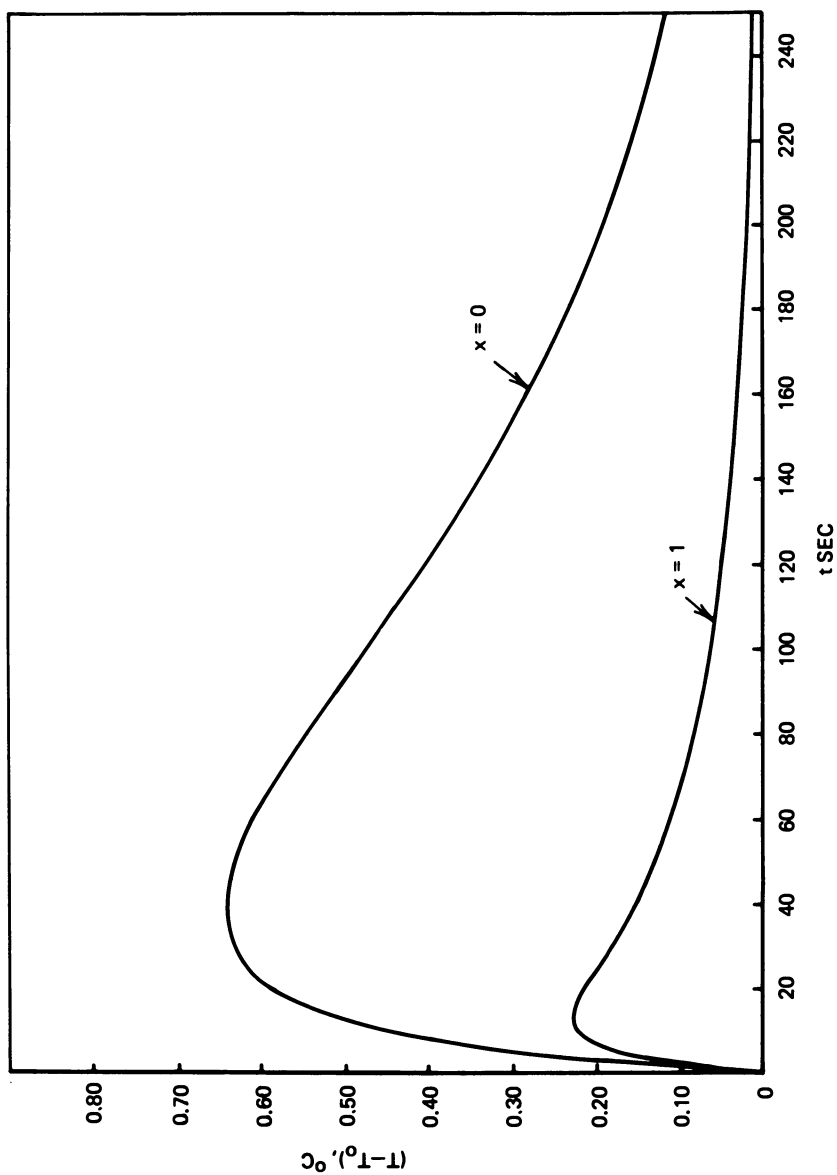


Figure 2. Sorption of i-octane on 13X at 403 K: temperature profiles calculated by the present model.

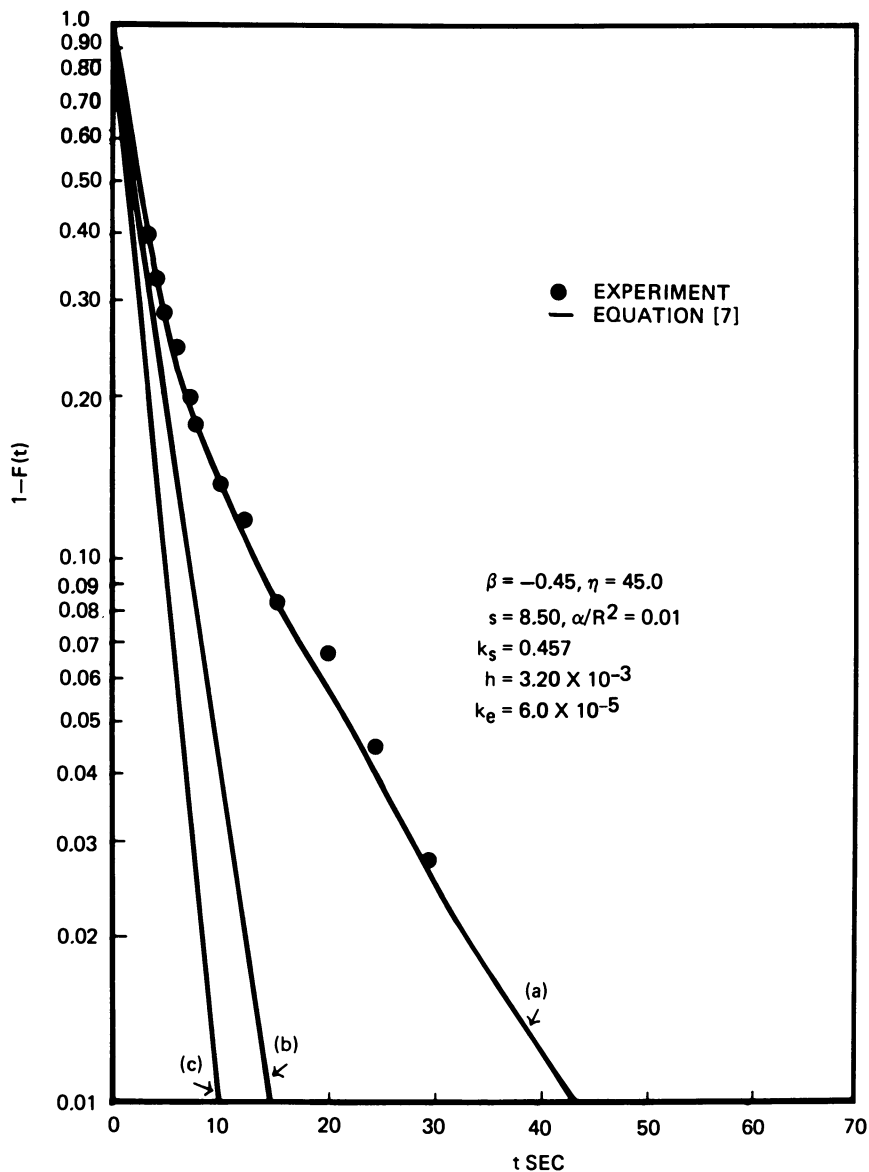


Figure 3. Sorption of n-pentane on 5Å at 523 K: (a) comparison of the experimental uptake with the best fit obtained by the present model; (b) uptake with no internal heat transfer resistance; and (c) uptake for an isothermal case.

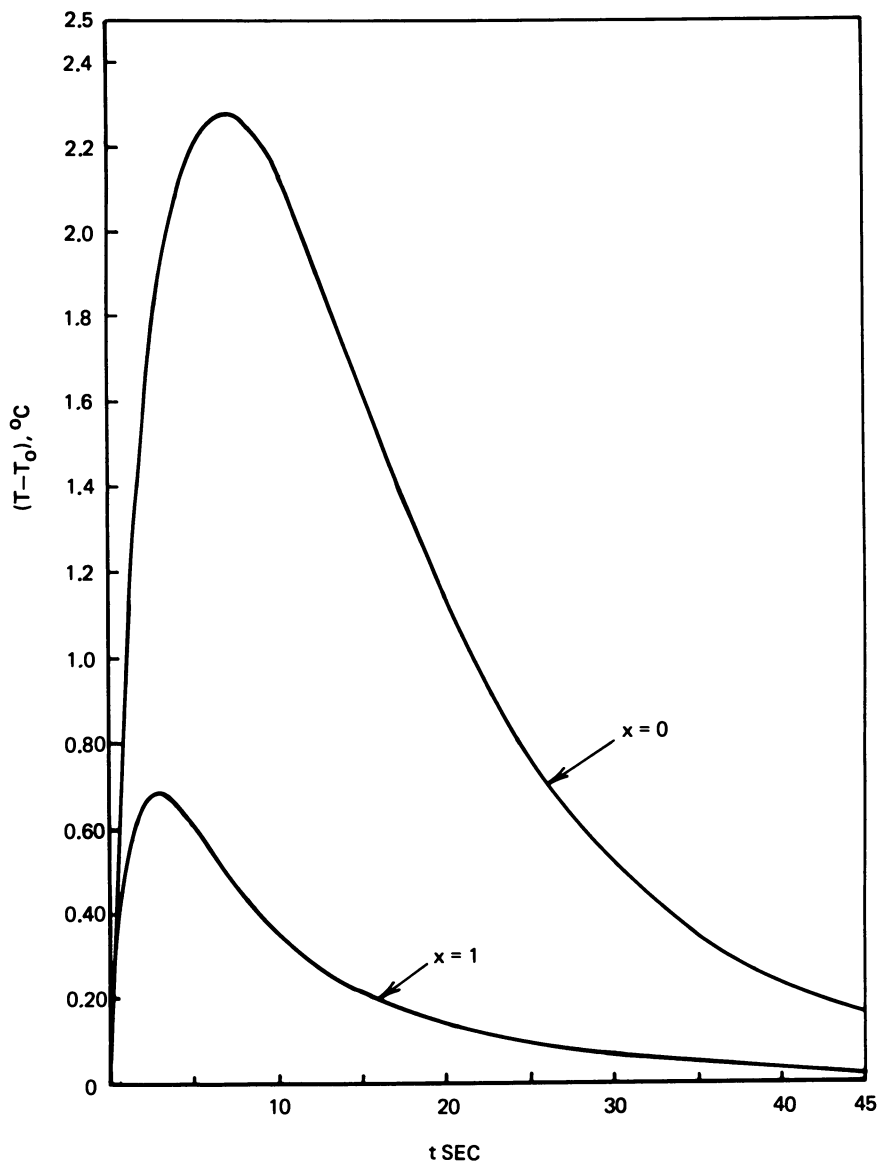


Figure 4. Sorption of n-pentane on 5A at 523 K: temperature profiles calculated by the present model.

Following the procedure developed by Cha and McCoy [31], the relationship between k in the Knudsen regime and k_g^o for a polyatomic gas may be written as:

$$\frac{k}{k_g^o} = \left[1 + \frac{\lambda}{d_p} \frac{4 + 9(\gamma - 1)}{A(\gamma + 1)} \right]^{-1} \quad (23)$$

where γ is the ratio of the specific heats of the gas at constant pressure and volume and A is a function of the Knudsen thermal accommodation coefficients of the heat exchanging surfaces. A depends on the nature of the gas molecules and the surfaces [30]. k_g^o was estimated using the method of Roy and Thodos and γ was obtained from the published data [33].

The mean free paths of *i*-octane and *n*-pentane at the conditions of the sorption experiments were calculated to be 750 and 2 microns, respectively. They are comparable with the average crystal diameters of, respectively, 39 and 3.6 microns for the 13X and 5A zeolites used in the tests. Using the above described procedure and $k = 4 \times 10^{-4}$ cal/sec/cm/K [34], $f = 0.5$ [8] and $A = 1.4$ we calculated k_e of, respectively, 5×10^{-6} and 1.2×10^{-4} cal/sec/cm/K for the *i*-octane-13X and *n*-pentane-5A systems. These numbers are in good agreement at least in the order of magnitude with the k_e values obtained from the analysis of sorption data considering the uncertainties in the theories and the values of the parameters (A , λ , f etc) used. It may be concluded that k_e can be low for an assemblage of microcrystals at low pressures and high temperatures and internal thermal resistance can be significant.

External Heat Transfer Coefficient

The external heat transfer coefficient is given by the sum of the conductive (h_c) and radiative (h_r) contributions. These depend on the shape and the size of the pan containing the adsorbent, area of exposed adsorbents, volume ratio of pan to adsorbent, emissivities of the adsorbent and the pan etc. We calculated an order of magnitude of h , for a sphere with equivalent volume of the adsorbent mass by using $h_c = k_g^o/R$ and $h_r = 4.33 \times 10^{-12} T^3$ [7]. The values for *i*-octane-13X and *n*-pentane-5A systems were found to be, respectively, 6.3×10^{-4} and 1.3×10^{-3} cal/cm²/sec/K. These values are in good agreement with those obtained from the analysis of the sorption data by the LDF model in view of the approximations made.

Parametric Study

Figure 5 shows the effect of η on the shape of the uptake curve for a given s and β . Figure 6 shows the corresponding dimensionless adsorbent temperature profiles at $x = 0$. The abscissa in Figures 5 and 6 are dimensionless time τ . Low η (low k_s , high k_e) corresponds to isothermal sorption and very large η (high k_s , low k_e) represents sorption under complete heat transfer control. The initial slope of the uptake curve is a strong function of η but the slope of the linear region at large τ is a weak function of η indicating dominance of heat transfer in that region. Figure 6 shows that the maximum temperature rise in the adsorbent is higher for larger values of η and it occurs at smaller values of τ . In real time, however, the maximum occurs at longer times for lower k_e for a given η and the adsorbent cools down slower.

Figure 7 shows the effects of the equilibrium parameter β on the uptake curve for a given η and s . Fastest adsorption occurs at $\beta = 0$ which corresponds to the isothermal case. The rate of uptake slows down considerably as β decreases. β affects the slopes of both the initial and the later portions of the uptake curve. This shows that uptake rate is very sensitive to the adsorbate loading and the heat of sorption. For a Langmurian system, β may be written as:

$$\beta = - \frac{q_{\infty}^2 \bar{n} \theta (1-\theta)}{c R_g T_o^2} \quad (24)$$

where \bar{n} is the Langmuir saturation capacity and $\theta (= n_{\infty}/\bar{n})$ is the fractional coverage of the adsorbate in the test. Equation (24) shows that β is a "U" shaped function of θ having a minimum at $\theta = 0.50$ and values approaching zero at $\theta = 0$ and 1. Consequently, the uptake will slow down as θ increases from 0-0.5 and become faster after $\theta \geq 0.50$. This would result in a "U" shaped dependence of diffusivity on coverage estimated by an isothermal model. This behavior has been experimentally observed [35].

Figure 8 shows the effect of β on the dimensionless temperature profile at $x=0$. Since β is not an explicit variable in equation (8), a single curve describes the dimensionless temperature profile in terms of τ . The actual temperature rise is lower as β decreases and the adsorbent takes longer time to cool down.

Figure 9 illustrates the effect of the Biot number, s , on the uptake curve for a given η and β . Figure 10 shows the corresponding dimensionless temperature profiles at $x = 0$. It may be seen from Figure 9 that s has small effect on the uptake curve at low τ but it strongly affects the

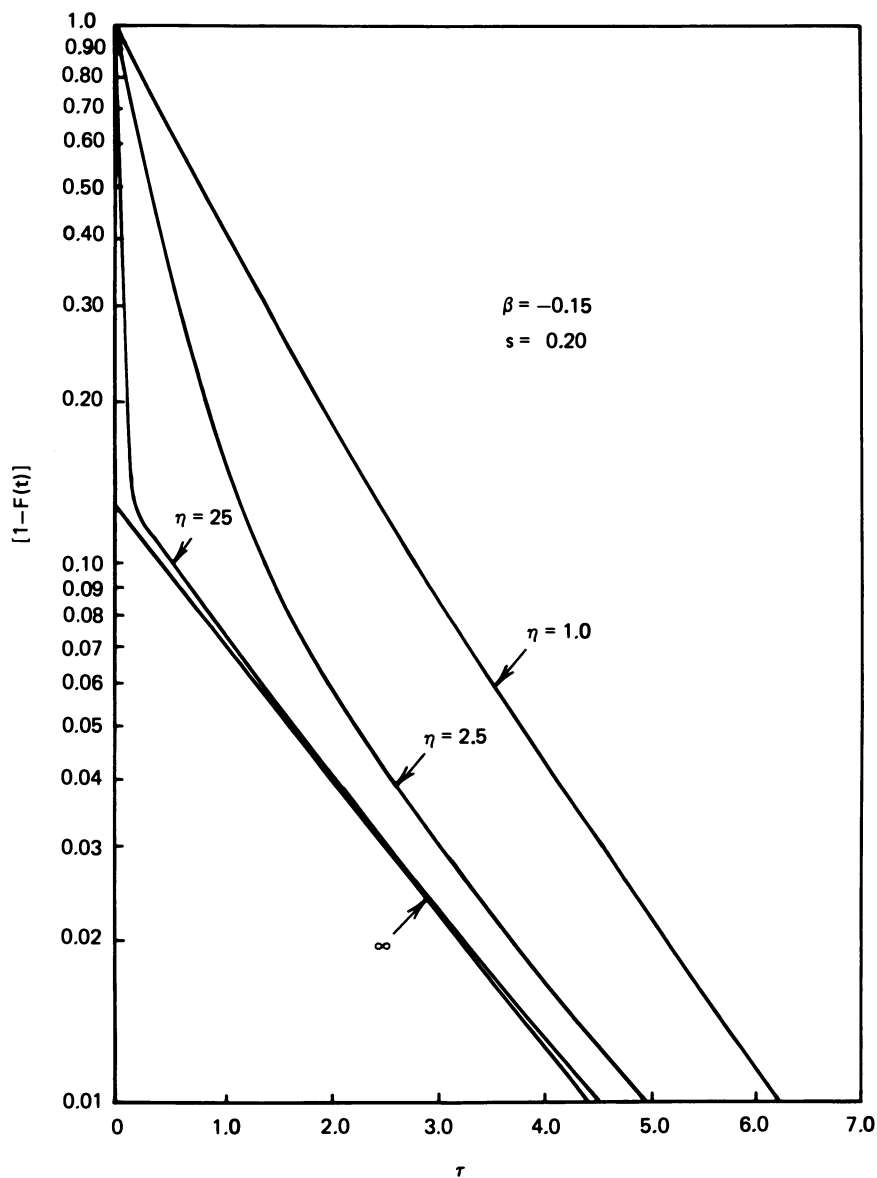


Figure 5. Effect of η on the uptake curves.

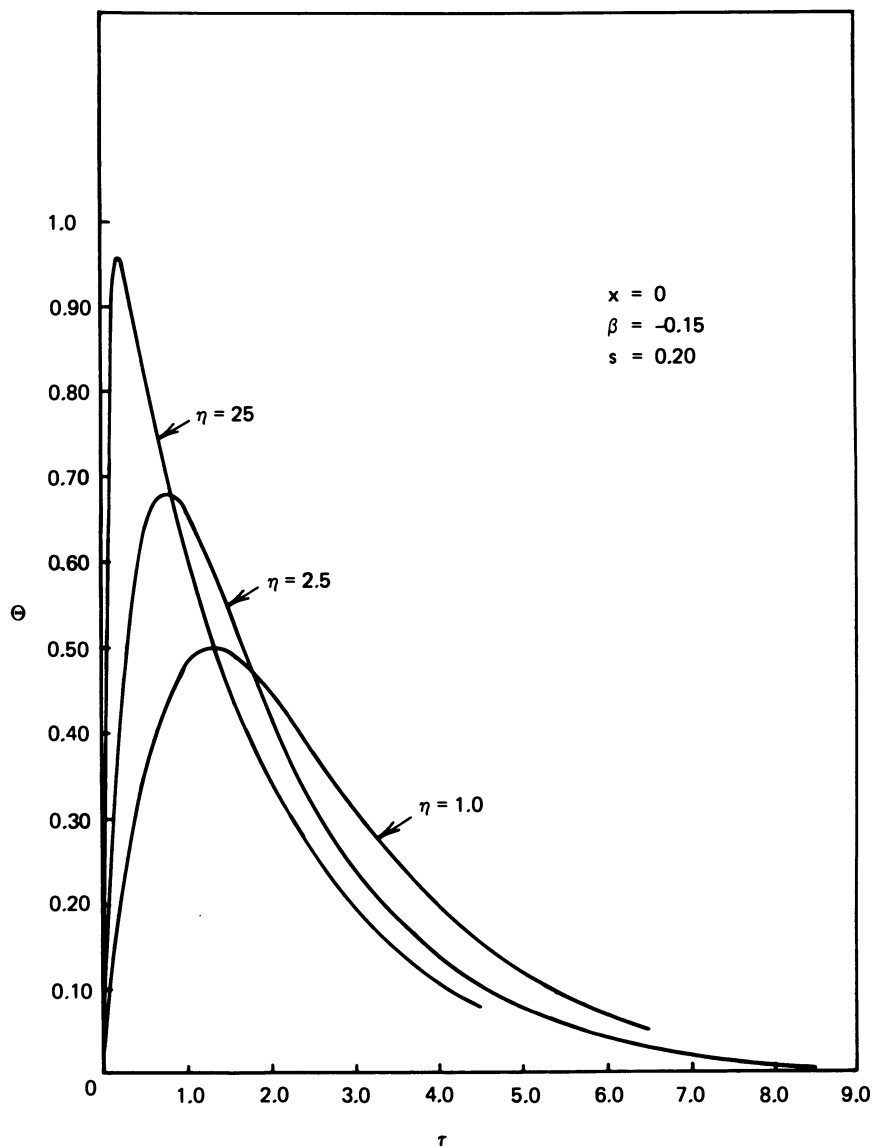


Figure 6. Effect of η on dimensionless temperature profiles.

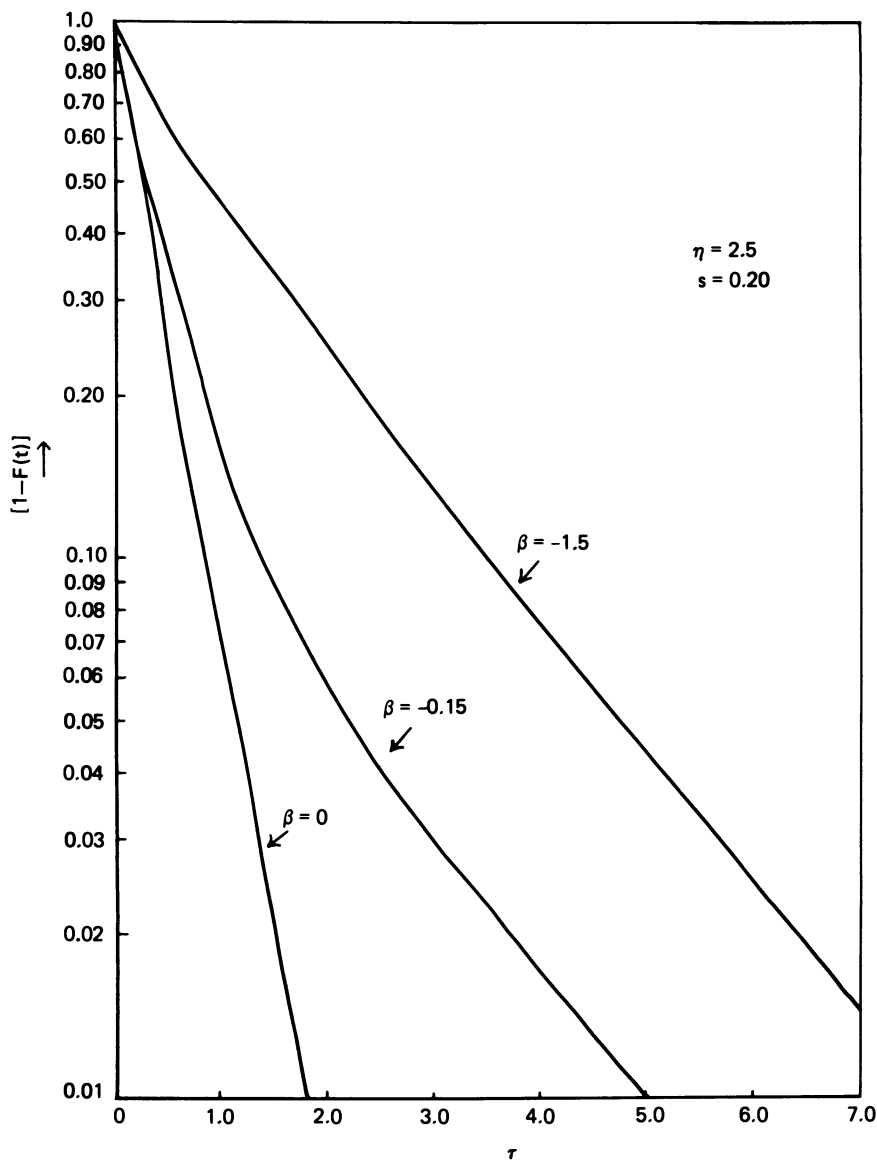


Figure 7. Effect of β on the uptake curves.

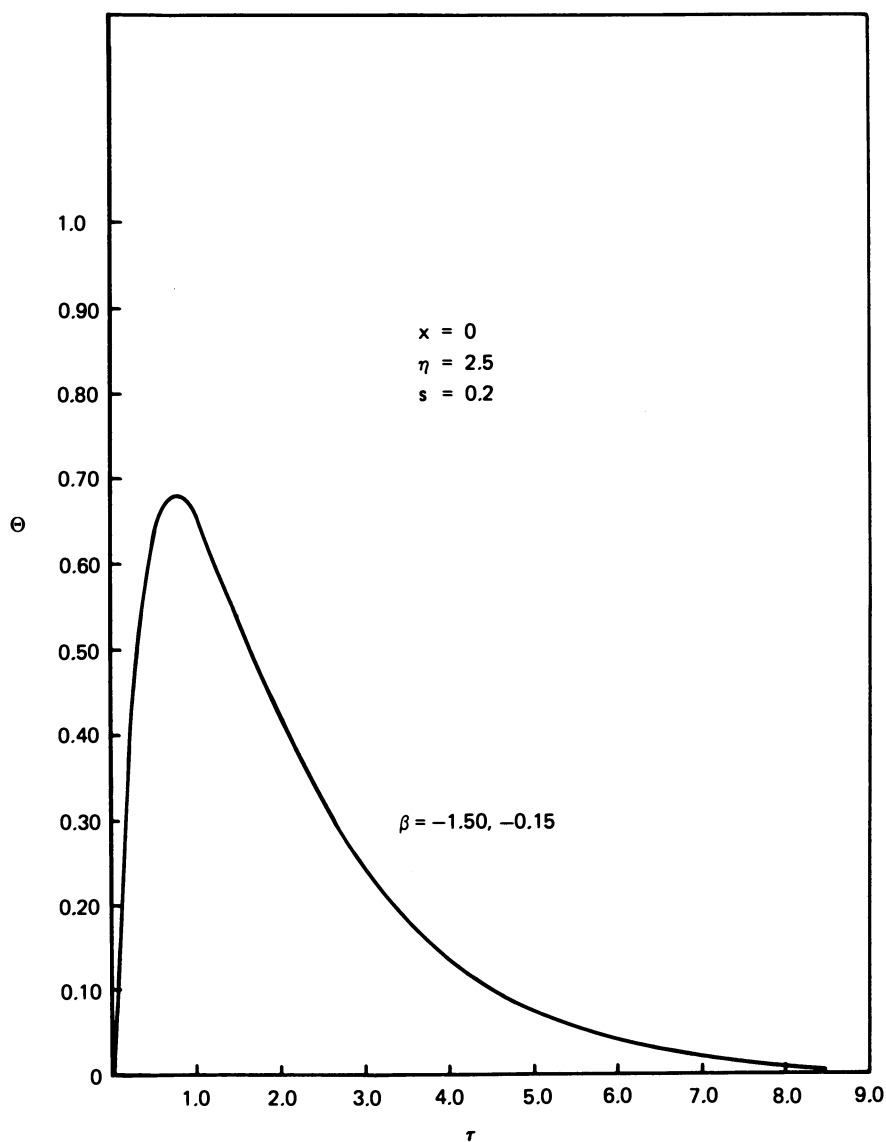


Figure 8. Effect of β on dimensionless temperature profiles.

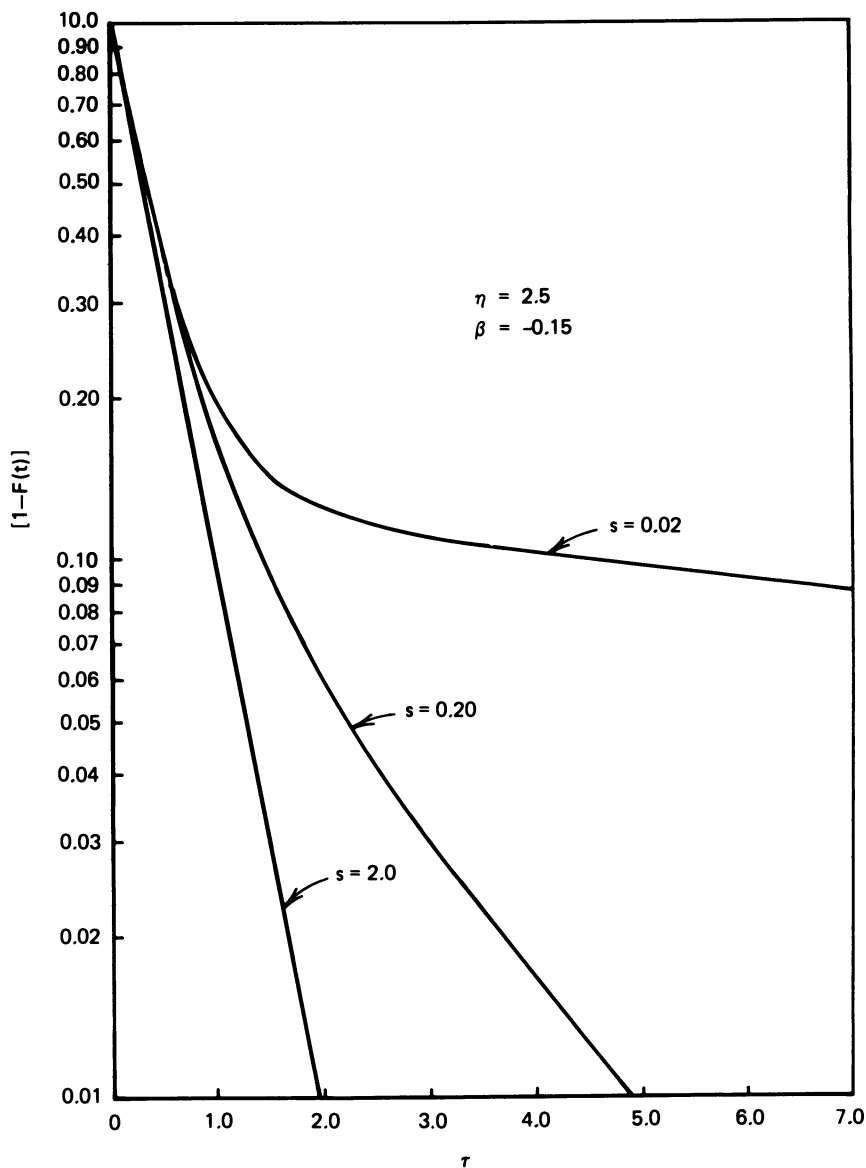


Figure 9. Effect of s on the uptake curves.

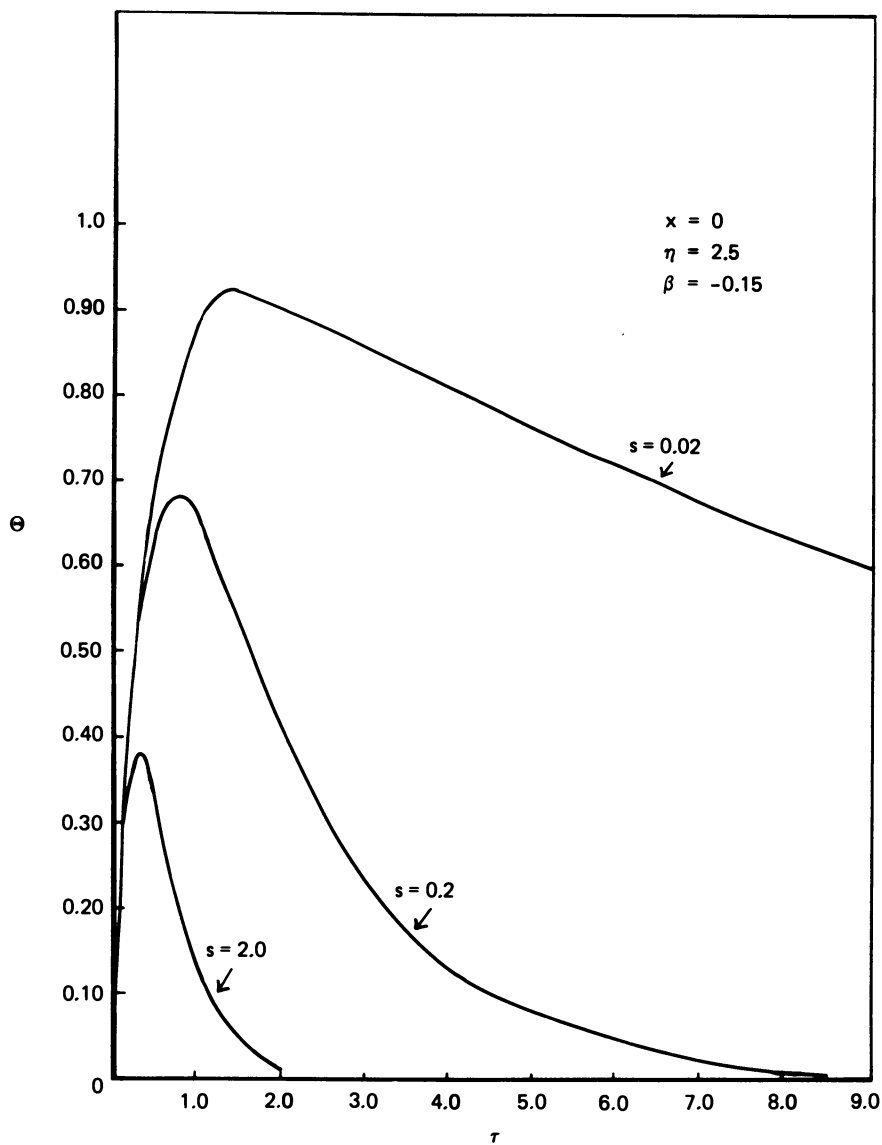


Figure 10. Effect of s on dimensionless temperature profiles.

uptake at large τ . Low s significantly slows down uptake in τ domain. In real time, however, smaller k (large s) for a given k , β and h produces slower uptake. Figure 10 shows that the dimensionless temperature rise in the adsorbent is higher for smaller s (low h , high k). In real time the adsorbent cools down faster for larger k . The parametric study shows that the interactions between the thermodynamic and the mass and the heat transport properties of the adsorption system during the sorption process is quite complex.

Conclusion

The proposed model for non-isothermal sorption kinetics can quantitatively describe uptake data for adsorption of i-octane on 13X and n-pentane on 5A zeolites. The study indicates that the principal resistance to mass transfer for these systems may be confined at the surface of the zeolite crystals. It is also found that the internal thermal resistance of the assemblage of the micron size zeolite crystals used in the kinetic test is significant which produces a substantial thermal gradient within the assemblage and slows down the heat dissipation from it.

Thus, an apparently slower mass uptake is observed as compared with the isothermal uptake or the case when heat transfer is controlled by the external film resistance. Consequently, ignoring the internal thermal resistance may lead to erroneously low mass transfer coefficient.

It is recommended that careful experimental measurement of radial temperature-time profile in the adsorbent mass be carried out during mass uptake experiments for more accurate analysis of the process.

Literature Cited

1. Zolotarev, P. P.; Izv. Akad. Nauk. SSSR. Ser. Khim., 1970, 1421; 1970, 2831.
2. Zolotarev, P. P. and Radushkevich, L. V., Dokl. Akad. Nauk. SSSR, 1970, 195, 1361.
3. Zolotarev, P. P. and Kalinichev, A. I., Russ. J. Phys. Chem. (English Trans.), 1971, 45, 1610; 1972, 46, 654.
4. Brunovska, A., Hlavacek, V., Ilavsky, J., and Valtyni, J. Chem. Eng. Sci., 1978, 33, 1395; 1980, 35, 757; 1981, 36, 123.
5. Chihara, K., Suzuki, M., and Kawazoe, K., Chem. Eng. Sci., 1976, 31, 505.
6. Armstrong, A. A., and Stannet, V., Die Makromolekulare Chemie., 1966, 90, 145.

7. Ruthven, D. M., Lee, L. K., and Yucel, H., AICHE J., 1980, 26, 16.
8. Ruthven, D. M., Lee, L. K., AICHE J., 1981, 27, 654.
9. Kocirik, M., Smutek, M., Bezus, A., and Zikanova, A., Coll. Czech. Chem. Comm., 1980, 45, 3392.
10. Kärger, J., and Caro, J., J.C.S., Faraday I., 1977, 73, 1363.
11. Kärger, J., Caro, J., and Bülow, M., Izv. Akad. Nauk. SSSR. Ser. Khim., 1977, 2666.
12. Bülow, M., Struve, P., Finger, G., Redszus, C., Ehrhardt, K. Schirmer, W., and Kärger, J., J.C.S. Faraday I., 1980, 76, 597.
13. Lykow, A. W., Kolloidzeitschrift, 1935, 71, 333; 1936, 74, 179.
14. Wicke, E., *ibid*, 1939, 86, 167.
15. Timofeev, D. P., and Erashko, I. T., Russ. J. Phys. Chem. (English Trans.) 1971, 45, 359.
16. Ilavsky, J., Brunovska, A., and Hlavacek, V., Chem. Eng. Sci., 1980, 35, 2475.
17. Glueckauf, E., and Coates, J. J., J. Chem. Soc., 1947, 1315.
18. Thomas, W. J., and Lombardi, J. L., Trans. Inst. Chem. Engrs., 1971, 49, 240.
19. Sircar, S., and Kumar, R., I&EC Proc. Des. & Dev. In press.
20. Sircar, S., and Kumar, R., I&EC Proc. Des. & Dev. In press.
21. Kidnay, A. J., Hija, M. J., and Dickson, P. F., Adv. Cryogenic Eng., 1969, 15, 46.
22. Carter, J. W., and Hussain, H., Trans. Inst. Chem. Engrs., 1972, 50, 69.
23. Masamune, S., and Smith, J. M., AICHE J., 1965, 11, 34.
24. Yucel, H., and Ruthven, D. M., J. Colloid and Interface Sci., 1980, 74, 186.
25. King, G., and Cassie, A. B. D., Trans. Faraday Soc., 1940, 36, 445.
26. Crank, J., "The Mathematics of Diffusion", Oxford University Press, London, 1956; p. 86.
27. Barrer, R. M., "The Properties and Application of Zeolites", ed. R. P. Townsend, Chem. Soc. Special Publ. 33, 1979; p. 3.
28. Vavlitis, A. P., Ruthven, D. M., and Loughlin, K. F., J. Colloid and Interface Sci., 1981, 84, 526.
29. Krupiczka, R., Int. Chem. Eng., 1967, 7, 122.
30. Dushman, S., "Scientific Foundation of Vacuum Technique", John Wiley, New York, 1962; p. 45.
31. Cha, C. Y., and McCoy, B. J., J. Chem. Phys., 1972, 56, 3265.

32. Deissler, R. G., and Boegll, J. S., Trans., A.S.M.E., 1958, 1417.
33. Reid, R. C., Prausnitz, J. M., and Sherwood, T. K., "The Properties of Gases and Liquids", McGraw-Hill, New York, 1977, p. 481.
34. Lee, L. K., and Ruthven, D. M., J.C.S. Faraday I., 1979, 79, 2406.
35. Ruthven, D. M., Separation and Purification Methods, 1976, 5, 189.

RECEIVED January 4, 1983

Recovery and Purification of Light Gases by Pressure Swing Adsorption

HSING C. CHENG and FRANK B. HILL
Brookhaven National Laboratory, Upton, NY 11973

A cell model is presented for the description of the separation of two-component gas mixtures by pressure swing adsorption processes. Local equilibrium is assumed with linear, independent isotherms. The model is used to determine the light gas enrichment and recovery performance of a single-column recovery process and a two-column recovery and purification process. The results are discussed in general terms and with reference to the separation of helium and methane.

Pressure swing adsorption (PSA) processes are widely applied industrially for gas separations. Applications are numerous and include hydrogen and helium recovery and purification, air drying, the production of oxygen from air, and the separation of normal paraffins from isoparaffins.

In spite of its widespread use, design information on PSA processes has been rather sparse in the open literature. In recent years, however, a beginning has been made in terms of the development of mathematical models of PSA processes. This paper is concerned with the further development of such models.

Modeling efforts to date have been confined to two processes: a single column recovery process and a two-column recovery and purification process.

The single-column process (Figure 1) is similar to that of Jones et al. (1). This process is useful for bulk separations. It produces a high pressure product enriched in light components. Local equilibrium models of this process have been described by Turnock and Kadlec (2), Flores Fernandez and Kenney (3), and Hill (4). Various approaches were used including direct numerical solution of partial differential equations, use of a cell model, and use of the method of characteristics. Flores Fernandez and Kenney's work was reported to employ a cell model but no details were given. Equilibrium models predict

0097-6156/83/0223-0195\$06.00/0
© 1983 American Chemical Society

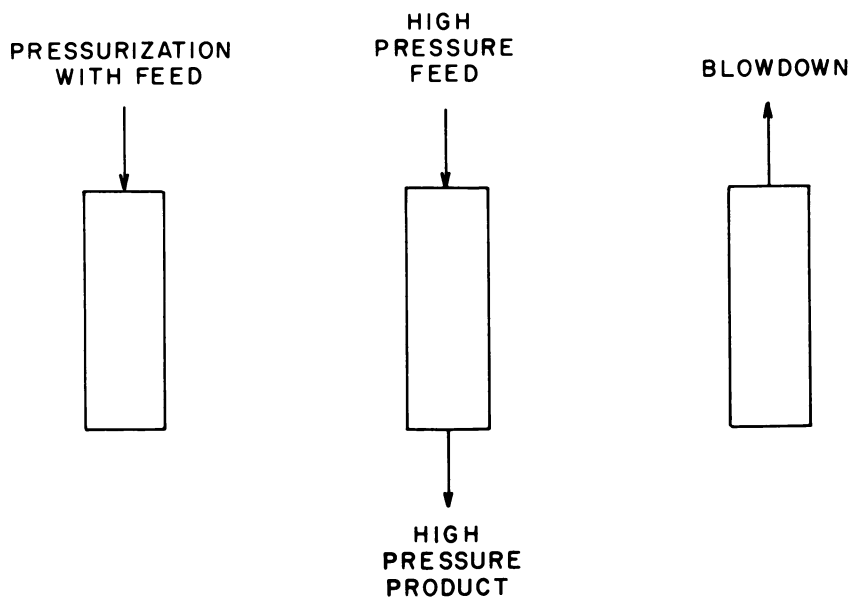


Figure 1. Steps in single-column PSA process.

that this process is not capable of producing the light component in pure form. Because of this fact the process is referred to here as a recovery process.

The two-column process (Figure 2) is the heatless adsorption process of Skarstrom (5). This process can perform both recovery and purification of a light component. Local equilibrium models of this process have been presented by Shendalman and Mitchell (6), Chan et al. (7), and Knaebel and Hill (8). In each case the method of characteristics was used. Models with finite mass transfer rates have been published by Kawazoe and Kawai (9), Mitchell and Shendalman (10), Chihara and Suzuki (11), and Richter et al. (12). In these models the method of characteristics and direct integration of partial differential equations were employed.

Much of the modeling work to date has dealt with the separation of binary mixtures composed of a carrier and an impurity. Such separation can be readily treated using the method of characteristics. While in some situations (Knaebel and Hill, (8), for instance) the same method can be used for binary mixtures of arbitrary composition, the cell model is readily and generally useful for this situation. It was this feature which prompted the use of the cell model in the present work.

In the present paper, a cell model is employed to simulate equilibrium isothermal PSA with a binary feed of arbitrary composition. Linear isotherms are assumed. The model equations derived are applied to the one- and two-column processes mentioned earlier to give a general description of their light component enrichment and recovery performance. Also some discussion is given of the effects of various operating parameters on the separation of methane and helium.

Cell Model

A gas mixture consisting of two components is separated using one or more adsorption beds. The beds are used in a cyclic process composed of steps involving column pressurization, depressurization (blowdown) and flow through the columns at constant pressure. Analysis of such separation processes in terms of a cell model proceeds as follows.

Each adsorption bed is considered to consist of N well-mixed cells, each cell being of length ΔZ , as shown in Figure 3. This figure depicts the notation used for process steps with flow from left to right. The same notation can be used for steps with flow in the opposite direction if the cells are renumbered starting from the right, i.e., if

$$i' = N - i + 1 \quad (1)$$

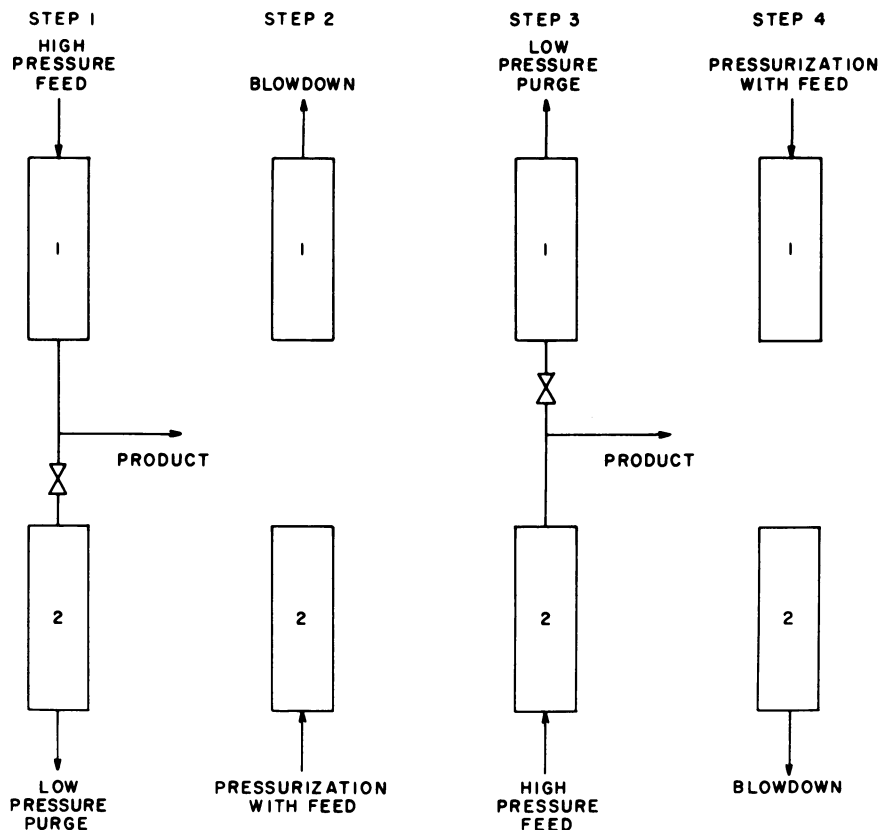


Figure 2. Steps in two-column PSA process.

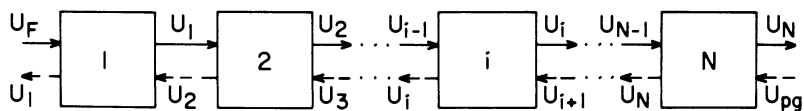


Figure 3. Flow diagram for cell model.

Because of interchange between the gas and the adsorbent, the velocity and composition of the gas phase within the bed change with position and time during both constant pressure steps and steps with changing pressure. Pressure is assumed to vary with time during pressure changes but not spatially. Also, pressure drop due to flow is negligible. Finally, heat effects are neglected and local equilibrium with linear isotherms is assumed throughout the bed. These isotherms are represented by

$$n_{\ell} = k_{\ell} \frac{P}{RT} y \quad (2)$$

$$n_h = k_h \frac{P}{RT} (1-y) \quad (3)$$

where y is the mole fraction of the less strongly adsorbed or light component.

With the foregoing assumptions, the process steps of interest may be described starting with two material balances, a balance for the light component and a total balance. The balances are taken on the first and i -th cells and are written for a differential time dt .

The balances on the light component can be expressed as

$$\frac{d(Py_1)}{dt} = -\beta_{\ell} \frac{U_1 y_1 P - U_F y_F P_H}{\Delta Z} \quad (4)$$

$$\frac{d(Py_i)}{dt} = -\beta_{\ell} P \frac{U_i y_i - U_{i-1} y_{i-1}}{\Delta Z} \quad (5)$$

$$i = 2, 3, \dots, N$$

and the total balance yields

$$\frac{dP}{dt} = (1-\beta) \frac{d(Py_1)}{dt} - \beta_h \frac{U_1 P - U_F P_H}{\Delta Z} \quad (6)$$

$$\frac{dP}{dt} = (1-\beta) \frac{d(Py_i)}{dt} - \beta_h P \frac{U_i - U_{i-1}}{\Delta Z} \quad (7)$$

$$i = 2, 3, \dots, N$$

where

$$\beta_{\ell} = \frac{\epsilon}{\epsilon + (1-\epsilon)\rho_s k_{\ell}} \quad (8)$$

$$\beta_h = \frac{\epsilon}{\epsilon + (1-\epsilon)\rho_s k_h} \quad (9)$$

$$\beta = \frac{\beta_h}{\beta_\ell} \leq 1 \quad (10)$$

Pressurization and Blowdown. For these steps, Eqs. (4), (5), (6) and (7) are combined by eliminating $d(Py_1)/dt$ between them, respectively, obtaining

$$\frac{dP}{dt} = -\beta_\ell \frac{V_i^P - V_F^P}{\Delta Z} = -\beta_\ell P \frac{V_i - V_{i-1}}{\Delta Z} \quad (11)$$

where

$$V_F = [\beta + (1-\beta)y_F] U_F \quad (12)$$

and

$$V_i = [\beta + (1-\beta)y_i] U_i \quad (13)$$

$$i = 1, 2, \dots, N$$

For a pressurization step feed gas enters the first cell at velocity U_F and there is no flow from the N -th cell, i.e. $U_N = 0$. Therefore, when Eq. (11) is written for cell N and again for cell i , a difference equation in V_i is obtained whose solution is

$$V_i = \frac{(N-i)P_H}{NP} V_F \quad (14)$$

A dimensionless time is defined as

$$d\tau = \frac{\beta_\ell V_F^P}{LP} dt \quad (15)$$

Using this definition and Eqs. (11), (12) and (15) in Eqs. (4) and (6), respectively, one obtains

$$\frac{dy_i}{d\tau} = - \left\{ \left[\frac{N-i}{\beta + (1-\beta)y_i} + 1 \right] y_i - \frac{N-i+1}{\beta + (1-\beta)y_{i-1}} y_{i-1} \right\} \quad (16)$$

$$i = 1, 2, \dots, N$$

with $y_0 = y_F$.

One can find the dimensionless time required to accomplish the full pressure change from P_L to P_H by substituting Eqs. (14) and (15) into Eq. (11) and integrating. The result is

$$\tau_P = \ln P_H/P_L \quad (17)$$

Thus the mole fraction profile after the pressure increase is calculated by integrating the N simultaneous differential equations represented by Eq. (16) from $\tau = 0$ to $\tau = \tau_P$.

For a blowdown step, gas leaves the bed through the N -th cell and there is no flow into the first cell, i.e., $U_F = 0$, and Eq. (11) written for cells N and i yields a difference equation in V_i whose solution is

$$V_i = \frac{1}{N} V_N \quad (18)$$

The appropriate dimensionless time is

$$d\tau = \frac{\beta_L V_N}{L} dt \quad (19)$$

Using this definition and Eqs. (11) and (18) in Eq. (6) one finds

$$\frac{dy_i}{d\tau} = - \left\{ \left[\frac{i}{\beta + (1-\beta)y_i} - 1 \right] y_i - \frac{i-1}{\beta + (1-\beta)y_{i-1}} y_{i-1} \right\} \quad (20)$$

$$i = 1, 2, \dots, N$$

As before, one can show that the length of dimensionless time required for the pressure decrease during blowdown is that given by Eq. (17). The dimensionless time definition in this case is given by Eq. (19). Hence the mole fraction profile after the pressure decrease is found by integrating Eq. (20) from $\tau = 0$ to $\tau = \tau_p$.

Constant Pressure Step. For treatment of this step Eqs. (4), (5), (6) and (7) can be combined, respectively, to yield

$$V_N = \dots = V_i = V_{i-1} = \dots = V_F \quad (21)$$

With this result, Eqs. (6) and (7) can be written

$$\frac{dy_i}{d\tau} = \frac{\beta}{1-\beta} N \left[\frac{1}{\beta + (1-\beta)y_i} - \frac{1}{\beta + (1-\beta)y_{i-1}} \right] \quad (22)$$

$$i = 1, 2, \dots, N$$

where dimensionless time is defined as

$$d\tau = \frac{\beta_L V_F}{L} dt \quad (23)$$

Equations (22) are integrated over the interval $\tau = 0$ to $\tau = \tau_F$ where τ_F is any desired value.

Equations (16), (20) and (22) each are a set of N simultaneous first order differential equations which can be integrated to give the mole fraction profile within the adsorption bed as a function of the dimensionless time τ during the step

under consideration. The transient profiles for a given PSA cycle are calculated by integrating these sets of equations cyclically in the proper order.

Single Column Bulk Separation Process. A three-step single column process was described by Hill (4) (Figure 1). The process is similar to the rapid PSA process of Jones et al. (1). The cycle for this process consists of pressurization with feed introduced through one end of a column followed by introduction of additional feed through the same end at high pressure with withdrawal of a product from the opposite end, and ending with blowdown with the exhausted gas leaving via the feed end only. Mole fraction profiles within the bed are calculated by integrating Eq. (16) from $\tau = 0$ to $\tau = \tau_P$ for the pressurization step. An experimentally significant initial condition is that of $y_1(0) = y_F$. The profile resulting from the integration of Eq. (16) to time τ_P then becomes the initial condition for the integration of Eq. (22) from $\tau = 0$ to $\tau = \tau_F$ for the feed step. The profile for $\tau = \tau_F$ then becomes the initial condition for the integration of Eq. (20) from $\tau = 0$ to $\tau = \tau_P$ for the blowdown step. Before performing the latter integration, the cells and the corresponding mole fractions are renumbered in accordance with Eq. (1) since the flow direction is reversed in the blowdown step. Then the next cycle is started by renumbering the cells and mole fractions and using the mole fractions as the initial condition for the next pressurization step. The cyclic integration of Eqs. (16), (22) and (20) is then continued until the cyclic steady state is reached.

Two indices of process performance which are of interest are the average steady state enrichment of the light component in the product stream defined as

$$E = y_{PRD}/y_F \quad (24)$$

and the steady state recovery of the light component in the product stream

$$\rho = E\theta \quad (25)$$

where the product cut, θ , is given by

$$\theta = \frac{N_{PRD}}{N_F + N_{PRS}} \quad (26)$$

Since at the cyclic steady state

$$N_F + N_{PRS} = N_{PRD} + N_{BD} \quad (27)$$

Eq. (26) may be expressed as

$$\theta = \frac{N_{\text{PRD}}}{N_{\text{PRD}} + N_{\text{BD}}} \quad (28)$$

The product mole fraction, y_{PRD} , in Eq. (24) is the average steady state mole fraction leaving the adsorber during the feed step, i.e.,

$$y_{\text{PRD}} = \int_0^{\tau_F} \frac{y_N(\tau)}{\beta + (1-\beta)y_N(\tau)} d\tau / \int_0^{\tau_F} \frac{1}{\beta + (1-\beta)y_N(\tau)} d\tau \quad (29)$$

where $y_N(\tau)$ is the mole fraction transient for the N -th cell during the feed step in a steady state cycle and is obtained from the integration of Eq. (22).

It can be shown that N_{PRD} , the moles of gas taken off as product at cyclic steady state during the feed step is

$$N_{\text{PRD}} = \frac{\varepsilon AL}{\beta_L} \frac{P_H}{RT} \int_0^{\tau_F} \frac{d\tau}{\beta + (1-\beta)y_N(\tau)} \quad (30)$$

Also N_{BD} , the moles of gas taken from the column during the blowdown step at the cyclic steady state, is

$$N_{\text{BD}} = \frac{\varepsilon AL}{\beta_L} \frac{P_H}{RT} \int_0^{\tau_P} \frac{e^{-\tau} d\tau}{\beta + (1-\beta)y_N(\tau)} \quad (31)$$

where in this equation $y_N(\tau)$ is the mole fraction transient from the N -th cell during the blowdown step of a steady state cycle and is obtained by integration of Eq. (20).

Two-Column Process. The heatless adsorption process (Figure 2) has two columns. Each column undergoes a four-step cycle. Three steps involve the same sequence as the single column process: pressurization with feed, feed at high pressure, and blowdown through the feed end. This is followed by a low pressure purge step with the purge being a fraction of the product from the other column and flowing from the product end to the feed end. For one column to provide purge for the other, the cycles in the two columns are 180° out of phase.

Modeling of this process proceeds in the same way as for the single-column process described above except for introduction of a purge step. The process is started with one column equilibrated with feed at high pressure and the other at low pressure. Eqs. (16), (20) and (22) are used as before with renumbering of cells and mole fractions at appropriate points in the cycle, but the purge step is inserted into the sequence at the appropriate point.

Three indices of performance for this process are of interest: E , ρ and H , the purge-to-total product ratio. The latter quantity takes the place of the purge-to-feed ratio in the heavy impurity-light carrier separation. For that separation it has been shown that the impurity is completely removed when the purge-to-feed ratio exceeds a critical value (7). When the heavy component content of the feed is above the impurity level, a ratio which is operationally more useful in determining whether a pure light gas can be obtained is the purge-to-total product ratio (8).

A total material balance around one column of the two-column process at cyclic steady state is

$$N_{PRS} + N_F + N_{PGF} = N_{PRD} + N_{BD} + N_{PG} \quad (32)$$

The extent of recovery of the light gas in the high pressure product is

$$\rho = \frac{(N_{PRD} - N_{PGF})}{N_{PRS} + N_F} E \quad (33)$$

It can be shown that H is given by

$$H = \frac{P_L}{P_H} \frac{\frac{\tau_{PGF}}{\beta + (1-\beta)y_{PGF}}}{\int_0^{\tau_F} \frac{d\tau}{\beta + (1-\beta)y_N(\tau)}} = \frac{P_L}{P_H} \frac{\tau_{PGF}}{\tau_F} \quad (34)$$

Results and Discussion

Eqns. (16), (20) and (22) were integrated numerically to obtain the separation performance of the one- and two-column processes. The GEAR package (13) was used for the integration after determining that it was faster than, say, Runge-Kutta methods. For all calculations $N = 50$ and $\epsilon = 0.40$. Dimensionless parameters varied were β , P_H/P_L , y_F , and, for the two-column process, H . Combinations of the parameters of β and P_H/P_L were chosen to correspond to the methane-helium system on BPL carbon. Adsorption isotherm data for methane at 25°C (14) were represented by

$$n_h = \frac{5.69 \times 10^{-4} P_h}{1 + 8.11 \times 10^{-2} P_h} \quad (35)$$

where P_h is in atm and n_h is in gm mole/gm carbon. Helium was taken to be inert. The adsorption coefficient k_h used to calculate β was evaluated as the slope of the straight line connecting points on the isotherm, Eqn. (35), corresponding to the high and low pressures P_H and P_L . With values of β and P_H/P_L

related in this way, the calculated process performance can be described in terms of both its general features and its applicability to the methane-helium separation.

Single-Column Process. Typical relations showing enrichment and recovery of the light component in the product as a function of product cut are shown in Figure 4 with feed light component mole fraction as a parameter. Figures 4(a) and 4(b) are for high and low pressures of 60 and 30 psia, for which $\beta = 0.083$. For Figures 4(c) and 4(d) the high pressure is increased to 300 psia. Because of the leveling off of the methane isotherm, β increases to 0.156. For any feed mole fraction the enrichment is greatest at small cuts. This follows from the fact that pressurization leads to a spatial fractionation within the column with high mole fractions of the light component near the closed end. Small cuts then displace gas enriched in the light component into the product stream. Enrichment also increases as the mole fraction of the light component in the feed decreases. As a comparison of Figure 4(a) and 4(c) shows, increasing the high pressure produces an increase in enrichment. However, because of the leveling off of the methane isotherm the increase is not as large as that expected for a linear isotherm (4).

As seen in Figures 4(b) and 4(d), recovery increases rapidly with cut at small cuts and levels off at large cuts. Small light component mole fractions in the feed and large pressure ratios favor high recoveries.

An example of the effect of pressure on the performance of the single column process for the methane-helium separation is shown in Table 1. Using Figure 4(b) and 4(d), the cuts corresponding to 80 percent recovery of helium were determined as a function of y_F and P_H/P_L . Then the enrichments and in turn the product mole fractions corresponding to these cuts were found from Figures 4(a) and 4(c). Except for the leanest feed mole fraction, $y_F = 0.005$, the use of the higher top pressure leads to a significantly higher product mole fraction.

Two-Column Process. Typical enrichment-cut and recovery-cut relations for this process are shown in Figure 5. For this figure $P_H = 60$ psia, $P_L = 30$ psia, and $\beta = 0.083$. For Figures 5(a) and 5(b), $y_F = 0.005$ and for Figures 5(c) and 5(d), $y_F = 0.1$. The parameter in Figure 5 is H , the purge-to-product ratio.

The maximum enrichment possible for the 0.5 percent helium feed is 200. For 10 percent helium it is 10. Pure helium is obtained with the 10 percent feed with $H = 0.8$ at cuts smaller than 0.018. At smaller values of H , pure helium cannot be produced. Very large enrichments are obtained at small cuts for 0.5 percent helium but pure helium is not obtained. This finding is consistent with the results of Knaebel and Hill (8) who

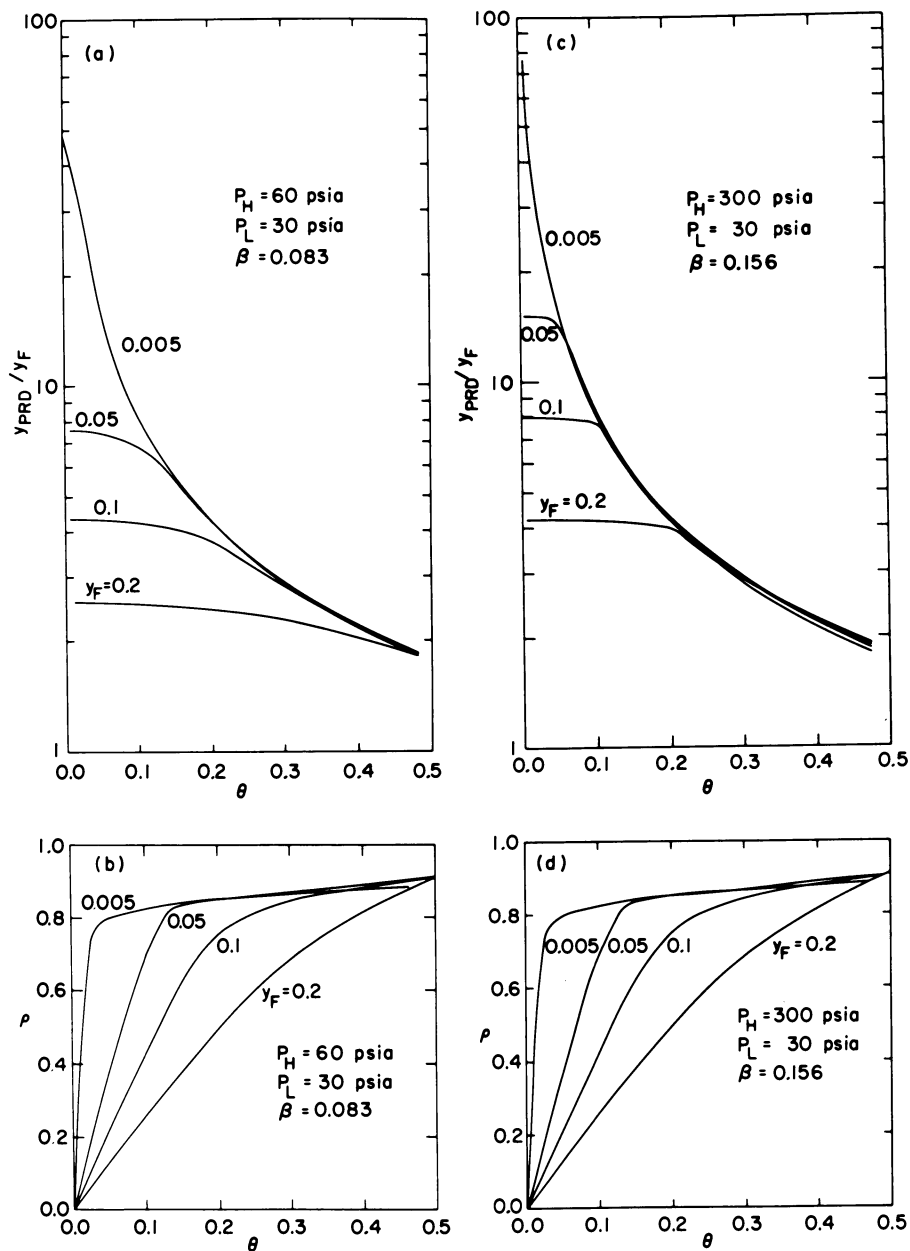


Figure 4. Light gas enrichment and recovery in product as a function of product cut in single-column PSA process.

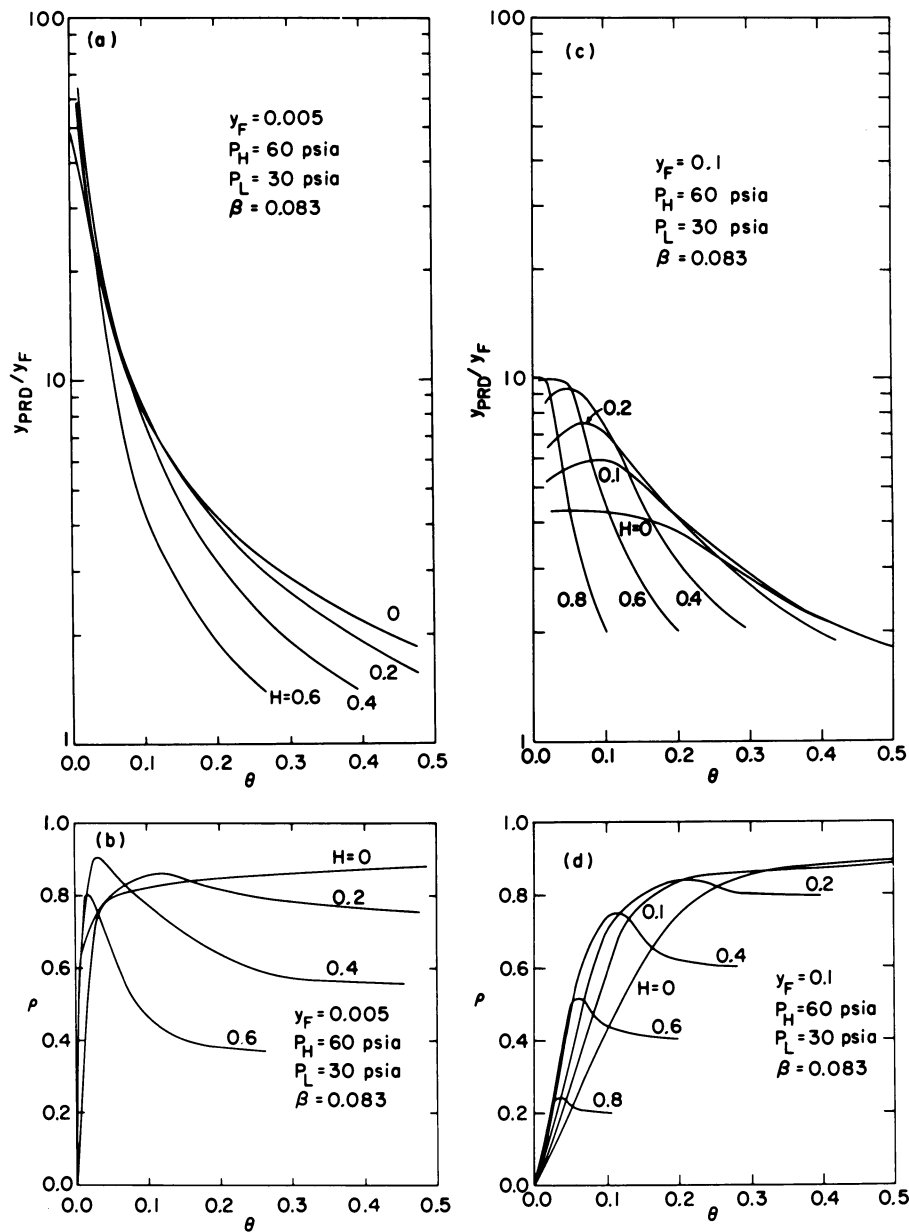


Figure 5. Light gas enrichment and recovery in product as a function of product cut in two-column PSA process.

Table I
Effect of Pressure on Single-Column
Process for Helium-Methane Separation

$\rho = 0.80$				
y_F	P_H/P_L	θ	E	Y_{PRD}
0.005	2	0.057	14	0.070
	10	0.063	13	0.065
0.05	2	0.128	8.2	0.41
	10	0.063	13	0.65
0.1	2	0.238	3.4	0.34
	10	0.107	7.5	0.75
0.2	2	0.364	2.13	0.43
	10	0.203	3.95	0.79

found that a critical pressure ratio (as well as a critical H) had to be exceeded to obtain pure light gas and that this ratio was higher the smaller the light gas content of the feed. The critical ratios for the conditions of Figure 5 cannot be calculated from the results of Knaebel and Hill since their results were obtained for the "shortest clean column" condition. But evidently a pressure ratio of 2.0 is high enough for perfect cleanup for a 10 percent helium feed but not high enough for a 0.5 percent feed.

The curves for $H = 0$ represent the performance of the single-column process. It is apparent that the single-column process is superior at large product cuts in terms of both enrichment and recovery. For small cuts, the two-column process is superior.

The effect of feed composition on enrichment at maximum recovery is shown in Table 2. Both high enrichment and good recovery are obtainable with the leaner feed composition, a result which is counter to intuition. The explanation lies in the fact that light gas losses in the purge and blowdown gas decrease as the feed becomes leaner in the light gas.

Table II

Enrichment at Maximum Recovery
Two-Column Process

$$\beta = 0.083 \quad P_H/P_L = 2$$

H	ρ_{\max}	$\theta_{\rho=\rho_{\max}}$	$E_{\rho=\rho_{\max}}$
---	---------------	-----------------------------	------------------------

$$y_F = 0.005$$

0.0	1.0	1.0	1.0
0.2	0.863	0.122	7.0
0.4	0.905	0.032	24.3
0.6	0.800	0.017	50.0

$$y_F = 0.1$$

0.0	1.0	1.0	1.0
0.2	0.835	0.2	4.28
0.4	0.750	0.115	6.5
0.6	0.522	0.062	8.4
0.8	0.244	0.037	6.6

Conclusion

The equations for a local equilibrium cell model of pressure swing adsorption processes with linear isotherms have been derived. These equations may be used to describe any PSA cycle composed of pressurization and blowdown steps and steps with flow at constant pressure. The use of the equations was illustrated by obtaining solutions for a single-column recovery process and a two-column recovery and purification process. The single-column process was superior in enrichment and recovery of the light component at large product cuts. The two-column process was superior at small cuts.

Acknowledgments

This work was supported by the Division of Chemical Sciences, U.S. Department of Energy, Washington, D.C., under Contract No. DE-AC02-76CH00016.

Notation

E	enrichment of light gas in product stream
H	molar purge-to-total product ratio
i	cell number
L	column length
n	concentration of sorbate in solid phase
N	number of moles entering or leaving adsorber per cycle or total number of cells
P	gas pressure
R	gas constant
t	time
T	temperature
U	interstitial gas velocity in bed
V	concentration velocity defined in Eq. (13)
y	gas phase mole fraction of light gas
ΔZ	cell length

Greek symbols

β	separation factor β_h/β_l
β_i	equilibrium ratio of gas capacity of component i to total capacity of gas and solid phases for component i
ϵ	void fraction
ρ	recovery of light gas
ρ_s	density of solid particles
θ	product cut, moles of product per mole of feed
τ	dimensionless time

Subscripts

BD	refers to blowdown
F	refers to feed
h	refers to heavy gas
H	refers to high pressure
l	refers to light gas
L	refers to low pressure
PG	refers to purge
PRD	refers to high pressure product
PRS	refers to pressurization

Literature Cited

1. Jones, R. L.; Keller, II, G. E.; Wells, R. C., U.S. Patent 4,194,892, March 25, 1980.
2. Turnock, P.; Kadlec, R. H. A.I.Ch.E. J. 1971, 17, 335.
3. Flores Fernandez, G.; Kenney, C. N. paper presented at San Francisco A.I.Ch.E. Meeting, November, 1979.
4. Hill, F. B. Chem. Eng. Commun. 1980, 7, 37.
5. Skarstorm, C. W. Ann. N.Y. Acad. Sci. 1959, 72, 751.
6. Shandalman, L. H.; Mitchell, J. E. Chem. Eng. Sci. 1972, 27, 1449.
7. Chan, Y. N. I.; Hill, F. B.; Wong, Y. W. Chem. Eng. Sci. 1981, 36, 243.
8. Knaebel, K. S.; Hill, F. B. paper presented at Washington A.S.M.E. Meeting, November, 1981.
9. Kawazoe, K.; Kawai, T. Kagaku Kogaku 1973, 3, 228.
10. Mitchell, J. E.; Shandalman, L. H. A.I.Ch.E. Symp. Ser. 1973, 39, 134, 23.
11. Chihara, K.; Suzuki, M. paper presented at 2nd World Congress of Chem. Eng., Montreal, Canada, October, 1981.
12. Richter, E.; Knoblauch, K.; Jüntger, H. paper presented at the 7th Int. Congr. of Chem. Eng. Chem. Equipment Des. and Automation, Chisa '81, Praha, Czechoslovakia, Aug. 31-Sept. 4, 1981.
13. Hindmarsh, A. C. "GEAR: Ordinary Differential Equation System Solver"; Lawrence Livermore Laboratory, Report UCID-30001, Revision 3, December, 1974.
14. Grant, K. J.; Manes, M. I.E.C. Fundamentals 1966, 5, 490.

RECEIVED December 28, 1982

Methane/Nitrogen Gas Separation over the Zeolite Clinoptilolite by the Selective Adsorption of Nitrogen

T. C. FRANKIEWICZ and R. G. DONNELLY

Occidental Research Corporation, PO Box 19601, Irvine, CA 92713

N_2 diffuses into the structural pores of clinoptilolite 10^3 to 10^4 times faster than does CH_4 . Thus internal surfaces are kinetically selective for N_2 adsorption. Some clino samples are more effective at N_2/CH_4 separation than others and this property was correlated with the zeolite surface cation population. An incompletely exchanged clino containing doubly charged cations appears to be the most selective for N_2 . Using a computer-controlled pressure swing adsorption apparatus, several process variables were studied in multiple cycle experiments. These included feed composition and rates, and adsorber temperature, pressure and regeneration conditions. N_2 diffusive flux reverses after about 60 seconds, but CH_4 adsorption continues. This causes a decay in the observed N_2/CH_4 separation. Therefore, optimum process conditions include rapid adsorber pressurization and short adsorption/desorption/regeneration cycles.

Nitrogen is weakly adsorbed on the surfaces of numerous zeolites. The surface attraction arises as a result of the nuclear induced quadrupole moment possessed by N_2 . The effect is weak and heats of adsorption for N_2 are low. Methane is a weakly polarizable molecule which, as a result of this polarizability, is also weakly adsorbed on zeolites. In general, H_{ADS} for CH_4 is equal to or slightly greater than H_{ADS} for N_2 and as a result an adsorption separation of these gases either does not occur or happens by a weakly selective CH_4 adsorption. In the 1950s, Habgood (1) discovered that he could selectively adsorb N_2 from a CH_4/N_2 mixture by cooling a 4A molecular sieve to between 0° and $-78^\circ C$. However, his system was limited by slow kinetics, a weak selectivity, and the need to "thermally" regenerate the sorbent.

0097-6156/83/0223-0213\$06.25/0

© 1983 American Chemical Society

Recently, we found that the naturally occurring zeolite clinoptilolite could selectively adsorb N_2 in the presence of CH_4 near ambient temperature. This paper will show the selectivity to be kinetic rather than thermodynamic and that only clinoptilolite (clino) with the appropriate surface cation population will effect the separation. In addition, we review our results from several series of pressure swing CH_4/N_2 separation experiments and show how to design a process to use this effect. An economic evaluation suggested the process would be economically viable for small plants (2×10^6 ft³/day).

Characterization of Clinoptilolite

Clinoptilolite is an abundant, naturally occurring zeolite whose structure has recently been determined (2,3). The clino structure is nearly identical to that of heulandite. A combination of lower Al^{+++} in the framework and an extra stable cation position appears to render clino thermally stable relative to heulandite.

Clino has a layer structure with the AC or (010) plane being impervious to gaseous diffusion of any kind. Parallel to the C-Axis (001) are alternating channels defined by 8- and 10-membered framework oxygen atom rings. The 8-member ring channel dimensions are about 4.6 x 4.0 Å while the larger channels are 7.0 x 4.3 Å. Parallel to the a-axis (100) are uniform 5.4 x 3.9 Å channels defined by 8-membered framework oxygen atom rings (4).

Early work on the catalytic behavior of clinoptilolite found that clinos from different geographic locations generally possessed widely differing properties (5). The most likely explanation is that naturally occurring clinos possess varying degrees of cation deficiency and that this deficiency variation results in a significantly altered pore accessibility. This property also leads to the unique CH_4/N_2 molecular sieving capability of this mineral. Table 1 shows how BET surface areas and CH_4/N_2 separations ability correlate with the degree of ion exchange in 4 clino samples.

The zeolites designated ZBS-14 and ZBS-15 are clinos from two separate deposits owned by an Occidental Petroleum subsidiary, Occidental Minerals, Inc. H-ZBS-15 is a decationized version of its parent. Ash Meadows is an ARCO owned deposit and represents a completely ion exchanged clino sample.

Heat of Adsorption Measurements

Using a gas chromatographic technique (6-11), apparent heats of adsorption

$$H_{ADS}(\text{apparent}) = H_{ADS}(\text{actual}) + E_a(\text{diffusion}) \quad (1)$$

were measured for Ar, N₂, and CH₄ on the samples listed in Table I and on several decationized and partially ion exchanged versions of the parent minerals. These results are listed in Table II. Note that for the most open clino, decationized ZBS-15, the heats of adsorption for CH₄ and N₂ are the same. As the zeolite is progressively re-cationized, the accessibility of CH₄ to the internal crystal surfaces progressively decreases. This is reflected in a lower determination for H_{ADS} (12). Finally, in the completely cation exchanged ash meadows sample, even H_{ADS} for N₂ begins to show a decrease. The conclusion is that given equal access to internal surfaces, CH₄ and N₂ will be equally adsorbed. However, molecular sieving can still effect a separation. Based upon an analysis of the H_{ADS} measurements and the g.c. peak shapes obtained, we can make a semi-quantitative assessment of the structural pore accessibility for several gases into the zeolites listed in Table II. This is shown in Figure 1. The shaded band represents the desired pore access cut-off for maximum CH₄/N₂ separation.

Capacity and Kinetics for CH₄/N₂ Adsorption

Given the ability of the clino ZBS-15 to effect CH₄/N₂ separation chromatographically, we measured a high pressure adsorption isotherm for N₂ and diffusion kinetics for CH₄ and N₂. A complete isotherm for CH₄ was not taken due to slow kinetics, but at low pressures (P_{CH₄} < 50 psia), CH₄ and N₂ capacities appeared to be similar. The apparatus used for both measurements is shown schematically in Figure 2. Gas adsorption capacities and rates are determined by following gas pressure vs. time. A Van der Waals equation of state is used to calculate total number of moles of gas in the ballast prior to adsorption and in the ballast and adsorber after adsorption is complete. The difference in these numbers is the adsorbed gas and the rate at which gas is adsorbed is directly related to the diffusion coefficient by equation (2). The apparatus is monitored and controlled by a Digital Equipment Company laboratory computer (MINC). During the determination of diffusion coefficients in a mixed gas system, a sample line is installed and bed samples analyzed on a quadrupole mass spectrometer. The mass spec is also monitored by the MINC with data acquired at 16 msec. intervals.

The adsorption isotherm for N₂ onto ZBS-15 at 20°C is shown in Figure 3.

The diffusion coefficient for a gas into a solid may be determined by measuring P vs t and making the plots exemplified by Figures 4(a) and 4(b). In Figure 4, the relative amount of gas adsorbed in the experiment, R from equation (2), is plotted vs.

Table I

Both Surface Areas and the Ability of Clinoptilolite
to Effect N₂/CH₄ Separation Are Correlated
With How Completely the Sample Is Ion Exchanged.

<u>Clino Sample</u>	<u>Total Ion Charge AI Content</u>	<u>Surface* Area</u>	<u>Ability to Separate N₂/CH₄</u>
H-ZBS-15	.12	71.9 m ² /g	None
ZBS-15	.38	52	Good
ZBS-14	.88	36	Modest
Ash Meadows	1.0	12	None

* N₂ BET measurements

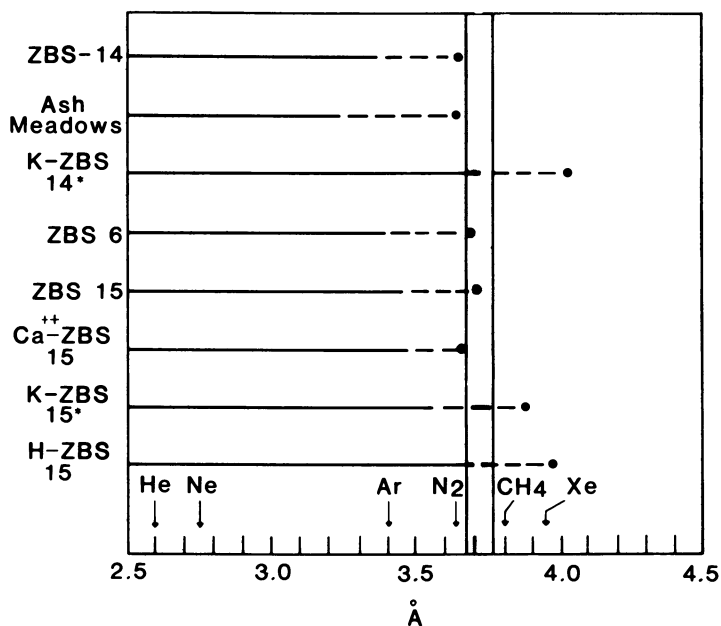
Table II

Apparent Heats of Adsorption for Several
Gases Over Various Clinoptilolites
(Kcal/Mole)

Apparent Heat of Adsorption

<u>Molecule Kinetic Diameter</u>	<u>Ar 3.40Å</u>	<u>N₂ 3.64Å</u>	<u>CH₄ 3.8Å</u>
<u>Zeolite</u>			
ZBS-14	0	5.0	0
K-ZBS-14*	4.2	5.1	5.1
ZBS-15	(-)	5.2	0
H-ZBS-15	4.2	5.3	5.1
Ca-ZBS-15*	3.8	5.9	1.2
K-ZBS-15*	3.7	5.3	0.8
Ash Meadows	(-)	3.8	0

*Partially Cation Exchanged
(-) not measured



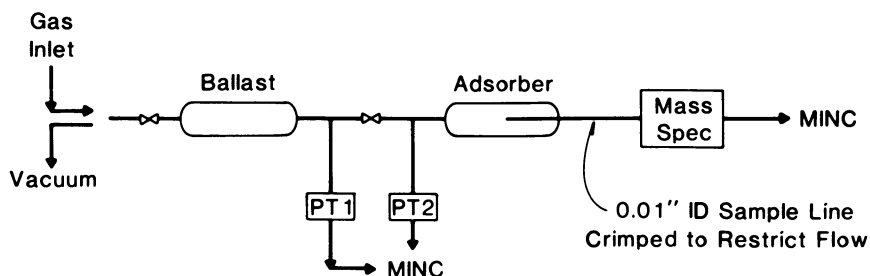
Easy Pore Access (—)

Hindered Pore Access (----)

Approx. Size Cut-Off for Pore Access (•)

* Partially Cation Exchanged

Figure 1. A semi-quantitative assessment of structural pore accessibility for several clino samples to a range of molecular kinetic diameters.



PT = Pressure Transducer

Figure 2. A schematic drawing of the apparatus used for the measurement of CH_4 and N_2 diffusion coefficients.

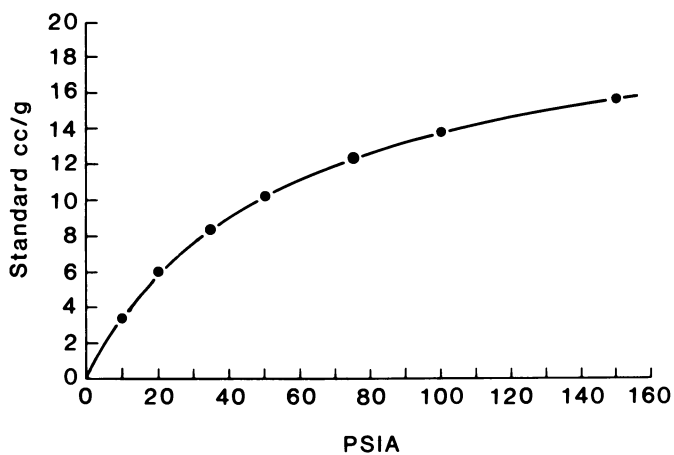


Figure 3. The adsorption isotherm (21 °C) for N_2 on the clinoptilolite designated ZBS-15.

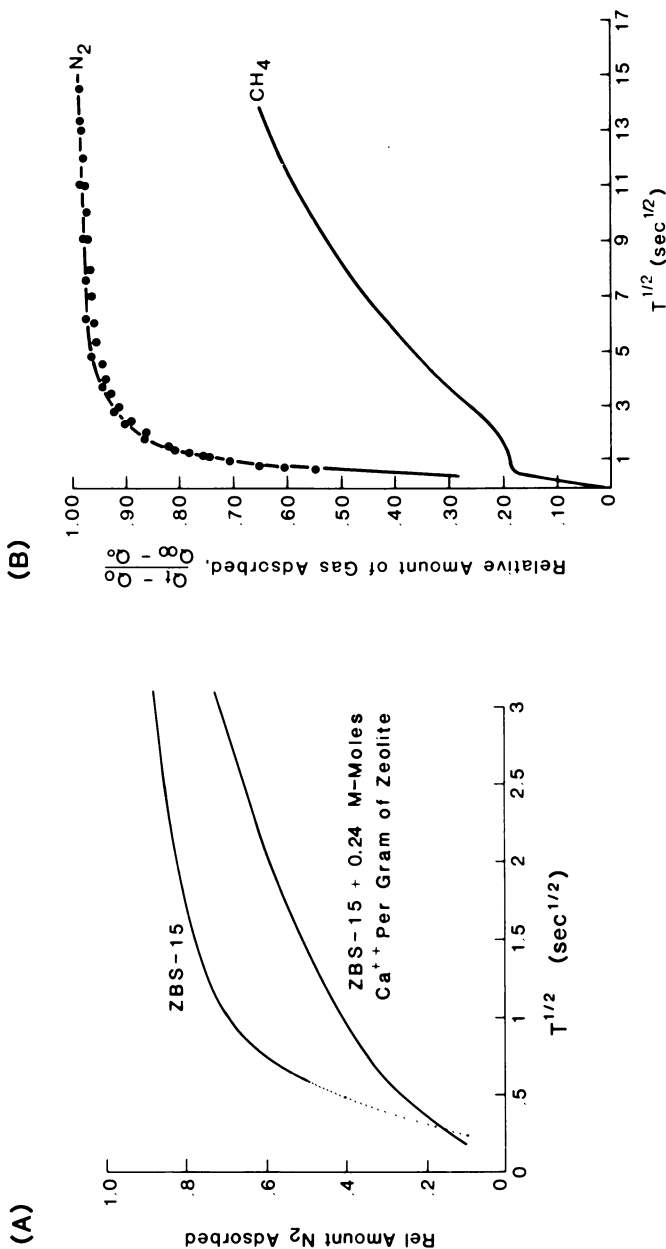


Figure 4. Representative curves are shown for the measurement of diffusion coefficients. (A) Curves are for N_2 adsorption onto the clinoptilolite (ZBS-15) and calcium impregnated ZBS-15. (B) Curves are for CH_4 and N_2 adsorption onto ZBS-15.

the square root of time. At sufficiently short times, the following equation is valid (13):

$$R = \frac{Q_t - Q_0}{Q_\infty - Q_0} = 2\frac{A}{V} \cdot \frac{1+K}{K} \cdot \sqrt{\frac{Dt}{\pi}} \quad (2)$$

$$K = \frac{(Q_0)_g - (Q_\infty - Q_0)}{Q_\infty} \quad (3)$$

where R = relative amount of gas adsorbed during run
 Q_0 = amt. of gas on the zeolite at $t = 0$
 Q_t = amt. of gas adsorbed at any time t
 Q_∞ = final amt. of gas adsorbed
 $(Q_0)_g$ = amt. of gas initially available for adsorption
 D = diffusion coefficient in cm^2/sec
 A/V = surface to volume ratio of the particle which is controlling diffusion

Representative results from diffusion measurements are illustrated in Figures 4(a) and 4(b) and tabulated in Table III. The "knee" in the CH_4 data at 0.2 relative adsorption indicates that about 20% of the total adsorption surface is rapidly accessed and is thus non-selective in CH_4/N_2 adsorption. Once this "external" surface region is saturated, adsorption occurs only in the crystallite structural pores, which are kinetically selective for N_2 . At very long times, adsorption approaches thermodynamic equilibrium, and there will be a tendency for the extra N_2 residing in structural pores to be replaced with CH_4 . Therefore, maximum separation at short times is predicted ($t < 9\text{-}25$ sec. in the case of ZBS-15), and separation will be higher in a process if subsequent gas-solid separation steps (e.g., depressurization) follow quickly. Significantly, measured diffusion coefficients were found to be independent of system pressure over a range of final pressures from 1 to 200 psia. Thus, the results presented here are likely to be applicable to real operating systems. Note that the addition of Ca^{++} to the ZBS-15 has a significant impact on the diffusion of both N_2 and CH_4 . The impact on N_2 is greater, however, and the ratio of the two diffusion coefficients drops somewhat. How this change affects pressure swing separation of the two gases will be discussed below.

Diffusion in Mixed Gas Systems

Since methane diffusion is much slower than nitrogen diffusion into clinoptilolite, it is reasonable to suspect that the presence of CH_4 on the zeolite surface will effectively slow the uptake of N_2 . If true, then it would be much more appropriate to measure D_{N_2} in the presence of CH_4 rather than in the pure gas system. To accomplish this, the apparatus of Figure 2 was modified by the addition of a 0.01" i.d. sample line which terminated

Table III

Summary Tabulation of Diffusion Coefficient
Measurements on ZBS-15 and Ca⁺⁺ Impregnated
ZBS-15, A/V = 1.67 x 10⁴

<u>Particle Size</u>	<u>Gas</u>	<u>Final System Pressure</u>	<u>D_{N₂}</u>	<u>D_{CH₄}</u>	<u>D_{N₂}/D_{CH₄}</u>
<u>As received ZBS-15</u>					
60 x 80 mesh	N ₂	27 psia	2.3x10 ⁻¹⁰ cm ² /sec		
"	N ₂	74	1.9x10 ⁻¹⁰		
20 x 50	N ₂	7	4x10 ⁻¹⁰		
6 x 10	CH ₄	11		1.2x10 ⁻¹⁴	2.0x10 ⁴
<u>Ca⁺⁺ impregnated ZBS-15</u>					
20 x 50 mesh	N ₂	12 psia	1.8x10 ⁻¹¹ cm ² /sec		
20 x 50	N ₂	172	1.7x10 ⁻¹¹		
20 x 50	CH ₄	11		5.8x10 ⁻¹⁵	3.1x10 ³

in the center of the zeolite adsorber. Adsorber gas composition was monitored by the MINC computer as analyzed every 16 msec. by the quadrupole mass spectrometer. System pressures were measured with Validyne pressure transducers and also monitored by the MINC. From this data, % N₂, % CH₄, and partial pressures of each gas can be calculated vs. time.

Figure 5 illustrates the mixed gas diffusion data for a pair of runs using 60% CH₄/40% N₂ as the feed gas. Note that N₂ adsorption is a maximum at about 10 seconds for ZBS-15 while CH₄ adsorption continues even after 15 minutes. It is important to realize that since N₂ diffusion reverses after 10 seconds, Q in equation (2) may be low and result in an artificially high value being calculated for D_{N₂}. With this caveat, D_{N₂} < 5 × 10⁻¹¹ cm²/sec for this mixed gas system over ZBS-15 (as received). Thus, the presence of methane in this gas mixture has reduced D_{N₂}/D_{CH₄} from 2.0 × 10⁴ (see Table III) to 3.3 × 10³. Table IV presents data for other gas mixtures with ZBS-15 and Ca⁺⁺ treated ZBS-15. Methane appears to have a lesser effect on N₂ diffusion in the Ca⁺⁺ treated ZBS-15, but the calculational caveat given above applies here as well.

The real impact of the difference in mixed gas diffusion rates for the two zeolites becomes apparent in Figure 6. Here Separation Factors vs Time are plotted for the two adsorbents. Note that for ZBS-15, maximum separation is observed at 20 seconds and has decayed to less than 1/2 of its maximum in the 90-180 sec. time frame which characterized most of the pressure swing experiments to be discussed below. The separation over Ca⁺⁺ treated ZBS-15 also decays but is still much improved over the as-received material even after 3 minutes.

The implications of Figure 6 for process design are significant. Using ZBS-15, a mean space time for an adsorber of about 20 seconds is optimum. For Ca⁺⁺ treated ZBS-15, this number can be increased to 60-120 seconds with no loss of separation relative to the parent zeolite. Due to very low initial pressure in the regenerated adsorber, the high pressure feed gas will expand and move very rapidly through the adsorber bed. As a result of this very short residence time (near t=0 in Figure 6), an initially poor separation CH₄/N₂ is predicted. Thus, initial adsorber effluent will be high in N₂ and may have to be discarded or recycled.

The Pressure Swing Separation of CH₄ and N₂

In order to investigate the process aspects of the pressure swing separation of CH₄ and N₂ the apparatus depicted in Figure 7 was constructed. Valves V1 through V5 are fitted with electric switching mechanisms that are interfaced to the MINC computer. The two pressure transducers, three mass flow meters, and column

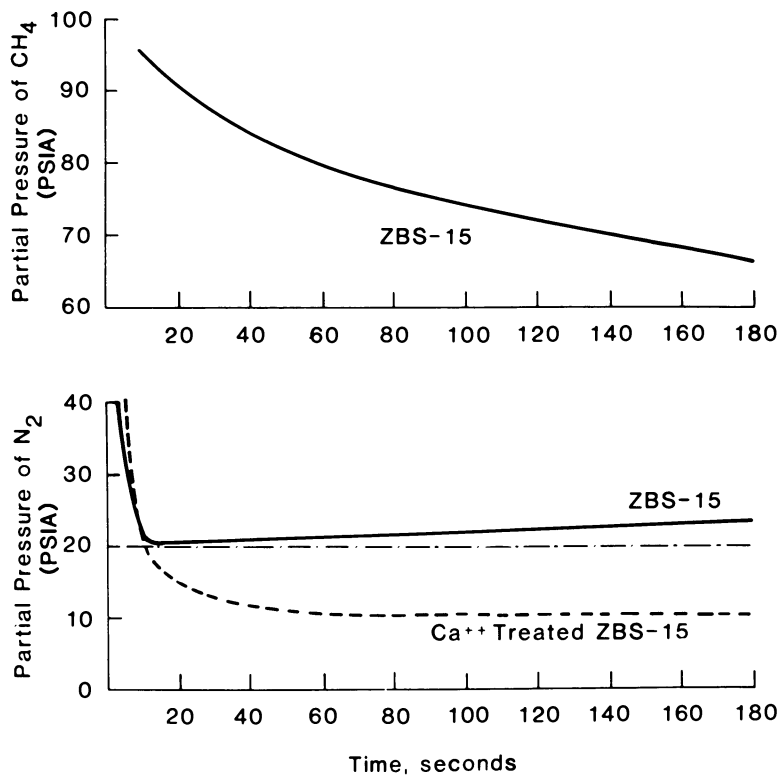


Figure 5. Partial pressure vs. time curves show how the addition of Ca^{++} to ZBS-15 improves its ability to retain N_2 .

Table IV

Diffusion Coefficients Were Measured Vs. Gas Composition for (1) ZBS-15 and (2) ZBS-15 + .24 m moles/g of Ca^{++} . The Presence of CH_4 Slows N_2 Diffusion.

<u>Zeolite</u>	<u>Feed Gas</u>	<u>D_{N_2}</u>	<u>$D_{\text{N}_2}/D_{\text{CH}_4}^*$</u>
(1) ZBS-15	N_2	$23 \times 10^{-11} \text{ cm}^2/\text{sec}$	2.0×10^4
	60% CH_4	5×10^{-11}	
	80% CH_4	4×10^{-11}	3.3×10^3
	90% CH_4	4×10^{-11}	
(2) ZBS-15 + .24 m moles Ca^{++}/g	N_2	$1.8 \times 10^{-11} \text{ cm}^2/\text{sec}$	3.1×10^3
	80% CH_4	1.2×10^{-11}	3.0×10^3
	90% CH_4	1.3×10^{-11}	

* D_{CH_4} is assumed to be unchanged from the pure gas measurement

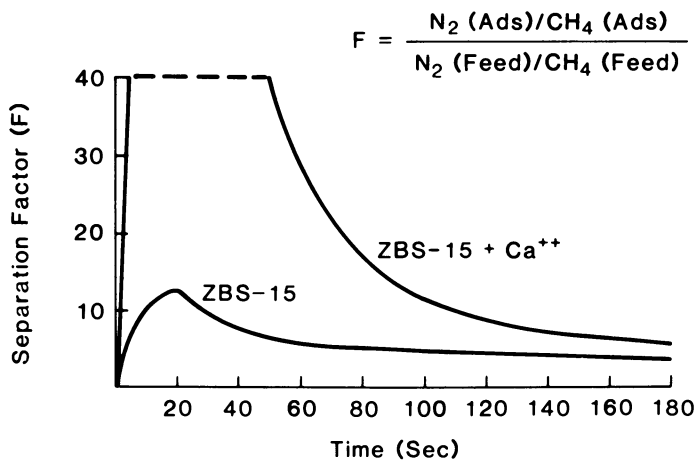


Figure 6. Ca^{++} impregnated ZBS-15 shows an enhanced ability to separate CH_4 and N_2 .

V = Electrically Operated Valve
 PT = Pressure Transducer
 FM = Mass Flow Meter
 BPR = Back Pressure Regulator
 C = Adsorption Column
 F = In-line Gas Filter

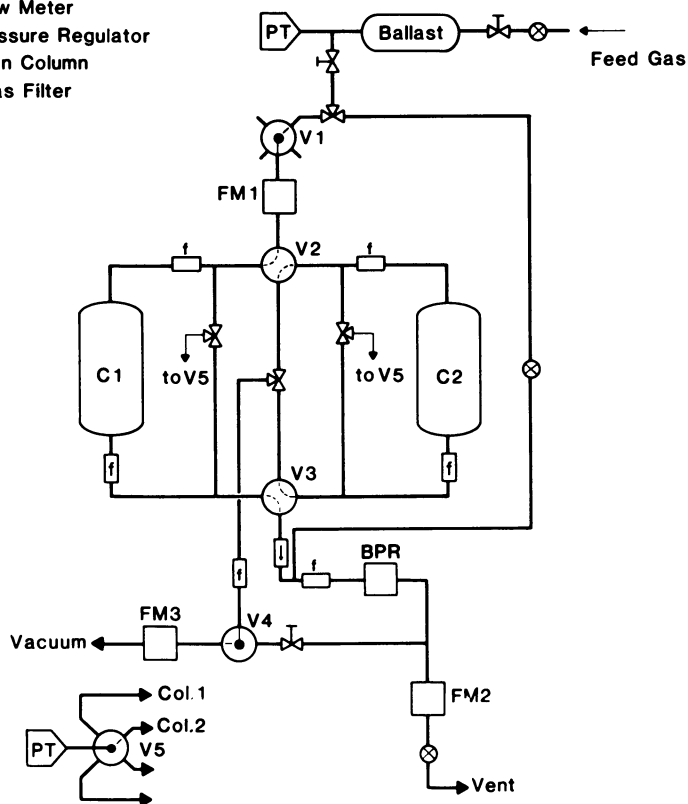


Figure 7. A schematic drawing of the computer-controlled pressure swing apparatus.

temperature are also monitored by the MINC. All gas effluent from the apparatus through vent or vacuum is sampled through a molecular leak valve for analysis by the quadrupole mass spectrometer. The mass spec in turn reports these compositions to the MINC. Once a run is initiated, the apparatus is under complete control of and monitored by the MINC.

The back pressure regulator (BPR) is set to give the desired pressure in the adsorption column (C1 or C2) being used. Although it is possible with this apparatus to involve both columns alternately in a separations experiment, this was not done during our runs so that all vent and vacuum regeneration gases could be analyzed for every cycle in the run. During a pressure swing run, gas enters the adsorption column, C1 or C2, through valve V2. Valve V3 is set to allow gas to exit the selected adsorber through the back pressure regular (BPR) as soon as the desired operating pressure is achieved. For depressurization, V3 is switched to allow the column exit gas to bypass the BPR and be vented through valve V4. V4 is a vacuum/vent selector and V5 allows a single pressure transducer to monitor system pressures at up to four selected points.

A sample data plot is shown in Figure 8. Feed gas is 40% N₂ and 60% CH₄. A mass balance is calculated for CH₄ and N₂ for each step in the process as well as for the complete adsorption cycle. The mass balance includes a Van der Waals calculation of the amount of gas stored in column voids and the volume of gas adsorbed on the zeolite. Typically, the independently calculated mass balances for CH₄ and N₂ were 100 ± 3%.

Table V lists the independent variables and their respective ranges which were included in this study. Dependent variables can be defined in numerous ways depending upon the objectives of the particular experimental series being conducted. Typically, a pressure swing adsorption cycle program is input to the apparatus's computer control program, e.g., per Figure 8, and the cycle repeated under computer control until the experimental objective is achieved. For this work, 6-24 cycles were normally used with total run times up to 8 hours.

Figures 9 and 10 illustrate changes in two dependent variables: dynamic N₂ adsorption capacities and CH₄/N₂ separation factors. Independent variables are column temperature, operating pressure, and time allowed for vacuum regeneration. This experimental series used a constant feed rate of 6.0 l/min over a time of 1.00 min into a 1" dia. x 24" long adsorber filled with 180g of zeolite. Column depressurization took place for 1.00 min. and this was followed by a variable length vacuum regeneration.

Adsorbent particle sizes, although not a design variable, did affect some results for hydrodynamic reasons. As can be seen from the centerpoints, a slight deterioration in column performance resulted with the switch from a 60 x 80 to a 6 x 10 mesh adsorbent. Although this effect was real and reproducible, the effects of the three design variables were generally more significant.

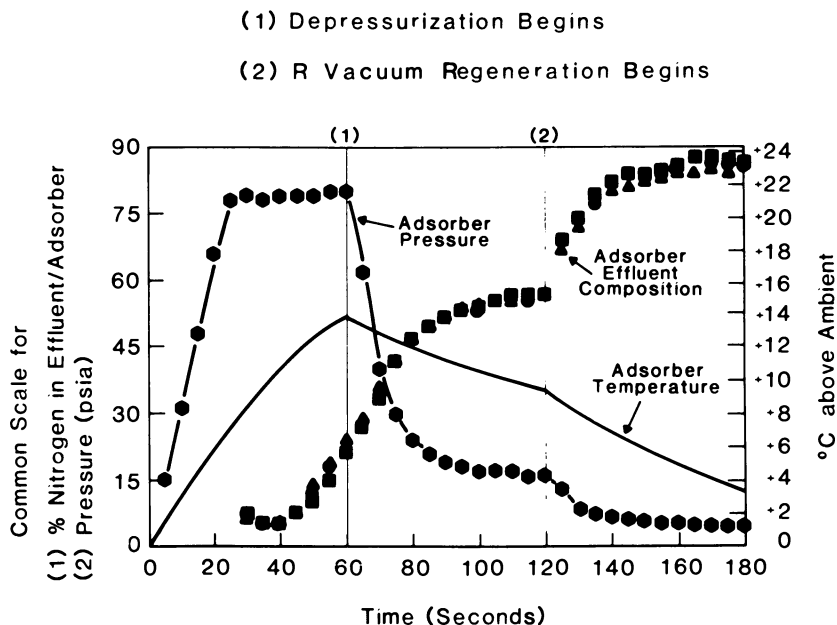


Figure 8. Adsorber parameters are plotted vs. time for a pressure swing run. Note the common scale for %N₂ and adsorber pressure.

Table V

Operational Variables and Variable Ranges Studied for the Pressure Swing Separation of CH₄ and N₂

Gas Feed Rate	16.7 - 50.0 scc/g. of zeolite-min.
Feed gas composition	10 - 40% N ₂
Adsorber Temperature	0° - 55°C
Operating Pressure	75 - 300 psia
Adsorber Granule Size	.18 - 3.5 mm
Column Regeneration	0 - 20 min. vacuum or CH ₄ purge

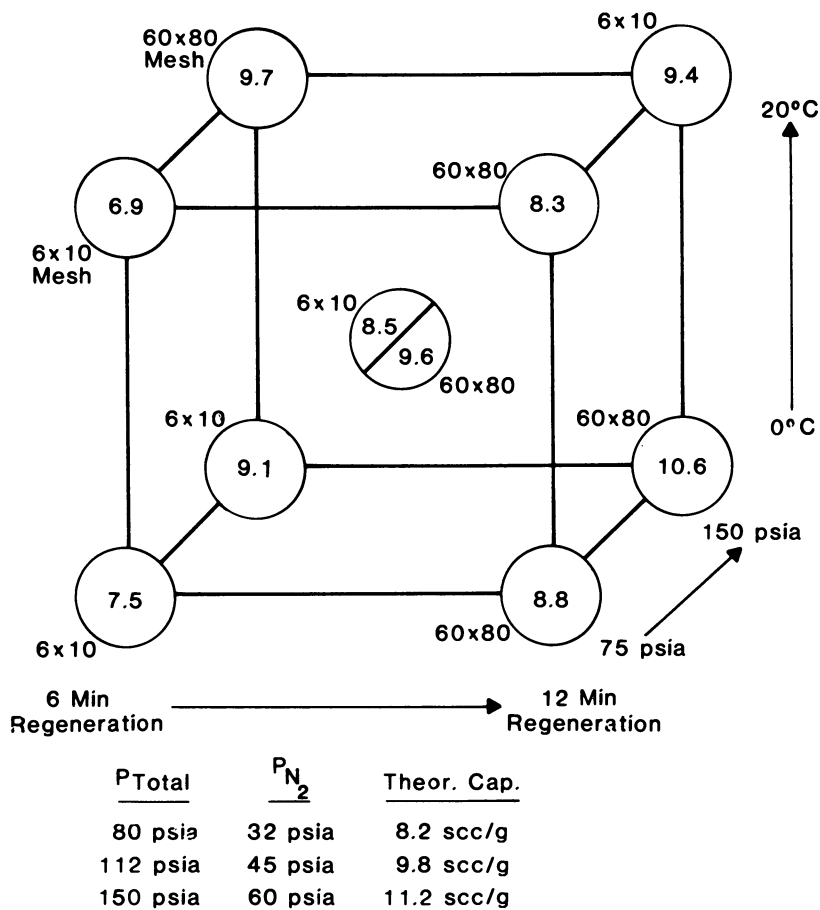
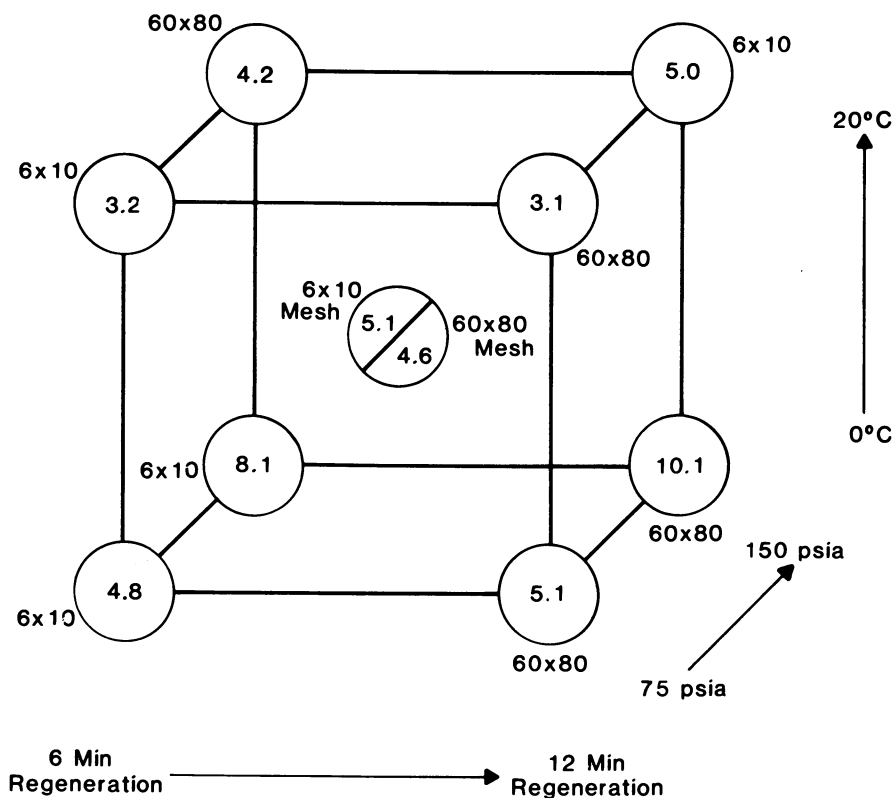


Figure 9. Average SCC of N_2 adsorbed per gram of the clino ZBS-15 for a 3 variable factorial design experimental series. Feed was 33.3 SCC/g of zeolite per cycle of 40% N_2 /60% CH_4 gas.



$$\text{Separation Factor} = \frac{\text{N}_2 (\text{ads})/\text{CH}_4 (\text{Ads})}{\text{N}_2 (\text{Gas})/\text{CH}_4 (\text{Gas})}$$

Figure 10. CH_4/N_2 separation factors for a 3 variable factorial design experimental series. Feed was 33.3 SCC/g of zeolite per cycle of 40% N_2 /60% CH_4 gas.

At the bottom of Figure 9, capacities derived from the clino N₂ adsorption isotherm (see Figure 3) are also listed. The factorial design results suggest that over 90% of the theoretical N₂ adsorption capacity can be dynamically used in a pressure swing process provided absorbent regeneration is adequate. Note that column temperature does not strongly affect dynamic N₂ adsorption capacity, but does influence N₂/CH₄ separation factors in the process. This results from a slowing of CH₄ adsorption kinetics as temperature is decreased.

The longest step in the pressure swing cycle for CH₄/N₂ over clinoptilolite is regeneration. Because this step involves vacuum and represents unproductive time in the process, regeneration was closely studied. Regeneration times were varied from 10 sec. to 20 minutes and regeneration mode was changed from vacuum (approx. 20 torr system pressure) to quiescent to CH₄ purge. The results for 5 of these runs are summarized in Figure 11 for a 20% N₂, 80% CH₄ feed gas. It appears that a vacuum regeneration time of at least 6 minutes is required to maintain product quality over multiple cycles. Other modes of regeneration were not successful and it appears that a process design cannot reasonably incorporate anything but vacuum regeneration.

Process Design & Economics

Using the detailed mass balance data for the experiments described above, a commercial process design was developed and subjected to an economic analysis. The process involves the use of 10 adsorber beds sized to handle 2.0 or 20.0 x 10⁶ SCF/day of feed gas containing 20-30% N₂ and 70-80% CH₄. The product varies from 90-95% methane depending upon the feed composition. Pressure swing separations costs were found to be \$.35/10⁶ Btu for the larger plant and \$1.20/10⁶ Btu for the smaller plant. Corresponding costs for cryogenic separation of the same feedstocks were estimated to be \$.29/10⁶ Btu for the 20 x 10⁶ SCF/day plant and \$1.66/10⁶ for the smaller plant. In all cases, capital charges assumed a 20% DCF-ROI. Thus pressure swing separation of CH₄/N₂ appears to be viable for small plants. Complete details of the process design and economic evaluation are being prepared for publication elsewhere.

Conclusions

The major points to be drawn from this work are:

The use of molecular sieving for the diffusive separation of molecules very close in size (3.64 Å vs 3.8 Å kinetic diameters) with commercially viable productivities is possible.

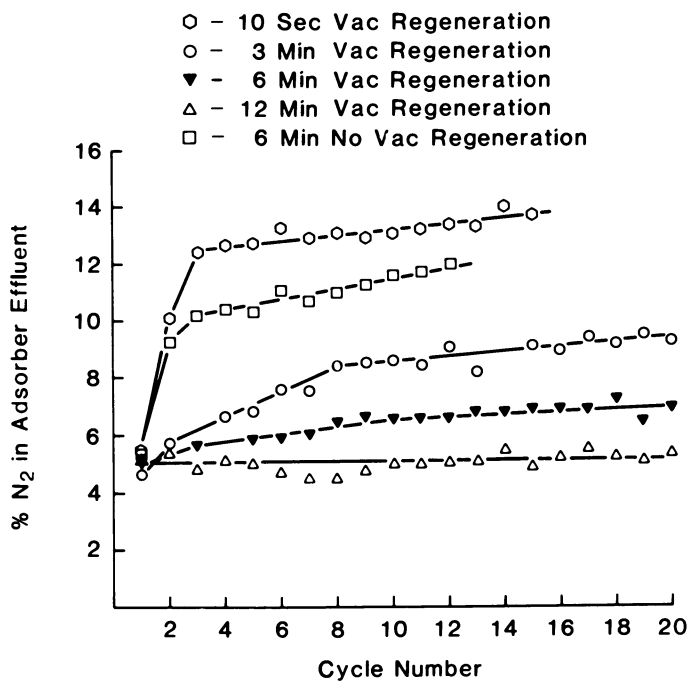


Figure 11. Product quality from an adsorber varies as the regeneration time is varied. Feed gas is 20%N₂/80%CH₄.

The surface cation population of the clinoptilolite adsorbent controls the effectiveness of CH₄/N₂ separation.

The pressure swing separation of CH₄/N₂ is economically viable for small plant sizes, but cryogenic separation is more attractive at larger plant sizes.

Adsorbent improvement and engineering optimization may yield additional cost improvements.

Prior to an actual field trial of this technology, additional research is required. This additional work includes:

Determining the effect of trace inorganic gases (H₂O, CO₂, H₂S...) on the separation.

Determining the effect of higher hydrocarbons on long-term adsorbent performance.

Optimization of CH₄ and N₂ adsorption kinetics through the control of adsorbent surface cation population.

Engineering optimization, especially in the areas of adsorber sizing and aspect ratio as well as process flow strategy.

Acknowledgments

We wish to express our gratitude to Dr. J. Shih for his assistance in the economic analyses and to Mr. L.A. Young for his process control and data analysis programming for these experiments. We also thank Occidental Minerals, Inc. for partial funding of this research.

Literature Cited

- (1) H.W. Habgood, U.S. Patent 2,843,219, 7/15/58.
- (2) A. Alberti, *TMPM Tschermaks, Min. Petr. Mitt.* 22, 25-37 (1975).
- (3) K. Koyama and Y. Takeuchi, *Zeitschrift fur Kristallographie* 145, 216-239 (1977).
- (4) A.B. Merkle and M. Slaughter, *American Mineralogist* 53, 1120-1138 (1968).
- (5) N.Y. Chen, et al., *Natural Zeolites*, L.B. Sand and F.A. Mumpton, ed., Pergamon Press, N.Y., 1967, p. 411.
- (6) S.A. Greene & H. Pust, *J. of Physical Chemistry* 65 (1), 55 (1958).
- (7) P.E. Eberly, Jr., *J. of Physical Chemistry* 65 (1), 68 (1961).

- (8) P.E. Eberly, and E.H. Spencer, *Trans, Fara. Soc.* 57, 289 (1961).
- (9) S. Ross, J.K. Saelens, and J.P. Olivier, *J. of Physical Chemistry* 66 (4), 696 (1962).
- (10) R.J. Neddenriep, *J. of Coll. & Interf. Science* 28 (2), 293 (1968).
- (11) *CRC Handbook for Chromatography, Vol. II.*, Gunter Zweig and J. Sharma, ed., CRC Press, West Palm Beach, Fla., 1972.
- (12) Donald W. Breck, *Zeolite Molecular Sieves*, J. Wiley & Sons, New York, 1974.
- (13) R.M. Barrer, *Molecular Sieve Zeolites II*, *Advances in Chemistry Series No. 102*, R.F. Gould, Ed., American Chemical Society, Washington, D.C., 1971.

RECEIVED December 27, 1982

Separation of Methane from Hydrogen and Carbon Monoxide by an Absorption/Stripping Process

VI-DUONG DANG

The Catholic University of America, Department of Chemical Engineering and Materials Science, Washington, DC 20064

An absorption/stripping process calculation using propane as the absorption solvent for separation of methane from hydrogen and carbon monoxide has been performed. Detailed material and energy balances for the process as well as the dimensions of the absorber and the stripper are reported. Other major pieces of equipment such as heat exchangers pumps, and compressors were evaluated in order to determine the equivalent electrical energy of the process as approximately 13550 cal(e)/gm-mole methane produced. The purity of methane in the final stream is 96% by volume at 100°F and 1000 psia. The present process appears to be a potential working process for methane separation in large quantity.

In coal gasification processes such as the flash hydrolysis or the Exxon catalytic process, methane is the major desired end product. However, methane is usually produced along with hydrogen and/or carbon monoxide. To obtain pipeline grade methane, it is necessary to develop economical methods of separating methane from hydrogen and/or carbon monoxide mixtures. The hydrogen and carbon monoxide are then recycled in the process. Several separation technologies such as absorption/stripping, cryogenic, clathrate formation have been examined (1). In this report, a method of absorption/stripping using propane as the solvent is presented. Absorption/stripping is a well-known chemical engineering operation and can be readily designed and constructed on a large scale. Therefore, the present method can be considered as a potentially useful method.

In the present work, a feed gas mixture of 40% CH₄, 45% H₂, and 15% CO at 100°F and 500 psia is to be separated. A production capacity of 250 x 10⁶ scf/day of CH₄ is assumed. The methane is delivered to the pipeline at 100°F and 1000 psia. For the application of absorption/stripping, it is desirable to utilize a

0097-6156/83/0223-0235\$06.00/0

© 1983 American Chemical Society

solvent which has a high solubility for methane. Table I shows some solubility data for methane in water and in various organic solvents. It is seen that methane has a higher solubility in propane than in any of the other solvents listed. Therefore, propane was chosen as the solvent for the absorption/stripping separation process investigated in this report.

Operating conditions for the absorption and stripping towers are important design parameters for the process. Due to vapor pressure and entrainment, propane will be present in the effluent gas streams from both the absorber and stripper. Usually this quantity of propane is not recovered and is considered an economic loss. The amount of propane in the gas phase is mainly dependent on the operating temperature and pressure of the towers.

Figure 1 shows the vapor pressure of some of the relevant compounds as a function of temperature. At -230.8°F and -184°F , the vapor pressure of propane is about 0.1 mm Hg and 1 mm Hg respectively. Absorption/stripping process is a conventionally practical process so it is decided to evaluate the separation of methane from hydrogen and carbon monoxide by this process. Since the operating pressures of the absorber and stripper are about 500 psia and 487 psia respectively, the mole fractions of propane in the outlet gas streams of the absorber and stripper are about 6.75×10^{-6} and 1×10^{-4} at -230.8°F and -184°F respectively. When the absorber operates at higher temperature as shown in Table II, propane losses increase. When the absorber and stripper operate at -230.8°F and -184°F respectively, the propane loss is equivalent to about 0.0850% and 3.28% respectively of the cost of methane assuming the cost of methane and propane is the same. This low percentage of propane loss was considered acceptable. Hence it was determined to operate the absorber at -230.8°F and the stripper at -184°F .

Process Description

A schematic process flow sheet is shown in Figure 2. Inlet gas, a mixture of methane, hydrogen and carbon monoxide at 100°F and 500 psia (stream 1) is successively cooled to -140°C by the outlet gas stream from the absorber and some recycle gas. The absorber is a packed column of 1-in. berl saddles with 50% void fraction. The rich liquid from the bottom of the absorber is heat exchanged with the bottom liquid from the stripper. The stripper is also a packed column with 1-in. berl saddles. The dissolved methane, hydrogen, and carbon monoxide is stripped out by heating at the bottom of the stripper. The outlet gas stream from the stripper is heated in a heat exchanger by a recycle gas stream and is further compressed to produce the final methane product at 100°F and 1000 psia.

To perform a further detailed process calculation on this multi-component absorption and stripping process, vapor liquid equilibrium data for methane, hydrogen, and carbon monoxide is

Table I. The Solubility of Methane in Water and in Organic Solvents at 77°F and at Pressures up to 140 Atmospheres

Pressure, atm	cc CH ₄ (at 77°F and 760 mm) dissolved in 1.0 cc solvent at pressure					
	20	40	60	80	100	140
Water	0.9	1.2	1.8	2.0	2.6	3.3
Methanol (1)	9.0	19.0	29.5	41.0	55.0	--
Ethanol	7.5	14.5	21.5	29.5	38.0	48.0 (120 atm)
Propane	41	83	125	174	200 (90 atm)	--
Butane	37	71	107	144	--	--
Pentane	33	63	97	129	164	--
Hexane	30	59	89	120	--	--
Octane	24	51	80	110	140	--
Cyclohexane	15	33	56	83	--	--
Benzene	11	24	41	59	80	--
Heavy Naphtha	10	20	31	43	--	--
Gas Oil	8	16	23	32	41	62

(1) The solubility of methane in n-propanol, isopropanol, n-butanol and iso-butanol is, within experimental error, the same as in methanol.

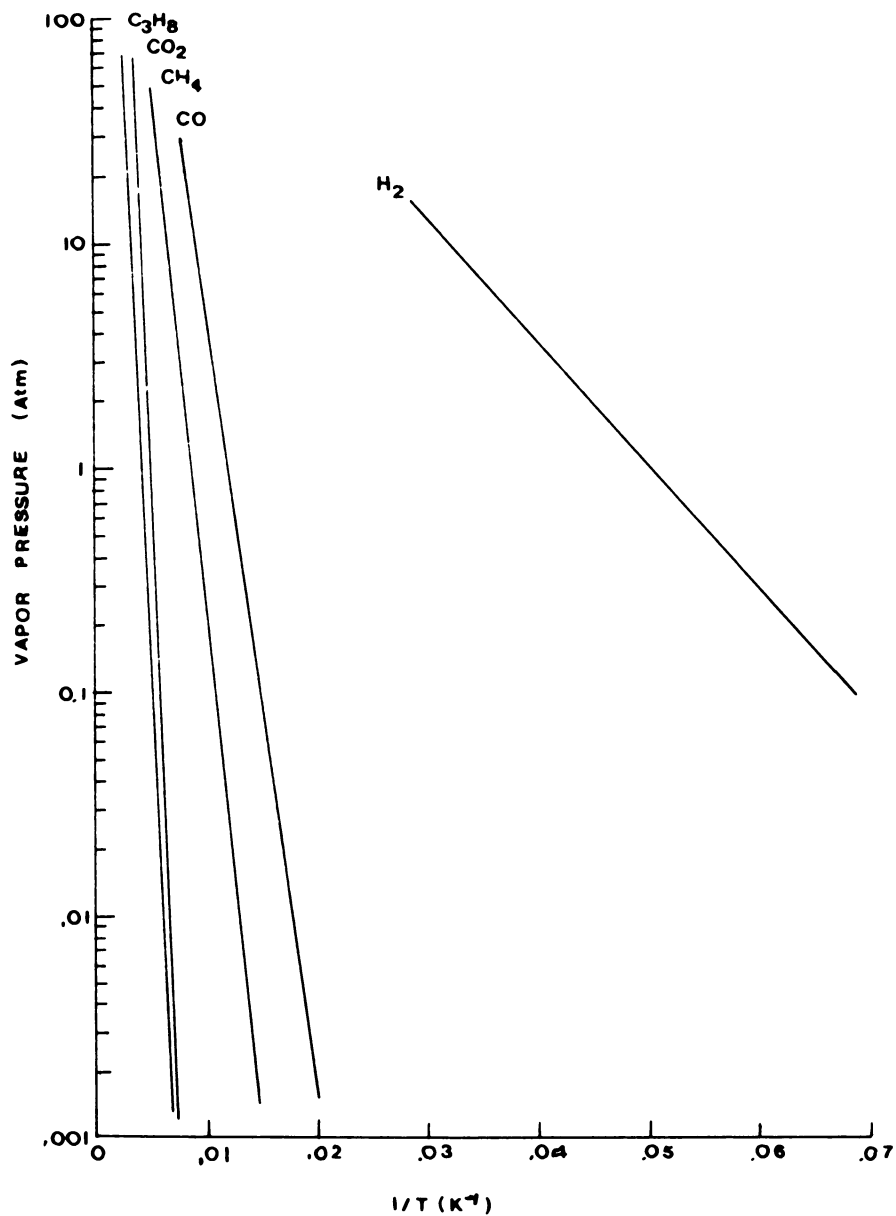


Figure 1. Vapor pressure of selected compounds vs. $1/T$.

Table II. Propane Losses at Different Absorber Temperatures
 (Stripper Temperature = -184°F)
 Plant Capacity: 250x10⁶ SCF/Day

T(°F)	lb/day loss of Propane			% of Propane Cost Loss Assuming Methane and Propane Cost to be the Same
	Absorber	Stripper	Absorber + Stripper	
- 58	2.79x10 ⁶			
- 76	1.58x10 ⁶			
-112	4.81x10 ⁵		1.19x10 ⁵	1.133
-148	1.11x10 ⁵	8415	1.319x10 ⁴	0.126
-200	4.77x10 ³	8415	8892	0.085
-230.8	4.77x10 ²	8415		

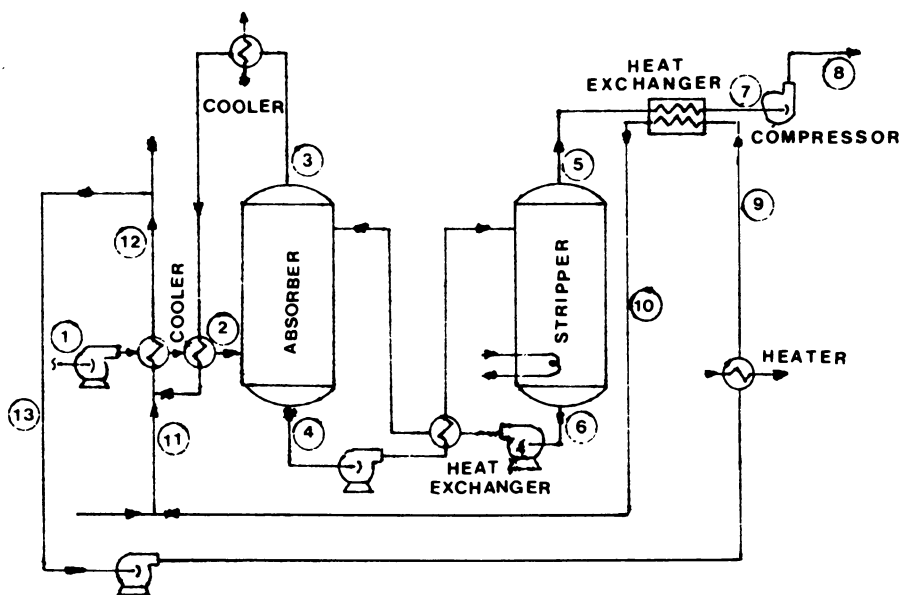


Figure 2. Flow diagram for methane separation by absorption/stripping method.

needed. Equilibrium K -values of methane and propane are obtained from DePriester (2). Solubility data for hydrogen in propane is obtained from Trust and Kurata (3). Solubility of carbon monoxide in propane is obtained from Prausnitz and Shair (4).

The absorber calculation is based on 1 lb-mole of gas stream entering into the bottom of the absorber. The entering liquid is fed at a rate of 1.5 lb-mole/lb mole of gas. For 95% methane removed, a preliminary estimate of methane absorbed is 0.38 lb-mole, carbon monoxide absorbed is 0.13 lb-mole, hydrogen absorbed is 0.1 lb-mole. The absorber is operated under isothermal conditions of -146°C . The liquid to gas mass ratio at the top of the tower is 3.85 while at the bottom it is 2.11 with an average value of 2.98. The key component is methane. Using a method of average absorption factor which for methane is 6.478 and 95% methane removal, it is possible to determine the number of theoretical transfer units to be 2. With these conditions, methane in the outlet gas stream of the absorber is 0.002 lb-mole, carbon monoxide is 0.13 lb-mole and hydrogen 0.44 lb-mole. The molar concentrations of the absorber effluent gas are CH_4 , 3.5×10^{-3} ; CO , 0.227; H_2 , 0.769; C_3H_8 , 6.75×10^{-6} . The molar concentrations in the liquid phase are CH_4 , 0.101; CO , 0.005; H_2 , 0.003; C_3H_8 , 0.891.

Absorber design requires the calculation of the quantity

$\frac{L}{G} \sqrt{\frac{\rho_G}{\rho_L}}$ which is 0.79 for the present case where L and G are mass

velocities of liquid and gas, ρ_L and ρ_G are densities of liquid and gas. At flooding conditions

$$\frac{G^2 \left(\frac{a_p}{\epsilon^3} \right) (\mu_L')^{0.2}}{g_c \rho_G \rho_L} = 0.05$$

where a_p is surface area of packing per unit tower volume, ϵ is fractional void volume of dry packing μ_L' is liquid viscosity, g_c is local gravitational constant. Therefore assuming 60% of flooding conditions, G is 2920 lb/hr ft². Since it is desired to produce 250×10^6 scf/day methane, the inlet gas flow into the absorber is 2.35×10^6 lb/hr.

From this and the gas mass velocity, it is determined that 3 towers are needed, each one with a diameter of 18.5 ft. The tower height is determined by the height of a transfer unit which is 20.7 ft. (5). Therefore, the height of the packed tower is 41.4 ft. Other detailed tower characteristics are given in Table III.

The stripping tower is operated at -120°C and 487 psia and the molar ratio of liquid to gas is 9.7. Again taking methane as the key component, and 95% methane stripped, about 0.0962 lb mole

Table III. Summary of Dimensions and Characteristics of Absorbers and Strippers

		<u>Absorbers</u>
Diameter of Absorber	=	18.5 ft
Number of Absorber	=	3
Height of Packed Tower	=	41.4 ft
Pressure Drop in Packed Tower	=	1.94 psia
Wall Thickness of Tower	=	2.98 in.
		<u>Strippers</u>
Diameter of Stripper	=	17.6 ft
Number of Stripper	=	3
Height of Packed Tower	=	22.8 ft
Pressure Drop in Packed Tower	=	0.41 psia
Wall Thickness of Tower	=	2.35 in.

of methane, 0.0045 lb-mole of carbon monoxide, 0.002 lb-mole of hydrogen are stripped. The preliminary estimates of the liquid to gas ratio is 26.7 at the top and 24.0 at the bottom with an average of 25.4. The average stripping factor for methane is 21.2 and two transfer units are needed. Under these conditions 0.0046 lb-mole of methane, 0.0032 lb-mole of carbon monoxide, and 0.00036 lb-mole of hydrogen remain in the bottom liquid phase. In the bottom outlet stream of the liquid phase, mole fractions of the chemical species are CH₄, 0.0051; CO, 0.0036; H₂, 0.0004; C₃H₈, 0.991. The outlet mole fraction of the gas phase from the stripper is CH₄, 0.960; CO, 0.019; H₂, 0.021; C₃H₈, 0.0001.

To design the stripper, again methane is chosen as the key component.

$\frac{L}{G} \sqrt{\frac{\rho_G}{\rho_L}}$ is taken to be 7.81. At flooding

$$\frac{G^2 \left(\frac{a}{\epsilon} \right) (\mu_L')^{0.2}}{g_c \rho_g \rho_L} = 0.0018$$

Therefore, the gas mass velocity is 1372 lb/hr ft² for 60% flooding condition with a gas mass flow of 1.28 x 10⁶ lb/hr. It is determined that 3 towers are required each one 17.6 ft in diameter. The height of a transfer unit is a 11.4 ft and the total height of a packed tower is 22.8 ft. Pressure drop in the tower is 0.41 lb/in². A summary of the composition of various streams is given in Table IV and stripper characteristics are given in Table III.

A thermal energy balance of the process is performed for the coolers, for streams 1 and 2 in Figure 2 and the heat exchanger between streams 5 and 7. The heat input for the heat exchanger between the absorber and the stripper is considered to be negligible. The electrical power input to the compressor is 5135 horsepower. The thermal energy load for the heater between streams 13 and 9 in Figure 2 is 2.2 x 10⁷ cal/min and for the cooler at the outlet gas stream from the absorber is 5.06 x 10⁷ cal/min. A further breakdown of the thermal energy requirement of the process is given in Table V. Detailed calculations are given in the Appendix. Combining the thermal energy and the pumping and compressing power required for the process as shown in Figure 2, the total thermal energy required is 30955 cal/g-mole which is about 11.8 times higher than the minimum ideal separation energy required which is calculated to be 2621 cal/g-mole CH₄.

Table IV. Temperature, Pressure, Flow Rate, and Mole Fraction of Different Numbered Streams in the Flow Diagram

Stream Number	Temp °F	Pressure psia	Flow Rate $\frac{\text{lb}}{\text{day}}$	Flow Rate $\left(\frac{\text{ft}^3}{\text{day}}\right)$	Mole Fraction			
					CH ₄	H ₂	CO	C ₃ H ₈
1	100	500	5.64×10^7	(2.32×10^7)	0.4	0.45	0.15	0
2	-230.8	500	5.64×10^7	(9.5×10^6)	0.4	0.45	0.15	0
3	-230.8	487	2.23×10^7	(8.68×10^6)	0.0035	0.769	0.227	6.75×10^{-6}
4	-230.8	500	8.48×10^8		0.1013	0.0025	0.0051	0.891
5	-184	485	3.06×10^7		0.96	0.021	0.019	0.0001
6	-184	487	8.12×10^8		0.0051	0.0004	0.0036	0.999
7	100	485	3.06×10^7		0.96	0.021	0.019	0.0001
8	100	1000	3.06×10^7	(4.64×10^6)	0.96	0.021	0.019	0.0001
9	110	487	7.1×10^6		0.0035	0.769	0.227	6.75×10^{-6}
10	-110	487	7.1×10^6		0.0035	0.769	0.227	6.75×10^{-6}
11	-100	487	1.77×10^8		0.0035	0.769	0.227	6.75×10^{-6}
12	90	487	2×10^8		0.0035	0.769	0.227	6.75×10^{-6}
13	90	487	7.1×10^6		0.0035	0.769	0.227	6.75×10^{-6}

Table V. Energy Requirement for the Separation of Methane
by Absorption/Stripping Using Propane

<u>Electrical Energy Requirement</u>	
Compressor Power (Horsepower)	= 5135
Pumping Power Required from Bottom of Absorber to Top of Stripper (Horsepower)	= 2.78×10^5
Pumping Power Required from Bottom of Stripper to Top of Absorber (Horsepower)	= 3.3×10^5
Pumping Power of Inlet Gas Blower (Horsepower)	= 4973
Estimated Pumping Power for Fluid Transport (Horsepower)	= 1796
<hr/>	
Total Pumping Power/g-mole methane produced	cal(ϵ)/g-mole = 12334
Equivalent Total Thermal Pumping Power/g-mole CH ₄	cal(t)/g-mole = 30834
<u>Thermal Energy Requirement</u>	
Thermal Energy Supplied to Heater Between Streams 13 and 9	cal(t)/g-mole = 36.5
Thermal Energy Load to Cooler in Absorber Outlet	cal(t)/g-mole = 84.1
<hr/>	
Total Thermal and Equivalent Electrical Energy	cal(t)/g-mole = 30955

Acknowledgment

Part of the work was performed at Brookhaven National Laboratory and was acknowledged hereby.

Literature Cited

1. Dravo Corporation "Hydrogasification Gas Processing Studies"; Contract CPD-7209, February 27, 1978.
2. DePriester, C. L. "Light-Hydrocarbon Vapor-Liquid Distribution Coefficients, Pressure-Temperature-Composition Charts and Pressure-Temperature Nomographs"; Chem. Eng. Progress Symp. 1953, 7, 49.
3. Trust, D. B.; Kurata, F. "Vapor-Liquid Phase Behavior of the Hydrogen-Carbon Monoxide-Propane Systems"; AIChE J. 1971, 17, 86.
4. Prausnitz, J. M.; Shair, F. H. "A Thermodynamic Correlation of Gas Solubilities"; AIChE J. 1961, 7, 682.
5. Bennett, C. O.; Myers, J. E. "Momentum, Heat and Mass Transfer"; 2nd ed., McGraw-Hill Co., 1974, pp. 571-574.

AppendixEnergy Calculation for the Separation of Methane from Process Gasification Stream Using Propane Absorption/Stripping

The energy calculations for the process are based on electrical and thermal energy. It is assumed that the heat exchanger between the absorber and the stripper operates ideally so no net heat loss or gain will be realized in this unit. The electrical energy requirements are for (1) the pumps between the absorber and the stripper, (2) the inlet gas blower, (3) the compressor at the end for the product methane, and (4) pumping power for fluid transport. Thermal energy is supplied for (1) the heater between streams 9 and 13, and (2) the cooler at the outlet of the absorber. The calculations will be performed separately in the following sections.

A. Pumping Power Required to Transport Fluid from Bottom of Absorber to Top of Stripper

$$\begin{aligned} \text{Liquid flow rate} &= 8.48 \times 10^8 \text{ lb/day} \\ &= \frac{8.48 \times 10^8 \text{ lb/day} \times 7.48 \text{ gal/ft}^3}{36.52 \text{ lb/ft}^3 \times 24 \text{ hr/day}} \\ &= 7.24 \times 10^6 \text{ gal/hr} = 1.21 \times 10^5 \text{ gal/min} \end{aligned}$$

$$\text{Density of liquid} = 36.52 \text{ lb/ft}^3$$

Height of stripping tower packing is 22.8 ft. Consider heading of the tower is 20% additional. Then the tower height ΔZ is 27.4 ft. The fluid is transported by 30 pipes and the diameter of the pipe is about 0.25 ft. The energy balance for each pipe is

$$\frac{g}{g_c} \Delta Z + 0.8 W_s + \frac{2fu^2L}{g_c D} = 0 \quad (\text{A-1})$$

$$\begin{aligned} \text{Velocity } u \text{ in each pipe} &= \frac{8.48 \times 10^8 \times 4}{24 \times 36.52 \times \pi \times 30 \times 0.25^2} \\ &= 6.56 \times 10^5 \text{ ft/hr} = 182.4 \text{ ft/sec} \end{aligned}$$

$$\text{Re} = \frac{u D \rho}{\mu} = \frac{182.4 \text{ ft/sec} \times 0.25 \text{ ft} \times 36.52 \text{ lb/ft}^3}{1.2 \times 10^{-2} \times \frac{36.52}{62.4} \times 6.72 \times 10^{-4}} = 3.53 \times 10^8$$

**American Chemical
Society Library**

1155 16th St. N. W.

Relative roughness factor and friction factor are taken to be 0.0006 and 0.004, respectively. Therefore, the frictional loss term is

$$1w_f = \frac{2 \times 0.004 \times 182.4^2 \times 37.4}{32 \times 0.25} = 1244 \text{ ft lb}_f/\text{lb}$$

From Eq. (A-1), we can calculate the loss per set of pipes (10 pipes) connecting each absorber and stripper is

$$W_s = \frac{-(1244 \times 10 + 27.4)}{0.8} = 15584 \text{ ft lb}_f/\text{lb}$$

The total electrical power required for the 30 pipes is

$$\begin{aligned} P &= \frac{15584 \text{ ft-lb}_f/\text{lb} \times 8.48 \times 10^8 \text{ lb/day} \times 5.05 \times 10^{-7} \text{ P hr/ft-lb}_f}{24 \text{ hr/day}} \\ &= 2.78 \times 10^5 \text{ P} \end{aligned}$$

B. Pumping Power Required to Transport Fluid from Bottom of Stripper to Top of Absorber

$$\begin{aligned} \text{Liquid flow rate} &= 8.12 \times 10^8 \text{ lb/day} \\ &= \frac{8.12 \times 10^8 \text{ lb/day} \times 7.48 \text{ gal/ft}^3}{36.52 \text{ lb/ft}^3 \times 24 \text{ hr/day} \times 60 \text{ min/hr}} \\ &= 1.15 \times 10^5 \text{ gal/min} \end{aligned}$$

Again we take 20% additional height for the height of the absorber which has a packing height of 41.4 ft so the total height of the absorber is 50 ft. Let's apply the same mechanical energy balance Eq. (A-1) to calculate the pumping power here. Velocity of the fluid is

$$U = \frac{8.12 \times 10^8 \times 4}{24 \times 36.52 \times \pi \times 30 \times 25^2} = 6.29 \times 10^5 \text{ ft/hr} = 174.9 \text{ ft/sec}$$

$$Re = \frac{uD\rho}{\mu} = \frac{174.9 \times 0.75 \times 36.52 \text{ lb/ft}^3}{1.2 \times 10^{-2} \times \frac{36.52}{62.4} \times 6.72 \times 10^{-4}} = 1.02 \times 10^9$$

Using the relative roughness factor and friction factor to be 0.0006 and 0.004 again. The frictional loss in the pipe is

$$1w_f = \frac{2 \times 0.004 \times 174.9^2 \times 50}{32.2 \times 25} = 1520 \text{ ft-lb}_f/\text{lb}$$

So the total energy required per set of pipe (10 pipes) connecting each stripper and absorber is

$$W_s = \frac{-(1520 \times 10 + 50)}{0.8} = 19063 \text{ ft-lb}_f/\text{lb}$$

The total pumping power is

$$P = \frac{19063 \text{ ft-lb}_f/\text{lb} \times 8.12 \times 10^8 \text{ lb/day} \times 5.05 \times 10^{-7} \text{ P hr/ft-lb}_f}{24 \text{ hr/day}}$$

$$P = 3.3 \times 10^5$$

C. Inlet Gas Blower

Incoming gas to absorber is $2.32 \times 10^7 \text{ ft}^3/\text{day}$. Main flow rate at absorber is 2920 lb/hr ft^2 at a density

$$\rho_g = \frac{PM_{av}}{Z_{av}RT}, \quad T = 230^\circ\text{F} = 127^\circ\text{K}$$

$$\text{CH}_4: \quad T_r = \frac{127}{191} = 0.665, \quad P_r = \frac{500}{14.7 \times 45.8} = 0.7426, \quad Z_c = 0.56$$

$$\text{CO}: \quad T_r = \frac{127}{133} = 0.955, \quad P_r = \frac{500}{14.7 \times 34.5} = 0.986, \quad Z_c = 0.32$$

$$\text{H}_2: \quad T_r = \frac{127}{33.3} = 3.814, \quad P_r = \frac{500}{14.7 \times 12.8} = 2.657, \quad Z_c = 0.98$$

$$Z_{av} = 0.4 \times 0.56 + 0.15 \times 0.32 + 0.45 \times 0.98 = 0.71$$

$$M_{av} = 0.4 \times 16 + 0.15 \times 28 + 0.45 \times 2 = 11.50$$

$$\rho_g = \frac{500 \times 11.5}{0.71 \times 10.73 \times 230} = 3.28 \text{ lb/ft}^3$$

$$\frac{G}{\rho_g} = \frac{2970 \text{ lb/hr ft}^2}{3.28 \text{ lb/ft}^3} = 905.5 \text{ ft/hr} = 0.25 \text{ ft/sec}$$

Number of tubes in absorber = n

$$U = \frac{2.32 \times 10^7 \text{ ft}^3/\text{day} \times 4}{24 \text{ hr/day} \times \pi \times n D^2 \text{ ft}^2} = \frac{1.231 \times 10^6}{n D^2} \text{ ft/hr} = \left(\frac{342}{n D^2} \right) \text{ ft/sec}$$

$$Re = \frac{u D \rho}{\mu} = \frac{342}{n D^2} \times \frac{D \times 3.28 \text{ lb/ft}^3}{0.007 \text{ cP} \times 6.72 \times 10^{-4}} = \frac{2.38 \times 10^8}{n D}$$

$$l w_f = \frac{2 f L U^2}{g_c D} = \frac{2 \times 0.004 \times 10 \text{ ft}}{32.2 D} \times \frac{342^2 \text{ sec}^2}{n^2 D^2} = \frac{291}{n^2 D^5} \text{ ft-lb}_f/\text{lb}$$

let n = 30, D = 0.25 ft

Frictional loss/tube = 330.63 ft-lb_f/lb

$$\frac{g}{g_c} \Delta Z + l w_f + n W_s = 0 \quad (\text{A-2})$$

gas flow = $2.32 \times 10^7 \text{ ft}^3/\text{day}$ (= $5.64 \times 10^7 \text{ lb/day}$)

Pressure drop in tower = 1.3 in H₂O/ft depth, $\Delta Z = 41.4 \text{ ft}$

$$\text{Total pressure drop} = \frac{1.3 \times 41.4 \text{ ft H}_2\text{O}}{12} \frac{g}{g_c} = 4.49 \text{ ft-lb}_f/\text{lb}$$

Applying Eq. (A-2) to one set of pipe (10 pipes) for incoming gas into the absorber, one gets

$$(41.4 + 4.49) + 330.63 \times 10 + n W_s = 0$$

$$W_s = - \frac{4.49 + 41.4 + 3306.3}{0.8} = - 4190.2 \text{ ft-lb}_f/\text{lb}$$

$$\text{Energy required} = \frac{5.64 \times 10^7 \frac{\text{lb}}{\text{sec}}}{24 \text{ hr/day} \times 3600 \text{ sec/hr}} \times \frac{4190.2}{550} = 4973 \text{ P}$$

D. Compressor at End of Product Methane Between Streams 7 and 8

$$P = \frac{3.03 \times 10^{-5}}{k-1} P_1 q_{f, m_1} \left[\frac{P_2}{P_1} \frac{k-1}{k} - 1 \right] \quad (\text{A-3})$$

where $k = \frac{C_p}{C_v} = 1.31$ for methane

For the present case

$$P = \frac{3.03 \times 10^{-5}}{1.31 - 1} \times 485 \text{ lb/in}^2 \times 144 \text{ in}^2/\text{ft}^2$$

$$\times \frac{4.64 \times 10^6 \text{ ft}^3/\text{day}}{24 \text{ hr/day} \times 60 \text{ min/hr}} \left[\left(\frac{1000}{485} \right)^{\frac{1.31}{1.31 - 1}} \right] - 1$$

$$P = 4108 \text{ P}$$

If the compressor is 80% efficient, then the power required = 5135 P.

E. Pumping Power for Fluid Transport

Pumping power is required to transport fluid in the streams 9, 10, and 13. Gas flow rate and density in these streams are 7.1×10^6 lb/day and 0.44 lb/ft³, respectively. Using a 0.25 ft diameter pipe, velocity in the pipe is

$$\frac{7.1 \times 10^6 \text{ lb/day} \times 4}{30 \times 0.44 \text{ lb/ft}^3 \times 24 \times 3600 \times \pi \times 0.25^2} = 127 \text{ ft/sec}$$

$$Re = \frac{u D \rho}{\mu} = \frac{127 \times 2.5 \times 0.44}{(0.0183 \times 23 + 0.009 \times 77) \times \frac{.44}{62.4} \times 6.72 \times 10^{-4}} = 2.65 \times 10^8$$

Relative roughness factor and friction factor are again taken to be 0.0006 and 0.004, respectively. Assuming the total transport line as 600 ft, frictional loss in fluid transport is

$$1w_f = \frac{2f u^2 L}{g_c D} = \frac{2 \times 0.004 \times 127^2 \times 600}{32.2 \times 0.25} = 9617 \text{ ft-lb}_f/\text{lb}$$

With 80% efficiency of the pump, total energy loss is 1.2×10^4 ft-lb_f/lb and the pumping power required is

$$P = \frac{1.2 \times 10^4 \text{ ft-lb}_f/\text{lb} \times 7.1 \times 10^6 \text{ lb/day} \times 5.05 \times 10^{-7} \text{ P-hr/ft-lb}_f}{24 \text{ hr/day}}$$

$$= 1796 \text{ P}$$

F. Thermal Energy Required in Heat Exchanger Between Streams 13 and 9

$$\begin{aligned}
 Q &= 7.1 \times 10^6 \text{ lb/day} \times 7 \text{ Btu/lb-mole } ^\circ\text{F} / 7.89 \text{ lb/lb-mole } (110-90) ^\circ\text{F} \\
 &= 1.13 \times 10^8 \text{ Btu/day} \\
 &= 1.3 \times 10^8 \text{ Btu/day} \times 252 \text{ cal/Btu} / 24 \text{ hr/day} \times 60 \text{ min/hr} \\
 &= 2.2 \times 10^7 \text{ cal/min}
 \end{aligned}$$

Thermal energy supplied to the heat exchanger

$$\begin{aligned}
 &= \frac{2.2 \times 10^7 \text{ cal/min} \times 24 \text{ hr/day} \times 60 \text{ min/hr} \times 16 \text{ g/g-mole}}{3.06 \times 10^7 \text{ lb/day} \times 454 \text{ g/lb}} \\
 &= 36.5 \text{ cal(t)/g-mole}
 \end{aligned}$$

G. Energy Required to the Cooler in Absorber Outlet Stream

$$\begin{aligned}
 (-Q) &= 2.23 \times 10^7 \text{ lb/day} \times 7 \text{ Btu/lb-mole } ^\circ\text{F} / 9.73 \text{ lb/lb-mole} \\
 &\quad (-156 + 146) \times 1.8 \\
 &= 2.89 \times 10^8 \text{ Btu/day} \\
 &= 2.89 \times 10^8 \text{ Btu/day} \times 252 \text{ cal/Btu} / 24 \text{ hr/day} \times 60 \text{ min/hr} \\
 &= 5.06 \times 10^7 \text{ cal/min}
 \end{aligned}$$

Energy supplied to the cooler

$$= \frac{5.06 \times 10^7 \text{ cal/min} \times 24 \text{ hr/day} \times 60 \text{ min/hr} \times 16 \text{ g/g-mole}}{3.06 \times 10^7 \text{ lb/day} \times 454 \text{ g/lb}}$$

It is also interesting to report the theoretical minimum energy requirement for the present process

$$W_{\text{min,T}} = RT \sum_j x_j F \ln \frac{P_2}{x_j F P_1}$$

For the present process, composition temperature and pressure of incoming gas are: CH₄, 0.4; H₂, 0.45; CO, 0.15; 100°F and 500 psia, respectively. Temperature and pressure of final product gases are at 100°F and 1000 psia. For complete separation

$$\begin{aligned}
 W_{\min, T} &= 1.98 \text{ Btu/lb-mole } ^\circ\text{R} \times 560^\circ\text{R} \left[0.4 \ln \frac{1000}{0.4 \times 500} \right. \\
 &\quad \left. + 0.45 \ln \frac{1000}{.45 \times 500} + 0.15 \ln \frac{1000}{.15 \times 500} \right] \\
 &= 1889 \text{ Btu/lb-mole} \times 252 \text{ cal/Btu} / 454 \text{ g-mole/lb-mole} \\
 &= 1049 \text{ cal/mole gas} / 0.4 \frac{\text{mole CH}_4}{\text{mole gas}} = 2621 \frac{\text{cal}}{\text{mole CH}_4}
 \end{aligned}$$

RECEIVED December 29, 1982

High-Temperature Hydrogen Sulfide Removal Using a Regenerable Iron Oxide Sorbent

S. S. TAMHANKAR and C. Y. WEN

West Virginia University, Department of Chemical Engineering,
Morgantown, WV 26506

A state-of-the-art review is presented of high temperature H_2S removal and sorbent regeneration using an iron oxide sorbent, with a particular emphasis on kinetic and mechanistic studies of the reactions involved. Selection criteria for a high temperature H_2S sorbent and the various sorbent regeneration options are first briefly discussed. Results are then presented on the kinetics of the various reactions involved in the absorption and the regeneration steps. These studies were conducted in a thermogravimetric analyzer (TGA). The weight change data obtained in the TGA was used in conjunction with x-ray and Mossbauer spectroscopic analyses of the solid samples to elucidate the mechanisms of the reactions. Conversion correlations are reported based on the grain model, which can be used for reactor design and for predicting reactor performance.

Significant effort is underway in the United States to develop and commercialize coal gasification processes for producing gaseous fuels. One of the major obstacles in the development of such a process is the presence of undesirable contaminants in the product gas stream. The major contaminant in coal gasification is hydrogen sulfide (H_2S), which is toxic, poisonous to downstream catalysts and extremely corrosive in nature. Control of H_2S in the fuel gas to a safe level is therefore essential. The H_2S removal requirements are even more critical when the fuel gas is used in combined cycle power generation or in fuel cells.

Conventional methods of H_2S removal use a cold scrubbing technique, wherein the gas needs to be cooled to near room temperature. Although such techniques are effective, they are associated with a loss of sensible heat of the gas. The other

0097-6156/83/0223-0255\$07.25/0

© 1983 American Chemical Society

disadvantages of cold scrubbing include restriction by availability of water, sludge disposal problem and condensation and mixing of tars with the scrubber water posing handling problems. In view of these, and mainly for thermal efficiency, removal of H_2S at high temperatures is very attractive. Besides, fuel cells and combined cycle power generation systems use the hot fuel gas directly. This further improves the overall thermal efficiency. Figure 1 shows a schematic of the integrated system configurations for various applications. The figure also includes the limit values of H_2S concentration for these applications. The subject of this paper is the bulk sulfur removal, whereby the H_2S concentration is brought down to about 200 ppm.

Sorbent Selection

The criteria used in selecting a suitable sorbent are: efficiency, sulfur capture capacity, kinetics, cost, physical strength and regenerability. Sorbent efficiency implies the maximum amount of H_2S that can be removed under a given set of operating conditions, based on the thermodynamic equilibrium of the system. Figure 2 (1) shows equilibrium H_2S conversions in the presence of various sorbent materials in relation to the EPA sulfur emission standards. At all the temperatures of interest iron-based sorbents seem to be satisfactory. Zinc oxide is probably the best in this respect, and can in fact be used for the final polishing step to reduce H_2S level to less than 1 ppm. Sulfur capture capacity of a sorbent depends on the stoichiometry of the reaction. In the temperature range of interest, iron oxide (Fe_2O_3) captures about 44 weight % sulfur.

An important asset of iron oxide as an H_2S sorbent is its reactivity. The results of a comparative study shown in Figure 3 (1) reveal that iron oxide is by far the most active among the oxides considered. This is an important factor in the choice of Fe_2O_3 as a sorbent.

Based on criteria of efficient H_2S removal above 1000°F, physical strength, regenerability, sorbent life and economic feasibility, laboratory tests (2,3) led to the selection of iron oxide mixed with fly ash, in extruded pellets, as a promising sulfur-removal sorbent.

In a commercial scale operation physical strength of the sorbent pellets is important, especially if a moving or a fluidized-bed reactor is used. Pellets of iron oxide alone are not strong enough; addition of a support material is necessary. In so doing, the percentage of iron oxide should be kept as high as possible to maintain the overall high efficiency of H_2S removal. Extensive tests were conducted at METC (4), and the best support and an optimum composition with it were found. This sorbent consisted of 45 weight %

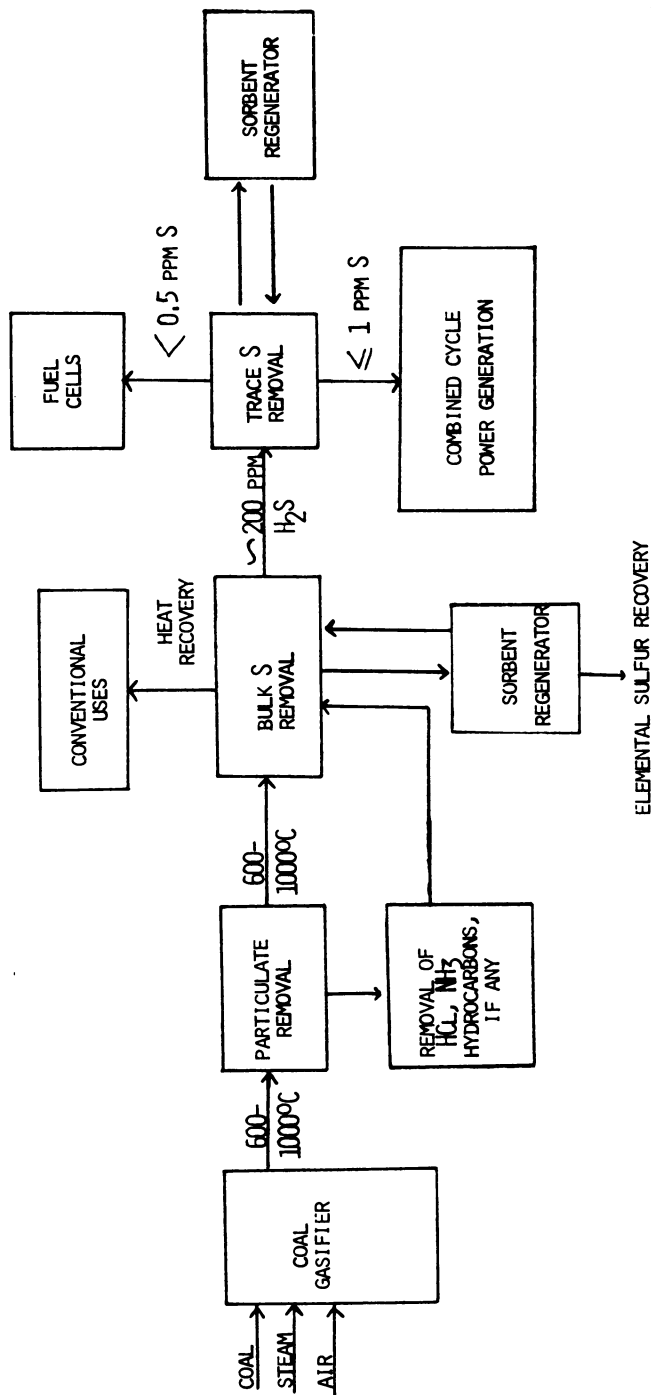


Figure 1. A schematic of an integrated coal gasification system for fuel cell or combined-cycle-power-generation applications.

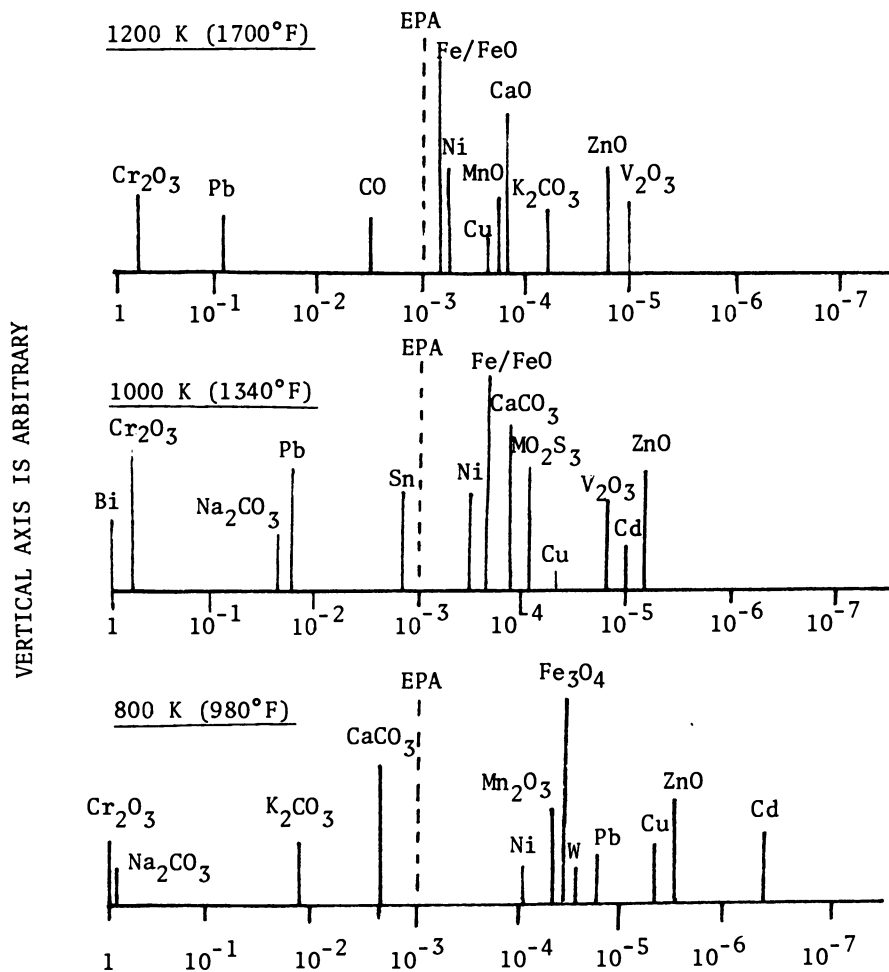
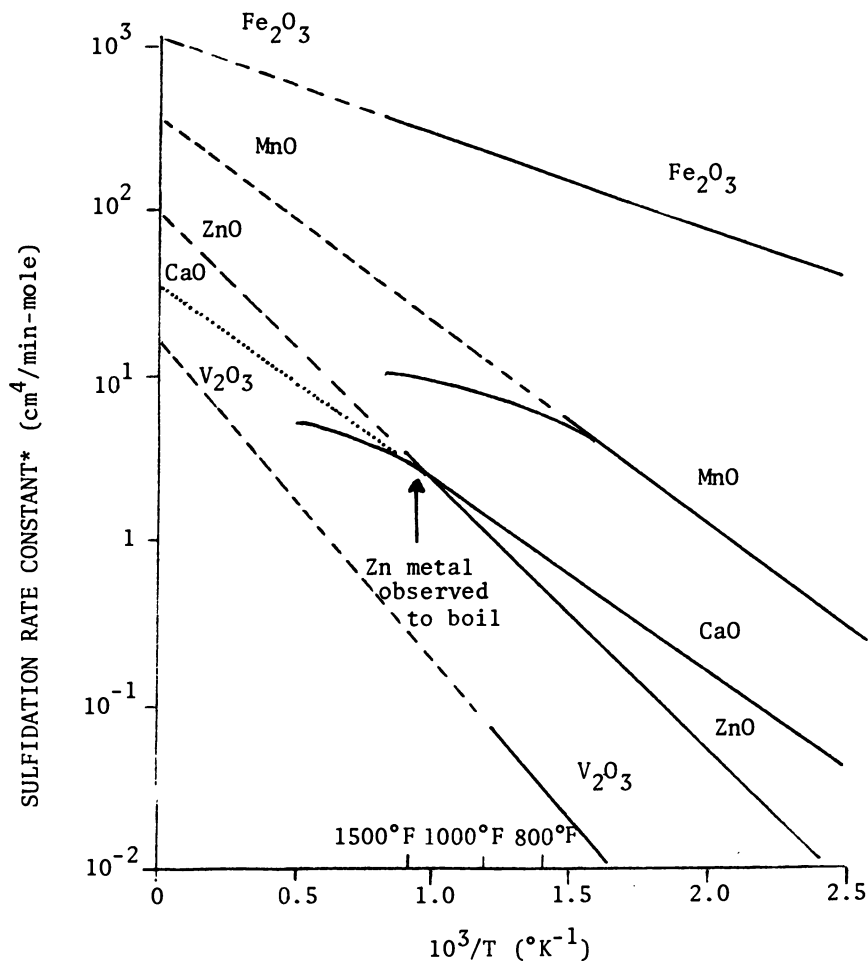


Figure 2. Equilibrium exit gas concentration of H_2S .



*Rates expressed per constant unit surfacd area

Figure 3. Kinetics of H_2S sorption by selected metal oxides.

Fe_2O_3 and 55 weight % silica, as support, with 1% sodium silicate as a binder. In the preliminary work fly ash was considered as a support material; but the maximum amount of iron oxide which could be incorporated with it was 25 weight %. Based on this and the other criteria discussed above, the iron oxide-silica composition was found to be the most suitable sorbent for bulk H_2S removal.

A simple method of regeneration of the sulfided sorbent is by its reaction with oxygen in air. With most metal sulfides this reaction results in sulfates at the temperatures of interest. Ferric sulfate has the lowest limit temperature of stability as shown in Table I (1). Hence, iron oxide is directly formed by regeneration in air. A major obstacle in

Table I
Final Product of Regeneration in Air
for Different Sorbents (Taken from Ref. 1)

Sulfide	→ Product	T(K)	Sulfide	→ Product	T(K)
FeS	→ $\text{Fe}_2(\text{SO}_4)_3$	< 950	CaS	→ CaSO_4	All
FeS	→ Fe_2O_3	<1680	NiS	→ NiSO_4	<1200
Cu_2S	→ CuSO_4	<1050	NiS	→ NiO	>1200
Cu_2S	→ CuO	<1300	ZnS	→ ZnSO_4	<1150
Cu_2S	→ Cu_2O	>1300	ZnS	→ ZnO	>1150
MnS	→ MnSO_4	<1100	MoS_2	→ MoO_3	<1350
MnS	→ Mn_2O_3	<1400	MoS_2	→ MoO_2	>1350
MnS	→ Mn_3O_4	>1400	CoS	→ CoO	>1000

the commercial development of a hot-gas desulfurization process has been the sorbent regeneration step. An efficient and economical method has not yet been established. Regeneration is discussed in more details in the next section.

As mentioned earlier, thermodynamically H_2S removal efficiency of ZnO is higher than that of Fe_2O_3 . ZnO is therefore considered for the second stage, wherein H_2S concentrations can be reduced from about 200 ppm to less than 1 ppm, as required for fuel cell or combined cycle power generation applications. A further step in the development of a hot-gas desulfurization process is the use of a mixture of iron and zinc oxides. This novel concept, emerged at METC, uses zinc ferrite formed from a mixture of Fe_2O_3 and ZnO, and is aimed at reducing H_2S concentration to the desired level in a single step. The results so far (5) indicate that the lowest H_2S breakthrough concentration attained in this system is 10 ppm at a temperature of 1000°F. This approach appears attractive, but additional work is necessary before a definite conclusion can be drawn.

Regeneration Options

An important consideration in a hot-gas desulfurization process is an efficient and economical method of regeneration of the spent sorbent. This requires that the sulfur in the spent sorbent be recovered in a useful form. As mentioned earlier, air-oxidation is a convenient way of regenerating the sulfided sorbent to its original form. In this process the sulfur in the sorbent is converted to sulfur dioxide (SO_2). The SO_2 thus formed can then be used to make H_2SO_4 , can be treated with limestone, or can be converted to elemental sulfur. The conversion to elemental sulfur can be achieved either by the Claus process or by treating SO_2 with a reductant such as carbon (Trail/Resox process). An attractive way of recovering sulfur is by reacting the SO_2 with iron sulfide itself to form iron oxide and elemental sulfur. Thus, if the SO_2 formed by the oxidation of iron sulfide is recirculated, elemental sulfur can be produced in a single step. The problem with this scheme is that the elemental sulfur needs to be separated from the exit stream by cooling, and the SO_2 needs to be reheated. Karr, et al. (6) and Schrodtt and Best (7) carried out experiments to test the feasibility of this scheme. The latter authors, using coal ash as the sorbent material, concluded that sulfur recovery by this method is both technically and economically unattractive. The same may not be true for the iron oxide-silica sorbent. More studies are necessary before a definite conclusion can be drawn.

One of the problems with regeneration by air-oxidation is the large heat of reaction, which makes temperature control difficult. In the SO_2 recycle scheme this problem can be alleviated since the reaction of iron sulfide with SO_2 is endothermic. Another option being considered more recently for moderating the temperatures is to mix steam with air. In an exploratory study done at Air Products and Chemicals, Inc. (APCI) (8) some interesting observations were made. With very high steam concentrations (>90%) in the steam-air mixture, significant quantities of elemental sulfur were formed. This again presents an interesting possibility of regenerating the spent sorbent and forming elemental sulfur in a single step. Further studies are necessary to enable assessment of this process. Kinetic studies on this system are in progress at present at West Virginia University and will be discussed later in this paper.

The overall H_2S removal process would consist of two stages: the absorption stage, in which the sorbent is converted to the sulfide form by its reaction with the H_2S in the feed gas, and the regeneration stage, wherein the sulfide is converted to an oxide. It thus represents a cyclic process. Fixed-bed, moving-bed and fluidized-bed operations have been considered for the purpose. Kinetic data are necessary for choosing a proper reactor type and for the design

of a reactor. In the remainder of this paper attention will be focused on this aspect. Some of the reactions involved in this system have been studied before in different contexts. However, the forms of reactants and the operating conditions used were different. It is important to study these reactions starting with the actual iron oxide-silica sorbent and under conditions close to the real situation.

Reaction Mechanisms and Kinetic Studies

The objectives of the studies at West Virginia University (WVU) were to identify the important reactions involved, to elucidate the mechanisms and to study their kinetics. Experiments were conducted in a thermogravimetric analyzer (TGA) apparatus; a general schematic of this is shown in Figure 4. In this method, a change in the weight of the solid sample during a reaction is continuously recorded as a function of time. If the stoichiometry and the reaction mechanism are determined, this weight change can be related to the solid conversion. The conversion-time data can then be correlated using an appropriate reaction model. In the following, important reactions, their mechanisms and the kinetic experiments are described for each of the steps, viz. H_2S absorption, sorbent regeneration by SO_2 recycle and regeneration by a steam-air mixture. The discussion on the first two steps is based on the previous publications (9,10) by the authors, which provide the details.

H_2S Absorption Stage. In order to identify reactions that would be important in this stage, reactions of the iron oxide sorbent were carried out in the TGA using different synthetic gas mixtures. A few important results of this study are shown in Figure 5. Curve A in this figure represents the actual reaction of Fe_2O_3 with a simulated gasifier product gas (containing N_2 , CO , CO_2 , H_2 and H_2S). As may be noted, the sample weight first rapidly decreased, reached a minimum and then slowly increased again. Two distinct reactions were suspected to be taking place. Hence, the sorbent was first reacted with a mixture of CO and H_2 , in the absence of H_2S . This reduction reaction, which is very rapid, is represented by curve B. The resulting sample was then reacted with H_2S to obtain curve C. An interesting observation made is that curve A can be obtained by adding curves B and C. Curve D is for the reaction of Fe_2O_3 with H_2S in the absence of CO and H_2 . Obviously, this reaction is much slower than any other reaction. Based on these observations it was concluded that the important reactions in the absorber are: the reduction of Fe_2O_3 to Fe and the subsequent sulfidation of Fe by H_2S , which is rate-controlling. In addition, if CO_2 or H_2O are present in the feed gas they would only affect the equilibrium of the reduction reactions, which can be accounted for based on the reported equilibrium data.

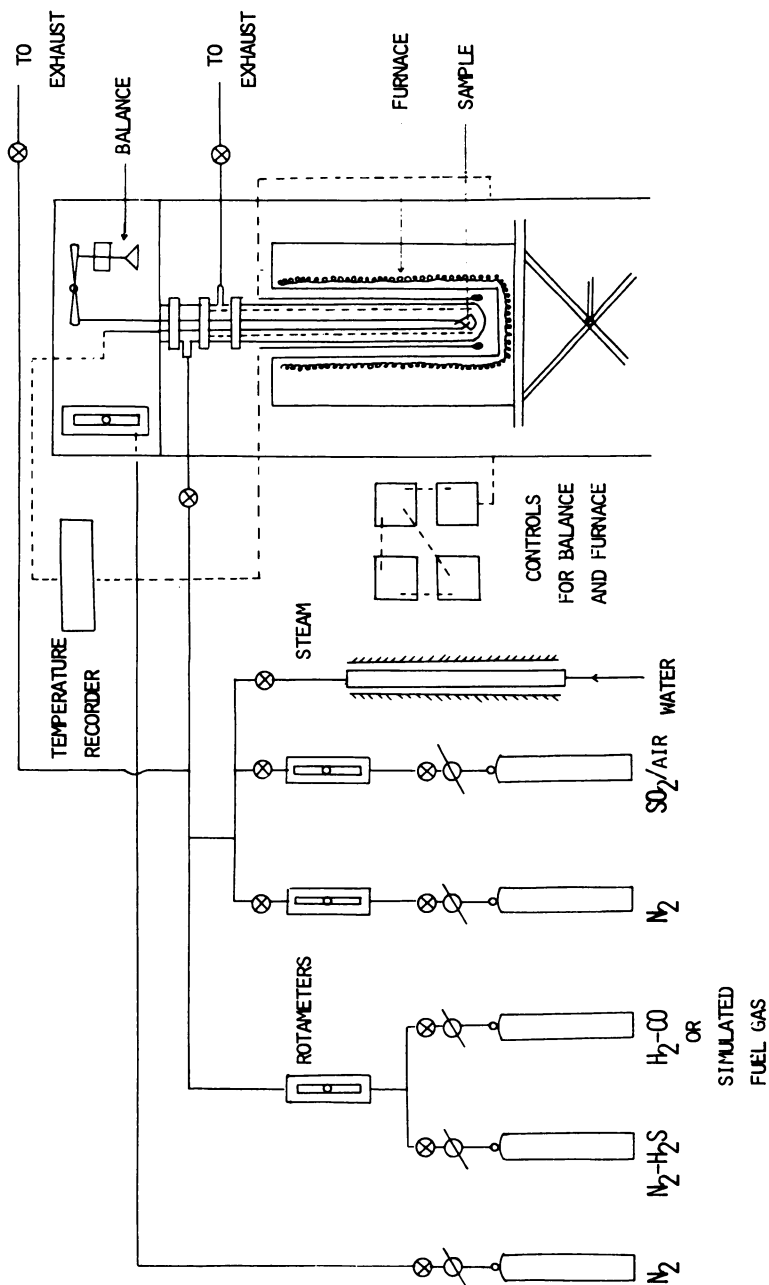


Figure 4. Schematic diagram of thermogravimetric analyzer (TGA) assembly.

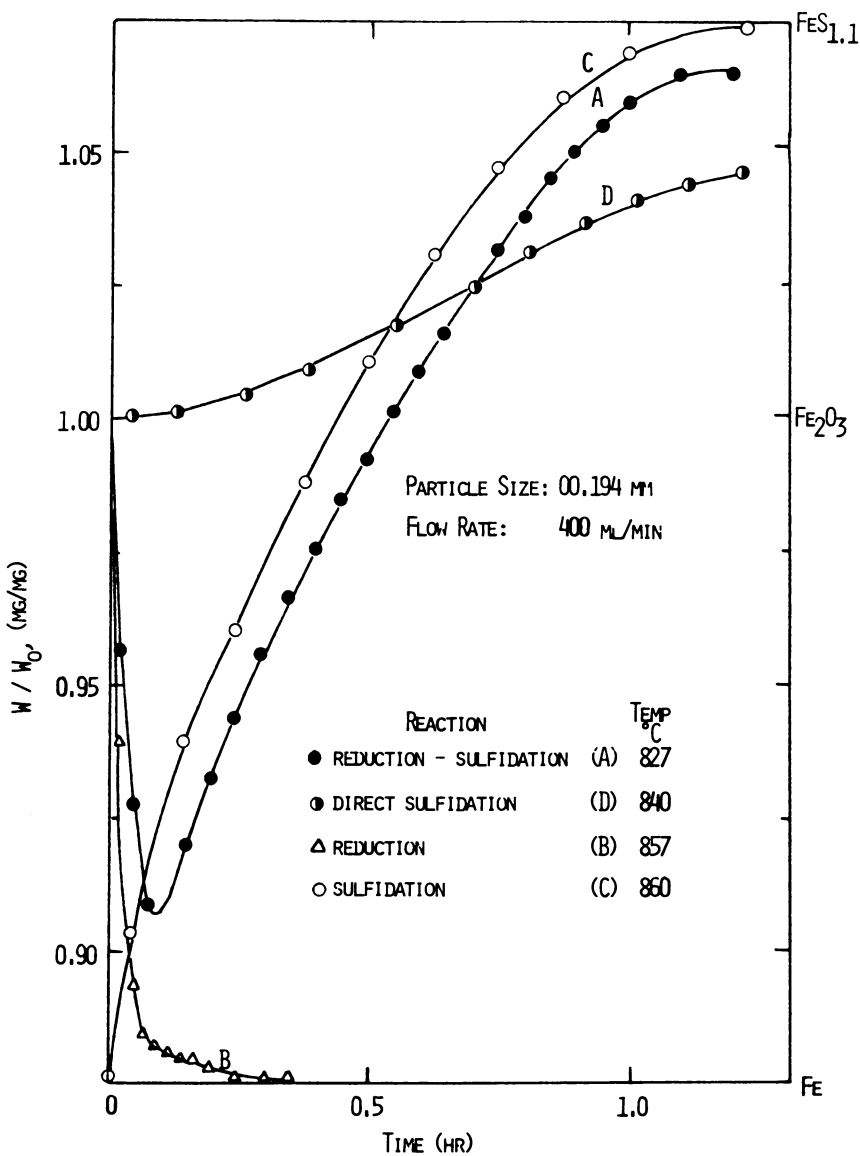
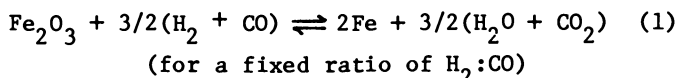
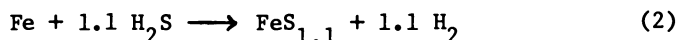


Figure 5. Comparison of weight change curves for reactions of iron oxide in different gas atmospheres.

The weight change data indicated that the reaction of Fe with H₂S results in a nonstoichiometric compound with the formula FeS_{1.1}. Mossbauer spectroscopic analysis of the samples confirmed this. The compound represents a pyrrhotite, a nonstoichiometric iron sulfide, which is well known in the Fe-S system. Based on the above observations, the reactions in an absorber can be written as follows:



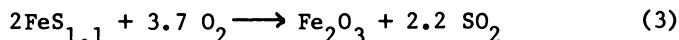
and



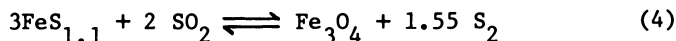
Thus, reactions considered here are those taking place under actual process conditions. Reactions (1) and (2) were studied separately in the TGA at different temperatures and with different particle sizes. Also, effect of the gas-phase reactant concentration was studied to evaluate the reaction order. In a few experiments the effects of the presence of H₂O in the feed gas on reaction (1) and that of H₂ on reaction (2) were investigated.

Regeneration by SO₂ Recycle Method. In this case, clearly, the two reactions, which need to be studied, are reactions of iron sulfide, FeS_{1.1} with O₂ and with SO₂. The reaction of FeS_{1.1} with O₂ was found to be very fast and formed Fe₂O₃ directly. No intermediates could be identified using Mossbauer spectroscopy.

The reaction of FeS_{1.1} with SO₂ was rather interesting. In this reaction, FeS_{1.1} was first converted to magnetite, Fe₃O₄, which was then slowly oxidized to Fe₂O₃. This is shown in Figure 6, where the minima in the weight change curves correspond to Fe₃O₄. This was also confirmed by x-ray and Mossbauer spectroscopic analyses. In fact it was found that up to the minimum point the only product formed was Fe₃O₄. These results are presented in Table II. Since the oxidation to Fe₂O₃ is relatively very slow only the first step was considered for the purpose here. Accordingly, the reactions in the regenerator would be



and



These two reactions were studied in the TGA under different operating conditions to obtain their kinetics. Reaction (3) is highly exothermic. Hence, low oxygen concentrations and

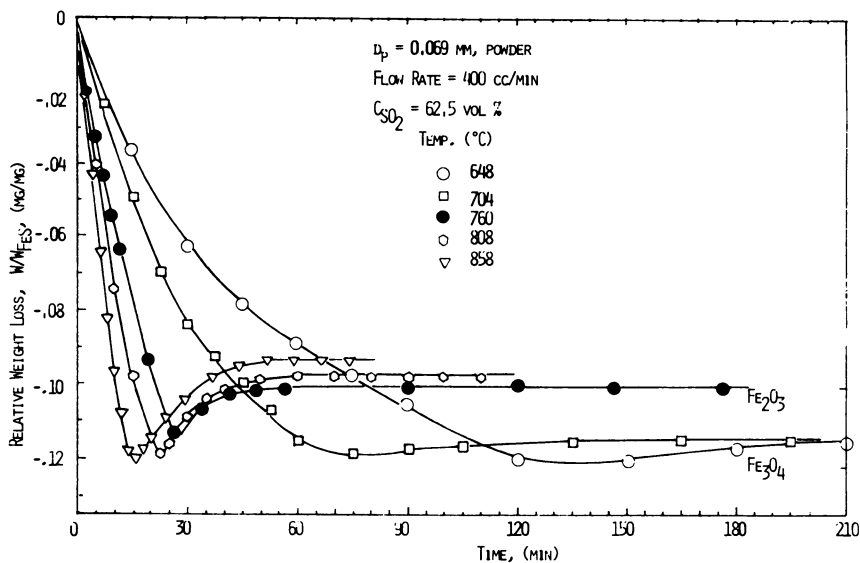


Figure 6. Effect of temperature on the weight loss of sulfided iron oxide sorbents in sulfur dioxide atmosphere.

Table II
 Experimental Conditions and the Results of the Mossbauer Analysis
 of Specimens Partially Reacted in SO₂ (1.5 x 6.0 mm pellets)

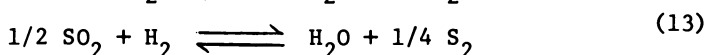
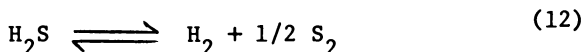
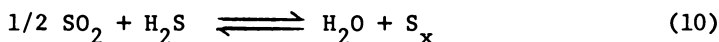
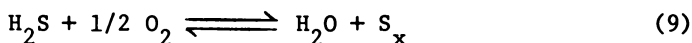
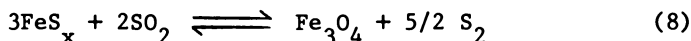
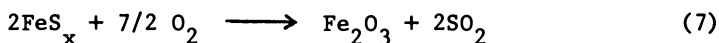
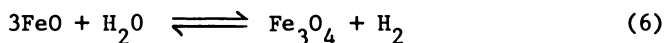
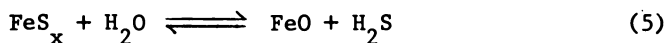
Run No.	Experimental conditions		Results of the Mossbauer analysis		
	C _{SO₂} (vol %)	T (°C)	Time (min)	atomic ratio based on weight change	conversion of FeS _{1.1} , X based on Mossbauer analysis
815	-	-	0.0	$\frac{\text{Fe}_3\text{O}_4}{\text{FeS}_{1.1}} = 0.00$	0.0
817-3	62.5	759	45.0	$\frac{\text{Fe}_3\text{O}_4}{\text{FeS}_{1.1}} = 4.00$	0.555
817-2	62.5	760	60.0	$\frac{\text{Fe}_3\text{O}_4}{\text{FeS}_{1.1}} = 6.66$	0.635
818-2	62.5	759	97.5	$\frac{\text{Fe}_3\text{O}_4}{\text{FeS}_{1.1}} = 7.00$	0.700

Reprinted with permission from Ref. 10. Copyright 1981, Pergamon Press, Ltd.

high gas flow rates were used to maintain near-isothermal conditions.

Regeneration by Steam-Air Mixtures. As mentioned earlier, preliminary exploratory work on this system was done at APCI. At APCI experiments were conducted in a fixed-bed reactor and product gas compositions were monitored. Typical results of this study are given in Table III (8). According to APCI equilibrium calculations very little elemental sulfur yields were predicted. However, high sulfur yields were obtained, particularly with high steam concentrations. This was an interesting observation, and detailed studies on this system were warranted. As before, the objectives of the studies at WVU are to identify the reactions, to elucidate the mechanisms and then to study their kinetics.

Based on the APCI results, a number of possible reactions can be postulated for the system iron sulfide - H₂O - O₂. These are listed below.



Reactions (7) and (8) are the same as reactions (3) and (4) identified in the previous regeneration scheme, while reactions (9) and (10) represent the Claus process. Reaction (12) is postulated here to be a major reaction responsible for the elemental sulfur formation, particularly in the absence of air. Kinetic and thermodynamic equilibrium data for the catalytic decomposition of H₂S have been reported in the literature (11,12).

To delineate the various possible reactions, in this study reaction of FeS_{1.1} with steam alone was investigated first. Experiments were carried out in the TGA using a steam-nitrogen mixture with the steam concentration of 94 percent by volume.

Table III
Effect of Water Content on Regeneration Product-Distribution
(Taken from the APCI Final Report, Ref. 8)

Run No.	2102	2118	2129
Regeneration Feed Gas, Mol Percent			
Water	85.0	95.0	95.0
Air	15.0	5.0	0.0
Sulfur Dioxide	0.0	0.0	0.0
Nitrogen	0.0	0.0	5.0
Sorbent	42 Percent Added Commercial Iron Oxide on Silica	42 Percent Added Commercial Iron Oxide on Silica	42 Percent Added Commercial Iron Oxide on Silica
Sorbent Volume, cc	40.0	40.0	40.0
GHSV	600.0	600.0	1200.0
Regeneration Duration, Hours	14.0	42.0	10.0
Reactor Block Temperature, °F	1000.0	1000.0	1000.0
Material Balance, Percent	95.0	145.0	64.0
Selectivity for Elemental Sulfur, Percent	22.0	75.1	56.3
Selectivity for Sulfur Dioxide, Percent	72.9	23.5	---
Selectivity for Sulfur Trioxide, Percent	5.1	1.4	4.5
Selectivity for Hydrogen Sulfide, Percent	---	---	39.2

Solid samples at various stages of conversion were analyzed by Mossbauer spectroscopy. The only product identified in this case was Fe_3O_4 . Hence, conversions can be calculated based on the weight change data. A comparison of conversions calculated based on the weight change data and those calculated based on the Mossbauer results is shown in Table IV. These results

Table IV
Results of Iron Oxide-Steam Reaction

Temperature = $695 \pm 4^\circ\text{C}$ Steam % = 94.0
Average Rate = 0.33 min^{-1} (Balance N_2)

Run No.	Time Min.	$\frac{\text{Fe}_3\text{O}_4}{\text{FeS}_{1.1}}$ wt. ratio By Mossbauer Analysis	Calculated From Mossbauer Results	Calculated From Wt. Loss Data
1	5	0.239	0.210	0.190
2	8	0.254	0.228	0.215
3	10	0.498	0.361	0.362
4	15	-	-	0.440
5	25	-	-	0.890

suggest that reactions (5) and (6) are taking place in this system. In addition, reaction (6) must be very rapid, so that at no stage FeO is identified in the solid samples. This is also found to be consistent with equilibrium calculations. Studies are now in progress to investigate the role of small concentrations of air in the system.

With respect to the overall mechanism, it is worthwhile to comment briefly on the APCI results of high elemental sulfur yields, even in the absence of air. The results suggest that the reaction responsible for the elemental sulfur formation under these conditions may be reaction (12). The main reason for this contention is the fact that transition metals and their sulfides are known to be very good catalysts for H_2S decomposition (11, 12). On the other hand, equilibrium constant for this reaction at the temperatures of study is rather small. But it is suspected that with the fixed-bed operation and with the possibility of some sulfur vapor adsorption on the solid, nonequilibrium conditions may be prevailing in the system. As a result, high sulfur yields could be obtained. This plausible explanation is only speculative, and more studies are necessary before a definite conclusion can be drawn. At WVU studies are in progress to obtain the kinetics of the reactions involved in this scheme.

Analysis of Conversion Data

To correlate the kinetic data obtained from the TGA experiments the grain model, developed by Szekeley and coworkers (13), was used. Accordingly, the solid particle is considered to be composed of small, non-porous grains. The gas has to diffuse through the interstitial spaces and then react at the grain surface. The reaction within the grain is considered to follow the shrinking core model (14). This is represented in Figure 7. In the present system, since the iron oxide (Fe_2O_3) is finely dispersed in the silica matrix, the grain model is considered appropriate.

In the absence of a resistance to the gas-film mass transfer, the overall rate of a noncatalytic gas-solid reaction is influenced by the chemical reaction and by pore diffusion. In general, at low temperatures and with a small particle size, the chemical reaction is likely to control the overall rate. The solid particle in this case reacts uniformly throughout and no concentration gradients exist within the particle. This situation is shown in Figure 8. On the other hand, at high temperatures and with large particles pore diffusion is expected to be important. In this case, reaction occurs at a sharp interface and the process can be described by a shrinking core model as shown in Figure 9. The assumptions used and the mathematical development of this model in the present context are presented in an earlier paper (9). An important assumption made here is that under a given set of conditions the overall reaction rate can be represented by the addition of rates for the pore diffusion and the chemical reaction control regimes, the two asymptotes represented in Figures 8 and 9. The approximate conversion-time equations based on these premises are given as follows (13):

$$t = t_1 F_1 + t_2 F_2 \text{ for a spherical pellet/particle} \quad (14)$$

and

$$t = t_1 F_1 + t_3 F_3 \text{ for a cylindrical pellet/particle} \quad (15)$$

where

$$t_1 = \frac{C_{\text{So}}}{bk'(C_{\text{Ao}} - C_{\text{Co}}/K)}; F_1 = 1 - (1-X)^{1/3} \quad (16)$$

$$t_2 = \frac{C_{\text{So}} r_o^2 (1+1/K)}{6bD_e (C_{\text{Ao}} - C_{\text{Co}}/K)}; F_2 = 1 - 3(1-X)^{2/3} + 2(1-X) \quad (17)$$

$$t_3 = \frac{C_{\text{So}} r_o^2 l_o^2 (1+1/K)}{4bD_e (C_{\text{Ao}} - C_{\text{Co}}/K) (r_o + l_o)^2}; F_3 = X + (1-X) \ln(1-X) \quad (18)$$

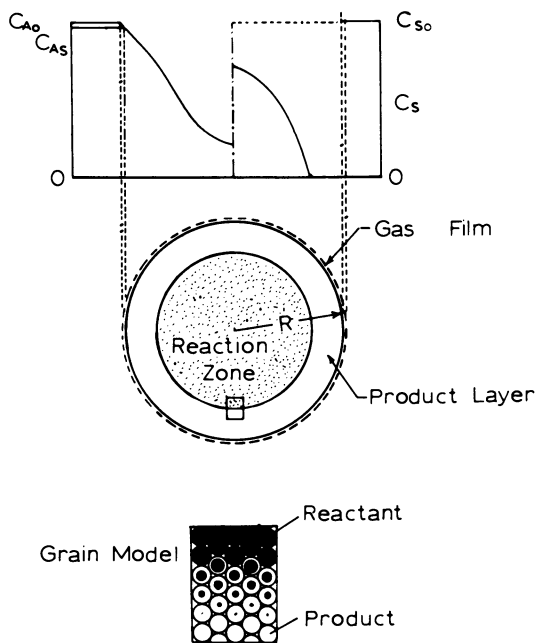


Figure 7. Schematic diagram of the grain model.

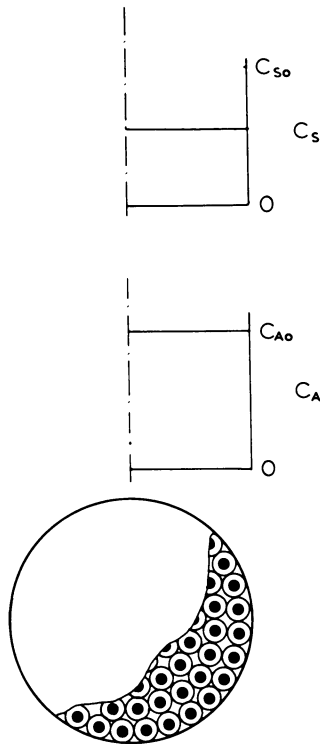


Figure 8. The grain model for a solid undergoing reaction under conditions of chemical reaction control.

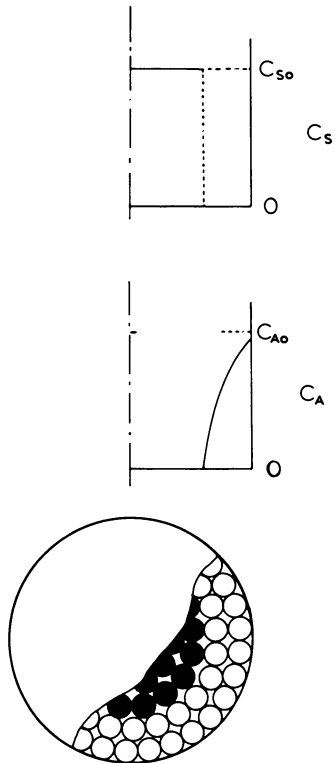


Figure 9. The grain model for a solid undergoing reaction under conditions of pore diffusion control.

C_{CO} = bulk concentration of the gaseous product, mole/cm³
 K = equilibrium constant
 t = time, sec, X = fractional conversion,
 C_{SO} = solid reactant concentration, mole/cm³
 b = stoichiometric coefficient
 k = rate constant, sec⁻¹
 C_{AO} = bulk concentration of the gaseous reactant, mole/cm³
 r_o = particle radius, cm
 l_o = length (for a cylinder), cm
 D_e = effective diffusivity, cm²/sec

Using the above equations and the experimental results in the asymptotic regions, intrinsic rate constants (k) and effective diffusivity (D_e) values were determined for reactions (1) to (4). These are given in Table V. Similar studies are in progress for the steam-air regeneration system. Notably, the activation energy value obtained for the intrinsic sulfidation reaction is unusually low. This is attributed to the reaction mechanism. The rate-controlling step seems to be the dissociative adsorption of H₂S on the solid surface, which has a low activation energy. Similar conclusions have been drawn by Turkdogan and Worrell (15,16) in their studies on the sulfidation of iron strips. This has a significance in the steam regeneration system, wherein the elemental sulfur formation is speculated to be due to a catalytic decomposition of H₂S.

To validate the grain model used and to substantiate the accuracy of the experimental data, the k and D_e values given in Table V were used to predict weight change curves for the reactions under different conditions. In all the cases the predicted and the experimental curves matched very well. Two such typical comparisons are illustrated in Figures 10 and 11 (9,10). Figure 10 shows the weight change curve for the reaction of iron oxide with a simulated coal gas, which was calculated by a combination of results for the reduction and the sulfidation reactions. In Figure 11 results are shown for the reaction of iron sulfide with SO₂, which illustrate a close agreement between the calculated values and the experimental values obtained by different analytical techniques.

Conclusion

The iron oxide-silica sorbent with 45 weight percent Fe₂O₃ appears to be very effective and efficient as a sorbent for the bulk sulfur removal from a hot low-/medium-Btu gas. The active sorbent form, which reacts with H₂S, is the metallic iron, Fe or the oxide FeO. This is due to the initial rapid reduction of Fe₂O₃ by the H₂ and the CO present in the fuel gas. On sulfidation of the sorbent a nonstoichiometric pyrrhotite, FeS_{1.1}, is formed. This reaction of Fe with H₂S is much slower compared to the reduction reaction.

Table V
Stoichiometric Coefficient, Rate Constant and Effective Diffusivity Values
Obtained for Different Reactions Using the Grain Model.

Reaction			
(1)	$\text{Fe}_2\text{O}_3 + 3/2 (\text{H}_2 + \text{CO})$	$2 \text{Fe} + 3/2 (\text{H}_2\text{O} + \text{CO}_2)$	$k'_r = 35550 \exp(-14,800/\text{RT}) \text{ sec}^{-1}$ $D_{\text{er}} = 0.06462 \exp(-5,000/\text{RT}) \text{ cm}^2/\text{sec}$
	$b = 2/3$		
(2)	$\text{Fe} + 1.1 \text{H}_2\text{S}$	$\text{FeS}_{1.1} + 1.1 \text{H}_2$	$k'_s = 158 \exp(-3,300/\text{RT}) \text{ sec}^{-1}$ $D_{\text{es}} = 0.24 \exp(-4,300/\text{RT}) \text{ cm}^2/\text{sec}$
	$b = 0.91$		
(3)	$3 \text{FeS}_{1.1} + 2 \text{SO}_2$	$\text{Fe}_3\text{O}_4 + 1.55 \text{S}_2$	$K'_{\text{SO}_2} = 7.8916 \times 10^3 \exp(-17,500/\text{RT}) \text{ sec}^{-1}$ $D_{\text{e}(\text{SO}_2)} = 0.246 \exp(-6,140/\text{RT}) \text{ cm}^2/\text{sec}$
	$b = 3/2$		
(4)	$2 \text{FeS}_{1.1} + 3.7 \text{O}_2$	$\text{Fe}_2\text{O}_3 + 2.2 \text{SO}_2$	$k'_{\text{O}_2} = 1 \times 10^5 \exp(-15,630/\text{RT}) \text{ sec}^{-1}$ $D_{\text{E}(\text{O}_2)} = 9.1 \exp(-5,370/\text{RT}) \text{ cm}^2/\text{sec}$
	$b = 0.54$		

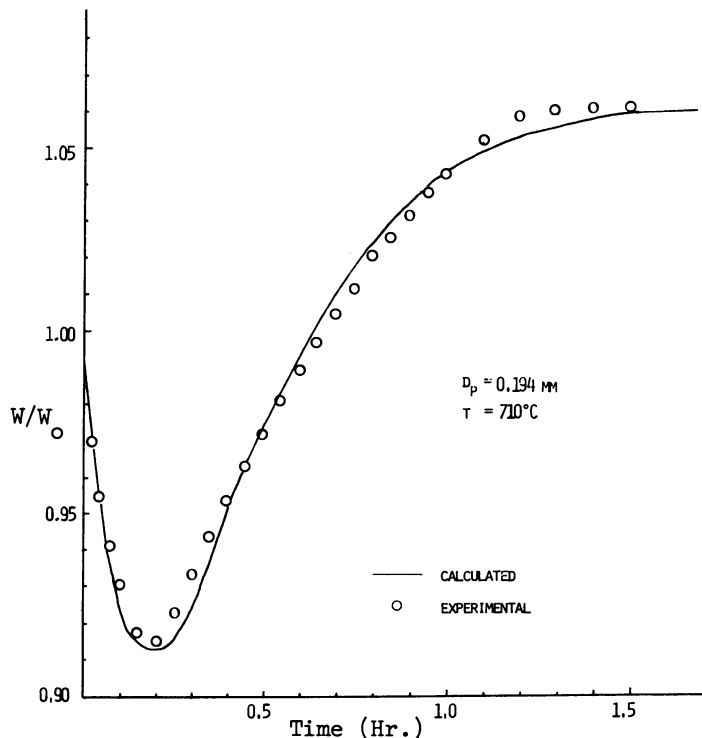


Figure 10. Comparison of calculated weight change curve with the experimental data for simultaneous reduction-sulfidation.

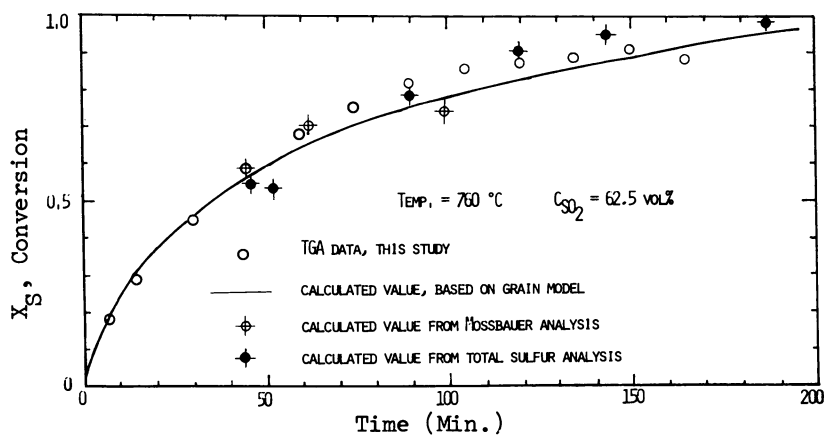


Figure 11. Comparison of the experimental data with the calculated values for pellets with size of 1.5 x 6.0 mm.

The key factor in the development of a commercial hot-gas desulfurization process is the regeneration of the spent sorbent. Two methods are discussed here: regeneration with an air-SO₂ mixture and regeneration with a steam-air mixture. The reaction of iron sulfide with air is very fast and exothermic, and forms Fe₂O₃ and SO₂ as the only products. Consequently the reaction rate is largely controlled by the pore diffusion mechanism. Reactions of iron sulfide with SO₂ and with steam are relatively much slower, and form Fe₃O₄ and elemental sulfur. The overall rate in these cases is largely controlled by the intrinsic chemical reaction.

Acknowledgments

The financial assistance for this work is provided by the U.S. Department of Energy, Morgantown Energy Technology Center.

Literature Cited

1. MERC Hot Gas Cleanup Task Force, "Chemistry of Hot Gas Cleanup in Coal Gasification and Combustion," MERC/SP-78/2, February 1978.
2. Lewis, P. S.; Shultz, F. G.; Wallace, W. E. Jr., "Sulfur Removal from Hot Producer Gas," presented at the 166th National Meeting, ACS Div. Fuel Chem., Chicago, Aug. 26-31, 1973.
3. Jenkins, D. M.; Lemmon, A. W. Jr., "Supplemental Report on Evaluation of High-Temperature Desulfurization Systems for Low- and Intermediate-Btu Gas," Battelle Columbus Labs. for the Tennessee Valley Authority Power Research Staff, Dec. 31, 1975.
4. Oldaker, E. C.; Gillmore, D. W., 172nd National Meeting, ACS, Div. Fuel Chem. Preprints 1976, 21(4), 79.
5. Grindley, T.; Steinfeld, G., "Development and Testing of Regenerable Hot Coal Gas Desulfurization Sorbents," Report DOE/MC/16545-1125 (DE82011114), Oct. 1981
6. Karr, C.; Rahfuse, R. V. Jr.; Langdon, P. E., J. Appl. Chem. Biotechnol 1972, 22, 613.
7. Schrodt, J. T.; Best, J. E., A.I.Ch.E. Symp. Ser. No. 175 1978, 74, 184.
8. Joshi, D.; Olson, J. H.; Hayes, M. L.; Shah, V., "Hot, Low-Btu Producer Gas Desulfurization in Fixed-Bed of Iron Oxide-Fly Ash," USDOE Contract FE-77-3-01-2757, Final Report, June 1, 1979.
9. Tamhankar, S. S.; Hasatani, M.; Wen, C. Y., Chem. Engng. Sci. 1981, 36, 1181.
10. Tseng, S. C.; Tamhankar, S. S.; Wen, C. Y., Chem. Engng. Sci. 1981, 36, 1287.

11. Fukuda, K.; Dokiya, M.; Kameyama, T.; Kotera, Y., Ind. Eng. Chem. Fundam. 1978, 17, 243.
12. Worrell, W. L.; Kaplan, H. I., in Heterogeneous Kinetics at Elevated Temperature, Plenum Press, 1979, p. 113.
13. Szekeley, J.; Evans, J. W.; Sohn, H. Y., "Gas-Solid Reactions," Academic Press, New York, 1976
14. Levenspiel, O., "Chemical Reaction Engineering," 2nd Edn., Wiley, New York 1972, p. 372.
15. Turkdogan, E. T., Trans. Met. Soc. AIME 1968, 242, 1655.
16. Worrell, W. L.; Turkdogan, E. T., Trans. Met. Soc. AIME 1968, 242, 1673.

RECEIVED December 7, 1982

INDEX

A

- Absorber**
 coal gasification methane recovery, dimensions and characteristics 241, 242*t*
 H₂S sorption by iron oxide reaction 265
- Absorption**
 carbon dioxide, after sulfur removal 40, 42–44*f*
 carbonyl sulfide by liquid CO₂ 33, 35, 36*f*
 properties of physical absorbents 37*t*
 slurry, carbon dioxide removal 42, 43*f*
 and stripping process, methane recovery, description 236, 240*f*, 241–45
 sulfur by liquid CO₂ 33, 34*f*, 35
 TGA studies of H₂S reactions of iron oxide sorbent 262, 264*f*
- Acetone**, effective molar or partial molar volume of CO₂ 55*t*
- Acid gas removal—See AGR**
- Activation energy**, diffusion 92
- Adsorbate loading**, average, equation 174
- Adsorbent**
 dimensionless temperature profiles 185–92
 dimensionless temperature, equation for non-isothermal LDF model 174, 176
 paraffin separation 159
 PSA process, carbon-based molecular sieve 156
 regeneration time effect on product quality 230, 231*f*
 suitable, characteristics 146
 temperature profile, complete heat transfer control 177
- Adsorbent mass**, gas sorption kinetics 173
- Adsorption bed**, two component mixture, PSA cell model 197
- Adsorption capacities**, nitrogen clinoptilolite adsorption 226, 228*f*, 229*f*
- Adsorption**
 gas
 criteria for when to use 146
 process state of the art 145–69
 purification process 162
 various commercial processes 147–67
 gas separation, future directions 164, 166–67

Adsorption—Continued

- isotherm, N₂ on clinoptilolite 218*f*
 isothermal, kinetics equation 177
 relative, methane and nitrogen clinoptilolite adsorption 215, 220, 221*t*
 selective, methane and nitrogen zeolite separation 213–32
- Adsorption bed**, two component mixture, PSA cell model 197
- Adsorption capacity**, nitrogen clinoptilolite adsorption 226, 228*f*, 229*f*
- Adsorptivity**, effect of pressure 154
- Advantages**, PSA processes 152
- AGR**
 Claus plant process 29
 CNG process description 30–35
 CO₂ condensation 33–35
 coal gasification, problems 29
 discussion and applications 27–28
 membrane separation from methane process 28, 30
- Air**
 oxidation regeneration of sulfided sorbent 261
 oxygen enrichment by membrane process 142
- Argon**, apparent heats of adsorption over various clinoptilolites 216*t*
- Arrhenius rate expression**, diffusion coefficient 93
- Assink**, NMR studies of sorption and transport in glassy polymers 106
- Axial pressure profile**, PSPP process 156

B

- Bead activated carbon**, use in solvent vapor removal 164
- Benzene**
 effective molar or partial molar volume of CO₂ 55*t*
 methane solubility at various pressures 236, 237*t*
- Bergbau Forschung** nitrogen production process 158*f*
- BET surface area**, correlation with ion exchange degree in clinoptilolite 216*t*
- Biot number**
 dimensionless uptake equation 176
 effect on dimensionless temperature profiles 191*f*, 192
 effect on uptake curves 185, 190*f*

- Blowdown equations, PSA cell
model 200, 201
- Boundary conditions, kinetics, LDF
model 174
- Butane
hydrogen recovery from isobutane
production 140, 141f
methane solubility at various
pressures 236, 237t
- C**
- Calcium
effect on clinoptilolite nitrogen
retention 223f, 224f
regeneration product in H₂S
removal 360t
- Calibration, problems in gas trans-
mission studies 77, 78
- Carbon-13 NMR
PVC-TCP systems 95f
relaxation rates 94, 96t
- Carbon, activated bead, solvent
vapor removal 164
- Carbon dioxide
cellulose acetate permeation rates
and separation factors 134, 135t
condensation in AGR process 33-35
in conditioned polycarbonate 120f
crystallization in CNG process 38-40
dew point in water-free crude gas 33, 34f
effect of mixed gas on
permeability 62, 63f
effective molar or partial molar
volume in various
environments 55t
liquid, physical properties 35-36f
permeability and time lag data for
gas transmission study 80, 81t
phase diagram 32f
in polycarbonate, sorption
isotherm 117, 118f
pressure effect on relaxation rate
and apparent diffusion coeffi-
cient in PVC 104, 105f
PVC sorption ranges 103
recovery use in enhanced oil
recovery 136
regeneration by triple point
crystallization 35-41f
removal
from natural gas 135
after sulfurous compound
absorption 40, 42-44f
slurry absorption 42, 43f
solid, solubility in various solvents 42, 43f
sorption and transport parameters
in lexan polycarbonate 65f
time lag diffusion in polycarbonate 122f
transport process in SRM 1470 83
triple point crystallization 39f
- Carbon disulfide, recovery, fluidized-
bed process 164
- Carbon monoxide
cellulose acetate permeation rates
and separation factors 134, 135t
effect of concentration of TCP
in PVC 98f
PVC-TCP gas transport and C-13
NMR parameters 96t
- Carbon tetrachloride, effective molar
or partial molar volume of CO₂ 55t
- Carbonyl sulfide, absorption by
liquid CO₂ 33, 35, 36f
- Cation deficiency, effect in naturally
occurring clinoptilolite 214
- Cell model, PSA light gas
separation 197-210
- Cellulose acetate membrane
cross section 127f
data 134, 135t
discussion 126, 127f
effect of hydrocarbons 131
hydrogen recovery 140-42t
water vapor removal 139
- Chain separation, activation energy
of diffusion 92
- Chain stiffness 92
- Chemical reaction, effect on adsorp-
tion rate in grain model 271
- Chemisorption, AGR process 28
- Chlorobenzene, effective molar or par-
tial molar volume of CO₂ 55t
- Chromatography, commercial gas
separation process 162, 163f
- Claus process
AGR process 29
desulfurization process conversion
to elemental sulfur 261
reactions 268
- Clinoptilolite
See also Zeolite
characterization 214
ion exchange, degree correlated
with surface area and separa-
tion ability 216t
- Closed cycle unit, triple point
crystallization 38, 39f
- CNG process
CO₂ crystallization 38-40
description and features 30-45
final CO₂ removal 40, 42-44f
- CNG Research Company, proprietary
AGR process development 28
- Coal gasification
AGR process development goals 30
gas composition 29
major contaminant 255
membrane hydrogen recovery 140
products 235
system schematic 256f

- Cobalt, regeneration product in
 H₂S removal 360*t*
- Concentration dependence
 local diffusion coefficient 57
 polymer properties, matrix model .. 113
 sorption and transport model 99
- Concentration dependence model,
 sorption and transport in glassy
 polymer system 112
- Concentration polarization, erratic
 permeability coefficient 14
- Concentration profile, triple-point
 crystallizer 40, 41*f*
- Condensation, CO₂ in AGR process .. 38–40
- Conditioning, penetrant induced in
 glassy polymers 48–57
- Contaminants, trace, coal gasification 29
- Conversion time, equations for
 grain model 271
- Conversions, H₂S, various sorbents 256
- Cooperative main chain motions
 effect on diffusion coefficient of
 glassy polymers 114
 in PVC-CO₂ 101, 104
- Copper, regeneration product in
 H₂S removal 360*t*
- Cost, criteria used in H₂S sorbent
 selection 256
- Crystallization
 CO₂ in CNG process 38–40
 triple point, CO₂ 35, 41*f*
- Cycles, gas adsorption process 147–52
- Cyclohexane, methane solubility at
 various pressures 236, 237*t*
- D**
- Density, adsorbent mass, LDF model 173
- Dew point, CO₂ in coal gasification 33, 34*f*
- Diffuse movements, polymer penetrant
 molecules 60
- Diffusion
See also Transport
 clinoptilolite adsorption of mixed
 gas systems 220, 222–24*t*
 effect of cooperative main-chain
 motions 97, 104
 mechanism in polymers 93–104
 mixed gas, zeolite 222, 224*f*
 molecular model of gases in a
 polymeric matrix 91–93
 rate determining step 92
- Diffusion coefficient
 apparent
 effect of CO₂ pressure in
 PVC 104, 105*f*
 effect of concentration of
 TCP in PVC 98*f*
 H₂ and CO 94, 96*t*
 Arrhenius form 91
 clinoptilolite nitrogen and methane
 adsorption 219*f*, 220, 221*t*
- Diffusion coefficient—*Continued*
 concentration dependency 59
 effect of main chain molecular
 motions 104
 equation 93
 glassy polymers 114, 115
 methane and nitrogen, measure-
 ment apparatus 217*f*
 simplified expressions 115, 116
- Diffusivity
See also Permeability
 effective, various grain model
 reactions 276*t*
 gas in glassy polymers 115
 intraparticle, use in nitrogen
 production 156
- Dimensionless time, pressurization
 step in PSA cell model 200
- Dimethyl ether, physical properties ... 37*t*
- Disadvantages, PSA processes 152
- Displacement purge cycle
 discussion 159–62, 166
 gas adsorption processes 149, 150*f*
- Distillation vs. gas adsorption,
 when to use 146
- Dual mode model
 discussion, Raucher and Sefcik
 and Assink NMR study 66
 permeability pressure
 dependence 119, 120*f*
 sorption and transport,
 discussion 100, 101, 106–8
- E**
- Efficiency, criteria used in selecting
 sorbent for H₂S removal 256
- Elf Aquitaine chromatographic
 separator 163*f*
- Enhanced oil recovery, application
 for membrane systems 136
- Energy calculations, various, coal
 gasification absorption and strip-
 ping methane recovery process 245–47
- Energy efficiency, physical absorption
 AGR processes 29
- Energy requirement, absorption and
 stripping methane recovery
 processes 243, 245*t*
- Enrichment
 helium, various feed gas
 compositions 14, 16*f*–20*f*
 light component in PSA single
 column process 202
- Enrichment permeabilities and separa-
 tion factors, helium 14–21
- Equations
 permeability of membrane 6, 8, 9*t*
 various, PSA cell model 199–204
- Equilibrium parameter
 dimensionless uptake equation 176

- Equilibrium parameter—*Continued*
 effect on dimensionless temperature profiles185, 189*f*
 effect on the uptake curves185, 188*f*
 Ethane, cellulose acetate permeation rates and separation factors ..134, 135*t*
 Ethanol, methane solubility at various pressures236, 237*t*
 Ethylene, effect on CO₂ sorption 62

F

- Feed composition, effect on enrichment in two column PSA process 208
 Fickian diffusion model, sorption mass transfer 172
 Fick's law
 concentration dependent equation .. 99
 diffusion equation 131
 dual mobility transport model 57
 transport of gases in polymers 90
 Flow rate
 effect on membrane gas enrichment136, 138*f*
 various component gases in absorption and stripping methane recovery process 244*t*
 Fluidized-bed/moving-bed process, solvent vapor removal164–66
 Flux
 characterization of SRM 76
 effect of mixed gas 48
 glassy polymer 57
 membrane separations14, 131
 reductions by non interacting penetrants 62
 steady state, equation 90
 time dependent decline138*f*, 139
 Fourier conduction, adsorbent heat transfer 172
 Frequency motions, high and low, polymer diffusion 92
 Fuel, synthetic, AGR step in production from coal 28

G

- Gas
 adsorption process
 description145, 147, 148*t*
 bulk separation
 process148*t*, 152–62, 164, 166–67
 coal gasification, TGA study of iron sorbent reactions 262
 composition effect on separation efficiency132–34
 control of solubility coefficient in polymer interactions 113
 crude coal gasifier 28
 deep sea diving, feed gas composition 6
 dehydration by membranes 139

Gas—*Continued*

- enrichment and recovery in single column PSA process205, 206*f*
 enrichment and recovery in two column PSA process205, 207*f*
 feed, composition for helium recovery 6*t*
 light, PSA recovery and purification195–210
 mixed
 dual sorption and transport model61–64
 effect on permeability 48
 non-isothermal sorption kinetics171–94
 purification148*t*, 162
 residual and permeate stream compositions related to stage cut136–38*f*
 separation
 basic equations131, 132
 mechanism 126
 parameters affecting efficiency132–34
 technical breakthrough in the application of membranes .. 126
 sorbed molecules, effect on polymer equilibrium 103
 sorption by glassy polymers, molecular environments 52
 Standard Reference Materials for transmission measurements75–88
 synthesis, solubility of solid CO₂ ..42, 43*f*
 transport and C-13 NMR parameters, PVC-TCP 96*t*
 transport mechanism in glassy polymers 89
 treatment in CNG AGR process 31*f*
 two component mixture, PSA cell model 197
 Gasification, AGR step in synthetic fuels production 28
 Gas oil, methane solubility at various pressures236, 237*t*
 Gas/polymer matrix model
See also Matrix model
 gas sorption and transport polymers112–16
 Grain model
 chemical reaction control conditions 273*f*
 correlation of kinetic data for H₂S iron oxide sorption 271
 pore diffusion control conditions 274*f*
 schematic diagram 272*f*
 validity 275

H

- Heat of adsorption
 measurements for clinoptilolite methane and nitrogen separation214, 215, 216*t*
n-pentane uptake on zeolite 180

- Heat capacity
 adsorbent mass, LDF model 173
 liquid-solid slurry absorbent 40
- Helium
 cellulose acetate permeation rates
 and separation factors 134, 135*t*
 enrichment
 permeabilities and separation
 factors 14-21
 various feed gas
 compositions 14, 16*f*-20*f*
 and methane separation, effect of
 pressure on single column
 PSA 208*t*
 recovery
 experimental loop schematic 2, 4*f*, 5*f*
 as function of pressure drop 14, 15*f*
 hypothetical system 21-23*f*
 membranes 1-24
 purity goals and requirements 3
- Henry's law
 concentration dependent equation 99
 diffusion equation 131
 glass polymer conditioning 52
 polymer penetrant mode 60
 transport of gases in polymers 90
- Heat transfer coefficient, external,
 zeolite LDF model 184
- Heat transfer resistance, effect on
 uptake curves 180
- Hexane, methane solubility at
 various pressures 236, 237*t*
- High pressure channel spacer, spiral-
 wound elements 128
- Hollow fiber, configuration of
 membrane elements 128
- Hydrocarbons
 effect on cellulose acetate
 membranes 131
 gas stream dehydration by cellulose
 acetate membranes 139
- Hydrogen
 cellulose acetate permeation rates
 and separation factors 134, 135*t*
 effect of concentration of TCP
 in PVC 98*f*
 PVC-TCP gas transport and C-13
 NMR parameters 96*t*
 recovery 140-42*t*, 166
- Hydrogen sulfide
 cellulose acetate permeation rates
 and separation factors 134, 135*t*
 removal from coal gasification
 products 255-78
 removal from natural gas 135
- I**
- Inert purge cycle,
 discussion 147, 159-62, 166
- Inhomogeneity, obstacle to the devel-
 opment of better SRM's 85
- Integrity verification,
 membranes 11, 12*f*, 13*t*
- Interchain cohesion 92
- Intersegmental gaps, polymers, redis-
 tribution by high pressure
 penetrants 52
- Ion exchange, clinoptilolite, degree
 correlated with surface area and
 separation ability 216*t*
- Iron, regeneration product in
 H₂S removal 360*t*
- Iron oxide
 results of steam regeneration
 reaction 270
 sorbent for high temperature
 H₂S removal 255-78
 sulfided, effect of temperature on
 weight loss in SO₂ atmospheres 266*f*
 weight change curve of reaction
 with simulated coal gas 276*f*
- Iron sulfide, reaction with SO₂ 276*f*
- Isooctane, zeolite uptake data, LDF
 kinetics model 178, 192
- Isomer separation processes,
 discussion 159-63*f*
- Isomerization process, total, paraffin
 separation 159, 161*f*
- IsoSiv process, paraffin separation 159
- Isosteric enthalpy of sorption, effect of
 sorbed gas concentration 114
- Isotherm
 adsorption of N₂ on clinoptilolite 218*f*
 equations for PSA cell model 199
 sorption, CO₂ in polycarbonate 117, 118*f*
 sorption, matrix vs. dual mode
 model for glassy polymers 118*f*
- Isothermal model, estimation of
 diffusivity dependence 185
- K**
- Kinetics
 adsorption, non-isothermal LDF
 model equations 173-78
 criteria used in H₂S sorbent
 selection 256
 high temperature H₂S sorption by
 iron oxides 262-70
 high temperature H₂S sorption by
 selected metal oxides 256, 258*f*
 mathematical models, non-iso-
 thermal sorption 172
 methane and nitrogen clinoptilolite
 adsorption 215, 220
- Knudsen effect, effective thermal
 conductivity 180

L

Langmuir, polymer penetrant mode ..	60
Langmuir isotherm, glassy polymer conditioning ..	52
Langmuir sorption capacity	
CO ₂ in various polymers, experimental compared with	
calculated ..	58f
glassy polymers ..	53, 54f
Langmuir system, equilibrium parameter ..	185
LDF model, non-isothermal ..	173
Lewis number, modified, reciprocal dimensionless uptake equation ..	176
effect on dimensionless temperature profiles ..	185, 187f
effect on uptake curves ..	185, 186f
Linear driving force model ..	173

M

Main chain motions	
C-13 rotating-frame relaxation rates ..	94
effect on diffusion of gases ..	97
of PVC, effect of CO ₂ ..	101
Magnetite, product of pyrrhotite and SO ₂ in iron oxide regeneration ..	265
Manganese, regeneration product in H ₂ S removal ..	360t
Manometers, electronic measuring technique to monitor gas flux ..	76
Mass balance, methane and nitrogen PSA clinoptilolite process ..	226, 227f
Material balance, equations, PSA cell model ..	199, 204
Mathematical model, behavior of adsorbent columns ..	173
Matrix model	
<i>See also</i> Gas polymer matrix model permeability pressure dependence ..	119, 120f
Mechanism	
glassy polymer diffusion ..	101-4, 112
high temperature H ₂ S sorption by iron oxides ..	262-70
in polymer diffusion ..	93-101
Mean free paths, isoctane and <i>n</i> -pentane, LDF model ..	184
Membranes	
cellulose acetate	
cross section of asymmetric ..	127f
effect of water ..	21
flat-sheet preparation ..	126
permeation and selectivity data ..	134
spiralwound semipermeable ..	6, 7f
definition of permeability ..	6
effect of high pressure drop ..	14
gas separations for chemical processes and energy applications	125-42

Membranes—Continued

integrity verification ..	11, 12f, 13t
parameters affecting gas separation efficiency ..	132-34
semipermeable, helium recovery ..	1-24
spiralwound, discussion ..	128-31
various applications for gas separations ..	135-42t
various element configurations ..	128-31
Methane	
apparent heats of adsorption over various clinoptilolites ..	216t
cellulose acetate permeation rates and separation factors ..	134, 135t
diffusion coefficient in clinoptilolite adsorption ..	219f, 221
effect on clinoptilolite nitrogen adsorption ..	222, 224t
and helium separation effect of pressure on single column PSA ..	208t
membrane AGR ..	135
separation from H ₂ and CO by adsorption and stripping process ..	235-46
variables for PSA on clinoptilolite ..	226, 227t, 228f, 229f
zeolite adsorption ..	213-32
Methanol	
methane solubility at various pressures ..	236, 237t
physical properties ..	35-37t
Methyl acetate, effective molar of partial molar volume of CO ₂ ..	55t
Model	
cell, PSA light gas separation ..	197-210
dual mobility transport ..	57
glassy polymers, matrix vs. dual mode ..	118f, 120f, 122f
non-isothermal sorption kinetics ..	172
Mole fraction, various component gases in absorption and stripping methane recovery process ..	244t
Mole fraction profile, PSA cell model ..	200-203
Molecular environments, gas sorption by glassy polymers ..	52
Molecular sieve	
carbon based, PSA process adsorbent ..	156
paraffin separation adsorbent ..	159
Molecular theory, diffusion of gases in a polymeric matrix ..	91
Molybdenum, regeneration product in H ₂ S removal ..	360t
Mössbauer analysis, sulfided iron oxide regeneration ..	265, 267t
Moving bed processes, future growth	166
Multiple bed process, PSPP ..	154

- N**
- Naphtha, heavy, methane solubility at various pressures 236, 237*t*
- Nickel, regeneration product in H₂S removal 360*t*
- Nitrogen
- apparent heats of adsorption over various clinoptilolites 216*t*
 - cellulose acetate permeation rates and separation factors 134, 135*t*
 - diffusion coefficient in clinoptilolite adsorption 219*f*, 221
 - effect of methane on clinoptilolite adsorption 222, 224*t*
 - permeability and time lag data for gas transmission study 80, 81*t*
 - permeation rate related to membrane integrity 11, 13*t*
 - production by PSA
 - process 156, 158*f*–60*f*, 164
 - related to helium enrichment 16*f*, 18*f*, 19*f*
 - variables for PSA on clinoptilolite 226, 227*t*, 228*f*, 229*f*
 - zeolite adsorption 213–32
- NMR, Assink study, support of dual mode model 66
- O**
- Octane, methane solubility at various pressures 236, 237*t*
- OlefinSiv, butene separation process .. 162
- Oxygen
- enrichment of air by membrane process 142
 - permeability and time lag data for gas transmission study 80, 81*t*
 - recovery by PSA, future 164
 - related to helium enrichment 16*f*, 18*f*, 19*f*
- P**
- Paraffins, separation by displacement purge and inert purge cycles 159, 161*f*
- Parameters, operating, typical spiralwound membrane units 131
- Parametric pumping 154
- Partial immobilization model, gas transmission study 83
- Penetrant
- diameter effect on activation energy of diffusion 92
 - effect on polymer cooperative motions 103
 - glassy polymers, effective molecular volume 53, 54*f*
 - induced conditioning in glassy polymers 48–57
- Pentane, methane solubility at various pressures 236, 237*t*
- n*-Pentane, zeolite uptake data, LDF kinetics model 178, 192
- Permeability
- See also* Diffusivity
 - calculated, matrix vs. dual mode models 119, 120*f*
 - coefficients, helium 14, 21
 - comparative data 13*t*
 - data, H₂ and CO in PVC-TCP 96*t*
 - effect of various mixed gas concentrations 62, 63*f*
 - glassy polymer, various partial pressures 48, 49*f*
 - membrane, equations 6, 8, 9*t*
 - SMR study, various gases 82*f*
- Permeability coefficient, steady state equation 90
- Permeability data, SRM evaluation study 80, 81*t*
- Permeance—*See* Permeability
- Permeate channel spacer, spiralwound elements 128
- Permeate enrichment, effect of feed composition 133*f*
- Permeate tube, spiralwound elements 128
- Permeation
- See also* Transport
 - mixed gas, dual mode sorption and transport models 47–71
- Permeation rates, various gases in cellulose acetate membranes 134
- Permselectivity, membranes, discussion 8, 11*t*, 19*f*, 20*f*, 22*f*
- PET
- CO₂, Langmuir sorption capacity .. 56*f*
 - gas transmission study, various gases 77
 - permeabilities and related quantities of various materials 84*t*
 - SRM inhomogeneity 83
- Phase diagram, CO₂ 32*f*
- Physical absorption, AGR process 28, 29
- Physical model, glass polymers
- conditioning 52
- Physical strength, criteria used in selecting H₂S sorbent 256
- Plasticization
- effect on permselectivity of membranes 48
 - rubber polymers vs. glassy polymers 59
- Plate and frame, configurations of membrane elements 128
- Poly(acrylonitrile), CO₂ Langmuir sorption capacity 56*f*
- POLYBED PSA process 152, 153*f*
- Poly(benzyl methacrylate), CO₂ Langmuir sorption capacity 56*f*
- Polycarbonate
- CO₂ Langmuir sorption capacity 56*f*

- Polycarbonate—*Continued*
 CO₂ sorption isotherm 117, 118f
 CO₂ in conditioned 120f
- Poly(ethyl methacrylate), CO₂ Langmuir sorption capacity 56f
- Poly(ethylene terephthalate)—*See* PET
- Polymer
 conditioning 103
 effect of high gas conditioning pressures 52
 glassy
 concentration dependent sorption and transport models 104–9
 conditioned nonequilibrium 52
 diffusion coefficient equation 115
 dual mobility transport model 57
 equilibrium densified 52
 gas transport and cooperative main chain motions 89–110
 Langmuir sorption capacity 53, 54f
 mathematical expression of sorption 117
 matrix and dual mode models as physical models 121
 matrix sorption and transport model 111–24
 penetrant induced conditioning 48
 segmental motion 49, 51f
 sorption and transport 97–109, 115
 various, CO₂ Langmuir sorption capacity 56f
 high and low frequency diffusion motions 92
 mathematical expression of gas transport 117, 119–21
- Polymer chains 91, 92
- Poly(methyl methacrylate)
 CO₂ Langmuir sorption capacity 56f
 effect of ethylene on CO₂ sorption level 63f
- Poly(phenyl methacrylate, CO₂ Langmuir sorption capacity 56f
- Poly(terephthalate), local effective diffusion coefficient for CO₂ 58f
- Polyvinyl chloride, CO₂ diffusion coefficient 59
- Pore accessibility, clinoptilolite 214, 215, 217f
- Pore diffusion, effect on rate in grain model 271
- Pressure
 effect on adsorptivity 154
 effect on permeability matrix vs. dual mode model 119, 120f
 effect on single column process for helium and methane separation 208t
 effect on time lag, matrix vs. dual model 121, 122f
 inside adsorbent mass, LDF model 173
- Pressure—*Continued*
 various component gases in adsorption and stripping methane recovery process 244t
 Pressure differential, factor in membrane gas separation 132
 Pressure profiles, PSPP process 156, 157f
 Pressure ratio, effect on separation efficiency 132–34
 Pressure sensors, calibration instability 78
 Pressure step, constant, equations for PSA cell model 201
 Pressure swing—*See also* PSA
 Pressure swing adsorption, recovery and purification of light gases 195–211
 Pressure swing cycle, gas adsorption process 149, 150f
 Pressure swing parametric pumping 152, 154–56
 Pressurization, equations, PSA cell model 200, 201
- Propane
 loss in absorption and stripping methane recovery 236, 238f, 238t
 methane solubility at various pressures 236, 237t
- PSA—*See also* Pressure swing
 PSA process
 basic comparison to Polybed PSA and PSPP 157t
 discussion 152–59, 164, 166
 methane and nitrogen clinoptilolite adsorption 222, 225f, 226–30
 single column bulk separation 196f, 202, 203
 two column bulk separation 198f, 203, 204
- Pumps, parametric, one-bed and three-bed pressure swing 155f
- PURASIV HR process, solvent vapor removal 165f
- Purification, gas 148t
- PVC
See also Poly(vinylchloride)
 antiplasticization-plasticization 93
 PVC-CO₂ system, cooperative main-chain motions 101, 104
 PVC-TCP system, gas transport and C-13 NMR parameters 96t
- Pyrrhotite, product of iron reaction with H₂S 265

R

- Rate constant, various grain model reactions 276t
- Reaction rate, representation for grain model 271
- Regeneration
 adsorber, PSA clinoptilolite process 230, 231f

- Regeneration—*Continued*
 criteria used in selecting H₂S
 sorbent 256
 in air, various H₂S sorbents 360*t*
 effect of water content on product
 distribution 269*t*
 options, hot gas desulfurization
 process 261
 reactions
 iron oxide by SO₂ recycle
 method 265–68
 sulfided iron oxide 268–70
- Relative humidity, gas, effect on
 separation process 134
- Relaxation rate
 C-13 NMR, PVC-CO₂ system 102*t*
 effect of CO₂ pressure in PVC 104, 105*f*
 effect of concentration of TCP
 in PVC 98*f*
 PVC-CO₂ system 101, 102*t*
- S**
- Selectivity, effective, effect of pressure
 ratio and membrane separation
 factor 133*f*
- Separation ability, correlation with ion
 exchange degree in clinoptilolite 216*t*
- Separation factor
See also Permselectivity
 effect on separation efficiency 132–34
 methane and nitrogen clinoptilolite
 PSA process 226, 228*f*, 229*f*
 various gases in cellulose acetate
 membranes 134
- Separation
 bulk gas processes 148*t*, 152
 bulk gas, PSA cell model 202, 203
 normal and iso-paraffins 159
- SEPAREX—*See* Cellulose acetate
 membranes
- Sewage wastewater treatment, mem-
 brane oxygenation systems 142
- Single bed process, PSPP 154
- Single column recovery process, PSA
 cell model 195
- Solubility
 methane, various solvents and
 pressures 236, 237*t*
 solid CO₂ in several solvents 42, 43*f*
- Solubility coefficient, gases in glassy
 polymers, equation 114, 116
- Solvent vapors, removal from air
 streams 164, 165*f*
- Sorbate mass transfer, LDF model 172
- Sorbent selection, high temperature
 H₂S removal from coal gasifi-
 cation products 256
- Sorption
See also Uptake
 adsorbent non-isothermality
 kinetics 172
- Sorption—*Continued*
 concentration dependence in glassy
 polymers 116
 concentration dependent model 104–9
 concept of unrelaxed volume 48–61
 dual mode vs. concentration
 dependent models 112
 dual mode model 48, 51*f*, 52, 60, 106–8
 equations 90
 glassy polymers 111, 117
 isooctane on zeolite 179*f*, 181*f*
 mixed gas model 61–64
n-pentane on zeolite 182*f*, 183*f*
 zero concentration, gas glassy
 polymer systems 115
- Sorption data, matrix model
 analysis 116–21
- Sorption model, various, discussion 99–101
- Sorption parameters, CO₂ in lexan
 polycarbonate 65*t*
- Spiralwound membrane element
 configuration 128–31
- SRM 1470—*See* PET
- SRM, gas transmission study,
 problems 85
- Stage cut, membrane gas separation,
 definition 136, 137*f*
- Standard Reference Material,
 definition 75
- Steam-air mixture, sulfided iron oxide
 regeneration 268–70
- Stoichiometric coefficient, various
 grain model reactions 276*t*
- Strippers, coal gasification methane
 recovery, dimensions and
 characteristics 241, 242*t*
- Sulfur capture capacity, criteria used
 in selecting H₂S sorbent 256
- Sulfur dioxide, sulfided iron oxide
 regeneration 265–68
- Sulfur, absorption by liquid
 CO₂ 33, 34*f*, 35
- T**
- Temperature
 gas, effect on the separation process 134
 glass transition, depression by
 diluents 114
 various component gases, absorp-
 tion and stripping methane
 recovery process 244*t*
- Temperature profiles
 adsorbent, dimensionless 185–92
 isooctane uptake on zeolite 180
n-pentane uptake on zeolite 180
- Temperature swing, gas processes 147, 162
- TGA curves, reactions of iron oxide
 in different gas atmospheres 265*f*
- Thermal conductivity, effective
 adsorbent mass, LDF model 173
 zeolites, LDF model 180

- Thermogravimetric analyzer (TGA),
use in study of reaction mechanisms and kinetics of H₂S sorption 262
- Time, dimensionless, various stages of PSA cell model 200, 201
- Time lag
diffusion of CO₂ in polycarbonate .. 122*f*
diffusion of a gas across a planar membrane 119, 121–22*f*
technique for measuring permeation gas 77
SMR study, various gases 80–82*f*
- Toray reverse PSA nitrogen production process 160*f*
- Transient transport measurements, validity of sorption and transport model 119, 121–22*f*
- Transmission
See also Permeation
calibration of SRM measurement system 77–79
rates in various packaging materials 76
study experimental design 79
- Transport
See also Diffusion
See also Permeation
concentration dependent model 104–9, 116
dual mode vs. concentration dependent models 112
equation, dual mode model 60
equations 90
glassy polymers 111, 117, 119–21
gas in PVC-TCP system 94–97
inconsistencies in dual mode model 106–8
mixed gas model 61–64
process, CO₂ in SRM 1470 83
transient state 119, 121–22*f*
zero concentration, gas glassy polymer systems 115
- Transport data
concept of unrelaxed volume 48–61
matrix model analysis 116–21
glassy polymer penetrant 57
various, discussion 99–101
- Transport parameters, CO₂ in lexan polycarbonate 65*t*
- Triple point
CO₂ crystallization 30, 35–41*f*
closed-cycle unit crystallization ... 38, 39*f*
- Tubular membrane element configurations 128
- Two-column recovery and purification process, PSA cell model 195

U

- Uptake
See also Sorption
complete heat transfer control equation 177
dimensionless, non-isothermal LDF model equation 174, 176
zeolite parametric study, LDF model 185–92

V

- Vacuum desorption, production of high purity nitrogen 156
Vapor phase process, commercial 159
Vapor pressure, various compounds in methane recovery 236, 238*f*
- Viscosity
gas, effect on the separation process 134
methanol and liquid CO₂ 35, 36*f*
- Volume
penetrant effective molecular, glassy polymers 53, 54*f*
unrelaxed, related to sorption and transport properties of glassy polymers 48–61

W

- Water
liquid, effect on membrane performance 21, 139
methane solubility at various pressures 236, 237*t*
removal, CNG AGR process 30, 33
vapor
cellulose acetate permeation rates and separation factors ... 134–35*t*
removal from hydrocarbon gas streams 139

Z

- Zeolite
See also Clinoptilolite
effective molar or partial molar volume of CO₂ 55*t*
isomer separations 159–63*f*
methane and nitrogen separation . 213–33
PSA process for nitrogen production 156–60*f*
sorption kinetics experimental data 178–92
- Zinc, regeneration product in H₂S removal 360*t*
- Zinc ferrite, sorbent for H₂S removal .. 260
- Zinc oxide, sorbent for H₂S removal from coal gasification products .. 256